Spectroscopic Characterization of Electronic and Magnetic Relaxation Phenomena in Molecular Systems

Thesis by

Ryan Dillon Ribson

In Partial Fulfillment of the Requirements

for the Degree of Doctor of Philosophy

CALIFORNIA INSTITUTE OF TECHNOLOGY

Division of Chemistry and Chemical Engineering

Pasadena, CA

2022

(Defended April 8, 2022)

Ryan Dillon Ribson
ORCID: 0000-0002-3755-5777

Sou pequenininho…

… mas eu vou chegar

- O Areia

Acknowledgments

It's a long road, and no one walks it alone. I've had the immense pleasure to work with and be inspired by so many people during my time at Caltech, and it's hard to put into words the impact that has had on my life and my career. First, I will thank my adviser, Prof. Ryan Hadt, who has given me the ability to explore diverse research interests and has supported me through and through. I would not be graduating if it weren't for you. I also owe so much to Prof. Theo Agapie, who was an immense mentor to me in my time here at Caltech. He pushed me to be critical and hardworking and to reach beyond my comfort zones to learn and think deeply. I would also like to thank Profs. Jonas Peters and Julie Kornfield, members of my committee, for their continued advice and support.

I'd like to thank some of the outstanding graduate students, postdoctoral scholars, and undergraduates I've overlapped with in the Agapie group, including Dr. Guy Edouard, Dr. Kyle Horak, Dr. Justin Henthorn, Dr. Davide Leonetti, Prof. Joshua Buss, Dr. Marcus Low, Dr. Jessica Sampson, Dr. Heui Beom Lee, Dr. Chris Reed, Dr. Nate Hirscher, Dr. Charlie Arnett, Dr. Gyeongshin Choi, Prof. Graham De Ruiter, Prof. Zhiji Han, Dr. Alejo Lifschitz, Dr. Siti Riduan, Dr. Arnaud Thevanon, Prof. Gwen Bailey, Prof. Manar Shoshani, Angela Shia, Anna Scott, Meaghan Bruening, Sam Xiong, Gavin Heim, Linh Le, and Mike He. I'd also like to thank those whom I've overlapped with in the Hadt lab, including Dr. Alec Follmer, Dr. Gautam Strocio, Dr. Daniel Bim, Dr. Brendon McNicholas, Ruben Mirzoyan, Jaron Tong, David Cagan, Kaitlin Luedecke, Nathanael Kazmierczak, Chris Totoiu, Wren Steifel, Kate Benson, Nate Lopez, and Grace Chen.

Dr. Gyeongshin Choi was my first mentor in graduate school and taught me the ins and outs of Schlenk line chemistry. Dr. Jay Winkler, Dr. Brian Sanders, and Dr. Oliver Shafaat all helped me to do experiments in BILRC and helped me in some of my first experiences running laser experiments. Hopefully, these were the first of many more to come. Dr. Mike Takase and Larry Henling provided incredible support in the crystallography center. Dr. David Vander Velde helped me run and troubleshoot numerous NMR experiments. Dr. Paul Oyala has been an incredible collaborator, running the EPR center here, and an incredible trivia partner.

Dr. Meaghan Deegan, Dr. Nina Gu, Dr. Matthew Chalkley, Dr. Javier Fajardo Jr., and Dr. David Schuman, thank you all for being friends and giving advice. It was incredible to start in a cohort with such amazing people.

Guy, I couldn't be the Batman, but I will always remember the chats, the jokes, and the advice that you gave me early on that has helped carry me through to the end. Chris, my first neighbor in Pasadena, I miss the hikes and adventures. You had my back at times when I was feeling so far down on myself, and I can't tell you how grateful I am for that.

Katie, thank you for margaritas, but most importantly thank you for your inquisitive and passionate spirit in the lab. We need more people in science like you, and I'm so excited to see what you do. Gautam, it felt like we were brothers in the Hadt lab. You were my first collaborator, and submitting that first paper together was a feeling I'll never forget. I miss getting the chance to grab beers, but I'm sure we'll have the opportunity again soon.

Manar, I can't tell you how much you've helped me. You were always there to talk, and your patience, kindness, and creativity I am still learning from today. You welcome people with

open arms and help to create the kind of community in science and beyond that's worth striving for. Can't wait to get to visit you in Texas.

Alec, wings and rings baby. You've always been willing to dig deep with me on the science, include me in your ideas and questions, and seek my advice, even if I didn't think I was capable myself. You are genuine, welcoming, and will stand up for what you think is right, and I've learned so much from just being around you. You've been a teacher and a brother to me through all this.

Jamie, you are the best roommate imaginable. Thank you for all the advice, help, and friendship you have given to me (and all the fried chicken, too). You're going to have to love Parsnip double for me when I'm gone. To Vera, Muito Tempo, and the rest of the Capoeira Batuque Pasadena crew, you took in a wounded wolf cub years ago, and I cannot repay the joy, kindness, and community you all welcomed me with. Thank you.

Finally, I'd like to thank my family. Mom and Dad, you have always been behind me, even if I sometimes made you worry. Cory and Danie, you always kept me connected and tethered. And Haley and Mochi, visiting home was always such a bright spot out of the year made even brighter by the two of you. I would have achieved nothing if it were not for all of you. I love you.

Thesis Abstract

The thesis herein describes the application of time-resolved spectroscopic techniques to the understanding of a variety of electronic and magnetic relaxation phenomena in molecular systems. Chapter I presents the techniques and theory behind transient absorption spectroscopy and electron paramagnetic resonance spectroscopy, which are two tools that are used throughout the thesis. Chapter II recounts the study of singlet fission in a series of bipentacene dipyridyl pyrrolides, including HDPP-Pent, Li_2(DPP-Pent)$_2$, and KDPP-Pent. Using transient absorption and kinetic modeling, we found that deprotonation and metal coordination induced a change in the rate of singlet fission (~7 fold increase going from HDPP-Pent to Li_2(DPP-Pent)$_2$) and ultimate triplet yield. Chapter III details the study of the temperature-dependent magnetic relaxation studies of S = ½ spin systems copper (II) phthalocyanine (CuPc) and vanadyl phthalocyanine (VOPc). Although the spin-lattice relaxation time (T_1) of CuPc is greater than that of VOPc at low temperatures (<30 K), the CuPc T_1's decline more substantially with temperature than those of VOPc, which we attribute to the increased spin-orbit coupling constant of Cu over V. Ultimately, the phase memory times (T_2) are T_1-limited in CuPc by 150 K, whereas room temperature coherence is observed in VOPc. In Chapter IV, 2,9-dialkyl substituted 1,10-phenanthroline complexes of Cu(I) are studied computationally to assign entatic energies to the steric contributions attributed to the ligand that dictate the electrochemical and photophysical properties of the complexes. We performed experimental validation of reduction potential, low-temperature emission bandwidth and excited state relaxation energies, and ^{3}MLCT lifetimes to support the computational work. In Chapter V, we present ongoing work toward the characterization of triplet and triplet pair states generated via singlet fission in HDPP-Pent, Li_2(DPP-Pent)$_2$, and KDPP-Pent

by time-resolved electron paramagnetic resonance spectroscopy in collaboration with Drs. Jens Niklas and Oleg Poluektov. Finally, in Chapter VI, we present data collected toward the photophysical characterization of a series of Ni(II) 2,2'-bipyridine aryl halide complexes synthesized by David Cagan, which are relevant for photochemical transformations. We provide supporting materials for Chapters II, III, and V in Appendices A, B, and C, respectively.

Published Content and Contributions

Ribson, R. D.; Choi, G.; Hadt, R. G.; Agapie, T. "Controlling Singlet Fission with Coordination Chemistry-Induced Assembly of Dipyridyl Pyrrole Bipentacenes." *ACS Cent. Sci.* **2020**, *6*, 2088 – 2096. https://doi.org/10.1021/acscentsci.0c01044

R.D.R. synthesized the dipyridyl pyrrole bipentacene ligand framework HDPP-Pent following a route developed by G.C., synthesized the Li and K complexes of the ligand, carried out all steady-state and time-resolved spectroscopies, performed all data analysis presented in the paper, and wrote the manuscript.

Follmer, A. H.; Ribson, R. D.†; Oyala, P. H.; Chen, G. Y.; Hadt, R. G. "Understanding Covalent versus Spin–Orbit Coupling Contributions to Temperature-Dependent Electron Spin Relaxation in Cupric and Vanadyl Phthalocyanines." *J. Phys. Chem. A.* **2020**, *124*, 9252 – 9260. https://doi.org/10.1021/acs.jpca.0c07860

R.D.R contributed equally to the manuscript with A.H.F., preparing the diamagnetically diluted polycrystalline samples of the S = ½ systems, characterizing with powder XRD, performing CW and pulsed EPR experiments, performing data analysis, and participating in writing the manuscript.

Strocio, G. D.; Ribson, R. D.; Hadt, R. G. "Quantifying Entatic States in Photophysical Processes: Applications to Copper Photosensitizers." *Inorg. Chem.* **2019**, *58*, 16800 – 16817. https://doi.org/10.1021/acs.inorgchem.9b02976

R.D.R. synthesized a series of Cu(I) bis-phenanthroline complexes and characterized them by cyclic voltammetry, low temperature luminescence, and steady-state and time-resolved optical absorption spectroscopy to support the theoretical findings of the paper. R.D.R. also helped prepare figures and edit the manuscript.

Table of Contents

List of Figures

List of Equations

List of Tables

Chapter I

Introduction

Introduction

Equilibrium has become an important concept in our models of chemistry and physics, allowing us to describe stable, stationary states of a physical system. Of importance to dynamic processes is how the system responds to a perturbation, or an input of energy, that pushes the system from its local equilibrium. For a molecule, this could be an absorption of a photon that places the molecule into an excited energetic state. If the molecule is perfectly isolated from its environment, the input energy remains within the molecule unless reemitted in the form of a photon. Due to coupling of the molecule with the environment, however, these excited states of the system are generally not persistent and will decay with time back toward either the ground state equilibrium or potentially toward a new equilibrium, which could take the form of a chemical change (e.g., isomerization, reactivity, etc.). This process by which energy is exchanged from the system under question to its environment is generally referred to as relaxation.[1–5] Understanding relaxation processes is key if we want to be able to control how energy input into a system can be transduced to do work. For molecular and materials systems, this could take the form of photoexcitation toward the generation of electron hole pairs that could be harvested for solar energy. Alternatively, the magnetic states of a molecular/material system can be manipulated with external fields for information storage and computing purposes.

This thesis explores disparate subjects, but all fall under the theme of understanding dissipative dynamics for a given application. Key tools are used to study these dynamic processes. As a result, we have dedicated this first chapter to descriptions of techniques that are endemic throughout this work: transient absorption (TA) spectroscopy and electron paramagnetic resonance (EPR) spectroscopy. We employed ultrafast TA measurements to study the evolution and relaxation of excited states in Chapters II, IV, and VI, looking at singlet fission in bipentacene

coordination complexes, Cu (I) bis-1,10-phenanthroline photosensitizers, and Ni (II) 2,2'-bipyridine complexes relevant to cross-coupling photocatalysis, respectively. In Chapter III, we employed continuous wave (CW) EPR and pulsed EPR to study magnetic relaxation in S = ½ qubit candidates copper (II) phthalocyanine and vanadyl phthalocyanine. In Chapter V, we explore the use of time-resolved EPR techniques to study high-spin triplet pair states that are generated via singlet fission.

Our discussion on TA spectroscopy centers around the general features observed in TA data and in the experimental setup required to perform data collection. For a rigorous theoretical treatment of TA, the reader is referred to other resources. For EPR, we delve into the origins of the spin Hamiltonian before discussing EPR spectroscopy and magnetic relaxation processes. We use the spin Hamiltonian formulation to fit data and frame our discussion on S = ½ systems in Chapter III. Additionally, we leverage the background presented here to explicitly derive the spin operators and Hamiltonian for triplet pair states, presented in Appendix C as companion to the singlet fission TREPR data of Chapter V.

Transient Absorption

Transient absorption (TA) spectroscopy is a technique used to probe the time-dependent absorption profile of a sample after it is excited by a pulsed laser.[6] The transient species generated by the excitation pulse can persist across a wide range of timescales, and we will focus on two: the ultrafast sub-picosecond regime and the nanosecond to millisecond regime. We will focus mostly on the general features of femtosecond transient absorption (fsTA) spectroscopy before detailing the spectrometer setup for fsTA and nanosecond transient absorption (nsTA) used in our lab. In common practice for fsTA, a narrow bandwidth pulsed laser source is used to provide the initial

excitation energy to the sample (the pump pulse), and a broadband white light pulse is used as the probe (Figure 1.1).

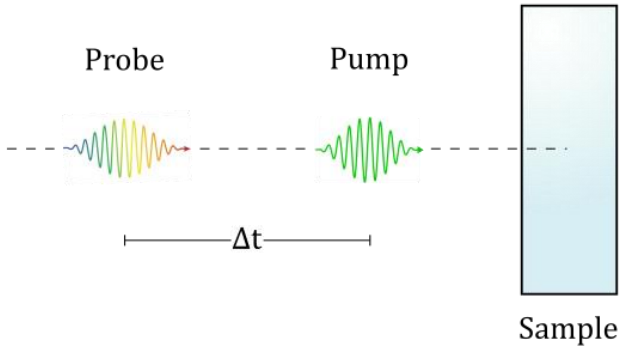

Figure 1.1 The narrow bandwidth pump and broad bandwidth probe pulses used in TA spectroscopy are spatially overlapped at the sample and then varied in temporal overlap (Δt) to generate the TA spectrum.

The pump and probe light are spatially overlapped at the sample such that the volume of sample that is excited by the pump pulse is also sampled by the probe. The timing delay (Δt) between the pump and probe may then be systematically varied to monitor the evolution of the absorption profile over time caused by the pump. Just as in steady-state absorption spectroscopy, the intensity of the various frequencies of light distributed in the probe will change by interacting with the sample. In this case, though, we have generated a nonequilibrium population in which a fraction of the molecules or species in our sample have been excited by the pump. As a result, the probe will be modulated by the presence of both ground and excited state species (Figure 1.2A).[6]

As we are interested in following the evolution of the excited states in the sample, the TA data is collected as a difference spectrum by subtracting the transmittance of light detected in a

shot with the pump on the sample ($T_{pump\ on}$) minus the intensity of light detected in a shot with the pump blocked from the sample ($T_{pump\ off}$), the latter of which should reflect the ground state absorption spectrum. This is written out in the equations below. The TA spectrum may be presented in terms of the change in transmittance (ΔT) or the change in absorbance (ΔA). All data presented in the following work is presented as ΔA or equivalently the change in optical density (ΔOD).

$$T = \frac{I}{I_0}$$

$$A = -\log(T) = \log\left(\frac{I_0}{I}\right)$$

$$\Delta T = T_{pump\ on} - T_{pump\ off} = \left(\frac{I}{I_0}\right)_{pump\ on} - \left(\frac{I}{I_0}\right)_{pump\ off}$$

$$\Delta A = A_{pump\ on} - A_{pump\ off} = \log\left[\left(\frac{I_0}{I}\right)_{pump\ on}\right] - \log\left[\left(\frac{I_0}{I}\right)_{pump\ off}\right]$$

$$\Delta A = \log\left[\left(\frac{I_0}{I}\right)_{pump\ on} \cdot \left(\frac{I}{I_0}\right)_{pump\ off}\right]$$

$$\Delta A = -\log\left(\frac{I_{pump\ on}}{I_{pump\ off}} \cdot \frac{I_{0_{pump\ off}}}{I_{0_{pump\ on}}}\right) \qquad Eqs.\ 1.1A - F$$

First, we define the standard expression for transmittance (T) and absorbance (A) in terms of the intensity of light after passing through the sample (I) and the intensity of light incident on the sample (I_0). Next, we define ΔT and ΔA in terms of the intensity of light passing through the sample with the pump on ($I_{pump\ on}$), the intensity of light passing through the sample with the pump off ($I_{pump\ off}$), the intensity of light incident on the sample with the pump on ($I_{0_{pump\ on}}$),

and the intensity of light incident on the sample with the pump off ($I_{0_{pump\ off}}$). As written in the expression for ΔA, the ratios $\frac{I_{pump\ on}}{I_{pump\ off}}$ and $\frac{I_{0_{pump\ off}}}{I_{0_{pump\ on}}}$ can be experimentally determined at a detection channel after the sample and at a reference detection channel, respectively.

The signal that arises in TA spectroscopy comes from the third-order nonlinear susceptibility in the light-matter interaction.[7] We will focus here on the general features observed in a transient absorption spectrum, which are ground state bleach (GSB), stimulated emission (SE), and excited state absorption (ESA), which is sometimes equivalently referred to as photoinduced absorption (PIA) (Figure 1.2). A GSB feature appears as a negative ΔA signal, generally aligns with the steady-state absorption profile of the sample and arises due to loss of ground state absorbing species due to the excitation. At a given wavelength in the bleach, there will be a greater number of photons passing through the sample with the pump on due to the reduction in population of ground state species than with the pump off ($I_{pump\ on} > I_{pump\ off}$), which leads to a negative ΔA signal as shown in the above expression. SE arises if the excited state species has an electric dipole-allowed transition back to the ground state. If this is the case, the radiation field in the probe can induce a transition from the excited state to the ground state along with the emission of a photon. As with the bleach, at a given wavelength in the SE feature, $I_{pump\ on} > I_{pump\ off}$ and SE will appear as a negative ΔA signal. ESA occurs when the radiation field of the probe pulse interacts with an excited state species generated by the pump and induces a dipole allowed transition from the excited state to an energetically higher lying excited state along with absorption of a photon. In this case, in the wavelength range covered by the ESA, $I_{pump\ on} < I_{pump\ off}$ and the ESA will appear as a positive ΔA signal (Figure 1.2B). The features in TA may have substantial overlap with each other.

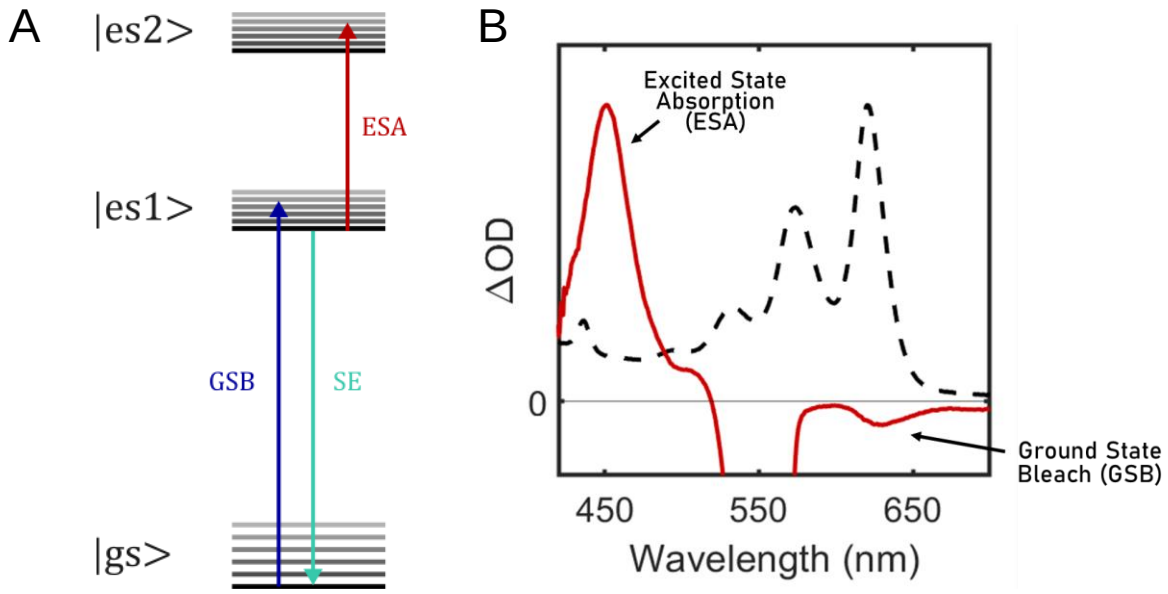

Figure 1.2 (A) A generalized Jablonski diagram depicting the various processes that can occur in TA spectroscopy. Here, we denote the ground state as |gs>, first excited state as |es1>, and the higher lying excited state as |es2>. **(B)** An example of the comparison between the ground state absorption spectrum (dashed black lines) and a time cut of the visible TA spectrum (solid red lines) of a pentacene derivative with a highlight given to the GSB and ESA features in the TA spectrum. The large negative feature centered around 550 nm is residual pump scatter.

Observing the change in intensity and spectral shape of the transient absorption features over time provides important kinetic information regarding the excited state relaxation processes at play in a given sample. For example, different excited states may exhibit distinct ESA features in the transient spectra, allowing us to ascertain which states may be populated following excitation and correlate their interconversion. The absolute assignment of an ESA feature is challenging, however, and requires supplementary experimental and/or computational validation.

Femtosecond Transient Absorption Setup

We will now discuss the experimental setup used throughout the work in this thesis to collect femtosecond transient absorption (fsTA) data in addition to some of the features of fsTA that are unique to probing ultrafast timescales. A general layout of the laser and fsTA spectrometer design is presented in Figure 1.3.

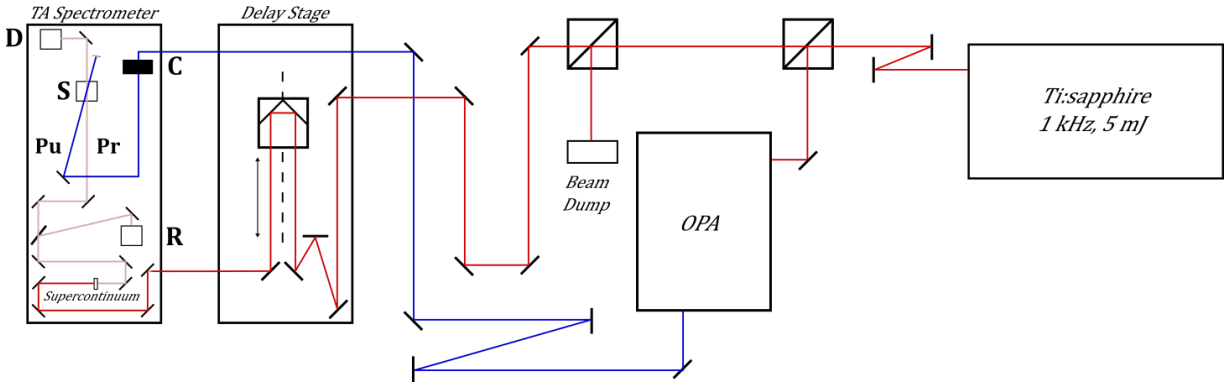

Figure 1.3 The general overview of the fsTA setup including Ti:sapphire laser source, OPA, delay stage, and TA spectrometer. Red lines represent 800 nm fundamental of the Ti:sapphire laser, blue represent variable wavelength output of the OPA used as the pump (**Pu**), and pink represent the supercontinuum probe (**Pr**). **D** ≡ detector channel, **S** ≡ sample, **C** ≡ chopper, **R** ≡ reference channel.

The source of both the pump and probe pulses utilized in the fsTA spectrometer is ultimately a femtosecond pulsed Ti:sapphire laser (Coherent Astrella, 5 mJ output, 1000 Hz repetition rate) with a maximum wavelength around 800 nm. The output of this Ti:sapphire laser is split by a 50:50 beamsplitter. Half of the beam is sent to an optical parametric amplifier (OPA, OPerA Solo), which is used to generate wavelength-tunable narrow bandwidth pump pulses, and the other half is used to generate the white light probe.

The OPA provides multiple options for the pump beam: either the signal or idler can be used directly or converted to higher frequencies via second harmonic generation (SHG), fourth harmonic generation (taking the SHG of the SHG), or sum frequency generation (SFG) by combining signal or idler with an additional portion of 800 nm light. With these options, the OPA can cover a wide range of output wavelengths from ~250 – 3000 nm.

The output of the OPA is routed into TA spectrometer (Helios Fire, Ultrafast Systems) where it is chopped using a mechanical chopper operating at 500 Hz, half of the repetition rate of the laser. The chopper functions to block every other shot of the pump so that the data can be divided into shots with pump on and shots with pump off. A neutral density filter allows for control over the final power incident at the sample.

The probe is generated using the other half of the 800 nm outputted from the Ti:sapphire laser. It is attenuated by another beamsplitter before being focused using telescoping lenses and routed into a physical delay stage. The delay stage consists of a set of mirrors mounted on a motorized track. Changing the position of the mirrors on the track changes the pathlength of the probe leg of the spectrometer and ultimately the timing between the arrival of the pump and probe pulses at the sample (Δt). The timing available is such that Δt's may be sampled in a positive (probe arrives at the sample after the pump) and negative (probe arrives at the sample before the pump) with time zero being the point at which pump and probe are directly overlapped in time at the sample. In a standard run, the time window (maximally out to 7.7 ns) can be selected and the delay stage is progressively moved along as a function of collection, building each time point successively. After the delay stage the 800 nm light is passed through an iris and neutral density filter onto a supercontinuum generating medium. The medium is different depending on the

wavelength range required of the probe spectrum (e.g., a CaF_2 plate is used for UV probe generation from 300 – 700 nm, a sapphire plate for visible probe generation from 400 – 800 nm).

There are three probes available: UV, visible, and NIR. Once the supercontinuum is generated it is passed through a filter to remove excess 800 nm light, and it is split into half that is focused through the sample and half that is focused into a reference channel. In both the sample and reference channels, a confocal mirror focuses the probe onto a fiber optic that leads to a diffraction grating and ultimately to a CCD array detector. The UV and visible probes utilize the same set of sample and reference detectors, and the NIR channel utilizes its own gratings and detectors.

Other Features in Femtosecond Transient Absorption Spectra

There are several other phenomena that impact fsTA datasets, some of which are unique to this ultrafast technique. The first we will discuss is group velocity dispersion (or temporal chirp), then cross-phase modulation, two-photon absorption, and stimulated Raman effects. Because we use a broadband probe, there are a wide range of wavelengths traveling in the white light pulse. In condensed media, the speed of light is not uniform but rather dependent on the wavelength of light. The result of this is that the blue end of the probe moves at a higher velocity than the red end. In other words, the shorter wavelength light will reach the sample and hit the detector at earlier times than the longer wavelengths in the probe. The chirp spreads the wavelengths of the probe on the time scales of hundreds of femtoseconds, and as a result, time zero in the spectrum will also be wavelength dependent. This effect is not distinguishable in spectroscopies with slower time resolution but contributes to the data matrix collected in fsTA.[8]

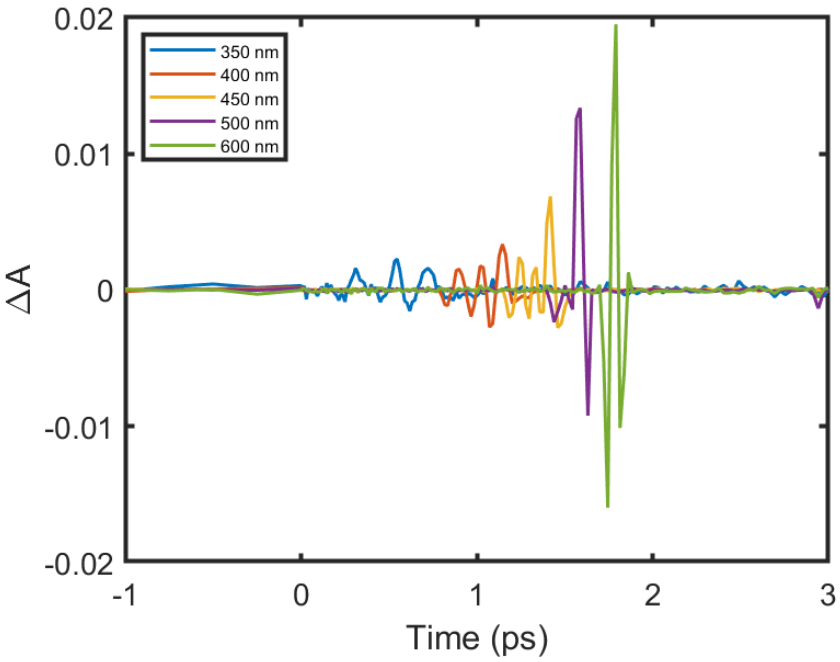

Figure 1.4 A plot of XPM observed in a THF sample with 550 nm pump along the time axis at 350, 400, 450, 500, and 600 nm. The temporal chirp can be observed as time zero is dependent on wavelength. The shape and width of the XPM signal is also dependent on the chirp.

Cross-phase modulation (XPM) is a nonlinear effect that occurs in fsTA because of the high photon densities available in the femtosecond pulses. XPM occurs in the probe pulse when it is spatially and temporally overlapped (at time zero) with the pump. The high electric field amplitude of the pump modulates the distribution of frequencies in the probe spectrum when they simultaneously interact at the sample. As a result, portions of the probe spectrum can have more or fewer photons when the pump is on the sample than when it is blocked, leading to an oscillatory pattern in the ΔA spectrum along both the time and wavelength axes (Figure 1.4). The XPM is

observable around delay time zero and allows us to follow the temporal chirp in a solvent blank sample.[8]

Other nonlinear effects can occur due to the spatial and temporal overlap of the pump and the probe including two photon absorption and stimulated Raman processes. Two photon absorption will appear as a positive ΔA signal, whereas stimulated Raman, like SE, will appear as a negative ΔA signal. The positions of these features are generally dependent on the pump wavelength being used. As with XPM, these features only persist around time zero and are generally modeled to decay within the instrument response time.[8]

Nanosecond Transient Absorption Setup

In addition to the Helios Fire fsTA spectrometer, we also can perform nsTA (EOS, Ultrafast Systems). The same pump pulse generated by the OPA is used as in the fsTA spectrometer. The probe, however, is generated using a white light laser that is focused onto the sample. The timing between pump and probe is then controlled digitally, allowing the buildup of the two-way dataset. The timing delay is not continuously swept through the time window of the experiment (maximally out to 500 μs) as the delay stage is in fsTA. Rather, the time delay sporadically fills in time points in the window and the dataset is progressively averaged.

Some Remarks on Data Analysis

In our TA setup, the signal is collected via diffraction of the white light probe onto a CCD array detector, allowing for easy construction of a two-dimensional data matrix along wavelength and time axes. If features in the TA spectrum are well resolved from each other, single wavelength exponential fitting may provide access to the relevant rate constants describing the evolution of the data. Often, there may be substantial overlap between spectral features in the data. Time

components of various decay processes may also be close and difficult to distinguish in a wavelength cut of the data. In this case, global and target kinetic analyses offer a powerful tool for fitting the TA data matrix to a prescribed physicochemical model. In both global and target kinetic analyses, the entire data matrix is fit along all times and wavelengths simultaneously, allowing us to fit spectral and time components based off of correlated changes in the data.[9–11]

There are some fundamental assumptions regarding the nature of TA data that we should review before discussing how kinetic analysis is applied to a given system. Much like steady-state absorption, we presume that the difference absorption spectra observed by TA are still described by the Beer-Lambert law that relates the absorbance (or differential absorbance ΔA) to the extinction coefficient at a given wavelength $\varepsilon(\lambda)$, the pathlength of the sample l, and the concentration of the absorbing species c. In TA spectroscopy, we examine the time-dependent evolution of the various photoexcited species by tracking their absorption difference spectra as a function of time. As such, the concentration c of the observed species will change over time given available relaxation pathways, and this parameter is best described by a time-dependent function, $c(t)$.

$$\Delta A(\lambda, t) = \varepsilon(\lambda) * l * c(t) \qquad Eq. 1.2$$

When there is more than one excited state being probed, the Beer-Lambert law describing the differential absorbance across the spectrum is summed over the number of species i.

$$\frac{\Delta A(\lambda, t)}{l} = \sum_i \varepsilon_i(\lambda) * c_i(t) \qquad Eq. 1.3$$

Here, we have omitted the optical pathlength l – as the excited state species are all generated in the same sample holder, this value is the same over all i components being summed

and can simply be treated as a scaling term absorbed into ΔA. An assumption implicit in this model is that ΔA is bilinear in functions of wavelength and time. That is to say that $\varepsilon_i(\lambda)$ are functions solely dependent on λ and that $c_i(t)$ are solely dependent on t so that these two sets of functions are independent of each other. This presumed separability belies much of the analytical techniques for decomposing the transient absorption data matrix. This separability inherently breaks down in ultrafast TA, but can be corrected or parameterized in a given model.

As discussed, the speed of light in condensed media is dependent on the wavelength of light, a phenomenon known as group velocity dispersion or temporal chirp. This chirp spreads the wavelengths on the time scale of hundreds of femtoseconds and would not be distinguishable with slower time resolution spectroscopies. As a result of the dispersion, the spectral shapes in the data become dependent on time and not just wavelength, i.e. $\varepsilon_i(\lambda) \rightarrow \varepsilon_i(\lambda, t)$. Commonly, the dispersion curve is fitted to a polynomial and the time axis is corrected for each wavelength accordingly. This reinstates the separability of the wavelength- and time-dependent functions in the above equation, aiding the decomposition of the data into linearly independent components. Otherwise, the dispersion curve needs to be parametrized and accounted for in the fitted model for data analysis.

Global and target kinetic analyses are a critical part of the toolkit for fitting transient absorption datasets. Both global and target analyses use nonlinear least squares fitting to find the best fit set of parameters to describe the dataset according to a particular kinetic model. Most often in the case of photophysical processes, we assume first order kinetics, which leads to exponential decay behavior. In the case of global kinetic analysis, the model applied is a sum of i exponentially decaying components. This is equivalent to a kinetic model in which there are i species that are decaying in parallel with each other, i.e. there is no conversion between the excited state species,

there is only decay back to the ground state. The expression for ΔA is given below and the fitted spectral components are referred to as decay associated spectra (DAS) or sometimes in the case of difference data decay associated difference spectra (DADS).[9]

$$\Delta A = \sum_i DAS_i \cdot e^{-k_i t} \qquad Eq.1.4$$

Although the parallel model may be physically relevant for some systems, it does not always map one-to-one with the physically relevant model for a given system. Target kinetic analysis implies the application of such a model. The simplest model to apply is a sequential one, in which the initially photoexcited species decays into the next excited state species and so on in tandem until the last species finally decays back to the ground state. Here the spectrally fit components are generally referred to as evolution associated spectra (EAS) or evolution associated difference spectra (EADS). The fitted kinetic components are identical between the parallel and sequential model. The major difference is that the EAS will be formed from linear combinations of the DAS. Once the kinetic model has converged to describe the trajectory of excited state species that are formed in the photodynamics, the spectra may be referred to as species associated spectra (SAS) or species associated difference spectra (SADS).[9]

In summary, in this section we have reviewed the general features of TA data, the experimental setup for TA data collection, and some general concerns regarding the analysis of TA data.

Spin Hamiltonian

The study of systems containing unpaired spins is greatly aided by the formalism of a spin Hamiltonian. The spin Hamiltonian expresses the interactions within the subsystem of unpaired

electrons solely in terms of electron spin operators. This formalism is commonly encountered in magnetic resonance spectroscopies as a tool to fit experimental data, as it allows for the description of the small energetic differences that arise due to spin-dependent interactions without calculation of the full molecular Hamiltonian.[12]

Electron Spin Angular Momentum

One of the simplest cases to begin our discussion of spin angular momentum is that of a single electron. The spin angular momentum for this lone electron can be visualized as a vector in three-dimensional Cartesian coordinates and is characterized by its magnitude and orientation defined by the x-, y-, and z-components of the vector. In quantum mechanics, the magnitudes of these components are quantized when acted upon by their respective operators. For example, the operator $\hat{S}_z$ acting on a given wavefunction returns the magnitude of the z-component of the spin angular momentum. The same goes for $\hat{S}_x$ and $\hat{S}_y$ that describe the x- and y-components of the spin, respectively. The spin angular momentum operator $\hat{S}$ can then be written as a vector containing the $\hat{S}_x$, $\hat{S}_y$, and $\hat{S}_z$ operators much as one would use a three-dimensional column vector to describe the x-, y-, and z-coordinates for a Cartesian vector.[12–16] However, we can only observe one of the three components (Figure 1.5), as follows.

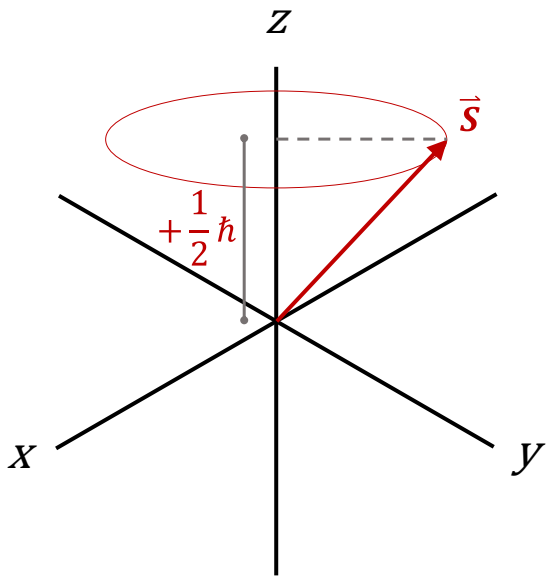

Figure 1.5 The total spin angular momentum, $\vec{S}$, of an electron represented as vector along the 3D Cartesian axes. The z-component of the spin angular momentum is labeled as $+\frac{1}{2}\hbar$. As we have drawn it here, this vector represents the spin in the $|\alpha\rangle$ or $\left|+\frac{1}{2}\right\rangle$ state. By defining the z-component of the spin angular momentum, the x- and y-components are undefined. As a result, the spin vector lies anywhere along the red circle (see text).

The spin operators for a single electron are given by the Pauli matrices and by convention are given in a basis that diagonalizes $\hat{S}_z$. Two eigenstates are returned when operated on by $\hat{S}_z$, either $+\frac{1}{2}\hbar$ or $-\frac{1}{2}\hbar$, and these states can be denoted as $|\alpha\rangle$ and $|\beta\rangle$, respectively (in the literature they may also be labeled by the m_s eigenvalue $\left|+\frac{1}{2}\right\rangle$, $\left|-\frac{1}{2}\right\rangle$). Here, and for the remainder of this thesis, we will write these operators and any resulting Hamiltonians in units of $\hbar$.[14]

$$\hat{S}_x = \frac{1}{2}\begin{bmatrix} 0 & 1 \\ 1 & 0 \end{bmatrix}$$

$$\hat{S}_y = \frac{i}{2}\begin{bmatrix} 0 & -1 \\ 1 & 0 \end{bmatrix}$$

$$\hat{S}_z = \frac{1}{2}\begin{bmatrix}1 & 0\\ 0 & -1\end{bmatrix} \qquad Eqs.\,1.5A - C$$

The square of the total spin (the square root of which gives the magnitude of the overall spin vector) is described by the operator $\hat{S}^2$ and is equal to the scalar product of the spin vector with its transpose. This gives the sum of the squares of the x-, y-, and z-components of the spin and is analogous to the Pythagorean theorem in three dimensions.

$$\hat{S}^2 = \hat{S}\cdot\hat{S} = \begin{bmatrix}\hat{S}_x & \hat{S}_y & \hat{S}_z\end{bmatrix}\begin{bmatrix}\hat{S}_x\\ \hat{S}_y\\ \hat{S}_z\end{bmatrix} = \hat{S}_x^2 + \hat{S}_y^2 + \hat{S}_z^2 \qquad Eq.\,1.6A$$

The $\hat{S}^2$ operator for the one electron case is written explicitly below.

$$\hat{S}^2 = \frac{3}{4}\begin{bmatrix}1 & 0\\ 0 & 1\end{bmatrix} \qquad Eq.\,1.6B$$

For a general spin system, the eigenvalue of the $\hat{S}^2$ operator is $S(S+1)$ when acting on a given spin state where S is the total spin quantum number of the state. The $\hat{S}_z$ operator reports on the total spin projection number M_s of a given eigenstate, and its eigenvalues will span $M_s \in \{-S,\ -(S-1),\ \dots,\ S-1,\ S\}$.

The commutation relations for the spin operators are as follows:

$$\left[\hat{S}^2, \hat{S}_x\right] = \left[\hat{S}^2, \hat{S}_y\right] = \left[\hat{S}^2, \hat{S}_z\right] = 0$$

$$\left[\hat{S}_x, \hat{S}_y\right] = \hat{S}_x\hat{S}_y - \hat{S}_y\hat{S}_x = i\hbar\hat{S}_z$$

$$\left[\hat{S}_y, \hat{S}_z\right] = \hat{S}_y\hat{S}_z - \hat{S}_z\hat{S}_y = i\hbar\hat{S}_x$$

$$\left[\hat{S}_z, \hat{S}_x\right] = \hat{S}_z\hat{S}_x - \hat{S}_x\hat{S}_z = i\hbar\hat{S}_y \qquad Eqs.\,1.7A - D$$

A representative calculation of $[\hat{S}_x, \hat{S}_y]$ is provided below. As shown, the order of operations matters. Application of the $\hat{S}_x$ operator followed by $\hat{S}_y$ does not lead to the same result as $\hat{S}_y$ followed by $\hat{S}_x$.

$$\hat{S}_x\hat{S}_y - \hat{S}_y\hat{S}_x = \frac{1}{2}\hbar\frac{1}{2}\hbar\begin{bmatrix}0 & 1\\ 1 & 0\end{bmatrix}\begin{bmatrix}0 & -i\\ i & 0\end{bmatrix} - \frac{1}{2}\hbar\frac{1}{2}\hbar\begin{bmatrix}0 & -i\\ i & 0\end{bmatrix}\begin{bmatrix}0 & 1\\ 1 & 0\end{bmatrix}$$

$$\hat{S}_x\hat{S}_y - \hat{S}_y\hat{S}_x = \frac{1}{4}\hbar^2\begin{bmatrix}i & 0\\ 0 & -i\end{bmatrix} - \frac{1}{4}\hbar^2\begin{bmatrix}-i & 0\\ 0 & i\end{bmatrix}$$

$$\hat{S}_x\hat{S}_y - \hat{S}_y\hat{S}_x = \frac{1}{4}\hbar^2\begin{bmatrix}2i & 0\\ 0 & -2i\end{bmatrix} = \frac{1}{2}i\hbar^2\begin{bmatrix}1 & 0\\ 0 & -1\end{bmatrix} = i\hbar\hat{S}_z \qquad Eq.\,1.8$$

Simultaneous measurement can only be made with operators that commute with each other, and thus have simultaneous eigenfunctions. Operators that commute relate to observable quantities that are statistically independent of each other, and thus the measurement of one does not impact the outcome of the measurement of the other, (i.e. the order of operations does not matter). These commutation relations demonstrate that the square of the total spin operator $\hat{S}^2$ can commute with any of the spin operators $\hat{S}_x$, $\hat{S}_y$, and $\hat{S}_z$; however, the operators $\hat{S}_x$, $\hat{S}_y$, and $\hat{S}_z$ do not commute with each other and as a result, the projection of the spin angular momentum onto all three Cartesian axes cannot be known simultaneously. This means that if the *z*-component of the spin angular momentum is measured, the spin projections onto the *x* and *y* axes are completely indeterminant (Figure 1.5). The *z*-axis is conventionally taken as the axis of quantization, and so the eigenvalues of the $\hat{S}^2$and $\hat{S}_z$ operators are used to define unique spin states in the spin Hamiltonian formalism.

For multispin systems, the total spin S is taken to be the sum of the individual electron spins:

$$Eq.\,1.9A$$

$$S = S_1 + S_2 + \cdots + S_n$$

This applies as well to the Cartesian components of the spin vector. For calculating the matrices for higher spin systems, this sum is to be taken as the Kronecker sum of the individual spin matrices (e.g., $S = S_1 \otimes I + I \otimes S_2$).

$$S_{x,y,z} = S_{1x,y,z} + S_{2x,y,z} + \cdots + S_n \qquad Eq.\,1.9B$$

From these equations, we can build spin operators for spin systems of higher multiplicity, which we can further apply in the construction of effective spin Hamiltonians.[14]

Electron-Magnetic Field Interaction: The Zeeman Hamiltonian

The intrinsic electron spin angular momentum gives rise to a magnetic dipole moment. Because of the negative charge of the electron, the electron magnetic dipole moment μ is aligned antiparallel to the total spin angular momentum $\vec{S}$. The explicit relationship between the spin angular momentum and the magnetic moment is given below where g_e is the electron g-factor (nearly 2.0023) and μ_B the Bohr magneton (9.27 x 10^{-27} m^2 A).

$$\vec{\boldsymbol{\mu}} = -g_e \mu_B \vec{\boldsymbol{S}} \qquad Eq.\,1.10$$

The magnetic moment gives intuition for how the system will behave in the presence of an externally applied magnetic field $\boldsymbol{B_0}$. Upon application of the external field, the magnetic moment will align with the field, by convention the z-axis. The two eigenstates of the system ($\left|+\frac{1}{2}\right\rangle$, $\left|-\frac{1}{2}\right\rangle$) will then be split in energy; this is known as the electronic Zeeman splitting. The $\left|-\frac{1}{2}\right\rangle$ state will have the z-component of its magnetic moment aligned parallel to $\boldsymbol{B_0}$, whereas the $\left|+\frac{1}{2}\right\rangle$ will have the z-component of its magnetic moment aligned antiparallel to $\boldsymbol{B_0}$ (Figure 1.6).

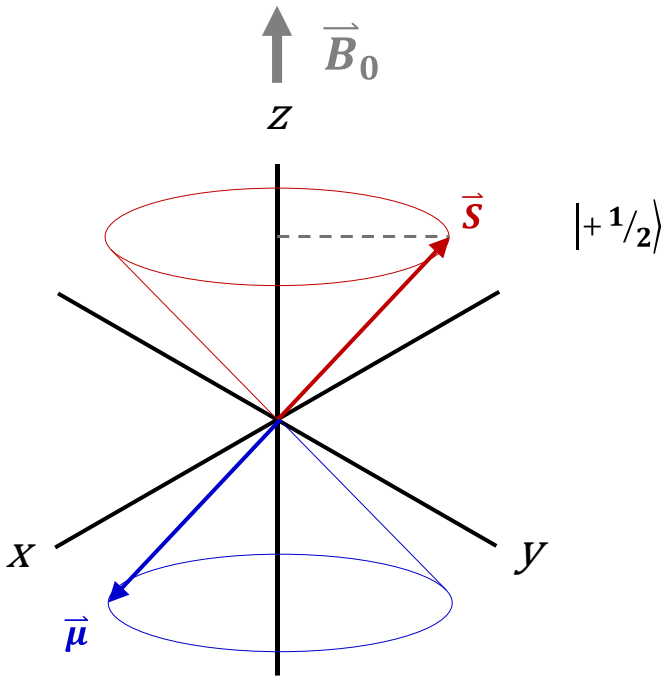

Figure 1.6 The electron magnetic dipole moment can be represented as a vector aligned antiparallel to the electron total spin angular momentum $\vec{S}$, shown here for the $|\alpha\rangle$ or $\left|+\frac{1}{2}\right\rangle$ state. The antiparallel alignment of the magnetic moment with the field raises the energy of this state relative to the parallel alignment in $|\beta\rangle$ or $\left|-\frac{1}{2}\right\rangle$.

The classical potential energy of a magnetic dipole in an external magnetic field is given by the following relationship.

$$U = -\vec{\mu} \cdot \vec{B} = g_e \mu_B \vec{S} \cdot \vec{B}_0 \qquad Eq. 1.11$$

In quantum mechanics, operators represent physical observables. The Hamiltonian operator for the Zeeman interaction, $\hat{H}_{zee}$, can therefore be written in terms of the spin angular momentum operators defined above, replacing the vector arrow notation with bolded symbols and

assuming an isotropic Zeeman interaction (i.e., invariant with respect to rotation as is the case for a free electron).

$$\hat{H}_{zee} = g_e \mu_B \boldsymbol{B^T} \cdot \boldsymbol{S}$$

$$\boldsymbol{S} = \begin{bmatrix} \hat{S}_x \\ \hat{S}_y \\ \hat{S}_z \end{bmatrix}$$

$$\boldsymbol{B} = \begin{bmatrix} B_x \\ B_y \\ B_z \end{bmatrix}$$

In addition to the spin angular momentum, the magnetic moment in a molecule includes orbital angular momentum due to the motion of charged electrons around the nucleus represented by the operators $\hat{L}^2, \hat{L}_x, \hat{L}_y, \hat{L}_z$. These operators have the same rules and commutators as spin angular momentum operators; in fact, these definitions exist for any quantum mechanical description of angular momentum. The magnetic moment arising from orbital motion couples to the electron spin magnetic moment (spin-orbit coupling). When orbital angular momentum is significant, the spin and orbital degrees of freedom may be summed by the standard rules of angular momentum addition to give the total angular momentum of the system $J = L + S$. This is often necessary in the case of free metal and lanthanide ions. Non-zero angular momentum arises from degeneracy in the ground state. For transition metal ions in a coordination complexes, the ligand field lifts the degeneracy present in the free ion, "quenching" the orbital angular momentum. Still, coupling between the ground electronic state and higher lying electronic states can yield small orbital angular momentum contributions that can be treated perturbationally.[12]

We can conceptualize the interaction of the electron spin with the orbital-induced magnetic fields as a perturbation of the effective magnetic field ($\boldsymbol{B_{eff}}$, differing from $\boldsymbol{B_0}$) experienced at the electron. Because the orbital degrees of freedom are spatially parametrized in the molecular frame, the $\boldsymbol{B_{eff}}$ experienced by the electron may be different in the molecular x-, y-, and z-directions given the orbital polarization. This means that the Zeeman response of the electron spin will be anisotropic and dependent on the orientation of the molecule with respect to the external field. As suggested, this dependence could be parametrized in a $\boldsymbol{B_{eff}}$ in the spin Hamiltonian, although it is equivalent to put the orientation dependence on the g value. In this case, the free electron g-value g_e is replaced by a 3×3 Cartesian $\boldsymbol{g}$ tensor as below:[14]

$$\widehat{H}_{zee} = \mu_B \boldsymbol{B^T} \cdot \boldsymbol{g} \cdot \boldsymbol{S}$$

$$\boldsymbol{g} = \begin{bmatrix} g_{xx} & g_{xy} & g_{xz} \\ g_{yx} & g_{yy} & g_{yz} \\ g_{zx} & g_{zy} & g_{zz} \end{bmatrix} \qquad Eq.\,1.13$$

The theoretically defined $\boldsymbol{g}$ tensor may have antisymmetric components. However, single crystal EPR measurements that probe orientation-dependent transitions measure the energetic separation of the Zeeman split sublevels and indirectly provide information on the matrix product $\boldsymbol{g} \cdot \boldsymbol{g^T}$, which is always symmetric. The experimental $\boldsymbol{g}$ tensor is derived from the experimentally-determined $\boldsymbol{g} \cdot \boldsymbol{g^T}$, and as a result, the experimentally-derived $\boldsymbol{g}$ tensor is always symmetric as well (i.e. $g_{xy} = g_{yx}, g_{xz} = g_{zx}, g_{yz} = g_{zy}$) and still reproduces the experimental spectrum. As for any real, symmetric matrix, $\boldsymbol{g} \cdot \boldsymbol{g^T}$ and $\boldsymbol{g}$ are diagonalizable and can be given in their principal frame:

$$\boldsymbol{g} = \begin{bmatrix} g_x & 0 & 0 \\ 0 & g_y & 0 \\ 0 & 0 & g_z \end{bmatrix} \qquad Eq.\,1.14A$$

Thus, the tensor can be fully parameterized by three values (g_x, g_y, g_z), and the full $\boldsymbol{g}$ tensor can be produced by any arbitrary rotation (R) of the principal axis system to the direction of the applied field.

$$\boldsymbol{g^{rot}} = R\boldsymbol{g}R^T \qquad Eq.\,1.14B$$

The classification of EPR spectra is typically done with respect to the symmetry of the g tensor. As previously mentioned, in the case where all principal values of $\boldsymbol{g}$ are equal ($g_x = g_y = g_z$), the system is termed isotropic. When two of the principal values are equivalent, the unique axis is taken as the z-axis ($g_x = g_y \neq g_z$) and the system is termed axial. For axial systems, it is common to refer to the principal g values rather as parallel or perpendicular ($g_{\parallel} = g_z, g_{\perp} = g_x = g_y$). Finally, when all three of the principal g values are distinct ($g_x \neq g_y \neq g_z$), the system is termed rhombic.[14]

Perturbative treatment of the spin-orbit coupling (SOC) provides a means of assessing which orbital wavefunctions are admixed into the ground state by the magnetic field (this depends on the nature of the orbital and the corresponding orbital angular momentum operators $\hat{L}_x, \hat{L}_y, \hat{L}_z$). As such, this procedure also gives a general expression for the elements of $\boldsymbol{g}$:[17]

$$g_i = g_e - \lambda \sum_{e \neq g} \frac{\langle \psi_g | \hat{L}_i | \psi_e \rangle \langle \psi_e | \hat{L}_i | \psi_g \rangle}{E_g - E_e} \qquad Eq.\,1.15A$$

Here, λ is the many-electron SOC constant ($\lambda = \pm\frac{\zeta}{2S}$ where ζ is the one-electron SOC constant for a given atom), ψ_g and ψ_e represent the ground state and excited state orbital wavefunctions, respectively; $\hat{L}_i$ is the orbital angular momentum operator for $i = x, y, z$; and E_g and E_e represent the energies of the ground and excited state orbitals, respectively. For a transition

metal complex, the orbital wavefunctions being summed over are generally the *d* orbitals. These sums have been calculated and give predictable integer values for a given combination of ground and excited orbital configurations. As such, this expression is sometimes represented in a simplified form as below:

$$g_i = g_e - \frac{n\lambda}{\Delta E} \qquad Eq.\,1.15B$$

Here, n is an integer coefficient that comes from the perturbation treatment and depends on which orbitals are mixed, and ΔE is the energetic separation between the states that are mixed. Additional terms may be added to the numerator of the fraction in this expression to account for covalency, *i.e.*, delocalization of the unpaired electron onto ligand-based orbitals.

Electron-Nucleus Interactions: Hyperfine Hamiltonian

Additional terms arise in the spin Hamiltonian due to an array of magnetic interactions that are possible within a molecule. The magnetic moments arising from nuclear spins within a paramagnetic molecule can interact with those of the electron spin system. This is known as the hyperfine interaction. As we did for the Zeeman interaction, we can define a hyperfine Hamiltonian $\widehat{H}_{HF}$ in terms of the electron spin operators ($\boldsymbol{S}$) and the nuclear spin operators ($\boldsymbol{I}$). The nuclear spin operators are defined just as the electron spin operators with I and M_I defining the total nuclear spin and magnetic sublevel, respectively.

$$\widehat{H}_{HF} = \boldsymbol{S} \cdot \boldsymbol{A} \cdot \boldsymbol{I} \qquad Eq.\,1.16$$

Just as we defined the g-tensor to describe the directional relationship between external field and electron spin, we define a hyperfine tensor $\boldsymbol{A}$ to describe the interaction between electron and nuclear spin. As with the g-tensor, the A tensor can be defined in its principal frame, which is

commonly taken to be aligned with the principal frame of the g tensor, although this is not strictly the case in low symmetry. Similarly, the principal values that define the A tensor can be isotropic, axial, or rhombic depending on the symmetry of the system. The isotropic components of the A tensor derive from a "contact term" defined by Fermi that requires the unpaired electron have non-zero probability density at the nucleus, which can only occur for *s*-orbitals or molecular orbitals with *s*-atomic orbital character admixed into the wavefunction. The anisotropic components of the A tensor arise from dipolar interactions between the electron and nuclear dipole. The general experimental impact of the hyperfine Hamiltonian is to split the observed transitions into $2I + 1$ transitions.

Electron-Electron Interactions: Exchange and Zero Field Splitting Hamiltonians

When there are more than one unpaired electron in a paramagnetic species, electron-electron interactions can have a significant impact on the energy levels of the system. Exchange and electronic dipolar interactions are the main contributors to the electron-electron terms in the spin Hamiltonian. Exchange energy as described by Dirac is a consequence of the permutation symmetries available to a given set of electrons that must obey the Pauli exclusion principle. The immediate and most common consequence is an energetic separation between states of different multiplicities, *e.g.*, the separation between singlet and triplet states. Electronic dipole-dipole interactions are the magnetic interactions between the electron magnetic moments akin to the hyperfine interaction. These dipolar interactions can lift the degeneracy of the magnetic sublevels at zero applied magnetic field, and this phenomenon is generally referred to as zero-field splitting. Via Kramers theorem, though, in a half integer spin system, each doublet with equal and opposite spin angular momentum will remain degenerate in the absence of a magnetic field (under time reversal symmetry).

For a system of *n* unpaired electrons, we can define a general Hamiltonian that sums over these electron-electron interactions in a pairwise fashion.[18]

$$\widehat{H} = \sum_{\substack{i,j=1 \\ i \neq j, i>j}}^{n} \boldsymbol{S_i} \cdot \boldsymbol{O_{ij}} \cdot \boldsymbol{S_j} \qquad Eq.\,1.17$$

Here, $\boldsymbol{S_i}$ and $\boldsymbol{S_j}$ are the vector operators for electron spin i and j, respectively, and $\boldsymbol{O_{ij}}$ is a rank two tensor describing the interaction between electron i and electron j. In general, a rank two Cartesian tensor is reducible into three irreducible spherical tensors: a scalar isotropic component, an antisymmetric vector product component, and a symmetric and traceless matrix component. The exchange and dipolar Hamiltonians can both be cast into a form as written above with tensors $\boldsymbol{J}$ and $\boldsymbol{D}$.

$$\boldsymbol{J} = \begin{bmatrix} J_{xx} & J_{xy} & J_{xz} \\ J_{yx} & J_{yy} & J_{yz} \\ J_{zx} & J_{zy} & J_{zz} \end{bmatrix}, \boldsymbol{D} = \begin{bmatrix} D_{xx} & D_{xy} & D_{xz} \\ D_{yx} & D_{yy} & D_{yz} \\ D_{zx} & D_{zy} & D_{zz} \end{bmatrix} \qquad Eq.\,1.18$$

It is not always necessary to include all components of the $\boldsymbol{J}$ and $\boldsymbol{D}$ tensors to describe the interactions. For instance, it is often sufficient for molecular systems to include only the isotropic component of exchange, in which case $J_{xy} = J_{xz} = J_{yx} = J_{yz} = J_{zx} = J_{zy} = 0$ and $J_{xx} = J_{yy} = J_{zz} = J$ where J is the isotropic exchange coupling constant. There are also a variety of exchange mechanisms regarding whether the exchange is between two immediate neighboring spin centers (direct exchange), mediated through an intervening atom or set of atoms (superexchange), or whether the spins are delocalized across centers as in conduction electrons (double exchange). Each can contribute to the exchange interaction depending on the nature of the system and can be described in a form as above.[18] The nomenclature here can be confusing, and certain terms are more common in molecular versus solid-state studies. For example, Anderson superexchange

details the isotropic contribution of superexchange, first detailed to explain antiferromagnetism in certain metal oxides. Dzyaloshinskii-Moriya interactions explicitly discuss the antisymmetric component the exchange from superexchange-type mechanisms that arise due to spin-orbit effects, which can be important particularly in magnetic materials.[19–22] Additionally, there are often conflicting conventions even for the form of the isotropic exchange Hamiltonian. The one that we use in this thesis is given below, where a positive J stabilizes the lowest spin multiplicity:

$$\widehat{H}_{ex} = J \sum_{\substack{i,j=1 \\ i \neq j, i>j}}^{n} \sum_{k=x,y,z} \hat{S}_{k_i} \otimes \hat{S}_{k_j} \qquad Eq. 1.19$$

For the zero-field splitting Hamiltonian, the magnetic dipolar interaction between electrons derived via correspondence from the classical dipole-dipole interaction energy gives the form of a symmetric, traceless tensor. Like the g- and A-tensors, it is commonly expressed in its principal axis system:

$$\boldsymbol{D} = \begin{bmatrix} D_x & 0 & 0 \\ 0 & D_y & 0 \\ 0 & 0 & D_z \end{bmatrix} \qquad Eq. 1.20$$

Because of the traceless condition ($D_x + D_y + D_z = 0$), only two values are needed to fully characterize the tensor, and often it is rewritten using the parameters $D = \frac{3}{2} D_z$ and $E = \frac{1}{2}(D_x - D_y)$. D here represents the axial component of the zero-field splitting and can be directly related to geometric considerations such as axial compression or elongation. E represents the transverse components of the zero-field splitting, and although systems that have non-zero E are termed rhombic, there is not always a clear geometric interpretation of this. The signs of D and E are often undetermined, but their absolute value can be experimentally determined. D and E are also

bounded by the condition that $E \leq \frac{1}{3}D$. Spin-orbit coupling also gives rise to a term that is bilinear in electron spins of the form shown here ($\boldsymbol{S} \cdot \boldsymbol{D} \cdot \boldsymbol{S}$). Both dipolar and spin-orbit coupling terms can contribute to the zero-field splitting Hamiltonian. The SOC-derived $\boldsymbol{D}$ tensor need not be traceless, however.[23] In organic systems, it is generally the case that the dipolar interactions are greater than those from SOC, whereas in transition metal systems the reverse is taken to be true. We will write the zero-field splitting Hamiltonian generally as below.

$$\hat{H}_{zfs} = \sum_{\substack{i,j=1 \\ i \neq j, i>j}}^{n} \boldsymbol{S_i} \cdot \boldsymbol{D} \cdot \boldsymbol{S_j} \qquad Eq.\,1.21A$$

When in the principal frame, this Hamiltonian can be written as:

$$\hat{H}_{zfs} = D\left(\hat{S}_z^2 - \frac{1}{3}\hat{S}^2\right) + E\left(\hat{S}_x^2 - \hat{S}_y^2\right) \qquad Eq.\,1.21B$$

Electron Paramagnetic Resonance Spectroscopy

Application of the magnetic field lifts the degeneracy of the $\left|+\frac{1}{2}\right\rangle$ and $\left|-\frac{1}{2}\right\rangle$ states as a function of the magnitude of the external field (Figure 1.7). This generates a spin polarization (and net magnetization) within the sample as the lowest energy eigenstate $\left|-\frac{1}{2}\right\rangle$ will be slightly more populated than the higher energy eigenstate. Electron paramagnetic resonance (EPR) spectroscopy utilizes microwave radiation to probe the transitions between the split spin sublevels. The traditional architecture of an EPR spectrometer involves a microwave source, an amplifier, a magnet, a resonator or cavity into which the sample is placed, and a detector. The resonator is critically coupled to the microwave source, and absorption and emission are detected as a change in the incident microwave intensity that is reflected out of the cavity.[24]

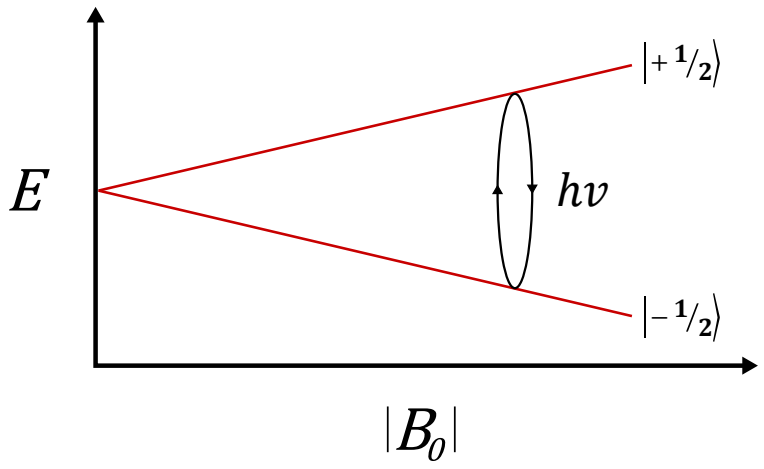

Figure 1.7 Zeeman splitting of the eigenstates of an S = ½ spin system, $\left|+\frac{1}{2}\right\rangle$ and $\left|-\frac{1}{2}\right\rangle$, as a function of the magnitude of the external magnetic field $\boldsymbol{B_0}$. The EPR spectrometer typically uses a tuned microwave frequency that fixes $h\nu$, and thus resonance occurs at specific values of the external magnetic field strength.

Most EPR spectrometers operate at a fixed microwave frequency and instead sweep the permanent magnetic field intensity to generate the absorption spectrum. By changing the magnetic field strength B_0, the splitting between spin sublevels is changed according to the Zeeman component of the spin Hamiltonian. Only when the splitting between particular spin sublevels approaches the microwave energy ($h\nu$) can the resonance condition be fulfilled and absorption/emission occur. There are additional selection rules that govern which transitions couple to the radiation field. The magnetic field component of the microwave radiation, $\boldsymbol{B_1}$, may be polarized perpendicular or parallel to the field lines of the permanent magnet, $\boldsymbol{B_0}$, leading to perpendicular and parallel modes of operation for the spectrometer. When in perpendicular mode, the allowed transitions follow the selection rule $\Delta M_s = \pm 1$. In parallel mode, the allowed

transitions follow $\Delta M_s = \pm 2$. All the EPR spectra presented in this thesis were collected in perpendicular mode.

In continuous wave (CW) EPR, the microwave is continuously applied to the resonator and the magnetic field is swept, generating the absorption spectrum. In practice, the external field is often modulated at a particular frequency and amplitude, lock-in detection is used at the modulation frequency giving higher sensitivity, and the change in microwave intensity as the field is oscillated within the modulation amplitude range is recorded. This means that CW EPR typically provides the first derivative of the absorption spectrum and is how such data is commonly presented.

Pulsed EPR Spectroscopy

Pulsed EPR employs microwave pulses to excite the spin system. Most modern-day nuclear magnetic resonance (NMR) spectrometers also operate in pulsed mode using radiofrequency radiation, and the following is general to all magnetic resonance spectroscopies; however, we choose to contextualize this discussion in terms of EPR. To visualize the action of microwave pulses as well as the various relaxation phenomena, it is helpful to consider the bulk magnetization vector of the sample. In a given EPR sample, there will be many individual spin centers excited by the microwave radiation. At thermal equilibrium, a small but distinguishable greater percentage of electron magnetic moments will be aligned with the externally applied field than anti-aligned as dictated by the Zeeman splitting and corresponding Boltzmann population. This gives rise to a net magnetic moment of the sample aligned with the field (the laboratory +z-axis as we have previously defined). In a classical sense, a magnetic dipole oriented at an angle ($\neq$ 0, 180°) to an external magnetic field will precess about the external field vector at the dipole's Larmor frequency. However, at equilibrium, none of the individual magnetic moments share phase

coherence – they are not precessing in phase with each other. As a result, there is no net x- or y-magnetization and the net magnetization vector $\boldsymbol{M}$ is parallel to the field $\boldsymbol{B_0}$ as depicted in Figure 1.8A.[25,26]

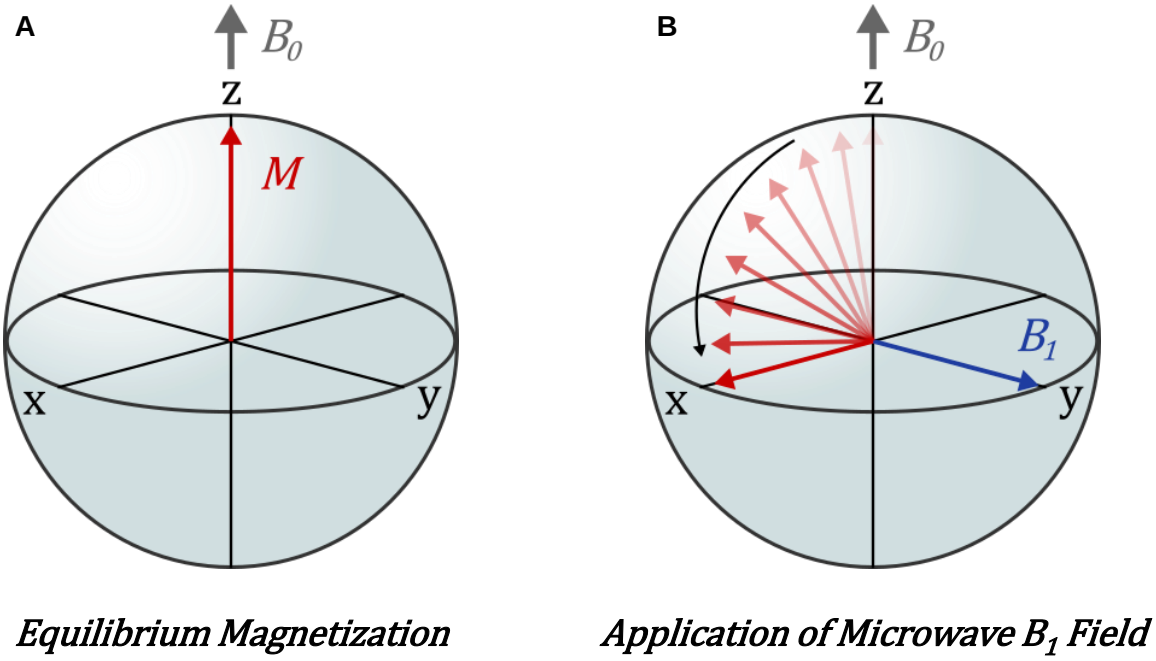

Figure 1.8 (A) The thermal equilibrium picture of the net magnetization vector $\boldsymbol{M}$ of a paramagnetic EPR sample in the externally applied field $\boldsymbol{B_0}$. **(B)** The action of a magnetic field $\boldsymbol{B_1}$ (from the microwave) applied along the +y-axis causes the net magnetization to rotate in the xz plane as portrayed in a rotating reference frame.

A helpful conceit in analyzing the evolution of the magnetization is a rotating reference frame. Once $\boldsymbol{M}$ forms a non-zero angle with $\boldsymbol{B_0}$, $\boldsymbol{M}$ will begin precessing at the Larmor frequency of the system of magnetic moments. If the laboratory reference frame is replaced with a frame that is itself rotating at this Larmor frequency, the complex precessional motion is removed from the

equations of motion. In perpendicular-mode EPR, a linearly polarized microwave is applied such that the magnetic field component of the microwave $\boldsymbol{B_1}$ field is perpendicular to the external field $\boldsymbol{B_0}$ and functions to tip $\boldsymbol{M}$ from its equilibrium position. In our rotating frame, the linearly polarized microwave can be decomposed into a linear combination of left- and right-circularly polarized components. By convention, only the component that rotates with the same sense of the Larmor precession of the spin system is taken as on resonant and the other is discarded. As a result, the $\boldsymbol{B_1}$ field appears static in the rotating frame and can be aligned within the frame by adjusting the phase of the microwave pulse.

We depict the action of $\boldsymbol{B_1}$ aligned along the +y-axis in the rotating frame in Figure 1.8B. Once $\boldsymbol{B_1}$ is turned on, $\boldsymbol{M}$ will begin to rotate in the xz plane about the +y-axis in a process known as Rabi nutation, and the angular frequency with which $\boldsymbol{M}$ precesses about $\boldsymbol{B_1}$ is known as the Rabi nutation frequency (Ω). The Rabi nutation frequency depends on both the magnetic moment being rotated (and therefore the spin angular momentum, characterized by S and M_s, of the excited spin system) as well as the strength of $\boldsymbol{B_1}$.[27]

$$\Omega_{M_s,M_s\pm1} = \omega_1\sqrt{S(S+1) - M_s(M_s \pm 1)} \qquad Eq.\,1.22$$

Here, the microwave field strength is expressed in angular frequency units $\omega_1 = \mu_B g B_1 \hbar^{-1}$. The microwave pulse is applied for a finite time duration τ. As a result, the angle θ that $\boldsymbol{M}$ is rotated by can be predicted using the nutation frequency as $\theta = \Omega\tau$. In fact, most often, pulse sequences are described by the rotation angles that each pulse enacts upon the magnetization. If $\boldsymbol{B_1}$ is applied for a pulse duration such that $\boldsymbol{M}$ is rotated from the +z-axis onto the +x-axis, this is described as a "$\frac{\pi}{2}$ pulse" (Figure 1.8B). As we will see, an important consequence of the spin-

dependent nutation frequency is that pulsed EPR can selectively probe transitions in manifolds of different spin multiplicity in one sample.

An important consideration is that here we have discussed the evolution of the bulk magnetism in terms of purely classical phenomena. However, the bulk magnetization is the macroscopic consequence of the many quantum mechanical spin systems we are probing within the sample. Via correspondence, we can describe the evolution of the classical magnetization *or* the evolution of the quantum mechanical state vector of a two-level system as a function of the applied fields. The state vector can similarly be represented in an axis system like what we have drawn for the magnetization in Figure 1.8, and this representation is known as the Bloch sphere. Rather than changing the amplitudes of x-, y-, and z-components of magnetization, the state vector evolves through changing complex probability amplitudes in the wavefunction brought on by the $\boldsymbol{B_1}$ field.

Paramagnetic Relaxation

Let us say we have performed a $\frac{\pi}{2}$ pulse as depicted in Figure 1.8B. The net magnetization is now perpendicular to the z-axis: the z-component of $\boldsymbol{M}$ is zero, and the phase coherence given to the spins via the microwave pulse has generated maximum transverse magnetization aligned along the x-axis. After the pulse is applied, this is a nonequilibrium state of the system. Over time, relaxation will return the magnetization back to its thermal equilibrium alignment along the z-axis. This complex relaxation can be decomposed into two separate processes. The first is relaxation of the z-component of magnetization back to its full equilibrium value (described as longitudinal relaxation and denoted by T_1). The second is the loss of phase coherence of the excited spin packet

and return of the x- and y-components of magnetization back to zero (described as transverse relaxation and denoted by T_2). These relaxation processes are depicted in Figure 1.9A and B.[14,25,28]

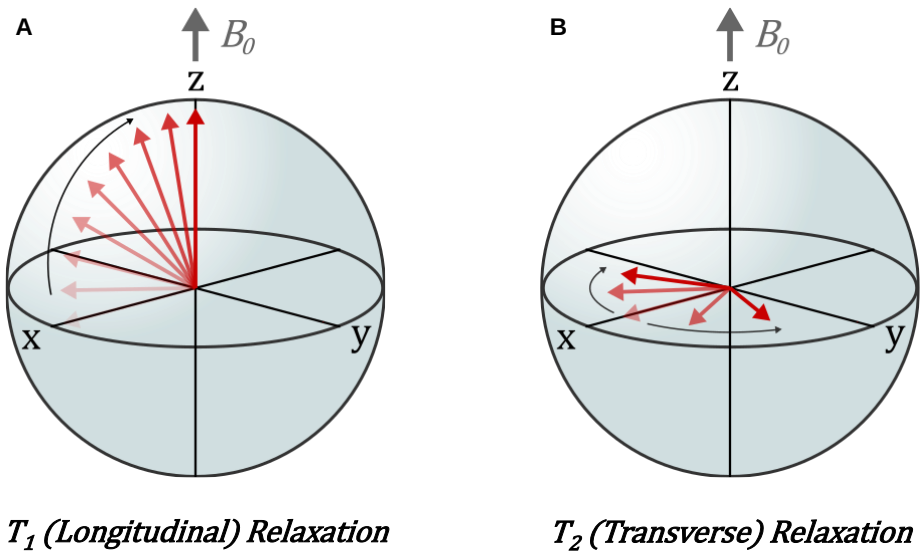

Figure 1.9 (A) Visualization of T_1, longitudinal relaxation or the return of the z-component of the magnetization. **(B)** Visualization of T_2, the transverse relaxation or loss of phase coherence / the x- and y-components of magnetization.

T_1 is sometimes referred to as spin-lattice relaxation. As this name suggests, T_1 relaxation arises due to an exchange of energy between the spin system and the surrounding environment. In solution-state NMR, it is generally the molecular tumbling motion that gives rise to the appropriate spectral density that can exchange energy with the nuclear spin system. In solid-state EPR, however, the molecular motions responsible for T_1 relaxation are generally lattice phonons and low-energy librations.

T_2, on the other hand, is sometimes referred to as spin-spin relaxation. Spin "flip-flop" processes in which two spins exchange their spin angular momentum does not affect the

longitudinal magnetization but can lead to dephasing of the transverse magnetization. Other phenomena can contribute to T_2 beyond spin-spin interactions, however. Dynamic fluctuations in local magnetic field, which can be due to other sources of magnetic fields in the sample such as nuclei, can give rise to instantaneous jumps in Larmor frequencies of particular spin packets, which leads to the loss of phase coherence as well.

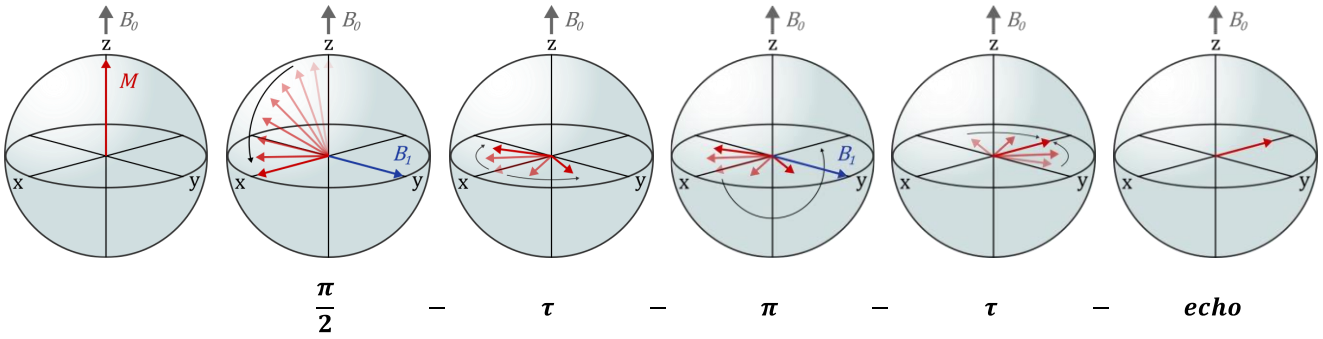

Figure 1.10 A visualization of the Hahn echo pulse sequence: $\frac{\pi}{2} - \tau - \pi - \tau - echo$. Static inhomogeneities that give rise to slightly different Larmor frequencies of the spin packets are refocused into an observable echo signal.

Transverse relaxation is commonly measured using a Hahn echo pulse sequence with varying delay times.[29] The Hahn echo sequence is defined in terms of the turning angles of the pulses as follows: $\frac{\pi}{2} - \tau - \pi - \tau - echo$ as shown in Figure 1.10. The $\frac{\pi}{2}$ pulse tips the magnetization into the transverse plane. The system is allowed to evolve for time τ, during which the spins will begin to dephase. A portion of the transverse magnetization loss will be due to spin relaxation, and a portion will be due to static inhomogeneities that cause various spins to precess and slightly different Larmor frequencies from each other. A π pulse rotates the magnetization by 180 ° while preserving the sense of rotation of the various spins, which results in a refocusing of

the spins after an additional time τ. A photon echo is then detected at a time 2τ after the initial $\frac{\pi}{2}$ pulse. The intensity of the photon echo will be proportional to how many of the spins may be refocused by the π pulse. The π pulse can refocus the magnetization loss caused by the static inhomogeneities (reversible), but not that caused by spin relaxation (irreversible). By observing the loss of echo intensity as a function of increasing the delay time t, the transverse relaxation rate can be estimated.

The echo intensity observed in the Hahn echo sequence can also be impacted by spectral diffusion. The bandwidth of microwave excitation is often much less than the linewidth of a given EPR spectrum. As a result, the excitation energy imparted to one spin packet may be exchanged with other off-resonant spins due to overlaps in the spin packet bandwidths. If a portion of the excitation population is moved out of resonance with the microwave radiation, it cannot be refocused by the π pulse. This contributes to the loss of echo intensity but is not directly T_2 relaxation. Because of this, often the experimentally derived relaxation time from a Hahn echo sequence is termed T_M, the phase memory time, which includes the contributions of T_2 as well as these diffusive processes.

T_1 can be estimated using an inversion recovery pulse sequence. Here, an initial π pulse is used to invert the magnetization to lie along the –z-axis. The spins are allowed to relax over time τ, during which the spins will reapproach their equilibrium alignment with the external field. The longitudinal magnetization is read out using a Hahn echo pulse sequence with a fixed delay time t. The T_1 relaxation time is then determined by varying the waiting time τ after the initial π pulse. As the magnetization is initially inverted, the phase of the echo will also be offset by 180 °, which is usually taken to be a negative signal relative to the positive signals detected in the standard Hahn echo sequence. As the magnetization relaxes back to its alignment along the +z-axis, the observed

echo intensity follows the magnetization beginning negative, passing through zero, and finally becoming positive until the equilibrium magnetization is recovered.

Theoretically, T_1 and T_2 are considered to follow first-order kinetics and exhibit monoexponential decay functions. In practice, however, diffusion processes and the distribution of spin packets excited by the microwave pulse often lead to stretched exponential behavior.

In summary, in this section we have examined spin angular momentum and the magnetic interactions in a system of unpaired electrons, constructing a spin Hamiltonian that can be used to calculate the small energetic splittings. EPR interrogates these level splittings and gives us information on the electronic structure of the system in the form of fitted parameters (e.g. the $\boldsymbol{g}$, $\boldsymbol{A}$, $\boldsymbol{J}$, and $\boldsymbol{D}$ tensors). Pulsed-EPR can provide information with respect to the longitudinal (T_1) and transverse magnetic (T_2) relaxation properties of the system.

Citations

(1) Siebrand, W. Nonradiative Processes in Molecular Systems. In *Dynamics of Molecular Collisions: Part A*; Miller, W. H., Ed.; Springer US: Boston, MA, 1976; pp 249–302. https://doi.org/10.1007/978-1-4615-8867-2_6.

(2) Bixon, M.; Jortner, J. Intramolecular Radiationless Transitions. *J. Chem. Phys.* **1968**, *48* (2), 715–726. https://doi.org/10.1063/1.1668703.

(3) Robinson, G. W.; Frosch, R. P. Electronic Excitation Transfer and Relaxation. *J. Chem. Phys.* **1963**, *38* (5), 1187–1203. https://doi.org/10.1063/1.1733823.

(4) Jortner, J.; Bixon, M. Radiationless Transitions in Polyatomic Molecules. *Israel Journal of Chemistry* **1969**, *7* (2), 189–220. https://doi.org/10.1002/ijch.196900032.

(5) Englman, R.; Jortner, J. The Energy Gap Law for Radiationless Transitions in Large Molecules. *Molecular Physics* **1970**, *18* (2), 145–164. https://doi.org/10.1080/00268977000100171.

(6) Berera, R.; van Grondelle, R.; Kennis, J. T. M. Ultrafast Transient Absorption Spectroscopy: Principles and Application to Photosynthetic Systems. *Photosynth Res* **2009**, *101* (2), 105–118. https://doi.org/10.1007/s11120-009-9454-y.

(7) Mukamel, S. *Principles of Nonlinear Optical Spectroscopy*; Oxford University Press, 1995.

(8) Lorenc, M.; Ziolek, M.; Naskrecki, R.; Karolczak, J.; Kubicki, J.; Maciejewski, A. Artifacts in Femtosecond Transient Absorption Spectroscopy. *Appl Phys B* **2002**, *74* (1), 19–27. https://doi.org/10.1007/s003400100750.

(9) van Stokkum, I. H. M.; Larsen, D. S.; van Grondelle, R. Global and Target Analysis of Time-Resolved Spectra. *Biochimica et Biophysica Acta (BBA) - Bioenergetics* **2004**, *1657* (2), 82–104. https://doi.org/10.1016/j.bbabio.2004.04.011.
(10) Mullen, K. M.; Stokkum, I. H. M. van. TIMP: An R Package for Modeling Multi-Way Spectroscopic Measurements. *Journal of Statistical Software* **2007**, *18*, 1–46. https://doi.org/10.18637/jss.v018.i03.
(11) Snellenburg, J. J.; Laptenok, S.; Seger, R.; Mullen, K. M.; Stokkum, I. H. M. van. Glotaran: A Java-Based Graphical User Interface for the R Package TIMP. *Journal of Statistical Software* **2012**, *49*, 1–22. https://doi.org/10.18637/jss.v049.i03.
(12) McWeeny, R. *Spins in Chemistry*; Dover Publications, 2004.
(13) McWeeny, R. On the Origin of Spin-Hamiltonian Parameters. *J. Chem. Phys.* **1965**, *42* (5), 1717–1725. https://doi.org/10.1063/1.1696183.
(14) Weil, J. A.; Bolton, J. R. Basic Principles of Paramagnetic Resonance. In *Electron Paramagnetic Resonance*; John Wiley & Sons, Ltd, 2006; pp 1–35. https://doi.org/10.1002/9780470084984.ch1.
(15) Abragam, A. *Electron Paramagnetic Resonance of Transition Ions*; Oxford Classic Texts in the Physical Sciences; Oxford University Press: Oxford, New York, 2012.
(16) Abragam, A. *The Principles of Nuclear Magnetism.*; Clarendon Press: Oxford, 1961.
(17) Solomon, E. I. Introduction. *Comments on Inorganic Chemistry* **1984**, *3* (5), 227–229. https://doi.org/10.1080/02603598408080072.
(18) Bencini, A.; Gatteschi, D. *EPR of Exchange Coupled Systems*; Courier Corporation, 2012.
(19) Anderson, P. W. Antiferromagnetism. Theory of Superexchange Interaction. *Phys. Rev.* **1950**, *79* (2), 350–356. https://doi.org/10.1103/PhysRev.79.350.
(20) Anderson, P. W. New Approach to the Theory of Superexchange Interactions. *Phys. Rev.* **1959**, *115* (1), 2–13. https://doi.org/10.1103/PhysRev.115.2.
(21) Dzyaloshinsky, I. A Thermodynamic Theory of "Weak" Ferromagnetism of Antiferromagnetics. *Journal of Physics and Chemistry of Solids* **1958**, *4* (4), 241–255. https://doi.org/10.1016/0022-3697(58)90076-3.
(22) Moriya, T. Anisotropic Superexchange Interaction and Weak Ferromagnetism. *Phys. Rev.* **1960**, *120* (1), 91–98. https://doi.org/10.1103/PhysRev.120.91.
(23) Boča, R. Zero-Field Splitting in Metal Complexes. *Coordination Chemistry Reviews* **2004**, *248* (9), 757–815. https://doi.org/10.1016/j.ccr.2004.03.001.
(24) Chechik, V.; Carter, E.; Murphy, D. *Electron Paramagnetic Resonance*; Oxford University Press, 2016.
(25) Schweiger, A.; Jeschke, G. *Principles of Pulse Electron Paramagnetic Resonance*; Oxford University Press, 2001.
(26) Hore, P. J.; Jones, J. A.; Wimperis, S. *NMR: The Toolkit : How Pulse Sequences Work*; Oxford University Press, 2015.
(27) Stoll, S.; Jeschke, G.; Willer, M.; Schweiger, A. Nutation-Frequency Correlated EPR Spectroscopy: The PEANUT Experiment. *Journal of Magnetic Resonance* **1998**, *130* (1), 86–96. https://doi.org/10.1006/jmre.1997.1285.
(28) Eaton, S. S.; Eaton, G. R. Relaxation Times of Organic Radicals and Transition Metal Ions. In *Distance Measurements in Biological Systems by EPR*; Berliner, L. J., Eaton, G. R., Eaton, S. S., Eds.; Springer US: Boston, MA, 2000; pp 29–154. https://doi.org/10.1007/0-306-47109-4_2.

(29) Hahn, E. L. Spin Echoes. *Phys. Rev.* **1950**, *80* (4), 580–594. https://doi.org/10.1103/PhysRev.80.580.

Chapter II

Singlet Fission in Coordination Complexes of Dipyridyl Pyrrole Bipentacenes

Introduction

Singlet fission is a multiexciton generating (MEG) process in organic chromophores by which a photon promotes electronic excitation to a singlet exciton that can then relax into a pair of triplet excitons. This pair of triplets is initially generated as an overall spin-correlated singlet state, and, often when in solid media, these triplets can diffuse and thermalize into individual excitons via Dexter-type triplet energy transfer. Thus, singlet fission is spin-allowed and can occur on ultrafast timescales in contrast to traditional intersystem crossing from the singlet to triplet manifold, which is typically slow in the absence of strong spin-orbit coupling.[1,2]

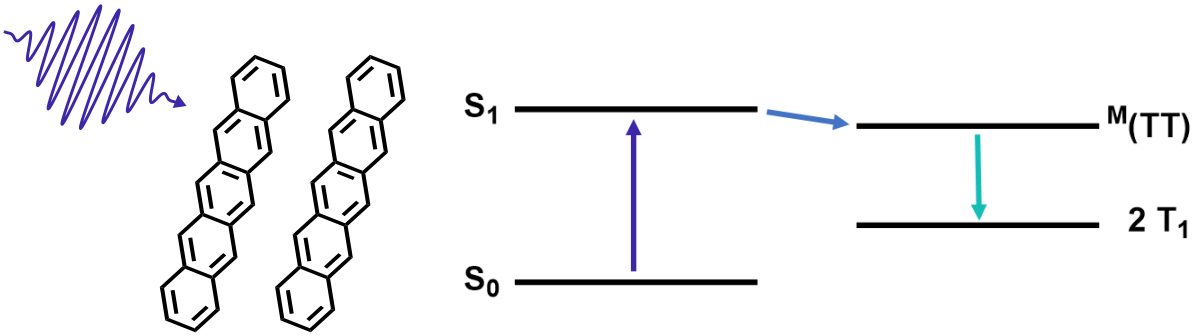

Figure 2.1 A schematic of singlet fission in a simplified Jablonski diagram and a depiction of a pair of pentacene molecules being excited by a photon.

Although singlet fission was first elucidated in the 1960s, the field was reinvigorated with the observation that MEG processes could be employed to surpass the Shockley-Quiesser efficiency limit of single-junction solar cells (~30%) to nearly 40%. A significant source of efficiency loss in solar cells is a result of thermalization of absorbed photon energy to the semiconductor band edge, which generally occurs on timescales faster than charge separation. As such, much of the energy imparted by the higher-energy portion of the solar spectrum is lost

thermally and is not converted into electrical energy. Higher efficiencies can be achieved in multijunction cells where semiconductor materials with varying bandgaps are layered such that each can most efficiently convert a different portion of the solar spectrum. However, such multijunction cells are often costly to make and may not be amenable to mass production.[3–8]

Singlet fission provides a competitive path to downconvert high-energy photons into lower energy (triplet) excitons that may be efficiently converted into photocurrent by a traditional semiconductor material, circumventing a portion of the thermalization loss. Singlet fission-based organic photovoltaics have even been realized with external quantum efficiencies exceeding 100% in pentacene/C60 junctions.[9–11]

In addition to the possibility of solar cell applications, singlet fission has also garnered attention for possible implications in quantum information science. The multiexcitonic state represents a maximally entangled state that can be described as a strong correlation between individual triplet excitons. Studies have suggested that the spin correlations in such states can persist out to μm scales in solid-state systems.[12–20]

Despite the possibilities offered by singlet fission, there remain challenges to realizing the potential of such systems. First, the range of chromophores that can demonstrate singlet fission is limited due to the energetic requirements. For the generation of two triplets from an excited singlet to be efficient, the adiabatic energy of the singlet excited state must be roughly twice the energy of the triplet such that energy is conserved in the transition (i.e. $E_{S_1} \approx 2E_{T_1}$). Second, the utility of singlet fission rests in the electronic structure of the triplet pair state, which is still not well understood. For example, strong interchromophore coupling may engender fast and efficient transfer from the singlet exciton to the triplet pair state, but may also hinder triplet separation, posing a challenge for efficient charge extraction, although there is a suggestion that the triplet

pair state may enable multielectron transfer at heterojunction interfaces. The persistence of spin correlation in the triplet pair state is also necessary for applications in quantum information science. Thus, in addition to the elucidation of novel chromophores for singlet fission, a deeper understanding of the electronic structure and dynamics that govern this process may aid in the engineering of singlet fission devices.[1]

Covalently linked chromophore dimers represent a way to control excitonic interactions using synthetically-tuned molecular scaffolds. Molecular bipentacenes, for example, have become an important tool for the study of singlet fission.[21–23] Singlet fission is exergonic and highly efficient in pentacene systems.[1,24,25] Much focus has been given to the nature of the synthetic linker on rates and efficiencies of singlet fission. For example, bipentacenes linked by a phenyl moiety can be perturbed by examining the *ortho*-, *meta*-, or *para*- configurations.[26] Oligophenyl linkers have been explored, extending the distance between pentacene moieties by increasing the number of intervening phenyl rings.[27] In addition to conjugated linkers, aliphatic groups have been explored to attenuate the through-bound coupling between pentacene rings.[28] Such studies have elucidated the importance of interchromophore coupling, Davydov splitting in molecular excited states, and have also permitted the observation of multiexcitonic quintet states by time-resolved electron paramagnetic resonance (TREPR) spectroscopy.[14,28–30]

Varying the covalent linker in these bipentacene systems has proven to be a versatile approach toward addressing fundamental aspects of SF.[31–41] However, disentangling the contributions of through-bond and through-space effects that give rise to the properties of a given system remain a challenge. In our studies, we have sought to study synthetic bipentacene systems covalently linked by ligand scaffolds capable of binding metal ions. In this way, we can examine

how a singular molecular bipentacene framework can give rise to tunable singlet fission by means of coordination-induced structural changes.

In our initial study, we synthesized and characterized the photophysics of a dipyridyl pyrrole-linked bipentacene (HDPP-Pent). We were able to deprotonate HDPP-Pent and form complexes with lithium and potassium cations forming Li_2(DPP-Pent)$_2$ and KDPP-Pent, a solution-state dimer and monomer structure respectively. These complexes maintain the same backbone linking the pentacene rings together while modulating the arrangement and interaction of the pentacenes and thus influence the rate of singlet fission. This series provides new ideas for the control of singlet fission via dimer self-assembly promoted by metal coordination.

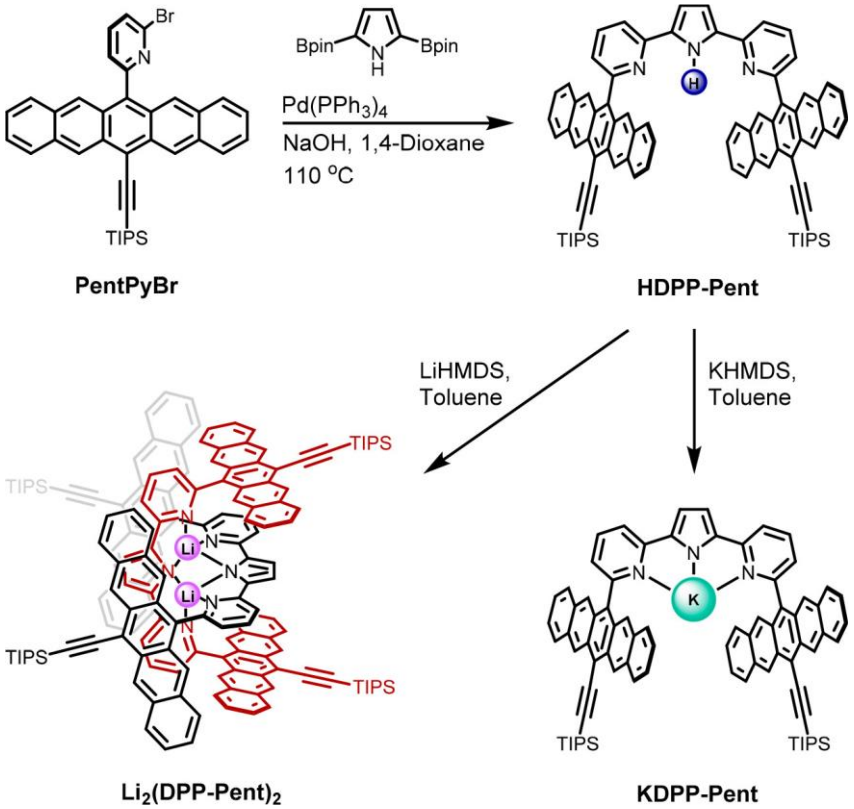

Figure 2.2 Synthesis of HDPP-Pent and MDPP-Pent complexes.

Synthesis and NMR Characterization

HDPP-Pent was synthesized from a monopentacene pyridyl bromide derivative PentPyBr, which we employ as a monopentacene reference compound in our optical spectroscopic studies. The ^{1}H NMR spectrum of HDPP-Pent is broad in the aromatic region, in contrast to the well-resolved scalar coupling between protons on the terminal rings of the pentacene moiety observed for PentPyBr. Variable temperature ^{1}H NMR from 20 to -80 °C reveals complex temperature-dependent behavior. The aromatic region broadens further cooling to -40 °C, and many new resonances grow in with further cooling.

HDPP-Pent serves as a ligand by protonolysis of the pyrrole N-H bond. Using a strong amide base such as lithium or potassium hexamethyldisilazide provides formation of Li_2(DPP-Pent)$_2$ or KDPP-Pent, respectively. Despite the broad features of the HDPP-Pent ^{1}H NMR spectrum, deprotonation leads to sharp and well-resolved spectra for the alkali metal complexes at room temperature. In comparison to the ^{1}H NMR spectrum of KDPP-Pent, it is evident that the protons on the dipyridyl pyrrolide moiety of Li_2(DPP-Pent)$_2$ are significantly upfield shifted. The singlet resonance corresponding to the pyrrolide ring proton is found at 4.38 and 7.03 ppm in the Li_2(DPP-Pent)$_2$ and KDPP-Pent spectra, respectively.

We carried out 2D rotating frame Overhauser enhancement spectroscopy (ROESY) on Li_2(DPP-Pent)$_2$, which showed through space ^{1}H-^{1}H coupling between protons on the dipyridyl pyrrolide backbone at 4.38 ppm (H_c) and 5.14 ppm (H_d) and the proton on the distal side of the pentacene ring at 9.12 ppm (H_a) (denoted by green and blue circles, respectively, in Figure 2.3B). No such cross-peaks are observed in the 2D ROESY spectrum of KDPP-Pent (Figure 2.3C). More information regarding the choice of 2D ROESY vs. 2D NOESY can be found in Appendix A.

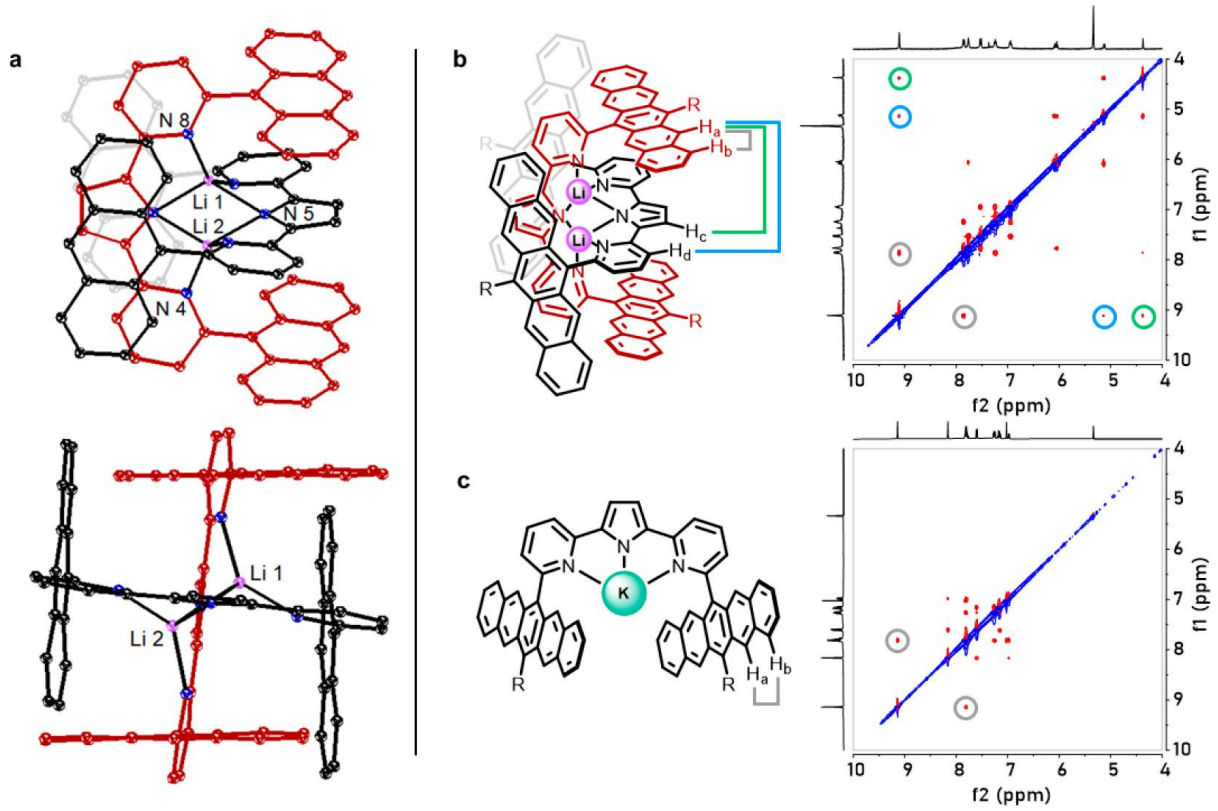

Figure 2.3 Structural data supporting dimeric Li_2(DPP-Pent)$_2$ and monomeric KDPP-Pent assignments in solution. (**A**) Crystallographic identification of a dimeric Li complex with an analogous ligand, DPP-Anth, in two perspectives, (**B**) proposed dimeric structure of Li_2(DPP-Pent)$_2$ and the corresponding through-space coupling highlighted in the respective 2D-ROESY spectrum, and (**C**) proposed monomeric structure of KDPP-Pent and the corresponding through-space coupling highlighted in the respective 2D-ROESY spectrum; R = triisopropylsilylethynyl.

Analysis of NMR Data

We interpret the broadness of the room temperature ^{1}NMR spectrum of HDPP-Pent as being due to conformational dynamics. Such dynamics may involve rotations around aryl-aryl linkages resulting in mixtures of conformers that interconvert on an intermediate timescale on the

order of the NMR experiment. The variable temperature data suggests this as well, although the complexity of this dataset occludes further interpretation. The multitude of resonances observed at -80 °C may result from a freezing out of multiple solution-state structures, monomeric or dimeric. The aromatic features are resolved upon deprotonation and metal coordination of the DPP-Pent framework as evidenced by the sharp spectra observed for Li_2(DPP-Pent)$_2$ and KDPP-Pent, suggesting the formation of single solution-state conformers or fast exchange processes.

The NMR data collected on Li_2DPP-Pent$_2$ strongly suggest a dimeric solution-state structure as proposed in Figure 2.B. The π-stacking interactions between the pentacene and sandwiched dipyridyl pyrrole units are consistent with the upfield shift exhibited by the dipyridyl pyrrole protons owing to enhanced chemical shielding by perturbation of the aromatic ring currents.[42,43] The cross-peaks in the 2D-ROESY spectrum between the pyrrole backbone protons and the protons on the far side of the pentacene also support a dimeric structure. The dipolar couplings that give rise to ROE are sensitive generally out to 5 Å, and this dimeric structure would bring the relevant nuclei into proximity for this interaction.[44,45] The spectra in Figure 2.3 were taken in CD_2Cl_2 to unambiguously assign the transitions observed in the aromatic region. Notably, the upfield shift and 2D ROESY cross-peaks are reproduced in toluene-*d8*. This suggests that the same dimeric structure is present in toluene, which we use for our transient optical measurements.

X-Ray quality single crystals of the pentacene derivatives have eluded us, but we have been able to crystallographically characterize a related lithium dipyridyl pyrrolide with anthracenyl moieties in place of the pentacenyl substituents, Li_2(DPP-Anth)$_2$ (Figure 2.3A). The structure of Li_2(DPP-Anth)$_2$ illustrates the formation of a dimeric species with two Li cations bridged by pyrrolide donors. We propose that Li_2(DPP-Pent)$_2$ has a similar geometry in solution.

The NMR data collected for KDPP-Pent stand in contrast to those of Li_2(DPP-Pent)$_2$. For KDPP-Pent, the dipyridyl pyrrole backbone protons do not display a significant upfield shift or observable cross-peaks between pyrrole and distal pentacene protons in the 2D ROESY spectrum. Therefore, we conclude that KDPP-Pent exists as a monomeric species in solution. We postulate that the small ionic radius of Li^+ permits dimer formation along with favorable π-π interactions, whereas the larger size of K^+ destabilizes such a structure.

Steady-State Absorption and Emission

The steady-state absorption spectra of PentPyBr, HDPP-Pent, Li_2(DPP-Pent)$_2$, and KDPP-Pent in toluene are compared in Figure 2.4A. As with most pentacene derivatives, the $S_1 \leftarrow S_0$ absorption band is observed with pronounced vibronic progression in the 500 – 650 nm region for all four compounds. A weaker vibronically structured band associated with the $S_2 \leftarrow S_0$ pentacene transition can also be observed in all spectra in the 400 – 450 nm region. Notably, the $S_1 \leftarrow S_0$ absorption in HDPP-Pent is roughly twice the intensity of that in PentPyBr with relatively little difference in peak positions (the λ_{max} of the $S_1 \leftarrow S_0$ 0-0 transition is at 622 nm in both spectra). As well, the relative intensities of the vibronic bands within the $S_1 \leftarrow S_0$ electronic transitions are relatively unchanged between HDPP-Pent and PentPyBr. The $S_1 \leftarrow S_0$ band in Li_2(DPP-pent)$_2$ is slightly broadened and the 0-0 band is modestly red-shifted by 5 nm (~130 cm^{-1}) from that of HDPP-Pent. Additionally, both Li_2(DPP-Pent)$_2$ and KDPP-Pent exhibit enhanced absorption intensity near 400 – 500 nm.

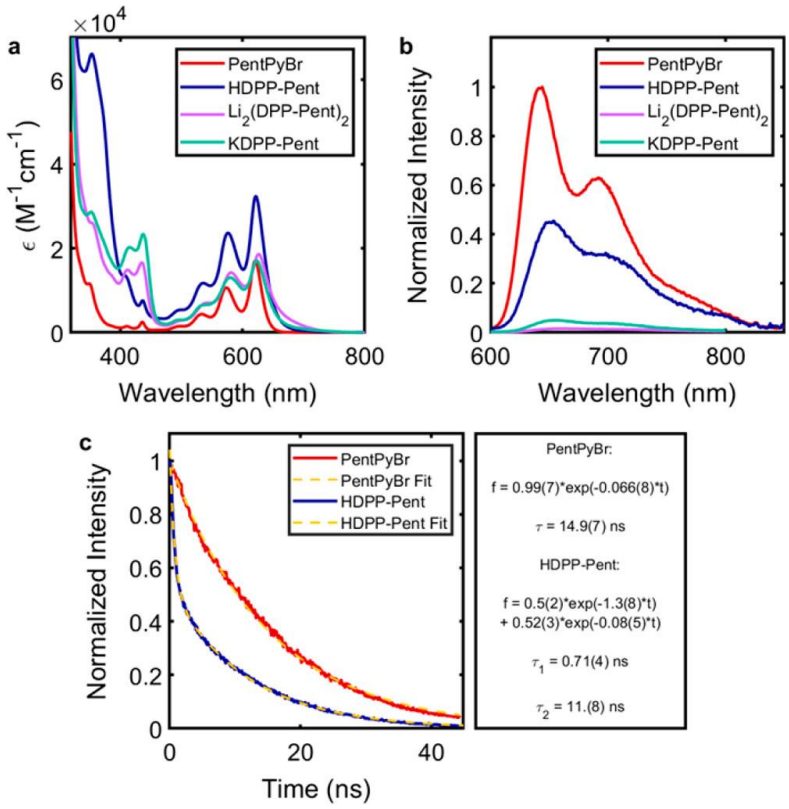

Figure 2.4 Steady-state absorption and emission spectra and time-resolved luminescence data of the pentacene series. Shown are the (**A**) absorption spectra; (**B**) the normalized emission spectra of PentPyBr (red), HDPP-Pent (blue), $Li_2(DPP\text{-}Pent)_2$ (purple), and KDPP-Pent (green) in toluene solutions; and (**C**) time-resolved luminescence traces and fits for PentPyBr (20 μM, toluene) and HDPP-Pent (20 μM, toluene). Note that the steady-state emission spectra are normalized by their relative integrated emission intensities.

Steady-state emission spectra for PentPyBr and HDPP-Pent are compared in Figure 2.4B. Here, the 0-0 emission band of HDPP-Pent (λ_{max} = 650 nm, ~ 15,400 cm^{-1}) is red-shifted from that of PentPyBr (λ_{max} = 640 nm, ~15,600 cm^{-1}) and broadened. The emission observed in this region is consistent with the $S_1 \rightarrow S_0$ fluorescence observed in related pentacene compounds.[46] We found the fluorescence quantum yield of PentPyBr in toluene to be 0.75, comparable to that reported for

TIPS-Pentacene. We found the fluorescence quantum yield of HDPP-Pent to be 0.43, significantly decreased in comparison to the single pentacene in PentPyBr. While Li_2(DPP-Pent)$_2$ and KDPP-Pent display similar emission profiles to HDPP-Pent, the integrated emission intensity is significantly reduced relative to HDPP-Pent.

Time-Resolved Luminescence

We collected time-resolved luminescence traces near the λ_{max} of the 0-0 emission band for PentPyBr (640 nm) and HDPP-Pent (650 nm) as shown in Figure 2.4C. The fluorescence decay for PentPyBr fits well to a monoexponential with a lifetime of ~15 ns. The fluorescence decay for HDPP-Pent, however, must be fit with a biexponential function with a first time constant of 0.71(4) ns and a second of 11.(8) ns. The latter of these two time constants is more consistent with the intrinsic fluorescence decay of the pentacene unit as observed in PentPyBr.

Emission Analysis

For efficient singlet fission (i.e. triplet yields approaching 200%), we expect the prompt fluorescence intensity to vanish, as the fission pathway must deplete the excited S_1 state more efficiently than emission. When singlet fission is sufficiently exothermic, which is the case for pentacene, the reverse triplet-triplet upconversion (fusion) becomes unfavorable, excluding delayed fluorescence. The observation of steady-state fluorescence intensity in HDPP-Pent already indicates that if singlet fission is occurring in this system, it is not operating at full efficiency. Nevertheless, the reduced fluorescence quantum yield of HDPP-Pent relative to PentPyBr suggests that a new, nonemissive relaxation pathway associated with the 0.71(4) ns time constant from the time-resolved luminescence experiment is present in the bipentacene that is not observed in the monopentacene. The biexponential decay of the luminescence signal also suggests that there may

be heterogeneous populations of HDPP-Pent that are excited in the process. For example, different conformers of HDPP-Pent may give rise to efficient pentacene-based emission, whereas others promote the faster nonradiative pathway.

Transient Absorption Spectroscopy – HDPP-Pent

To provide deeper insight into the nature of the nonradiative relaxation process in HDPP-Pent, we performed femtosecond transient absorption (fsTA) spectroscopy on PentPyBr and HDPP-Pent. The fsTA data of PentPyBr (Appendix A, Figure A.14) reveal a single major excited state absorption (ESA) with a λ_{max} around 450 nm (~22,200 cm^{-1}), which is consistent with previous assignments of absorption within the singlet excited state manifold (^{1}ESA) of related pentacene compounds. The observed ^{1}ESA decays monoexponentially over the time window, consistent with the time-resolved fluorescence data.

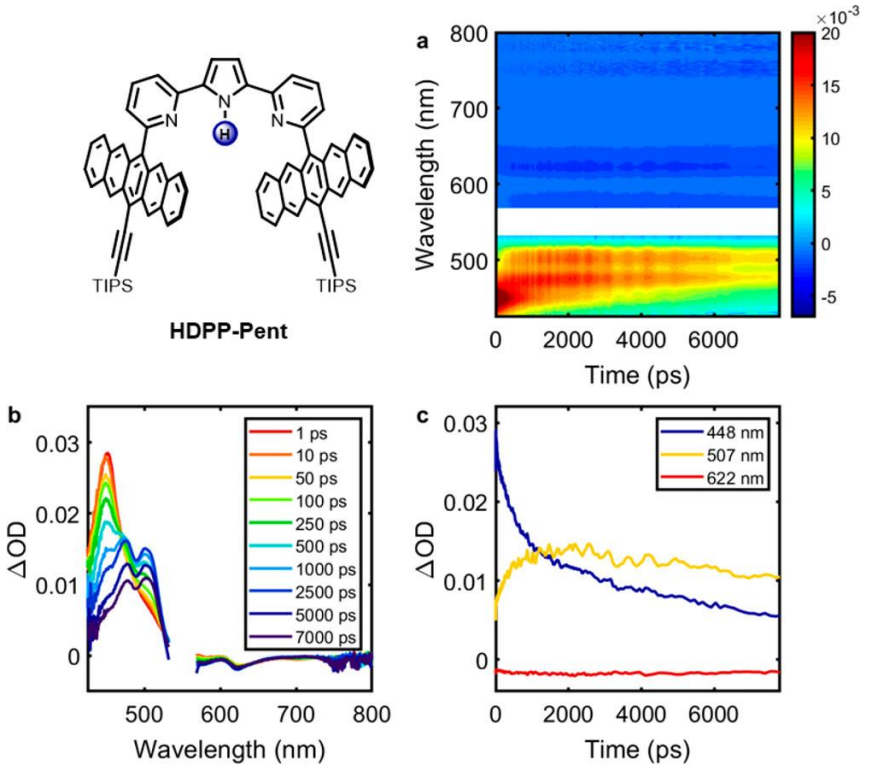

Figure 2.5 Visible transient absorption spectra—HDPP-Pent. The visible femtosecond transient absorption spectra of HDPP-Pent (50 μM, toluene) after excitation at 550 nm (0.100 μJ/pulse) are depicted: (**A**) contour plot, (**B**) spectral traces at various time delays, and (**C**) selected time traces at 448, 507, and 622 nm.

The fsTA data for HDPP-Pent are given in Figure 2.5. A ^{1}ESA at 450 nm is observed at early time delays, but it decays across the fsTA spectrum with the concomitant rise of a new, vibronically structured ESA with a λ_{max} = 510 nm (~19,600 cm^{-1}). This new ESA is consistent with previous literature reports that assign this band to transitions arising from triplet states pentacene (^{3}ESA). It is notable that in these prior reports, there is often little distinguishing the triplet pair excited state from an uncoupled triplet in the visible portion of the TA spectrum. In support of this assignment, we carried out photosensitization experiments in which binary mixtures of anthracene and HDPP-Pent are excited at 360 nm. At this wavelength, anthracene is preferentially excited at the given concentrations, undergoes intersystem crossing, and subsequently can undergo triplet-triplet energy transfer with HDPP-Pent as a means of independently preparing the free triplet state on HDPP-Pent. The long-lived triplet spectrum of HDPP-Pent acquired in these photosensitization experiments corresponds directly to the long-lived species observed in the direct excitation experiments (ESA λ_{max} = 510 nm), corroborating our assignment of this feature as a ^{3}ESA. This triplet signal is not appreciably observed for PentPyBr. The nanosecond TA (nsTA) data for HDPP-Pent (Appendix A, Figure A.10) reveal the decay of triplet signal back to baseline. Comparing the TA data of PentPyBr and HDPP-Pent suggests that the nonradiative pathway in HDPP-Pent may be associated with a transition from the S_1 to the T_1 or ^{M}(TT) states, as indicated by rise of the prominent ^{3}ESA feature with the correlated decay of the ^{1}ESA feature.

Kinetic Modeling

Kinetic modeling was carried out using global and target kinetic analysis on an interpolated dataset of the fsTA and nsTA spectra of HDPP-Pent in order to capture the complete relaxation dynamics. Using target analysis, the entire TA dataset is fitted over all wavelengths and all time delays with the application of a kinetic model. The preparation of the composite dataset and full description of the model applied to HDPP-Pent is provided in Appendix A along with fits for the individual fsTA and nsTA spectra for reference.

The results of our time-resolved luminescence data were used to inform our TA modeling as an independent probe of the S_1 dynamics, leading to a four-component model in which components 1 and 2 equally reflect the ^{1}ESA spectrum, and components 3 and 4 represent the ^{3}ESA spectrum. Component 1 decays into components 3 and 4 equally with a rate constant k_1; component 2 decays to the ground state with rate constant k_2; and components 3 and 4 decay to the ground state decay with rate constants k_3 and k_4, respectively.

This model was applied in two cases: one in which k_1 and k_2 were allowed to vary freely, and one in which k_1 and k_2 were fixed to 1.4 and 0.08 ns^{-1}, respectively, as obtained directly from the time-resolved fluorescence fits. The results of the free and fixed fittings are shown in Appendix Tables A.1 and A.2, respectively. Of note, the results for k_1, k_3, and k_4 are remarkably consistent between the two fits. Even when allowed to vary, the fit of k_1 gives a time constant $\tau_1$of 0.74(6) ns, consistent with the $\tau \sim 0.71$ ns obtained from emission data. This k_1 corresponds to the nonradiative transition from S_1 to T_1 within our model. k_2 shows the largest divergence in the two fits: τ_2 = 4.9(5) ns when allowed to vary from the fixed value of 11.(8) ns. Both values are consistent with the fluorescence lifetime, though error may come from the overlapping of spectral features in the combined fs/nsTA data.

Triplet Yield Estimation – HDPP-Pent

We estimated the triplet yield after direct excitation of HDPP-Pent from the transient absorption data and kinetic modeling. First, the extinction coefficient of the HDPP-Pent triplet absorption spectrum at 510 nm was determined via the triplet energy transfer method using anthracene as a triplet donor under pseudo-first-order kinetic conditions.[47–49] The extinction coefficient of the anthracene triplet spectrum at has previously been reported in toluene.[49] From this, we approximate the extinction coefficient of the HDPP-Pent triplet spectrum at 510 nm to be roughly 49,000 M^{-1} cm^{-1}.

We must be cautious in directly applying the Beer-Lambert law to estimate the concentration of photogenerated triplets in the TA spectrum of HDPP-Pent. Comparing early time traces of the fsTA spectrum where the singlet spectrum dominates to later time traces dominated by the triplet features, it is evident that the ^{1}ESA has spectral intensity at 510 nm that overlaps with the ^{3}ESA feature. As we know from the time-resolved luminescence data, there should be population of the singlet excited state of HDPP-Pent throughout the time scale of the fsTA spectrum owing to the contributions associated with the 11.(8) ns time constant. This means that even when the triplet spectrum at 510 nm reaches its maximum ΔOD intensity, there may be nonnegligible contribution to that signal from the other population of singlet excited HDPP-Pent.

As is shown explicitly in Appendix A, the target model can be used to decompose the maximum ΔOD into its contributions from the ^{1}ESA and ^{3}ESA as 2.8 and 10.0 mOD respectively, using the species associated spectra (SAS) and corresponding concentration profiles. Therefore, after direct excitation of HDPP-Pent in toluene solution, the value of 10.0 mOD for the effective ^{3}ESA intensity provides an estimated triplet yield of ~100%.

Analysis of Singlet Fission in HDPP-Pent

Comparison of the steady-state and time-resolved emission data for HDPP-Pent and PentPyBr indicates that there is at least a population of excited HDPP-Pent molecules that undergo a faster nonradiative relaxation process that is not significant in the monopentacene reference. We collected fs/nsTA data for both samples to further examine this pathway. In HDPP-Pent, the decay of the ^{1}ESA gave rise to significant ^{3}ESA intensity, whereas in PentPyBr, only the decay of the ^{1}ESA was observed. The HDPP-Pent data were modeled given a kinetic scheme in which two populations of HDPP-Pent S_1 state are present and they decay in diverging pathways. This supports the assignment of the fast relaxation time observed in the time-resolved luminescence to be associated with singlet to triplet conversion.

Finally, the triplet yield of HDPP-Pent is estimated to be 100% out of a maximum 200%. As previously noted, the fluorescence quantum yield of HDPP-Pent is 43%. The weighting coefficients of the exponential decays observed in the time-resolved luminescence data are also ~0.5 each. Taken together, these data are self-consistent with a model in which nearly half of the photogenerated singlets give rise to double the number of triplets. We therefore assign the nonradiative transition in HDPP-Pent as intramolecular singlet fission.

Li_2(DPP-Pent)$_2$ and KDPP-Pent

The HDPP-Pent analysis provides a foundation to understand the dynamics exhibited by the alkali metal complexes. The fsTA data for Li_2(DPP-Pent)$_2$ are shown in Figure 2.6. At early time delays, there is a ^{1}ESA feature with a λ_{max} at 450 nm that decays and gives rise to a strong ^{3}ESA centered at 515 nm (~19,400 cm^{-1}). The composite fs/nsTA data of Li_2(DPP-Pent)$_2$ can be kinetically modeled with either a three- or four-component model. In the three-component model,

the S_1 state is converted into the triplet manifold with a time constant τ_1 = 96.(2) ps; the triplet feature is fitted to a biexponential decay with time constants τ_2 = 23.(3) ns and τ_3 = 35.(0) μs. In the four-component model, the S_1 state is converted to the triplet manifold with a time constant τ_1 = 0.11(1) ns, and the triplet feature is fitted to a triexponential decay (τ_2 = 10.(7) ns, τ_3 = 0.1(3) μs, and τ_4 = 50.(1) μs).

Biexponential decays observed for the triplet features are not uncommon in the transient absorption spectra of fission-active bipentacenes. The two decay components are typically ascribed to geminate triplet pair recombination and free/decorrelated triplet decay processes (the former typically on the faster timescale than the latter). Triexponential triplet decays have also been fitted in the singlet fission literature. Notably, this is seen in related adamantane-derived bi- and tetra-pentacene systems reported by Hetzer et al. In that study, the authors compared the transient absorption data to time-resolved EPR experiments collected on their bipentacene species, assigning the three decay components to $^1(T_1T_1)$, $^5(T_1T_1)$, and free T_1.

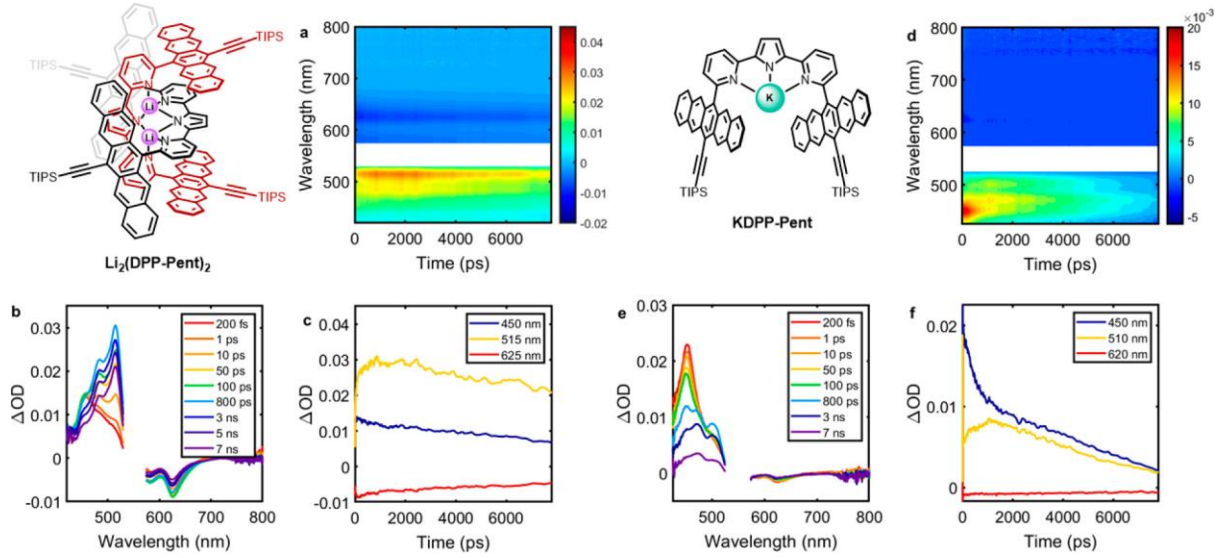

Figure 2.6 Visible transient absorption spectra—$Li_2(DPP\text{-}Pent)_2$ and KDPP-Pent. The visible femtosecond transient absorption spectra of $Li_2(DPP\text{-}Pent)_2$ and KDPP-Pent (50 μM, toluene) are shown after excitation at 550 nm (0.100 μJ/pulse). $Li_2(DPP\text{-}Pent)_2$: (**A**) contour plot, (**B**) spectral traces at various time delays, and (**C**) selected time traces at 450, 515, and 625 nm. KDPP-Pent: (**D**) contour plot, (**E**) spectral traces at various delay times, and (**F**) selected time traces at 450, 510, and 620 nm.

Here, in the absence of additional corroborating evidence, we err on the side of caution and discuss the data in the context of both models. The singlet fission rate is not significantly altered between the two fits. When including a third decay component for the triplet spectral features, though, the fastest triplet lifetime shortens slightly from 23 to 11 ns. In addition, we note that an additional singlet component that decays in parallel to the productive fission pathway could be added to each model; however, the fitted results for each component were not substantially different from the original model, and the rate constants corresponding to the added singlet component had substantially higher standard errors from the fit.

We performed triplet-triplet photosensitization experiments with mixtures of anthracene and $Li_2(DPP\text{-}Pent)_2$ in toluene solution, yielding an extinction coefficient for the $Li_2(DPP\text{-}Pent)_2$ triplet spectrum at 515 nm of ~52,000 M^{-1} cm^{-1}. We applied this value to the fsTA spectrum after direct excitation at 550 nm gives us an approximate triplet yield of 195%. Ground state bleach analysis via the method of Eaton et al. estimates a triplet yield of 186%.[50] Using these two methods, we place the triplet yield of $Li_2(DPP\text{-}Pent)_2$ in the range 186%-195%, considerably higher than in HDPP-Pent.

In the case of KDPP-Pent, the fsTA data show the decay of the ^{1}ESA to a broad feature suggestive of the overlapping singlet and triplet absorption bands observed in HDPP-Pent (Figure

2.5). The nsTA data reveal a structured ^{3}ESA that decays biexponentially. The kinetics could be fitted with both the three-component model applied to the Li_2(DPP-Pent)$_2$ dataset and the four-component model used for HDPP-Pent. There is some absorption intensity in the 400 – 500 nm region in the singular value decomposition of the residual matrix of the three component fit that is adequately accounted for in the four-component model. With regards to the two models, the fittings place a singlet fission time constant in KDPP-Pent around 400 – 600 ps. Despite the qualitative similarity between the K- and HDPP-Pent TA data, little emission intensity was observed from the K complex, and no time-resolved luminescence could be acquired, which suggests that KDPP-Pent may represent an intermediate case between HDPP-Pent and the Li complex.

Comparisons within the DPP-Pent Series

HDPP-Pent undergoes intramolecular singlet fission with a time constant of τ_{SF} of ~730 ps and an estimated 100% triplet yield. Li_2(DPP-Pent)$_2$ is nearly 7-fold faster (τ_{SF} ~ 100 ps) than HDPP-Pent and occurs with higher efficiency (186 – 195% triplet yield). KDPP-Pent, though, demonstrates a rate of singlet fission of 400 – 600 ps, which is similar to HDPP-Pent.

We considered several possibilities for the origin of the rate enhancement observed in Li_2(DPP-Pent)$_2$. First, the NMR data collected on HDPP-Pent demonstrate temperature-dependent conformational dynamics. This suggests that when we excite the solution of HDPP-Pent during the TA experiment, we are exciting a heterogeneity of conformations that are slow to interchange even on the NMR timescale. Some of these conformations may be more or less favorable for intramolecular singlet fission than others, depending on the interpentacene coupling. By deprotonating HDPP-Pent and binding the DPP-Pent moiety to a metal center, we expect the coordination complex to be more rigid than the flexible linker. We posit that this would lead to a

greater uniformity of ground state conformations and could promote greater interactions between the pentacene subunits, leading to more efficient singlet fission. That said, the Li and K complexes both exhibit sharp, well-defined ^{1}H NMR spectra, so structural rigidification alone does not explain the rate enhancement in Li_2(DPP-Pent)$_2$.

Second, the ionic DPP-cation interaction introduces an electric dipole in the vicinity of the pentacene subunits, where a potential Stark effect could influence singlet fission within the system by perturbing the electronic coupling between the relevant excitonic states of the molecule. Li^+ and K^+ have quite different ionic radii (90 and 152 pm, respectively) and we propose there to be two Li^+ cations at the center of the Li_2(DPP-Pent)$_2$ dimer. As a result, we would expect the Li and K complexes to exhibit distinct electric field influences, but at this point it is unclear the extent to which this would differentiate the two.

Third, NMR data supports the assignment of dimeric and monomeric solution-state structures for Li_2(DPP-Pent)$_2$ and KDPP-Pent, respectively. The Li complex exhibits π-stacking interactions between the pentacene rings mediated by a DPP moiety sandwiched in between. Such an π-interaction may enhance the electronic coupling between the two pentacene rings, favoring faster singlet fission. Additionally, the Li dimer brings together four pentacene subunits per molecule as opposed to two (Figure 2.2C). In our proposed structure of Li_2(DPP-Pent)$_2$, the pentacene rings of one DPP-Pent unit are nearly orthogonal to the pentacene rings of the other DPP-Pent unit. This may lead to small overlap between the π-orbitals of the pentacenes, but small structural perturbations or molecular motions could give rise to nonnegligible coupling between the localized states of these pentacenes and impact both singlet fission as well as triplet pair/free triplet distribution over the molecule. We find it likely that this combination of structural

perturbations (including the π-stacking and dimer formation) leads to a pronounced rate enhancement in Li_2(DPP-Pent)$_2$ relative to KDPP-Pent.

Despite the 7-fold rate enhancement in Li_2(DPP-Pent)$_2$, there is little sacrificed in terms of triplet lifetimes. Compared to the ~38 ns and 36 μs lifetimes observed in HDPP-Pent, we find lifetimes of 23 ns and 35 μs in Li_2(DPP-Pent)$_2$ when fitted with a biexponential decay. The faster decay lifetimes in Li_2(DPP-Pent)$_2$ does shorten to 11 ns when fitted to a triexponential, with intermediate and long lifetimes of 100 ns and 50 μs.

Comparison to Previously Reported Bi- and Polypentacenes

In many of the reported bipentacene systems, when there is an increase in the rate of singlet fission, there is also typically an increase in the rate of triplet decay. This has been explained in some bipentacene series by suggesting that the stronger interpentacene electronic coupling that leads to faster singlet fission also simultaneously promotes enhanced triplet-triplet annihilation pathways. The series of phenylene-linked dimers initially reported by Zirzlmeier et al. displays increasing rates of singlet fission going from *meta*- (63 ps) to *para*- (2.7 ps) to *ortho*- (500 fs) and shows a related decrease in triplet pair lifetimes (2.2 ns, 17.3 ps, and 12 ps, respectively). Likewise, the oligophenylene-bridged bipentacenes linked in the 2,2' position reported by Sanders et al. show an analogous increase in singlet fission rate with concomitant reduction in triplet pair lifetimes with decreasing linker units (τ_{SF} from 220 to 20 ps to 760 fs; τ_T from 270 to 16.5 ns to 450 ps for two to one to zero bridging phenylene spacers, respectively). In these cases, conjugated linkers permit strong electronic coupling between pentacenes, which can be modulated via substitution patters on the linker or by increased linker length. Nonconjugated linkers have also been explored, as these systems tend to attenuate the through-bond interpentacene electronic coupling.

Nevertheless, similar trends (increased singlet fission rate with decreased triplet/triplet pair lifetime) have also been observed in such species.

In the DPP-Pent series reported here, the pentacene units are linked in the 6,6'-position by the DPP ligand scaffold. The optimal geometry for the pentacene units is likely orthogonal to the pyridine rings due to steric constraints. In addition to the length of the linking DPP unit, this likely weakens through-bond coupling between the pentacene rings. This is reflected in the relatively slower rate of singlet fission in HDPP-Pent compared to the directly linked *ortho*-, *meta*-, and *para*-phenylene dimers or the oligophenylene-linked systems. In Li_2(DPP-Pent)$_2$, we propose that through-space π-stacking interactions via the intermediary DPP moiety provide an alternative coupling pathway. The rate of singlet fission in Li_2(DPP-Pent)$_2$ (τ_{SF} ~ 100 ps) is still slower than other bipentacenes displaying strong direct pentacene-pentacene π-interactions (typically less than 1 ps) or in the crystalline materials pentacenes are brought in close contact (3 – 4 Å) in the crystal packing. In molecular systems that lack the ability for the triplets to diffuse away from each other, the through-space coupled pentacene dimers tend to have fast triplet pair annihilation pathways, whereas Li_2(DPP-Pent)$_2$ exhibits ns-μs triplet pair/triplet lifetimes.

As previously discussed, the Li complex also has four pentacene units, which could favor a faster rate of singlet fission and slower rate of triplet-triplet annihilation. For example, by comparing adamantyl-linked bi- and tetra-pentacene systems, Hetzer et al. suggested that additional chromophores may effectively delocalize the triplet pair state, providing a favorable entropic factor to the rate of fission. The authors report that the tetra-pentacene species likewise shows very little deviation in the triplet lifetimes from the bipentacene system, despite the faster rate of fission.

The higher-order structure enforced by lithium coordination in Li_2(DPP-Pent)$_2$ likely impacts the photophysics of the system in several ways. First, the through-space π-interactions establish an important coupling pathway that leads to the rate enhancement from HDPP-Pent and KDPP-Pent; however, because the coupling is mediated via the dipyridyl pyrrolide, this interaction is tempered such that the generated triplet pair is longer lived than in other π-stacked bipentacenes. This may work in conjunction with the entropic favorability of having four pentacene rings within a single molecular dimer over which the triplets may diffuse or delocalize.

Conclusion

In summary, we have synthesized the molecular bipentacene system HDPP-Pent that serves as a ligand scaffold. By deprotonation and complexation, we may change the structural morphology and interchromophore interactions in solution in order to effectively tune singlet fission. We propose that the π-stacking interactions and dimeric structure revealed in Li_2(DPP-Pent)$_2$ are critical to its increased singlet fission efficiency compared to the parent HDPP-Pent. This approach highlights the importance of through-space, geometric perturbations that influence singlet fission beyond strict through-bond interactions. Use of coordination chemistry as a means of orienting and controlling excitonic interactions in bipentacene compounds is presented as a new tool for studying singlet fission in molecular systems.

Citations

(1) Smith, M. B.; Michl, J. Singlet Fission. *Chem. Rev.* **2010**, *110* (11), 6891–6936. https://doi.org/10.1021/cr1002613.

(2) Smith, M. B.; Michl, J. Recent Advances in Singlet Fission. *Annual Review of Physical Chemistry* **2013**, *64* (1), 361–386. https://doi.org/10.1146/annurev-physchem-040412-110130.

(3) Swenberg, C. E.; Stacy, W. T. Bimolecular Radiationless Transitions in Crystalline Tetracene. *Chemical Physics Letters* **1968**, *2* (5), 327–328. https://doi.org/10.1016/0009-2614(68)80087-9.

(4) Merrifield, R. E.; Avakian, P.; Groff, R. P. Fission of Singlet Excitons into Pairs of Triplet Excitons in Tetracene Crystals. *Chemical Physics Letters* **1969**, *3* (3), 155–157. https://doi.org/10.1016/0009-2614(69)80122-3.

(5) Merrifield, R. E. Magnetic Effects on Triplet Exciton Interactions. *Pure and Applied Chemistry* **1971**, *27* (3), 481–498. https://doi.org/10.1351/pac197127030481.

(6) Shockley, W.; Queisser, H. J. Detailed Balance Limit of Efficiency of P-n Junction Solar Cells. *Journal of Applied Physics* **1961**, *32* (3), 510–519. https://doi.org/10.1063/1.1736034.

(7) Hanna, M. C.; Nozik, A. J. Solar Conversion Efficiency of Photovoltaic and Photoelectrolysis Cells with Carrier Multiplication Absorbers. *Journal of Applied Physics* **2006**, *100* (7), 074510. https://doi.org/10.1063/1.2356795.

(8) Paci, I.; Johnson, J. C.; Chen, X.; Rana, G.; Popović, D.; David, D. E.; Nozik, A. J.; Ratner, M. A.; Michl, J. Singlet Fission for Dye-Sensitized Solar Cells: Can a Suitable Sensitizer Be Found? *J. Am. Chem. Soc.* **2006**, *128* (51), 16546–16553. https://doi.org/10.1021/ja063980h.

(9) Rao, A.; Wilson, M. W. B.; Hodgkiss, J. M.; Albert-Seifried, S.; Bässler, H.; Friend, R. H. Exciton Fission and Charge Generation via Triplet Excitons in Pentacene/C60 Bilayers. *J. Am. Chem. Soc.* **2010**, *132* (36), 12698–12703. https://doi.org/10.1021/ja1042462.

(10) Ehrler, B.; Wilson, M. W. B.; Rao, A.; Friend, R. H.; Greenham, N. C. Singlet Exciton Fission-Sensitized Infrared Quantum Dot Solar Cells. *Nano Lett.* **2012**, *12* (2), 1053–1057. https://doi.org/10.1021/nl204297u.

(11) Ehrler, B.; Musselman, K. P.; Böhm, M. L.; Friend, R. H.; Greenham, N. C. Hybrid Pentacene/a-Silicon Solar Cells Utilizing Multiple Carrier Generation via Singlet Exciton Fission. *Appl. Phys. Lett.* **2012**, *101* (15), 153507. https://doi.org/10.1063/1.4757612.

(12) Smyser, K. E.; Eaves, J. D. Singlet Fission for Quantum Information and Quantum Computing: The Parallel JDE Model. *Sci Rep* **2020**, *10* (1), 18480. https://doi.org/10.1038/s41598-020-75459-x.

(13) Weiss, L. R.; Bayliss, S. L.; Kraffert, F.; Thorley, K. J.; Anthony, J. E.; Bittl, R.; Friend, R. H.; Rao, A.; Greenham, N. C.; Behrends, J. Strongly Exchange-Coupled Triplet Pairs in an Organic Semiconductor. *Nature Phys* **2017**, *13* (2), 176–181. https://doi.org/10.1038/nphys3908.

(14) Tayebjee, M. J. Y.; Sanders, S. N.; Kumarasamy, E.; Campos, L. M.; Sfeir, M. Y.; McCamey, D. R. Quintet Multiexciton Dynamics in Singlet Fission. *Nature Phys* **2017**, *13* (2), 182–188. https://doi.org/10.1038/nphys3909.

(15) Bayliss, S. L.; Weiss, L. R.; Mitioglu, A.; Galkowski, K.; Yang, Z.; Yunusova, K.; Surrente, A.; Thorley, K. J.; Behrends, J.; Bittl, R.; Anthony, J. E.; Rao, A.; Friend, R. H.; Plochocka, P.; Christianen, P. C. M.; Greenham, N. C.; Chepelianskii, A. D. Site-Selective Measurement of Coupled Spin Pairs in an Organic Semiconductor. *Proceedings of the National Academy of Sciences* **2018**, *115* (20), 5077–5082. https://doi.org/10.1073/pnas.1718868115.

(16) Lubert-Perquel, D.; Salvadori, E.; Dyson, M.; Stavrinou, P. N.; Montis, R.; Nagashima, H.; Kobori, Y.; Heutz, S.; Kay, C. W. M. Identifying Triplet Pathways in Dilute Pentacene Films. *Nat Commun* **2018**, *9* (1), 4222. https://doi.org/10.1038/s41467-018-06330-x.

(17) Wan, Y.; Wiederrecht, G. P.; Schaller, R. D.; Johnson, J. C.; Huang, L. Transport of Spin-Entangled Triplet Excitons Generated by Singlet Fission. *J. Phys. Chem. Lett.* **2018**, *9* (23), 6731–6738. https://doi.org/10.1021/acs.jpclett.8b02944.

(18) Nagashima, H.; Kawaoka, S.; Akimoto, S.; Tachikawa, T.; Matsui, Y.; Ikeda, H.; Kobori, Y. Singlet-Fission-Born Quintet State: Sublevel Selections and Trapping by Multiexciton Thermodynamics. *J. Phys. Chem. Lett.* **2018**, *9* (19), 5855–5861. https://doi.org/10.1021/acs.jpclett.8b02396.

(19) Chen, M.; Krzyaniak, M. D.; Nelson, J. N.; Bae, Y. J.; Harvey, S. M.; Schaller, R. D.; Young, R. M.; Wasielewski, M. R. Quintet-Triplet Mixing Determines the Fate of the Multiexciton State Produced by Singlet Fission in a Terrylenediimide Dimer at Room Temperature. *Proceedings of the National Academy of Sciences* **2019**, *116* (17), 8178–8183. https://doi.org/10.1073/pnas.1820932116.

(20) Matsuda, S.; Oyama, S.; Kobori, Y. Electron Spin Polarization Generated by Transport of Singlet and Quintet Multiexcitons to Spin-Correlated Triplet Pairs during Singlet Fissions. *Chem. Sci.* **2020**, *11* (11), 2934–2942. https://doi.org/10.1039/C9SC04949E.

(21) Hetzer, C.; Guldi, D. M.; Tykwinski, R. R. Pentacene Dimers as a Critical Tool for the Investigation of Intramolecular Singlet Fission. *Chemistry – A European Journal* **2018**, *24* (33), 8245–8257. https://doi.org/10.1002/chem.201705355.

(22) Sanders, S. N.; Pun, A. B.; Parenti, K. R.; Kumarasamy, E.; Yablon, L. M.; Sfeir, M. Y.; Campos, L. M. Understanding the Bound Triplet-Pair State in Singlet Fission. *Chem* **2019**, *5* (8), 1988–2005. https://doi.org/10.1016/j.chempr.2019.05.012.

(23) Korovina, N. V.; Pompetti, N. F.; Johnson, J. C. Lessons from Intramolecular Singlet Fission with Covalently Bound Chromophores. *J. Chem. Phys.* **2020**, *152* (4), 040904. https://doi.org/10.1063/1.5135307.

(24) Wilson, M. W. B.; Rao, A.; Clark, J.; Kumar, R. S. S.; Brida, D.; Cerullo, G.; Friend, R. H. Ultrafast Dynamics of Exciton Fission in Polycrystalline Pentacene. *J. Am. Chem. Soc.* **2011**, *133* (31), 11830–11833. https://doi.org/10.1021/ja201688h.

(25) Rao, A.; Wilson, M. W. B.; Albert-Seifried, S.; Di Pietro, R.; Friend, R. H. Photophysics of Pentacene Thin Films: The Role of Exciton Fission and Heating Effects. *Phys. Rev. B* **2011**, *84* (19), 195411. https://doi.org/10.1103/PhysRevB.84.195411.

(26) Zirzlmeier, J.; Lehnherr, D.; Coto, P. B.; Chernick, E. T.; Casillas, R.; Basel, B. S.; Thoss, M.; Tykwinski, R. R.; Guldi, D. M. Singlet Fission in Pentacene Dimers. *PNAS* **2015**, *112* (17), 5325–5330. https://doi.org/10.1073/pnas.1422436112.

(27) Sanders, S. N.; Kumarasamy, E.; Pun, A. B.; Trinh, M. T.; Choi, B.; Xia, J.; Taffet, E. J.; Low, J. Z.; Miller, J. R.; Roy, X.; Zhu, X.-Y.; Steigerwald, M. L.; Sfeir, M. Y.; Campos, L. M. Quantitative Intramolecular Singlet Fission in Bipentacenes. *J. Am. Chem. Soc.* **2015**, *137* (28), 8965–8972. https://doi.org/10.1021/jacs.5b04986.

(28) Basel, B. S.; Zirzlmeier, J.; Hetzer, C.; Reddy, S. R.; Phelan, B. T.; Krzyaniak, M. D.; Volland, M. K.; Coto, P. B.; Young, R. M.; Clark, T.; Thoss, M.; Tykwinski, R. R.; Wasielewski, M. R.; Guldi, D. M. Evidence for Charge-Transfer Mediation in the Primary Events of Singlet Fission in a Weakly Coupled Pentacene Dimer. *Chem* **2018**, *4* (5), 1092–1111. https://doi.org/10.1016/j.chempr.2018.04.006.

(29) Papadopoulos, I.; Zirzlmeier, J.; Hetzer, C.; Bae, Y. J.; Krzyaniak, M. D.; Wasielewski, M. R.; Clark, T.; Tykwinski, R. R.; Guldi, D. M. Varying the Interpentacene Electronic Coupling to Tune Singlet Fission. *J. Am. Chem. Soc.* **2019**, *141* (15), 6191–6203. https://doi.org/10.1021/jacs.8b09510.

(30) Basel, B. S.; Hetzer, C.; Zirzlmeier, J.; Thiel, D.; Guldi, R.; Hampel, F.; Kahnt, A.; Clark, T.; Guldi, D. M.; Tykwinski, R. R. Davydov Splitting and Singlet Fission in Excitonically Coupled Pentacene Dimers. *Chem. Sci.* **2019**, *10* (13), 3854–3863. https://doi.org/10.1039/C9SC00384C.

(31) Sanders, S. N.; Kumarasamy, E.; Pun, A. B.; Appavoo, K.; Steigerwald, M. L.; Campos, L. M.; Sfeir, M. Y. Exciton Correlations in Intramolecular Singlet Fission. *J. Am. Chem. Soc.* **2016**, *138* (23), 7289–7297. https://doi.org/10.1021/jacs.6b00657.

(32) Sanders, S. N.; Kumarasamy, E.; Pun, A. B.; Steigerwald, M. L.; Sfeir, M. Y.; Campos, L. M. Intramolecular Singlet Fission in Oligoacene Heterodimers. *Angewandte Chemie International Edition* **2016**, *55* (10), 3373–3377. https://doi.org/10.1002/anie.201510632.

(33) Fuemmeler, E. G.; Sanders, S. N.; Pun, A. B.; Kumarasamy, E.; Zeng, T.; Miyata, K.; Steigerwald, M. L.; Zhu, X.-Y.; Sfeir, M. Y.; Campos, L. M.; Ananth, N. A Direct Mechanism of Ultrafast Intramolecular Singlet Fission in Pentacene Dimers. *ACS Cent. Sci.* **2016**, *2* (5), 316–324. https://doi.org/10.1021/acscentsci.6b00063.

(34) Kumarasamy, E.; Sanders, S. N.; Tayebjee, M. J. Y.; Asadpoordarvish, A.; Hele, T. J. H.; Fuemmeler, E. G.; Pun, A. B.; Yablon, L. M.; Low, J. Z.; Paley, D. W.; Dean, J. C.; Choi, B.; Scholes, G. D.; Steigerwald, M. L.; Ananth, N.; McCamey, D. R.; Sfeir, M. Y.; Campos, L. M. Tuning Singlet Fission in π-Bridge-π Chromophores. *J. Am. Chem. Soc.* **2017**, *139* (36), 12488–12494. https://doi.org/10.1021/jacs.7b05204.

(35) Mandal, A.; Chen, M.; Foszcz, E. D.; Schultz, J. D.; Kearns, N. M.; Young, R. M.; Zanni, M. T.; Wasielewski, M. R. Two-Dimensional Electronic Spectroscopy Reveals Excitation Energy-Dependent State Mixing during Singlet Fission in a Terrylenediimide Dimer. *J. Am. Chem. Soc.* **2018**, *140* (51), 17907–17914. https://doi.org/10.1021/jacs.8b08627.

(36) Hetzer, C.; Basel, B. S.; Kopp, S. M.; Hampel, F.; White, F. J.; Clark, T.; Guldi, D. M.; Tykwinski, R. R. Chromophore Multiplication To Enable Exciton Delocalization and Triplet

Diffusion Following Singlet Fission in Tetrameric Pentacene. *Angewandte Chemie International Edition* **2019**, *58* (43), 15263–15267. https://doi.org/10.1002/anie.201907221.

(37) Casillas, R.; Adam, M.; Coto, P. B.; Waterloo, A. R.; Zirzlmeier, J.; Reddy, S. R.; Hampel, F.; McDonald, R.; Tykwinski, R. R.; Thoss, M.; Guldi, D. M. Intermolecular Singlet Fission in Unsymmetrical Derivatives of Pentacene in Solution. *Advanced Energy Materials* **2019**, *9* (2), 1802221. https://doi.org/10.1002/aenm.201802221.

(38) Basel, B. S.; Young, R. M.; Krzyaniak, M. D.; Papadopoulos, I.; Hetzer, C.; Gao, Y.; Porte, N. T. L.; Phelan, B. T.; Clark, T.; Tykwinski, R. R.; Wasielewski, M. R.; Guldi, D. M. Influence of the Heavy-Atom Effect on Singlet Fission: A Study of Platinum-Bridged Pentacene Dimers. *Chem. Sci.* **2019**, *10* (48), 11130–11140. https://doi.org/10.1039/C9SC04410H.

(39) Papadopoulos, I.; Gao, Y.; Hetzer, C.; Tykwinski, R. R.; Guldi, D. M. Singlet Fission in Enantiomerically Pure Pentacene Dimers. *ChemPhotoChem* **2020**, *4* (10), 5168–5174. https://doi.org/10.1002/cptc.202000016.

(40) Chen, M.; Bae, Y. J.; Mauck, C. M.; Mandal, A.; Young, R. M.; Wasielewski, M. R. Singlet Fission in Covalent Terrylenediimide Dimers: Probing the Nature of the Multiexciton State Using Femtosecond Mid-Infrared Spectroscopy. *J. Am. Chem. Soc.* **2018**, *140* (29), 9184–9192. https://doi.org/10.1021/jacs.8b04830.

(41) Zirzlmeier, J.; Casillas, R.; Reddy, S. R.; Coto, P. B.; Lehnherr, D.; Chernick, E. T.; Papadopoulos, I.; Thoss, M.; Tykwinski, R. R.; Guldi, D. M. Solution-Based Intramolecular Singlet Fission in Cross-Conjugated Pentacene Dimers. *Nanoscale* **2016**, *8* (19), 10113–10123. https://doi.org/10.1039/C6NR02493A.

(42) Shetty, A. S.; Zhang, J.; Moore, J. S. Aromatic π-Stacking in Solution as Revealed through the Aggregation of Phenylacetylene Macrocycles. *J. Am. Chem. Soc.* **1996**, *118* (5), 1019–1027. https://doi.org/10.1021/ja9528893.

(43) Platts, J. A.; Gkionis, K. NMR Shielding as a Probe of Intermolecular Interactions: Ab Initio and Density Functional Theory Studies. *Phys. Chem. Chem. Phys.* **2009**, *11* (44), 10331–10339. https://doi.org/10.1039/B822560E.

(44) Bothner-By, A. A.; Stephens, R. L.; Lee, J.; Warren, C. D.; Jeanloz, R. W. Structure Determination of a Tetrasaccharide: Transient Nuclear Overhauser Effects in the Rotating Frame. *J. Am. Chem. Soc.* **1984**, *106* (3), 811–813. https://doi.org/10.1021/ja00315a069.

(45) Bax, A.; Davis, D. G. Practical Aspects of Two-Dimensional Transverse NOE Spectroscopy. *Journal of Magnetic Resonance (1969)* **1985**, *63* (1), 207–213. https://doi.org/10.1016/0022-2364(85)90171-4.

(46) Walker, B. J.; Musser, A. J.; Beljonne, D.; Friend, R. H. Singlet Exciton Fission in Solution. *Nature Chem* **2013**, *5* (12), 1019–1024. https://doi.org/10.1038/nchem.1801.

(47) Bensasson, R.; Land, E. J. Triplet-Triplet Extinction Coefficients via Energy Transfer. *Trans. Faraday Soc.* **1971**, *67* (0), 1904–1915. https://doi.org/10.1039/TF9716701904.

(48) Compton, R. H.; Grattan, K. T. V.; Morrow, T. Extinction Coefficients and Quantum Yields for Triplet—Triplet Absorption Using Laser Flash Photolysis. *Journal of Photochemistry* **1980**, *14* (1), 61–66. https://doi.org/10.1016/0047-2670(80)85068-4.

(49) Nielsen, B. R.; Jørgensen, K.; Skibsted, L. H. Triplet—Triplet Extinction Coefficients, Rate Constants of Triplet Decay and Rate Constant of Anthracene Triplet Sensitization by Laser Flash Photolysis of Astaxanthin, β-Carotene, Canthaxanthin and Zeaxanthin in Deaerated Toluene at 298 K. *Journal of Photochemistry and Photobiology A: Chemistry* **1998**, *112* (2), 127–133. https://doi.org/10.1016/S1010-6030(97)00285-2.

(50) Eaton, S. W.; Shoer, L. E.; Karlen, S. D.; Dyar, S. M.; Margulies, E. A.; Veldkamp, B. S.; Ramanan, C.; Hartzler, D. A.; Savikhin, S.; Marks, T. J.; Wasielewski, M. R. Singlet Exciton Fission in Polycrystalline Thin Films of a Slip-Stacked Perylenediimide. *J. Am. Chem. Soc.* **2013**, *135* (39), 14701–14712. https://doi.org/10.1021/ja4053174.

Chapter III

Temperature Dependent Electron Spin Relaxation in Cupric and Vanadyl Phthalocyanines

Introduction

Quantum information science (QIS) is a growing field that encompasses a range of technologies that take advantage of quantum properties such as coherence and entanglement. These technologies include quantum computing, cryptography, as well as quantum sensing and metrology.[1] These applications broadly regard the writing, reading, and transfer of information in some form. The fundamental unit of information in QIS is the quantum bit or "qubit." In contrast to classical computation, in which a bit can occupy a 0 or 1 state, the qubit may be initiated into a coherent superposition of the two states, which can be described by any linear combination of the basis states (i.e. $\alpha|0\rangle + \beta|1\rangle$ where α and β are, in general, complex numerical constants and by typical convention $|\alpha|^2 + |\beta|^2 = 1$). For a single qubit, states can be represented by a vector on a unit sphere, known as a Bloch sphere, as shown in Figure 3.1.

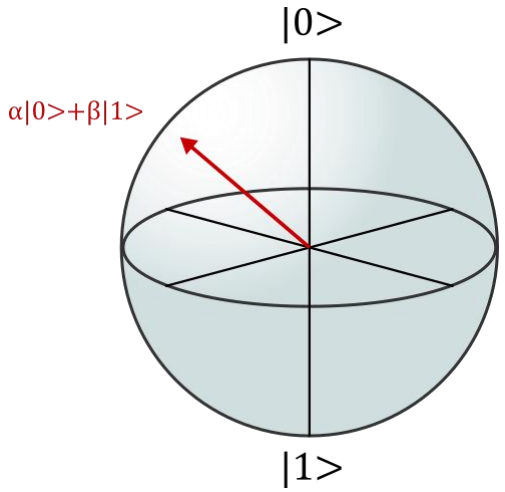

Figure 3.1 The Bloch sphere representation of an arbitrary superposition state $\alpha|0\rangle + \beta|1\rangle$.

The ability to parallelize qubits in superposition states provides quantum algorithms benefits over classical algorithms when applied to certain types of problems. Quantum

computation may promise enhanced speed when it comes to factoring large numbers (e.g., Shor's algorithm), searching databases, and simulating quantum systems among other problems that pose challenges to classical computing architectures.

In 2000, DiVincenzo put forth a set of rules for the implementation of a qubit in a quantum computing framework: (1) the physical system implementing the qubits should be scalable and the qubits themselves well-defined, (2) the qubit should be readily initialized into a simple initial state, (3) the qubit should exhibit a long coherence lifetime within which operations can be performed, (4) there must be universally applicable quantum gates or operations to perform on the qubit system, and (5) each qubit should be individually addressable. These guidelines have availed researchers in the field toward fundamental understanding and implementation of quantum information systems.[1]

A qubit, by the definition given above, represents any quantum object encompassing a two-level system. This could be the spin states of an S = ½ particle, the vertical and horizontal polarizations of a photon, the quantized flux, charge, or phase states of designed superconducting loops, or the ground and excited electronic states of an atom or molecule.[2–4] Particularly in the case of molecular systems, there are generally many more available spin and electronic states than two. However, we often treat a given transition by considering just two states (an upper and lower) when they are separated by an energy that is resonant with an external radiation field. If the coupling of the two qubit states to the other internal states of the system remains small, the case when the other states are disparate in energy from the relevant states, the two-level system approximation holds. Efforts have been made to describe individual qubits with greater than two levels. Although sometimes named with respect to the number of states in the manifold, such systems are often collectively referred to as "qudits," regardless of the number of states.

Each type of qubit candidate has both advantages and disadvantages for its implementation in QIS architectures. For example, superconducting qubit circuits are macroscopic objects that behave quantum mechanically and can be manufactured by photo- or electron-beam lithography. Superconducting qubits allow for tailoring of resonant frequencies and interqubit coupling. Single qubits may also be addressed by application of external electric or microwave fields. However, superconducting qubits typically require exceptionally low temperatures (often milli-Kelvin ranges) for successful operation and protection from decoherence. This poses a challenge to scalability as well as high operational costs due to the refrigerator requirement.[2] Qubits based on nuclear or electronic spin can boast long coherence lifetimes and may be robust to decoherence at higher temperatures, which may aid in scalability and operational costs. However, the energy levels of single atom spin systems cannot readily be tuned as they are intrinsic to the atom. Atomic spin defects in solid-state semiconductors have long been proposed as a potential platform for QIS and systems such as P defects in SiC or N-vacancy centers in diamond have found important applications.[5–9] Still, tailorability of individual qubit Hamiltonian parameters, control of qubit placement within the material, and control of interqubit interaction remains challenging. Molecular spin qubits have therefore garnered attention for the ability to tune the Hamiltonian of a given spin system as well as to control qubit-qubit spacing and coupling by synthetic design.[3,4]

For an electron spin qubit in an externally applied magnetic field, the system may be initialized and operated on by a microwave pulse resonant with the Zeeman splitting of the spin sublevels. The states of the system may therefore be read out via pulsed electron paramagnetic resonance (EPR) spectroscopy.[10–21] In EPR, the bulk magnetization of the sample is measured. Once the net magnetization is rotated from its alignment with the external field by the microwave pulse, the system will reapproach equilibrium via magnetic relaxation pathways. The important

magnetic relaxation parameters are the spin-lattice or longitudinal relaxation time (T_1) and the spin-spin or phase memory time (T_M) (see Introduction for further information on T_1 and T_M).

The phase memory time, and more specifically T_2, report on the decoherence time of the qubit system. It has been estimated that T_2 lifetimes greater than 100 μs are necessary to perform desired gate sequences using a qubit. However, in pursuit of qubit technologies approaching room temperature, we must also consider the spin-lattice relaxation behavior of the system. At low temperatures, the T_1 time is generally much longer than the T_M. However, as the temperature increases, the T_1 time will decrease, often rapidly so. As the T_1 time reflects the return of the z-component of the magnetization vector, this also forces the transverse components to zero, limiting the ability to manipulate and read out coherence. It is this regime in which we describe T_M as being T_1-limited and is the focus of the current study.[22,23]

Here we examine two S = ½ metal complexes in the context of their magnetic relaxation properties as it pertains to quantum information science: Cu(II) phthalocyanine (CuPc) and vanadyl (VOPc) phthalocyanine.[24–27] The temperature-dependent magnetic relaxation behavior of VOPc was previously characterized in various dilutions in diamagnetic titanyl phthalocyanine (TiOPc) matrices by Atzori et al.[14] These works stand in a long line of investigation into paramagnetic relaxation processes in inorganic coordination complexes. The foundational theory of spin-lattice relaxation was laid by Van Vleck, Pryce, Orbach, and others. G. R. and S. S. Eaton have further expanded the experimental study of orientation-, field-, and temperature-dependent magnetic relaxation in organic and inorganic systems.[23,28–37]

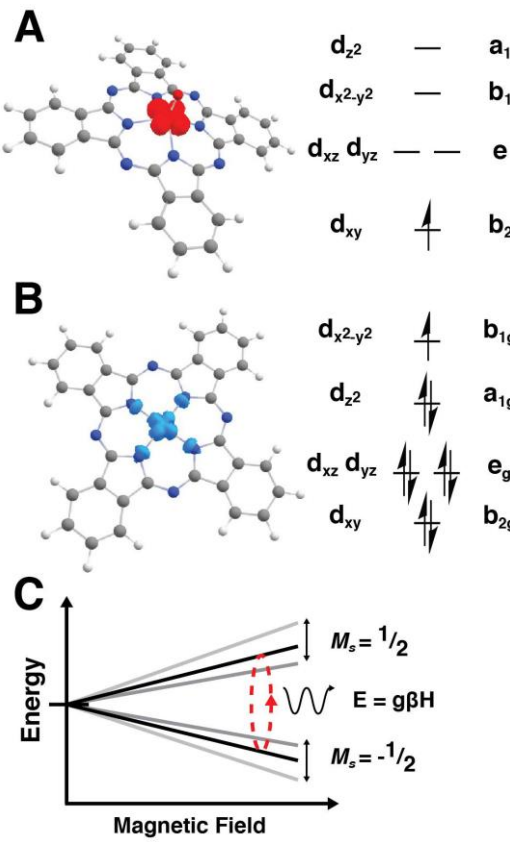

Figure 3.2 Spin densities and qualitative 3d-orbital energy diagrams for (**A**) VOPc and (**B**) CuPc. (**C**) Zeeman splitting of the M_s sublevels of an S = ½ system and the effects of spin-phonon-induced modulation of the energy splitting (gray lines) and coherence (red-dashed ellipse).

Results

According to prior literature, we prepared polycrystalline samples of VOPc diluted in a diamagnetic TiOPc matrix at 1:1000 and 1:100 VOPc/TiOPc concentrations. We examined the PXRD patterns of both mixtures and found them to be consistent with previously reported data for the type II polymorph. We collected the X-band CW EPR spectra for each sample and they are consistent with each other, exhibiting the expected eight-line powder pattern for V^{IV} (the almost 100% naturally abundant ^{51}V has a nuclear spin I = 7/2). Notably, these spectra also feature the presence of an additional isotropic EPR transition centered around g ~ 2, consistent with an organic

radical. Such radical impurities have commonly been observed in metal- and metal-free phthalocyanine EPR spectra. Echo-detected field sweeps (EDFSs) of the two samples taken at 5 and 60 K are likewise consistent with previous reports. The EDFS, T_1 inversion recovery, and T_m Hahn echo sequences were collected across a range of temperatures from 5 – 300 K for both samples.

Orientation Dependence of T_1 and T_m in VOPc

We compare here the T_1 and T_m times estimated from inversion recovery and two pulse Hahn echo experiments collected at four magnetic field positions, 303 ($g_{||}$, $M_I = -5/2$), 329 ($g_{\perp}$, $M_I = -3/2$), 335.6 ($g_{||}$ and $g_{\perp}$, $M_I = -1/2$), and 386 mT ($g_{||}$, $M_I = +5/2$) at X-band. We carried out identical experiments at four magnetic field positions at Q-band: 1197.5 ($g_{||}$, $M_I = -5/2$), 1214 ($g_{\perp}$, $M_I = -3/2$), 1218 ($g_{\perp}$, $M_I = -1/2$), and 1265.5 mT ($g_{||}$, $M_I = +5/2$). The assignments of the M_I eigenvalues involved in the transitions are kept consistent with Du et al. We chose these magnetic field positions to sample a variety of resonance conditions near extrema for parallel and perpendicular orientations to the field and various hyperfine sublevels.

There is a small observable orientation dependence of T_1 in 1:1000 VOPc at X-band, but it remains across the temperature range sampled. We observe slightly longer T_1 times on the wings of the spectrum at the peaks associated with the $M_I = -5/2$ and $+5/2$ transitions of $g_{||}$, although there is overall little differentiation between M_I sublevel transitions.[35] We observe a similar orientation dependence on T_1, although there is an unexpected rise in the T_1 times collected at the 1218 mT feature at 110 K. Although this rise was reproducible, we are as yet unsure of its origin.

There is a slight orientation dependence in the T_m values as well, and we similarly observe the parallel extrema of the $M_I = -5/2$ and $+5/2$ having longer T_m times than at the perpendicular

positions. The sensitivity of T_m's to orientation has been previously ascribed to molecular motions, particularly those that can move a given spin system out of resonance with the microwave pulse that ultimately refocuses the spin packet, as this leads to decoherence. For an axial system such as VOPc, it is convenient to consider the molecular z-axis and its orientation relative to the B_0 field of the spectrometer. Owing to the anisotropy of the spin system, the resonant magnetic field changes upon rotating the molecular z-axis away from parallel to perpendicular orientations with respect to the external field. Importantly, the resonant field changes more rapidly with the rotation angle nearing perpendicular orientations. This contextualizes the orientation dependence of T_m observed as low frequency motions will impact the resonance field of a spin system near perpendicular orientations, leading to greater decoherence, more so than at parallel orientations. For example, in CuTTP and VOTTP (TTP = 5,10,15,20-tetratolylporphyrin), the phase memory times declined as the applied field approaches resonant conditions with intermediate orientations.[23] Due to the axial nature of VOPc and CuPc, we therefore expect that out-of-plane motions that disturb the transition metal center will be most relevant for shortening T_m's at a given position.

Frequency Dependence of T_1 and T_m in VOPc

At Q-band, the EDFS spectra of VOPc exhibit sharper features than at X-band owing to the better resolved vanadium hyperfine transitions. We observe these same transitions across the 5 to 300 K range in the EDFSs. The trends in T_1's and T_m's across the temperature range are similar to those observed at X-band. Although the T_1 trend is similar at each field position at X-band, the T_1's obtained at 1218 mT are notably longer than those measured at other positions throughout the temperatures examined. Previous reports examined the relaxation behavior of VOTTP-COOH (TTP-COOH = 5-(4-carboxyphenyl)-10,15,20,-tri(tolyl)porphyrin) at S-, X-, and W-band and found that at higher temperatures the T_1's become similar irrespective of the spectrometer

frequency. We similarly observe this trend in T_1's above 50 K in our VOPc samples. In this temperature range, Raman and local mode mechanisms may dominate spin-lattice relaxation, and these pathways are expected to be frequency-independent. At low temperatures, as is observed for VOTTP-COOH, direct processes dominate relaxation and give rise to faster relaxation rates going from S- to X- to W-band.[36] The direct process is proportional to B_0^4 for a Kramers system.[37] We observe, overall, quite comparable T_1 times between our VOPc data collected at X-band versus Q-band.

The T_m times follow a similar pattern observed for T_1 in that the phase memory times measured at 1218 mT were markedly longer than those measured at other field positions at Q-band. The T_m's measured at 1218 mT at Q-band were comparable to those measured in the X-band experiments, whereas the T_m's collected at other positions measured at Q-band were generally shorter than the corresponding times measured at X-band.

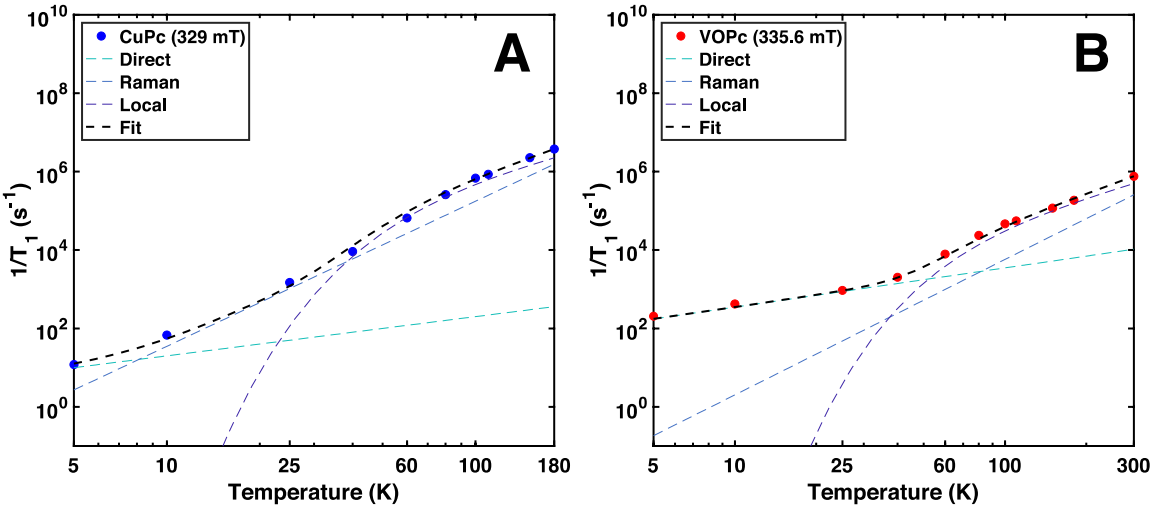

Figure 3.3 Fits of the temperature dependence of $1/T_1$ vs. temperature to direct, Raman, and local mode processes for (A) CuPc (329 mT) and (B) VOPc (335.6 mT) 1:1000 preparations at X-band.

Temperature Dependence of T_1 and T_m in VOPc

Atzori et al. reported spin-lattice relaxation times of the 1:1000 VOPc/TiOPc samples to be 14 ms at 4.3 K, 0.22 ms at 40 K, and 1.1 μs at 300 K. Across the field positions sampled, we found comparable T_1 relaxation times of 3.3-9.6 ms at 5 K, 0.38 – 0.64 ms at 40 K, and 0.84 – 2.9 μs at 300 K. The T_1 temperature dependence of VOPc in 0.5 mM D_2SO_4 solution was previously studied and exhibited a T_1 of 45 μs at 99 K.[26] In general, we observe shorter T_1's in the 1:100 VOPc sample compared to the 1:1000 dilution. This is consistent with higher concentrations of the paramagnetic center leading to greater spin-spin mediated relaxation.

We fit the temperature-dependent spin-lattice relaxation rates of 1:1000 VOPc/TiOPc measured at 335.6 mT at X-band as shown in Figure 3.3. This sharp, near-isotropic lineshape at 335.6 mT is a result of the coincidence of the perpendicular and parallel resonances in the $M_I = -1/2$ hyperfine sublevel and is referred to as the "powder-position" in vanadyl-systems.[38] We fit the data to a direct, Raman, and local mode process using Appendix B Eq. B5 (more information regarding fitting is found in Appendix B).[33] The fitted parameters are given in Table 1. For VOPc, we determined a direct process coefficient A_{dir} = 35 K^{-1} s^{-1}) which dominates at low temperature, a Raman contribution with coefficient B_{ram} = 1.1 x 10^4 s^{-1} and Debye temperature θ_D = 119.6 K, and local mode contribution with coefficient C_{loc} = 5.2 x 10^5 s^{-1} and effective mode temperature Δ_{loc} = 295.1 K). We focused our sampling in the high temperature range as we are principally interested in the regime where T_m becomes T_1-limited. Undersampling in the low temperature limit likely leads to a poor estimation of the direct coefficient. That said, the parameters we obtained are in good agreement with similar fits reported for VOTTP doped in diamagnetic ZnTTP (A_{dir} = 11.5 K^{-1} s^{-1}, B_{ram} = 1.1 x 10^4 s^{-1}, θ_D = 100 K, C_{loc} = 4.0 x 10^5 s^{-1}, Δ_{loc} = 350 K).[33]

Table 3.1. Fitting parameters of the 1:1000 CuPc and VOPc samples at X-band for direct (A_{dir}), Raman (B_{ram}), local mode coefficients (C_{loc}) as well as the Deby temperature (θ_D) and power dependence of Raman (n) and local mode activation energy (Δ_{loc})

	CuPc (329 mT)	VOPc (335.6 mT)
A_{dir} ($K^{-1}s^{-1}$)	2	35
B_{ram} (s^{-1})	$2.732 \cdot 10^5$	$1.069 \cdot 10^4$
C_{loc} (s^{-1})	$6.201 \cdot 10^6$	$5.226 \cdot 10^5$
θ_D (K)	112.8	119.6
n	3.7	3.455
Δ_{loc} (K)	272.1	295.1

The temperature dependence of T_m is relatively small until it becomes T_1 limited near 300 K.[39] The 1:1000 sample showed largely temperature-independent T_m's ranging from 2.0 to 2.5 μs across all field positions between 5 and 150 K, decreasing to 1.38 and 1.46 μs at 329 and 335.6 mT, respectively, at 300 K, which is consistent with the previous report from Atzori et al. For all field positions, we find a maximum phase memory time near 40 K. Increasing the temperature from 40 K, there is a weak decline in T_m until becoming T_1-limited. Cooling from 40 K to 5 K, there is also a decline in T_m. Such a phenomenon has been noted in other V(IV) systems. In one example, such a decline was postulated to result from low-temperature tunneling of methyl rotations in alkyl ammonium counterions to the V(IV) complex.[32] VOPc and TiOPc lack methyl

groups or similarly fluxional moieties, so the observation of this low-temperature phenomenon may require further consideration.

Orientation Dependence of T_1 and T_m in CuPc

Analogous to the VOPc/TiOPc dilutions, we chose to study CuPc in a dilute diamagnetic matrix by preparing CuPc/ZnPc-doped samples at 1:1000 and 1:100 concentrations. The CuPc/ZnPc samples were prepared by dissolving the respective metal phthalocyanines in concentrated H_2SO_4, followed by reprecipitation over ice. Previous reports used this method to selectively generate the α-CuPc polymorph.[40] However, the PXRD patterns observed for CuPc/ZnPc samples do not strictly match reported diffraction patterns for either α- or β-CuPc.[41,42]

We collected the T_1 and T_m relaxation times at four field positions and observed similar temperature-dependent behavior at each field. At 5 K, the T_1 and T_m collected on the 1:1000 sample exhibit dependence on the field position – T_1's of 160 ms (306 mT), 83 ms (329 mT), 15 ms (339 mT), and 51 ms (342 mT); T_m's of 4.4 μs (306 mT), 10 μs (329 mT), 0.6 μs (339 mT), and 4.9 μs (342 mT). The spread in relaxation times is apparently larger at low temperature than what was observed for VOPc, with the relaxation times recorded at 339 mT being shortest consistently for the CuPc sample. Upon increasing the temperature above 30 K, the T_1's coalesce across the field positions to roughly similar values. T_m then becomes T_1 limited at 150 K with a value around 400 ns. The decreased T_1 time of the 339 mT feature relative to the other field positions may be due to greater contributions of the organic radical to relaxation pathways as evidenced by the changing intensity of the radical feature with increased temperature in the EDFS and higher relative concentration compared to the 1:100 sample. In the 1:100 CuPc/ZnPc sample, the T_1's are on average shorter than those for the 1:1000 sample by nearly an order of magnitude

from 5 to 50 K. The T_1's collected on the 1:100 sample then follow a similar trend in values compared to the 1:1000 sample at higher temperatures.

As discussed for VOPc, T_m is sensitive to the alignment of the principal axes of the spin with the external field of the spectrometer. CuPc exhibits resonances at noncanonical orientations, leading to anisotropy larger than the microwave quantum of X-band (~0.3 cm^{-1}) and Q-band (~1.1 cm^{-1}). There is also strong nitrogen superhyperfine structure resulting from the coordinating nitrogens in the phthalocyanine ring. Furthermore, the organic radical contributes to signal at 339 mT in the midst of the Cu electron spin transitions, whereas for VOPc the radical feature was more isolated from the vandyl spin transitions. As a result of these factors, strict assignment of orientation and hyperfine eigenvalues at a given field position is challenging.

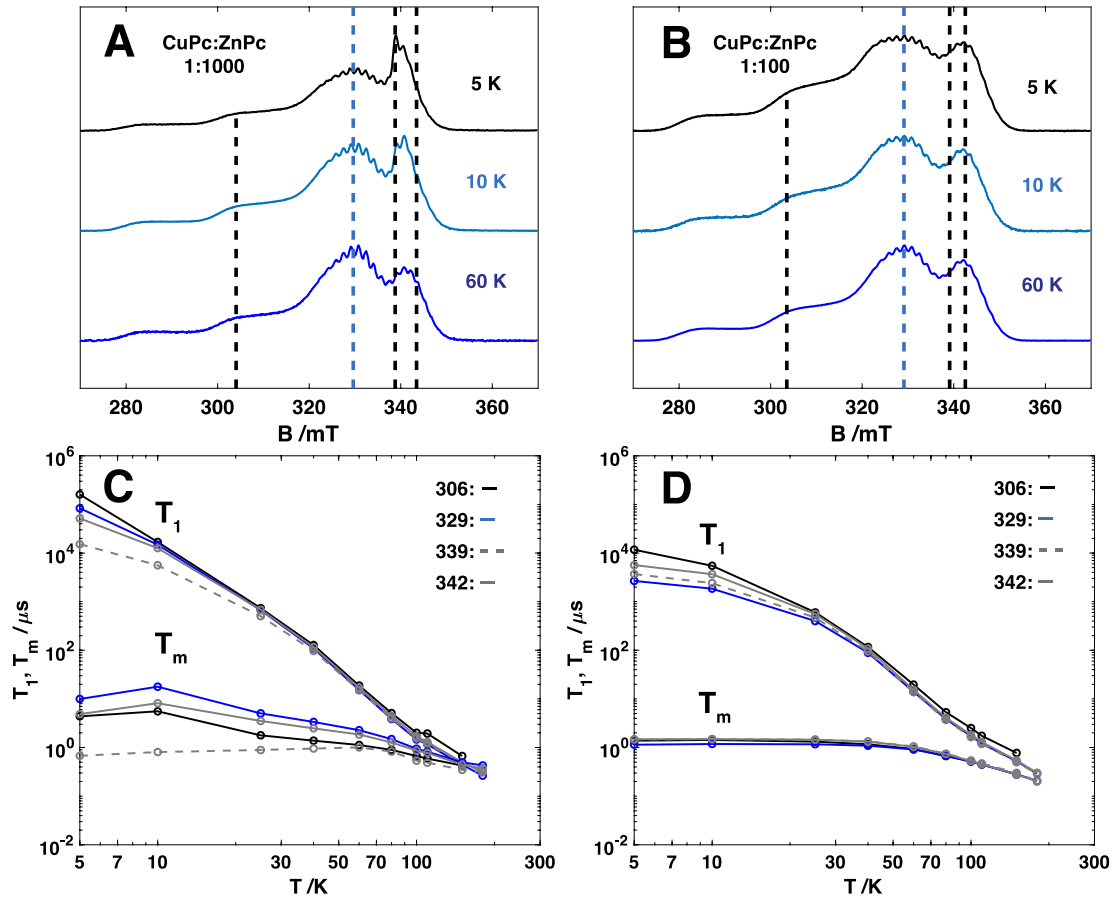

Figure 3.4 Echo-detected EPR X-band field sweeps of CuPc/ZnPc (**A**) 1:1000 and (**B**) 1:100 at 5, 10, and 60 K. Dashed lines indicate field positions where relaxation data were obtained. Comparison between the field-position-dependent behavior of the T_1 and T_M relaxation times for 5 – 180 K for CuPc/ZnPc (**C**) 1:1000 and (**D**) 1:100.

Frequency Dependence of T_1 and T_m in CuPc

We made Q-band EDFS T_1 and T_m measurements on the CuPc samples to compare to those collected at X-band. The position of maximum echo intensity in the EDFS in the 1:100 sample shifts to slightly higher field positions with increasing temperature. The organic radical feature appears in the spectra centered at 1218 mT. The relative intensities of this organic radical feature and the CuPc signal change over the temperature range and is likely due to changes in the total

integrated Cu signal intensity and the shot repetition time (SRT) used for the experiments. The separation of the radical signal from those arising from CuPc is more significant at Q-band than at X-band, but may still reflect the lower T_1's recorded at 1188 and 1190 mT at low temperatures compared to the analogous 339 and 334 mT positions at X-band (Figure 3.4). At approximately 25 K, the T_1 times recorded at X-band and Q-band become roughly the same. At low temperatures, the T_1's measured at X-band are generally longer than those measured at Q-band. This is consistent with the expected frequency dependence of the direct process as discussed for VOPc.

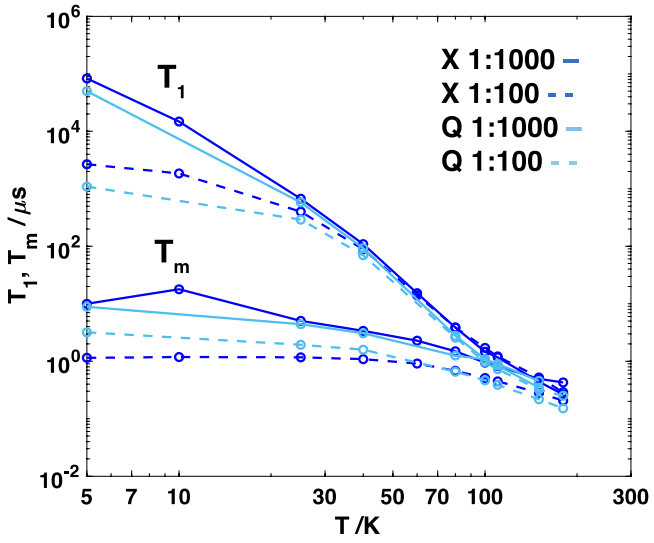

Figure 3.5 Comparison between the T_1 and T_M times vs. temperature for the 329 and 1188 mT features in CuPc at X-band and Q-band, respectively, for the 1:1000 and 1:100 preprarations.

The similar T_1 and T_m trends in temperature were observed regardless of sample concentration or microwave frequency, which suggests that the organic radical is likely not the dominant factor contributing to the different relaxation times between VOPc and CuPc. It is possible that the CuPc/ZnPc samples are influenced by the nonuniform polymorph distribution

observed by PXRD. To that end, we prepared a separate CuPc/ZnPc sample following the procedures used for VOPc/TiOPc samples (DCM/CF_3CO_2H/IPA) as discussed in Appendix B. In this sample, we observe similar T_1 and T_m times and temperature dependent trends, suggesting that the sample preparation and polymorph does not strongly change the observed relaxation.

Temperature Dependence of T_1 in CuPc

We fit the temperature-dependent spin-lattice relaxation rates measured in the 1:1000 CuPc/ZnPc sample at 329 mT to a direct, Raman, and local mode process as we did for VOPc. We found a direct process coefficient $A_{dir} = 2\ K^{-1}\ s^{-1}$, Raman coefficient $B_{ram} = 2.7 \times 10^5\ s^{-1}$ and Debye temperature $\theta_D = 112.8$ K, local mode coefficient $C_{loc} = 6.2 \times 10^6\ s^{-1}$ and average mode equivalent temperature $\Delta_{loc} = 272.1$ K (Table 1). This is consistent with what has been observed for CuTTP doped in ZnTPP ($A_{dir} = 19.5\ K^{-1}\ s^{-1}$, $B_{ram} = 4.8 \times 10^5\ s^{-1}$, $\theta_D = 120$ K, $C_{loc} = 1.5 \times 10^6\ s^{-1}$, $\Delta_{loc} = 250$ K).[33] As with the VOPc data collection, we have few points at low temperatures, and the direct process coefficient should be taken as approximate.

Unlike VOPc, the spectral features of the EDFS in the CuPc samples change distinctly at X-band going from 5 K to 60 K, in particular for the 1:1000 sample. This is evident in the shape and relative intensities of the signals around 329 and 339 mT. As previously mentioned, this effect is presumably influenced by the organic radical at low temperatures, whereas the short SRTs employed during higher temperature experiments will tend to minimize contributions from long-lived radical relaxation. The T_m's observed in the 1:1000 sample are longer than those of the 1:100 sample by half an order of magnitude at low temperatures up to 150 K, but exhibit little to no temperature dependence.

As with VOPc and CuTTP, there is a low-temperature decline in T_m observed in the CuPc samples. For both CuPc samples, the maximum T_m is observed near 10 K with a distinct decline moving toward lower temperatures and a gradual decline with increasing temperature until T_m becomes T_1-limited at 150 K.[33,39] In both CuPc and VOPc, the lack of temperature dependence in T_m is consistent with the restricted mobility within doped matrices.[23,36]

Discussion

We compare the temperature-dependent relaxation behavior of VOPc and CuPc 1:1000 samples measured at 335.6 and 329 mT, respectively. While the T_1 and T_m times of CuPc are longer than those of VOPc at low temperature, CuPc decoherence times become T_1-limited by ~150 K and there is a steep dropoff. Ultimately, coherence lifetimes could not be obtained for the CuPc sample past 180 K. In comparison, the VOPc T_m times only become T_1-limited close to room temperature due to the more gradual decline in T_1 over the temperature range compared to CuPc. This speaks to stronger Raman- and local mode-induced spin-lattice relaxation in CuPc samples than in VOPc. This is reflected in the fits of our T_1 data as well. The coefficients found by the fitting procedure for Raman and local mode processes in CuPc are an order of magnitude larger than those obtained for VOPc (Table 1). We can consider this in the context of the relative spin-orbit coupling of VOPc and CuPc. The many-electron SOC constant ($\lambda=\pm\zeta/2S$) is significantly larger for Cu(II) (λ = -830 cm^{-1}) than for V(IV) (λ = 250 cm^{-1}).[43] The Raman and local mode processes directly reflect the differences in SOC strength; therefore, the increased magnitude of the SOC coefficient in CuPc leads to an increased sensitive to temperature for spin-lattice relaxation.[37]

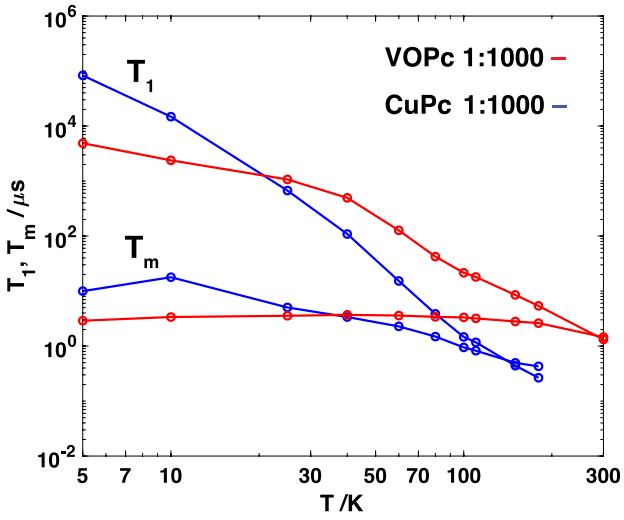

Figure 3.6 Comparison between X-band T_1's and T_M's vs. temperature for the 335.6 and 329 mT features in VOPc (red) and CuPc (blue), respectively.

We rationalize our observations based off literature precedent and ligand field theory.[18,44] Briefly, in C_{4v} or D_{4h} symmetry (appropriate for VOPc and CuPc respectively), a generalized expression for an S = ½ molecular g value from perturbation theory is given as:[45]

$$g_{mol} = g_e - \frac{n\lambda\alpha_1^2\beta_1^2}{\Delta E} \qquad Eq.3.1$$

Where g_e is the free-electron g value, ΔE is the energetic separation between the ground and a particular ligand field excited state, n is an integer constant, and β_1 and α_1 are coefficients reflecting covalencies between the d- and ligand-based orbitals in the ground and excited states, respectively. These parameters all contribute to the effective g value at a given orientation of the field with respect to the molecular frame. The static shift in molecular g values reflects the magnitude of SOC contributions to the ground state wavefunction. Modulation of SOC dominates the mechanisms of spin-lattice relaxation. As a result, the factors that minimize the impact of fluctuations of the SOC are implicit within the expression for g_{mol} such as increasing covalency,

increasing ΔE, or reducing λ. Such factors have previously been discussed by others in the field, such as Eaton et al., and inform our understanding of relaxation in these S = ½ systems. We will detail the three contributions below.

Ground state orbital angular momentum of a free ion is quenched by the introduction of a ligand field, removing degeneracy of the states. This quench is achieved in both C_{4v} and D_{4h} symmetries of VOPc and CuPc, respectively. By perturbational treatment of spin-orbit coupling, higher lying spin-orbital eigenfunctions of the zero-order Hamiltonian will be mixed (slightly) into the ground state wavefunction by an applied magnetic field due to terms in the perturbation Hamiltonian. This reintroduces orbital angular momentum contributions to the ground state observables, such as the g value. Indeed, this is the origin of Eq. 3.1. The greater the separation between excited state and ground state, the less that state will mix and contribute to the g shift (as seen in the inverse dependence of g_{mol} on ΔE. It is therefore important to consider the symmetry of the ground state wavefunction and the manifold of ligand-field excited states when considering transition metal electron spin qubit candidates. To the best of our knowledge, the specific ligand-field transitions contributing to the g values of CuPc and VOPc have not been specifically observed, likely due to the intense intraligand π-π* transitions that dominate the electronic absorption spectrum. The energies of the transitions that contribute to $g_{\|}$ were recently calculated to be similar in energy for CuPc and VOPc (22,165 and 22,745 cm^{-1}, respectively).[18] Thus, we would not expect the energetic separation of the ligand-field states to be the major contributor to the differential spin-lattice relaxation times in the V and Cu complexes regarded here. The energies of these excited states are also significantly higher than the Debye temperatures we calculated for CuPc (112.8 K/78 cm^{-1}) and VOPc (119.6 K/83 cm^{-1}), which affirms our decision not to include Orbach-type relaxation mechanisms into our model.

We next consider ligand-metal covalency. We expect the covalency to be significantly larger in CuPc relative to VOPc as the unpaired electron in CuPc lies in the $d_{x^2-y^2}$ orbital, which is oriented along the Cu-N bonds. In VOPc, the electron is located in d_{xy} and not along the V-N bond.

This is reflected experimentally in the observation of significant superhyperfine coupling between the electron spin and the ^{14}N nuclear spin (I = 1) on the $g_{\perp}$ features in CuPc EPR spectra with A(^{14}N) = [45-50, 40-48] MHz. We were unable to resolve ^{14}N superhyperfine structure in the EPR spectra of VOPc. The simulated line width (full-width at half-maximum) of VOPc is 1.5 mT (42 MHz at g = 2); this places an approximate upper bound on the four equivalently coupled ^{14}N hyperfine constants as A(^{14}N) < 10.5 MHz or less than a quarter than that observed in CuPc. Although increased covalency should benefit prolonged spin-lattice relaxation times, we observe more significant phonon/vibrational mode-mediated relaxation with increased temperature in CuPc relative to VOPc. It may be the case then that despite the more covalent Cu-ligand interaction, the magnitude of the SOC constant in Cu remains a large contributor to spin-lattice relaxation.

Finally, we will touch on hyperfine-mediated spin-lattice and phase memory relaxation. CuTTP was demonstrated to have similar Cu (~630 MHz) hyperfine and (~43 MHz) superhyperfine coupling constants to those we observe for CuPc (~650 and ~45 MHz for Cu and N, respectively). Single crystal and powder studies of CuTTP doped into ZnTTP have previously shown that the observed T_1 times are independent of orientation and insensitive to the contributions from ligand superhyperfine, which further supports the importance of the SOC coupling constant to the temperature dependence of the relaxation times.[23,35]

Conclusions

In summary, CuPc exhibits order of magnitude longer T_1 times than VOPc at low temperatures (5 K). However, the T_1 times decline more rapidly with increasing temperature in CuPc than in VOPc, which we attribute to more significant contributions of Raman and local vibrational mode relaxation pathways. In line with this, the T_m times become T_1-limited in CuPc around 150 K and coherence cannot even be detected past 180 K, whereas the T_1-limiting regime occurs near 300 K for VOPc. As mentioned, the goal for molecular qubit candidates is to produce qubits that exhibit long coherence times (>100 μs) at high temperatures. The T_m time is largely temperature-independent until becoming limited by T_1. So, consideration must go to both increasing the T_m time of a given qubit candidate (which can be accomplished by removing nuclear spins as a source of spin flip-flop or hyperfine-mediated relaxation) as well as to extending the T_1 time at higher temperatures to allow for coherence to be observed (which can be considered by taking into account symmetry and spin-orbit interaction).

Citations

(1) DiVincenzo, D. P. The Physical Implementation of Quantum Computation. *Fortschritte der Physik* **2000**, *48* (9–11), 771–783. https://doi.org/10.1002/1521-3978(200009)48:9/11<771::AID-PROP771>3.0.CO;2-E.

(2) Clarke, J.; Wilhelm, F. K. Superconducting Quantum Bits. *Nature* **2008**, *453* (7198), 1031–1042. https://doi.org/10.1038/nature07128.

(3) Atzori, M.; Sessoli, R. The Second Quantum Revolution: Role and Challenges of Molecular Chemistry. *J. Am. Chem. Soc.* **2019**, *141* (29), 11339–11352. https://doi.org/10.1021/jacs.9b00984.

(4) Wasielewski, M. R.; Forbes, M. D. E.; Frank, N. L.; Kowalski, K.; Scholes, G. D.; Yuen-Zhou, J.; Baldo, M. A.; Freedman, D. E.; Goldsmith, R. H.; Goodson, T.; Kirk, M. L.; McCusker, J. K.; Ogilvie, J. P.; Shultz, D. A.; Stoll, S.; Whaley, K. B. Exploiting Chemistry and Molecular Systems for Quantum Information Science. *Nat Rev Chem* **2020**, *4* (9), 490–504. https://doi.org/10.1038/s41570-020-0200-5.

(5) Dolde, F.; Jakobi, I.; Naydenov, B.; Zhao, N.; Pezzagna, S.; Trautmann, C.; Meijer, J.; Neumann, P.; Jelezko, F.; Wrachtrup, J. Room-Temperature Entanglement between Single Defect Spins in Diamond. *Nature Phys* **2013**, *9* (3), 139–143. https://doi.org/10.1038/nphys2545.

(6) Hanson, R.; Gywat, O.; Awschalom, D. D. Room-Temperature Manipulation and Decoherence of a Single Spin in Diamond. *Phys. Rev. B* **2006**, *74* (16), 161203. https://doi.org/10.1103/PhysRevB.74.161203.
(7) Wang, J.-F.; Yan, F.-F.; Li, Q.; Liu, Z.-H.; Liu, H.; Guo, G.-P.; Guo, L.-P.; Zhou, X.; Cui, J.-M.; Wang, J.; Zhou, Z.-Q.; Xu, X.-Y.; Xu, J.-S.; Li, C.-F.; Guo, G.-C. Coherent Control of Nitrogen-Vacancy Center Spins in Silicon Carbide at Room Temperature. *Phys. Rev. Lett.* **2020**, *124* (22), 223601. https://doi.org/10.1103/PhysRevLett.124.223601.
(8) Widmann, M.; Lee, S.-Y.; Rendler, T.; Son, N. T.; Fedder, H.; Paik, S.; Yang, L.-P.; Zhao, N.; Yang, S.; Booker, I.; Denisenko, A.; Jamali, M.; Momenzadeh, S. A.; Gerhardt, I.; Ohshima, T.; Gali, A.; Janzén, E.; Wrachtrup, J. Coherent Control of Single Spins in Silicon Carbide at Room Temperature. *Nature Mater* **2015**, *14* (2), 164–168. https://doi.org/10.1038/nmat4145.
(9) Herbschleb, E. D.; Kato, H.; Maruyama, Y.; Danjo, T.; Makino, T.; Yamasaki, S.; Ohki, I.; Hayashi, K.; Morishita, H.; Fujiwara, M.; Mizuochi, N. Ultra-Long Coherence Times amongst Room-Temperature Solid-State Spins. *Nat Commun* **2019**, *10* (1), 3766. https://doi.org/10.1038/s41467-019-11776-8.
(10) Sproules, S. Molecules as Electron Spin Qubits. In *Electron Paramagnetic Resonance*; 2016; pp 61–97. https://doi.org/10.1039/9781782629436-00061.
(11) Graham, M. J.; Zadrozny, J. M.; Shiddiq, M.; Anderson, J. S.; Fataftah, M. S.; Hill, S.; Freedman, D. E. Influence of Electronic Spin and Spin–Orbit Coupling on Decoherence in Mononuclear Transition Metal Complexes. *J. Am. Chem. Soc.* **2014**, *136* (21), 7623–7626. https://doi.org/10.1021/ja5037397.
(12) Graham, M. J.; Krzyaniak, M. D.; Wasielewski, M. R.; Freedman, D. E. Probing Nuclear Spin Effects on Electronic Spin Coherence via EPR Measurements of Vanadium(IV) Complexes. *Inorg. Chem.* **2017**, *56* (14), 8106–8113. https://doi.org/10.1021/acs.inorgchem.7b00794.
(13) Tesi, L.; Lucaccini, E.; Cimatti, I.; Perfetti, M.; Mannini, M.; Atzori, M.; Morra, E.; Chiesa, M.; Caneschi, A.; Sorace, L.; Sessoli, R. Quantum Coherence in a Processable Vanadyl Complex: New Tools for the Search of Molecular Spin Qubits. *Chem. Sci.* **2016**, *7* (3), 2074–2083. https://doi.org/10.1039/C5SC04295J.
(14) Albino, A.; Benci, S.; Tesi, L.; Atzori, M.; Torre, R.; Sanvito, S.; Sessoli, R.; Lunghi, A. First-Principles Investigation of Spin–Phonon Coupling in Vanadium-Based Molecular Spin Quantum Bits. *Inorg. Chem.* **2019**, *58* (15), 10260–10268. https://doi.org/10.1021/acs.inorgchem.9b01407.
(15) Lunghi, A.; Sanvito, S. How Do Phonons Relax Molecular Spins? *Science Advances 5* (9), eaax7163. https://doi.org/10.1126/sciadv.aax7163.
(16) Escalera-Moreno, L.; Suaud, N.; Gaita-Ariño, A.; Coronado, E. Determining Key Local Vibrations in the Relaxation of Molecular Spin Qubits and Single-Molecule Magnets. *J. Phys. Chem. Lett.* **2017**, *8* (7), 1695–1700. https://doi.org/10.1021/acs.jpclett.7b00479.
(17) Atzori, M.; Tesi, L.; Benci, S.; Lunghi, A.; Righini, R.; Taschin, A.; Torre, R.; Sorace, L.; Sessoli, R. Spin Dynamics and Low Energy Vibrations: Insights from Vanadyl-Based Potential Molecular Qubits. *J. Am. Chem. Soc.* **2017**, *139* (12), 4338–4341. https://doi.org/10.1021/jacs.7b01266.
(18) Mirzoyan, R.; Hadt, R. G. The Dynamic Ligand Field of a Molecular Qubit: Decoherence through Spin–Phonon Coupling. *Phys. Chem. Chem. Phys.* **2020**, *22* (20), 11249–11265. https://doi.org/10.1039/D0CP00852D.

(19) Ariciu, A.-M.; Woen, D. H.; Huh, D. N.; Nodaraki, L. E.; Kostopoulos, A. K.; Goodwin, C. A. P.; Chilton, N. F.; McInnes, E. J. L.; Winpenny, R. E. P.; Evans, W. J.; Tuna, F. Engineering Electronic Structure to Prolong Relaxation Times in Molecular Qubits by Minimising Orbital Angular Momentum. *Nat Commun* **2019**, *10* (1), 3330. https://doi.org/10.1038/s41467-019-11309-3.

(20) Atzori, M.; Morra, E.; Tesi, L.; Albino, A.; Chiesa, M.; Sorace, L.; Sessoli, R. Quantum Coherence Times Enhancement in Vanadium(IV)-Based Potential Molecular Qubits: The Key Role of the Vanadyl Moiety. *J. Am. Chem. Soc.* **2016**, *138* (35), 11234–11244. https://doi.org/10.1021/jacs.6b05574.

(21) Fataftah, M. S.; Krzyaniak, M. D.; Vlaisavljevich, B.; Wasielewski, M. R.; Zadrozny, J. M.; Freedman, D. E. Metal–Ligand Covalency Enables Room Temperature Molecular Qubit Candidates. *Chem. Sci.* **2019**, *10* (27), 6707–6714. https://doi.org/10.1039/C9SC00074G.

(22) Weil, J. A.; Bolton, J. R. Basic Principles of Paramagnetic Resonance. In *Electron Paramagnetic Resonance*; John Wiley & Sons, Ltd, 2006; pp 1–35. https://doi.org/10.1002/9780470084984.ch1.

(23) Du, J.-L.; Eaton, G. R.; Eaton, S. S. Electron Spin Relaxation in Vanadyl, Copper(II), and Silver(II) Porphyrins in Glassy Solvents and Doped Solids. *Journal of Magnetic Resonance, Series A* **1996**, *119* (2), 240–246. https://doi.org/10.1006/jmra.1996.0079.

(24) Bonizzoni, C.; Ghirri, A.; Atzori, M.; Sorace, L.; Sessoli, R.; Affronte, M. Coherent Coupling between Vanadyl Phthalocyanine Spin Ensemble and Microwave Photons: Towards Integration of Molecular Spin Qubits into Quantum Circuits. *Sci Rep* **2017**, *7* (1), 13096. https://doi.org/10.1038/s41598-017-13271-w.

(25) Stepanow, S.; Mugarza, A.; Ceballos, G.; Moras, P.; Cezar, J. C.; Carbone, C.; Gambardella, P. Giant Spin and Orbital Moment Anisotropies of a Cu-Phthalocyanine Monolayer. *Phys. Rev. B* **2010**, *82* (1), 014405. https://doi.org/10.1103/PhysRevB.82.014405.

(26) Bader, K.; Winkler, M.; Slageren, J. van. Tuning of Molecular Qubits: Very Long Coherence and Spin–Lattice Relaxation Times. *Chem. Commun.* **2016**, *52* (18), 3623–3626. https://doi.org/10.1039/C6CC00300A.

(27) Warner, M.; Din, S.; Tupitsyn, I. S.; Morley, G. W.; Stoneham, A. M.; Gardener, J. A.; Wu, Z.; Fisher, A. J.; Heutz, S.; Kay, C. W. M.; Aeppli, G. Potential for Spin-Based Information Processing in a Thin-Film Molecular Semiconductor. *Nature* **2013**, *503* (7477), 504–508. https://doi.org/10.1038/nature12597.

(28) Van Vleck, J. H. Paramagnetic Relaxation and the Equilibrium of Lattice Oscillators. *Phys. Rev.* **1941**, *59* (9), 724–729. https://doi.org/10.1103/PhysRev.59.724.

(29) Van Vleck, J. H. Paramagnetic Relaxation Times for Titanium and Chrome Alum. *Phys. Rev.* **1940**, *57* (5), 426–447. https://doi.org/10.1103/PhysRev.57.426.

(30) Stevens, K. W. H. The Theory of Paramagnetic Relaxation. *Rep. Prog. Phys.* **1967**, *30* (1), 189–226. https://doi.org/10.1088/0034-4885/30/1/305.

(31) Orbach, R. On the Theory of Spin-Lattice Relaxation in Paramagnetic Salts. *Proc. Phys. Soc.* **1961**, *77* (4), 821–826. https://doi.org/10.1088/0370-1328/77/4/301.

(32) Lin, C.-Y.; Ngendahimana, T.; Eaton, G. R.; Eaton, S. S.; Zadrozny, J. M. Counterion Influence on Dynamic Spin Properties in a V(IV) Complex. *Chem. Sci.* **2019**, *10* (2), 548–555. https://doi.org/10.1039/C8SC04122A.

(33) Zhou, Y.; Bowler, B. E.; Eaton, G. R.; Eaton, S. S. Electron Spin Lattice Relaxation Rates for S = 12 Molecular Species in Glassy Matrices or Magnetically Dilute Solids at Temperatures between 10 and 300 K. *Journal of Magnetic Resonance* **1999**, *139* (1), 165–174. https://doi.org/10.1006/jmre.1999.1763.
(34) Zhou, Y.; Bowler, B. E.; Eaton, G. R.; Eaton, S. S. Electron Spin Lattice Relaxation Rates for S = 12 Molecular Species in Glassy Matrices or Magnetically Dilute Solids at Temperatures between 10 and 300 K. *Journal of Magnetic Resonance* **1999**, *139* (1), 165–174. https://doi.org/10.1006/jmre.1999.1763.
(35) Du, J.-L.; More, K. M.; Eaton, S. S.; Eaton, G. R. Orientation Dependence of Electron Spin Phase Memory Relaxation Times in Copper(II) and Vanadyl Complexes in Frozen Solution. *Israel Journal of Chemistry* **1992**, *32* (2–3), 351–355. https://doi.org/10.1002/ijch.199200041.
(36) Eaton, S. S.; Harbridge, J.; Rinard, G. A.; Eaton, G. R.; Weber, R. T. Frequency Dependence of Electron Spin Relaxation for ThreeS = 1/2 Species Doped into Diamagnetic Solid Hosts. *Appl. Magn. Reson.* **2001**, *20* (1), 151–157. https://doi.org/10.1007/BF03162316.
(37) Eaton, S. S.; Eaton, G. R. Relaxation Times of Organic Radicals and Transition Metal Ions. In *Distance Measurements in Biological Systems by EPR*; Berliner, L. J., Eaton, G. R., Eaton, S. S., Eds.; Springer US: Boston, MA, 2000; pp 29–154. https://doi.org/10.1007/0-306-47109-4_2.
(38) Nagarajan, V.; Müller, B.; Storcheva, O.; Köhler, K.; Pöppl, A. Structure and Bonding of [VIVO(Acac)2] on the Surface of AlF3 as Studied by Pulsed Electron Nuclear Double Resonance and Hyperfine Sublevel Correlation Spectroscopy. *Phys. Chem. Chem. Phys.* **2009**, *11* (31), 6849–6854. https://doi.org/10.1039/B903826B.
(39) Atzori, M.; Tesi, L.; Morra, E.; Chiesa, M.; Sorace, L.; Sessoli, R. Room-Temperature Quantum Coherence and Rabi Oscillations in Vanadyl Phthalocyanine: Toward Multifunctional Molecular Spin Qubits. *J. Am. Chem. Soc.* **2016**, *138* (7), 2154–2157. https://doi.org/10.1021/jacs.5b13408.
(40) Abkowitz, M.; Chen, I.; Sharp, J. H. Electron Spin Resonance of the Organic Semiconductor, A-Copper Phthalocyanine. *J. Chem. Phys.* **1968**, *48* (10), 4561–4567. https://doi.org/10.1063/1.1668028.
(41) Hoshino, A.; Takenaka, Y.; Miyaji, H. Redetermination of the Crystal Structure of α-Copper Phthalocyanine Grown on KCl. *Acta Cryst B* **2003**, *59* (3), 393–403. https://doi.org/10.1107/S010876810300942X.
(42) Schmidt, M. U. Polycyclic Pigments. In *Industrial Organic Pigments*; John Wiley & Sons, Ltd, 2004; pp 421–566. https://doi.org/10.1002/3527602429.ch3.
(43) Figgis, B. N. *Introduction to Ligand Fields*; Interscience Publishers: New York, 1966.
(44) Shrivastava, K. N. Lattice-Dynamical Contributions to g-Values. *J. Phys. C: Solid State Phys.* **1982**, *15* (18), 3869–3876. https://doi.org/10.1088/0022-3719/15/18/005.
(45) Solomon, E. I. Introduction. *Comments on Inorganic Chemistry* **1984**, *3* (5), 227–229. https://doi.org/10.1080/02603598408080072.

Chapter IV

Entatic Effects on the Photophysical Processes in Copper Photosensitizers

Introduction

The ability to control the functional properties of transition metal coordination complexes is critical to our understanding and implementation of transition metal catalysts, photosensitizers, and metalloenzymes. Although many of the electronic properties of transition metal centers are determined first by the identity of the metal, oxidation state, and ligand-field symmetry of the inner coordination sphere, secondary coordination sphere effects including sterics may significantly impact the ground and excited state potential energy surfaces. Such an effect is observed in biology where the fold of a protein, long range hydrogen bonding, and electrostatics can serve to distort the ligand field at the metal site. The metal center may thus persist in an otherwise energetically activated geometry, known as the entatic or rack-induced state.[1–15]

In analogy to the entatic state observed in some metalloproteins, secondary coordination sphere steric effects have been detailed in small molecule coordination complexes, notably in Cu(I) bis-phenanthrolines (bis-phen).[16–25] Cu(I) bis-phen complexes have garnered interest for their potential uses as first-row transition metal photosensitizers and thermally activated delayed fluorescence emitters. Cu(I) bis-phen complexes exhibit a pseudo-tetrahedral ground state geometry. The visible absorption spectrum of Cu(I) bis-phen complexes is typically dominated by metal-to-ligand charge transfer (MLCT) transitions.[17,18,20,23] Absorption into the ^{1}MLCT state generates a transient, formally Cu(II) center. Cu(II) is destabilized in a tetrahedral coordination environment and will tend to undergo Jahn-Teller tetragonal distortions towards a planar geometry, as illustrated in Figure 4.1. Intersystem crossing (ISC) then permits formation of a long-lived ^{3}MLCT state. Steric restraints can be introduced at the 2- and 9-positions on the phenanthroline moiety that attenuate the degree of flattening that occurs in the excited state. As a result, the

reorganization/excited state relaxation energies may be modulated, and the resulting excited state lifetimes of the ^{3}MLCT state can be tuned over orders of magnitude.

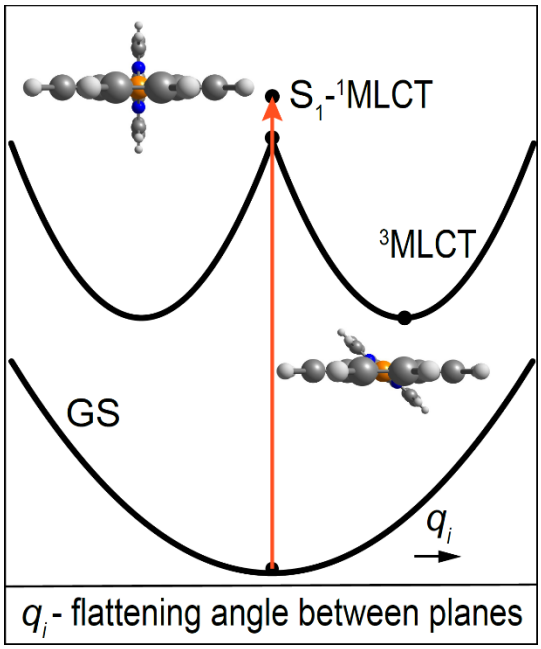

Figure 4.1 ^{3}MLCT excited state structural distortion in Cu(I) bis-phenanthroline complexes and their generalized excited state potential energy surfaces. The steric effects under consideration here inhibit the flattening of the dihedral angle upon formation of the ^{3}MLCT excited state.

In this study we attempt to quantify the steric contributions to the ground and excited state potential energies surfaces involved in a range of Cu(I) bis-phen complexes by combined computational and experimental methods. In doing so, we demonstrate that the trends in the excited state lifetimes with respect to ligand sterics are rationalized in terms of the energy gap law.[26,27] We will initially focus on the experimental contributions made to the project as a part of this thesis, which include synthesis, cyclic voltammetry, steady-state absorption and emission spectroscopy, as well as transient absorption (TA) spectroscopy to validate the computationally observed trends in reduction potential and ^{3}MLCT lifetimes in the context of previous work on

such complexes. We will then summarize the computational work that comprised the core of the study.

Experimental Results

To the goal of providing benchmark characterization of Cu(I) bis-phen complexes for the computational studies in this work, we focused our attention on several 2,9-dialkyl-substituted Cu(I) bis-phen complexes with increasing steric bulk in the 2,9-positions. $[Cu(phen)_2][PF_6]$[28], $[Cu(dmp)_2][PF_6]$[29], and $[Cu(dsbp)_2][PF_6]$[28] were synthesized according to literature procedures (dmp = 2,9-dimethyl-1,10-phenanthroline, dsbp = 2,9-di-*sec*-butyl-1,10-phenanthroline). We report here the synthesis and characterization of the related Cu(I) complex of 2-methyl-1,10-phenanthroline ($[Cu(mmp)_2][PF_6]$).[30] The key parameters we targeted for benchmarking are the ground state reduction potential for the Cu(I/II) couple ($E°$), the excited state relaxation energies (γ), and the ^{3}MLCT excited state lifetimes (τ). Cyclic voltammetry was performed to assess the Cu(I/II) reduction potential of the complexes. Gaussian fitting of low temperature emission data provides access to excited state relaxation energies via the fitted full-width half-maxima (FWHM) of the Gaussian bands.[31] Finally, transient absorption allows us to track the excited state dynamics of the complexes and measure the excited state lifetimes.

Synthesis of $[Cu(mmp)_2][PF_6]$

$[Cu(mmp)_2][PF_6]$ was synthesized according to a modified literature procedure.[30] A solution of 2-methyl-1,10-phenanthroline (194.2 mg, 1.0 mmol) in MeCN (3 mL) was added to $[Cu(MeCN)_4][PF_6]$ (186.4 mg, 0.5 mmol) under $N_{2(g)}$ atmosphere. The deep red solution was then stirred for fifteen minutes and Et_2O (~20 mL) was added to precipitate the product, which was then recrystallized via slow vapor diffusion of Et_2O into a concentrated DCM solution of the product.

The resulting crystals were collected and washed with Et_2O, yielding the product (near quantitative yield). ^{1}H NMR (400 MHz, $CDCl_3$): δ 2.48 (s, 6H), 7.81 (d, 2H), 7.88 (dd, 2H), 8.06 (m, 4H), 8.50 (d, 2H), 8.57 (d, 2H), 8.86 (d, 2H), ppm. ^{13}C NMR (400 MHz, $CDCl_3$) δ 25.99, 125.29, 125.94, 126.16, 127.06, 127.46, 129.59, 137.03, 137.24, 143.31, 143.71, 148.81, 158.02 ppm.

Cyclic Voltammetry

The Cu(I/II) reduction potential for $[Cu(phen)_2][PF_6]$, $[Cu(dmp)_2][PF_6]$, and $[Cu(mmp)_2][PF_6]$ were estimated using cyclic voltammetry (CV). CV was carried out with a Pine Instrument Company AFCBP1 biopotentiostat with the AfterMath software package. Measurements were performed in a three electrode cell, consisting of a glassy carbon working electrode (⌀ = 3.0 mm), a silver wire counter electrode, and a platinum wire reference electrode under a $N_{2(g)}$ atmosphere at room temperature in an M. Braun glovebox. Cyclic voltammograms were taken of 2 mM solutions of Cu bis-phen complex and 0.1 M $[Bu_4][PF_6]$ electrolyte in dry dichloromethane. The ferrocene/ferrocenium (Fc/Fc^+) redox couple or alternatively the decamethylferrocene/decamethylferrocinium (Fc^*/Fc^{*+}) redox couple were used as internal reference standards for all measurements. Those redox potentials referenced to Fc^*/Fc^{*+} could then be converted to potentials vs. Fc/Fc^+ by using the measured difference in redox potentials of the Fc^*/Fc^{*+} and Fc/Fc^+ under our conditions.[32,33]

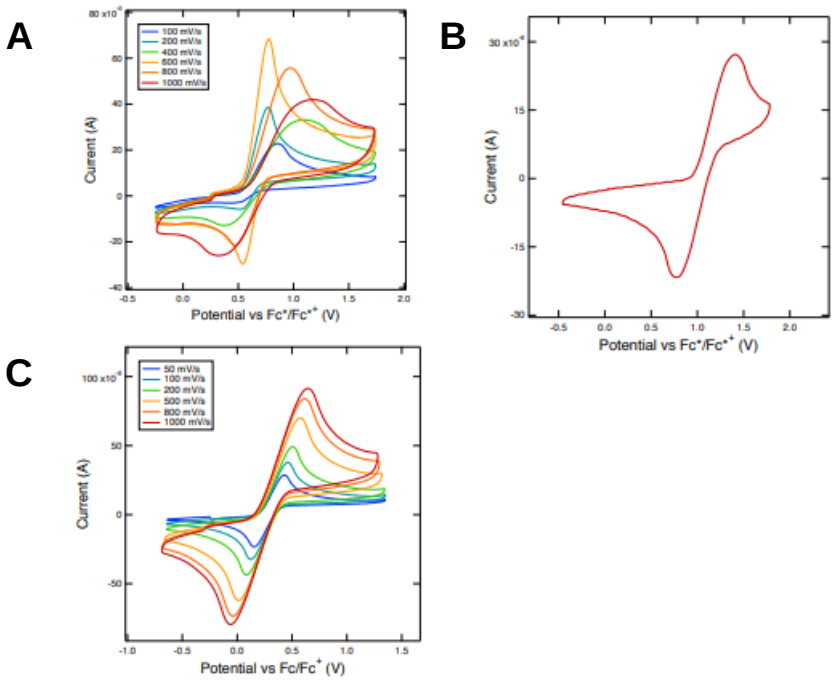

Figure 4.2 Electrochemical data (CVs) for a variety of Cu(I) bis-phen complexes. **(A)** scan rate dependence of $[Cu(phen)_2][PF_6]$ referenced vs Fc^*/Fc^{*+}; **(B)** CV data for $[Cu(dmp)_2][PF_6]$ referenced vs Fc^*/Fc^{*+}; **(C)** scan rate dependence for $[Cu(mmp)_2][PF_6]$ referenced vs Fc/Fc^+.

The CV data collected on $[Cu(phen)_2][PF_6]$ (scan rate dependence), $[Cu(dmp)_2][PF_6]$ (CV), and $[Cu(mmp)_2][PF_6]$ (scan rate dependence) are presented in Figure 4.2. Although $[Cu(dmp)_2][PF_6]$ and $[Cu(mmp)_2][PF_6]$ exhibit cleanly reversible Cu(I/II) redox events, $[Cu(phen)_2][PF_6]$ requires high scan rates to display relatively reversible CV features. Addition of ferrocene allows us to reference the reduction potential of each complex versus the ferrocene/ferrocenium couple. We convert these values versus NHE to compare across complexes reported in the literature as shown in Table 4.1.

77 K Luminescence Experiments

77 K emission spectra were collected in the Beckman Institute Laser Resource Center using a modified Jobin Yvon Spec Fluorolog-3 instrument employing two Ocean Optics EQDPro CCD spectrometers spanning 300 – 930 nm for detection. Samples run were 1 mM solutions of $[Cu(dsbp)_2][PF_6]$, $[Cu(dmp)_2][PF_6]$, and $[Cu(mmp)_2][PF_6]$ in 1:1 toluene/dichloromethane after being degassed by sparging with $N_{2(g)}$ for 10 minutes. Samples were added to an EPR tube and glassed at 77 K in liquid N_2. The sample compartment of the fluorimeter was purged with $N_{2(g)}$ for 10 min prior to introduction of the sample. The glassed samples were then transferred to a vacuum-sealed double-walled glass Dewar containing liquid N_2. Samples were excited with a xenon arc lamp, employing a monochromator for wavelength selection, and emission was collected at 90 °. Once collected, emission spectra were fit to a minimum of three Gaussian peaks of equal full-width half-maximum using nonlinear least squares estimation of the coefficients with the nonlinear regression fitting package in MATLAB. The excited state relaxation energy was then calculated from the fitted full-width half-maximum values.

The collected 77 K emission spectra for $[Cu(dsbp)_2][PF_6]$, $[Cu(dmp)_2][PF_6]$, and $[Cu(mmp)_2][PF_6]$ are shown in Figure 4.3 along with the Gaussian fitting obtained from the data. Emission at 77 K could not be observed for $[Cu(phen)_2][PF_6]$.[31]

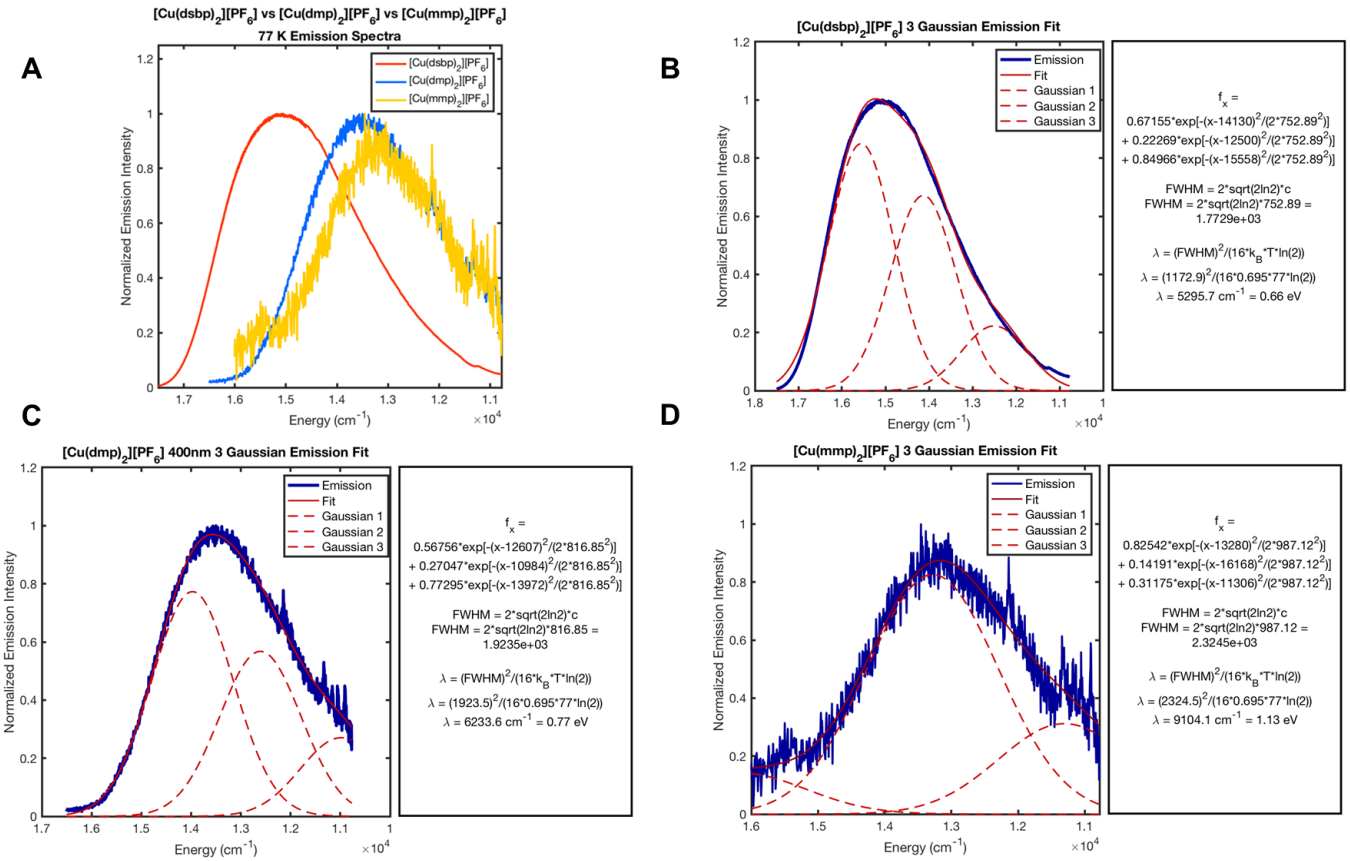

Figure 4.3 77 K emission spectra collected for $[Cu(dsbp)_2][PF_6]$, $[Cu(dmp)_2][PF_6]$, and $[Cu(mmp)_2][PF_6]$ with 400 nm excitation with **(A)** normalized emission spectra of the three complexes overlayed with each other and the emission profile of **(B)** $[Cu(dsbp)_2][PF_6]$, **(C)** $[Cu(dmp)_2][PF_6]$, and **(D)** $[Cu(mmp)_2][PF_6]$ fitted to a sum of three Gaussian curves (total fit shown in solid red, individual curves in dashed red).

In Figure 4.3A the overlay of the normalized emission traces shows a blue shift in the emission maximum λ_{max} with increasing steric bulk in the 2,9-positions of the phenanthroline (dsbp > dmp > mmp). The signal-to-noise ratio also improves with increasing bulk due to overall higher emission intensity. This is consistent with previous literature. As the increasing bulk prevents relaxation of the ^{3}MLCT into a tetragonal geometry, this potential energy surface is displaced

higher in energy relative to the ground state, resulting in higher energy emission. The excited state relaxation parameters acquired via Gaussian fitting also support this: dsbp (0.66 eV) < dmp (0.77 eV) < mmp (1.13 eV). As the steric bulk hinders relaxation into the tetragonal geometry, the excited state relaxation energy will be less for bulkier substituents.

Steady-State and Transient Absorption Spectroscopy

In order to characterize the optical properties $[Cu(mmp)_2][PF_6]$, we collected steady-state absorption spectra as well as transient absorption spectra. We present the steady-state absorption data in Figure 4.4, performing Beer-Lambert analysis to ascertain the extinction coefficient at the λ_{max} of the MLCT absorption band at 455 nm.

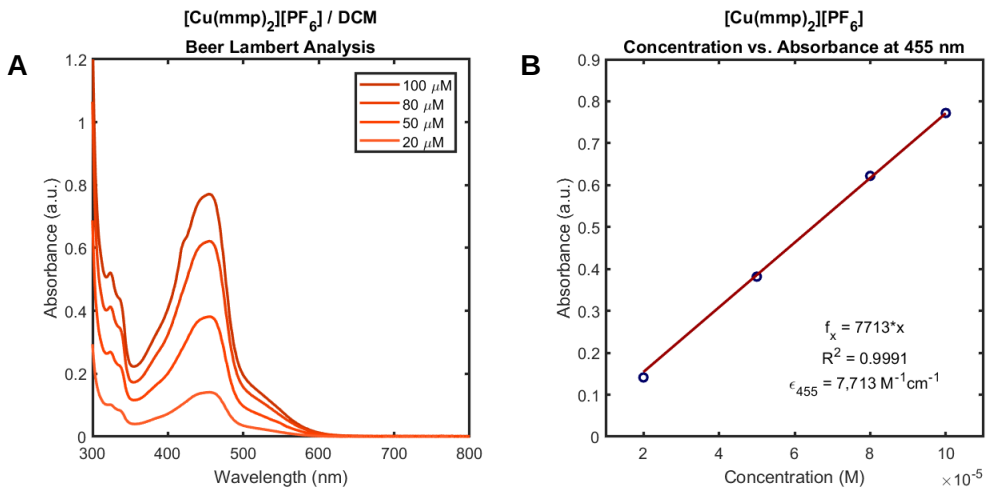

Figure 4.4 (A) Concentration dependent visible absorption spectra for $[Cu(mmp)_2][PF_6]$ in DCM **(B)** Concentration dependent absorbance at 455 nm and linear fit to extract the extinction coefficient.

Ultrafast transient absorption spectroscopy was acquired on the $[Cu(mmp)_2][PF_6]$ sample with excitation at 410 nm. The spectra are shown in Figure 4.5 along with single wavelength kinetic fitting to ascertain the ^{3}MLCT excited state lifetime.

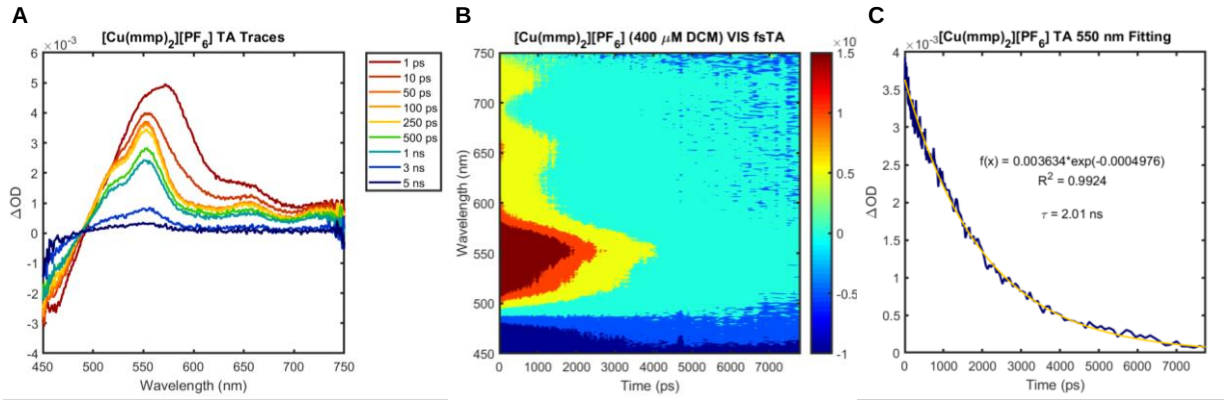

Figure 4.5 (A) Time cuts of the fsTA spectrum of $[Cu(mmp)_2][PF_6]$ in DCM showing the spectral evolution over time; **(B)** a 2D plot of the data matrix over the time course of the instrument; **(C)** Single wavelength exponential fitting at 550 nm after the initial ~50 ps to extract the ^{3}MLCT lifetime τ.

The time cuts of the fsTA spectrum show an excited state absorption (ESA) feature in the visible region spanning 500 – 750 nm. Over the first tens of picoseconds, the broad ESA blue shifts and sharpens into a long-lived ESA feature. This is consistent with previous TA experiments on Cu(I) bis-phen complexes, and the long-lived feature is consistent with the ^{3}MLCT state. We fit the long-lived component near its maximum at 550 nm at times after the broad ESA feature blue shifts to the long-lived ESA (~50 ps). This gives us a ^{3}MLCT excited state lifetime $\tau = 2.01$ ns.

Computational Results

2,9-Alkyl Substituted Copper(I) Bis-phenanthrolines

The reduction potentials ($E°$s) and ^{3}MLCT excited state lifetimes (τ) for a variety of Cu(I) bis-phen complexes have been reported in the literature.[17,18,23,31,34–38] Among these are six homoleptic Cu(I) bis-phen complexes differing only in the alkyl group at the 2,9-position of the phenanthroline ligand (*viz*., 1,10-phenanthroline (phen), 2,9-dimethyl-1,10-phenanthroline (dmp), 2,9-dibutyl-1,10-phenanthroline (dbp), 2,9-dineopentyl-1,10-phenanthroline (dnpp), 2,9-di-*sec*-butyl-1,10-phenanthroline (dsbp), and 2,9-di-*tert*-butyl-1,10-phenanthroline (dtbp)). Solely changing the alkyl group at the 2,9-positions tunes the Cu(I/II) $E°$ over ~600 mV and ^{3}MLCT lifetimes by greater than four orders of magnitude (e.g., from 140 ps (bis-phen) to 3.26 μs (bis-dtbp) in DCM).[18] These systematic structure/function variations thus provide an opportunity to quantify steric contributions in photophysical processes. Indeed, our examination of these complexes demonstrates that tuning the steric bulk of the alkyl chains at the 2,9-positions has a quantifiable effect on τ. In the following sections, we first correlate experimental and computational $E°$s to evaluate potential entatic state contributions. Analyses are then extended to ground state inner sphere reorganization energies (λ_is) for Cu(I/II) redox and, finally, to Cu(I/II) ^{3}MLCT excited state inner sphere relaxation energies (γ_is) and energy gaps. As shown below, entatic energies depend on the model used to quantify them. For Cu-photosentizers, we have determined that excited state relaxation energies provide a means to quantify purely steric contributions to ^{3}MLCT dynamics (*vide infra*).

As pointed out recently for Cu(I) bis-phen complexes,[39] variations in $E°$s and τs reflect the same structural distortion (Figure 4.1); therefore, one can draw a correlation between these experimental observables to quantify entatic contributions to photophysical dynamics. Experimental and calculated $E°$s for Cu(I) bis-phen and the 2,9-alkyl substituted complexes are given in Table 4.1 and Figure 4.6. The best agreement between theory and experimental $E°$s in

DCM is observed for the BP86 functional. Thus, if not specified, calculated values correspond to values obtained using the BP86 exchange correlation functional. Within this functional, the best agreement is observed for the bulkier substituents (e.g., bis-dbp, -dsbp, and -dtbp). For bis-phen and -dmp, however, the calculated *E*°s (1.071 and 1.259 V, respectively) are higher than those observed experimentally (0.84 and 0.99 V, respectively). Furthermore, there is a fairly large *E*° difference between bis-phen and bis-dmp complexes relative to the other complexes with *E*°s reported in the literature (Table 4.1). For a more reliable overall comparison across the series, it is useful to fill this gap. Doing so is also important for analyzing ^{3}MLCT lifetimes and relaxation energies (*vide infra*). We therefore synthesized the homoleptic Cu(I) complex with a 2-methyl-1,10-phenanthroline (mmp) ligand (bis-mmp)[30] and measured its *E*° (0.99 V) and photophysical properties for the first time. Similar to bis-phen and -dmp, the calculated *E*° (1.145 V) is higher than that observed experimentally. We return to this difference below (*vide infra*).

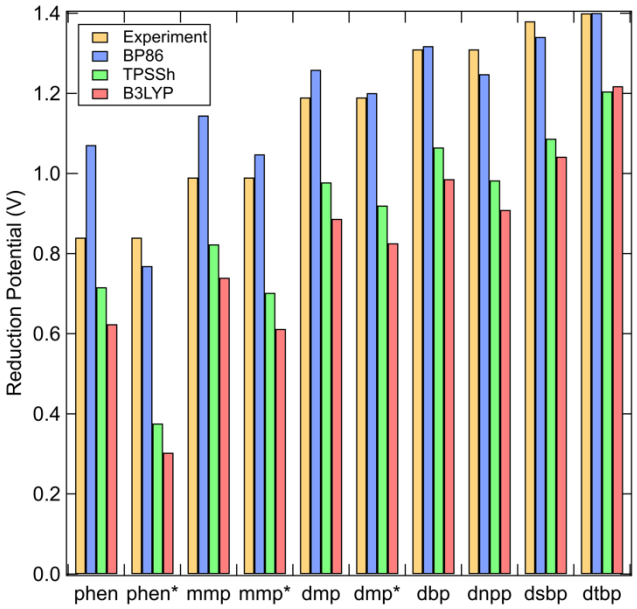

Figure 4.6 Comparison between experimental and calculated E°s for phen and 2,9-alkyl substituted complexes.

Table 4.1. Experimental and Calculated $E°$s (V vs. NHE) for 2,9-alkyl substituted bis-phen complexes.

Ligand	BP86 (eV)	TPSSh (eV)	B3LYP (eV)	Experiment (V)	BP86 – Exp. (V)
phen	1.071	0.716	0.624	0.84[a]	0.23
phen*	0.769	0.376	0.303	0.84[a]	-0.07
mmp	1.145	0.823	0.740	0.99[a]	0.16
mmp*	1.048	0.702	0.612	0.99[a]	0.06
dmp	1.259	0.978	0.887	1.19[a]	0.07
dmp*	1.201	0.920	0.826	1.19[a]	0.01
dbp	1.318	1.065	0.987	1.31[b]	0.01
dnpp	1.248	0.983	0.909	1.31[b]	-0.06
dsbp	1.341	1.087	1.042	1.38[b]	-0.04
dmp-dtbp	1.459	1.243	1.197		
dtbp	1.401	1.205	1.218	1.40[c]	0.00

*Optimized structure includes a weak H_2O interaction as discussed in the text.

[a] This work

[b] Ref 34

[c] Ref 38

As discussed above for $E°$, there is a nearly three order of magnitude gap between the τs of bis-phen and bis-dmp complexes (0.14 vs. 90 ns, respectively). We therefore measured the

^{3}MLCT lifetime of bis-mmp in DCM. The absorption data and corresponding transient absorption data for bis-mmp are given in Figures 4.4 and 4.5 (excitation at 410 nm). Fits to the decay of the excited state absorption at 550 nm give a lifetime of 2 ns. Note that the correlations presented in Figures 4.6 and 4.7 below predicted a similar lifetime for bis-mmp *a priori*; this observation points to the predictive and interpretive power of the correlations addressed herein. The latter in particular is elaborated on through comparisons to other Cu(I)-based photosentizers in the Discussion section.

Experimental ln(τ)s are correlated to experimental *E*°s for bis-phen and the 2,9-alkyl substituted Cu(I) complexes in Figure 4.7. Given the broad range of structures, *E*°s, and lifetimes over these seven complexes, this linear correlation can provide a means to estimate an entatic energy. The slope and y-intercept of the correlation between ln(τ) and *E*°, along with the corresponding regression analysis at the 95% confidence interval, provides an entatic energy of 3.2 ± 0.7 kcal/mol (0.14 ± 0.03 eV) for one order of magnitude change in τ. The experimental τs of the complexes considered in Figure 4.7 span many orders of magnitude; translating to this experimental window in ^{3}MLCT lifetime equates to an entatic energy of 12.9 ± 2.9 kcal/mol (0.56 ± 0.13 eV) for a four orders of magnitude change in τ.

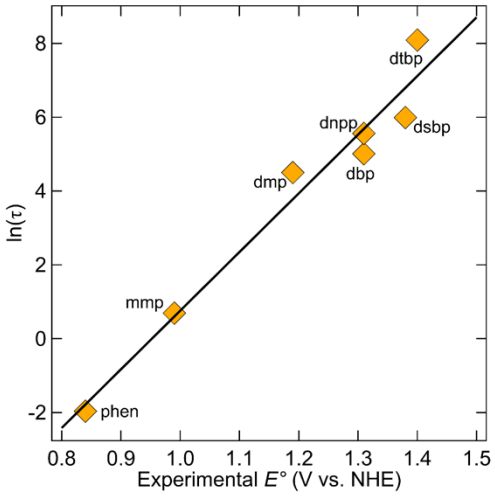

Figure 4.7 The correlation between experimental $E°$s and ln(τ)s for bis-phen and 2,9-alkyl substituted Cu(I) complexes. The linear fit has an $R^2 = 0.963$ and the equation $y = (15.89\ V^{-1})x + 15.14$.

While the correlation between $E°$ and ln(τ) is a potentially attractive means of determining entatic energies, solvation contributions can affect the Cu(I/II) $E°$. For instance, $E°$ for bis-dmp can shift quite dramatically when measured in different coordinating solvents (e.g., a shift of -0.16 or -0.29 V is observed moving from DCM to CH_3CN or DMSO, respectively[31]). This solvent effect was successfully modeled assuming fast, reversible coordination upon oxidation, with little solvent binding to Cu(I).[31] In addition to ground state redox, solvent interactions have also been invoked and discussed for Cu-based excited state ^{3}MLCT formation and decay.[18] In the former case, coordination to Cu(II) stabilizes the oxidized state relative to the reduced state; this differential oxidation state stabilization decreases $E°$. Here, however, focusing solely on noncoordinating DCM allows us to effectively reduce contributions from direct solvent coordination to Cu(II) as much as possible and therefore provide a more accurate quantification of entatic contributions to

E°. Nonetheless, despite being carried out in DCM, the electrochemical data for Cu(I) bis-phen is quasi-reversible, and high scan rates (>600 mV/s) are required. Thus, for the less solvent protected ligand sets, there are likely interactions between the oxidized state and some combination of solvent, electrode surface, and/or counter ion that can potentially contribute to *E*°. However, this selective interaction for Cu(II) is not accounted for using continuum solvation calculations, and we therefore attribute the discrepancies noted above (*vide supra*) between calculated and experimental potentials for bis-phen, -mmp, and -dmp complexes to this differential oxidation state stabilization. Note the deviations between experiment and theoretical *E*°s are 0.23, 0.16, and 0.07 V for bis-phen, -mmp, and -dmp, respectively, supporting the diminished differential oxidation state stabilization across this series as ligand bulk is increased. Importantly, this observation also suggests that solvent contributions can affect the correlation between *E*° and ln(τ), and thus the quantification of entatic contributions. For example, using the computational values of *E*°, which should represent a limit where no differential Cu(II) interactions are present, the correlation between *E*° and ln(τ) gives entatic energies of 1.7 ± 0.5 (0.07 ± 0.02 eV) and 6.8 ± 2.1 kcal/mol (0.29 ± 0.09 eV), respectively, for one and four orders of magnitude change in τ. These values are less than the 3.2 ± 0.7 (0.14 ± 0.03 eV) and 12.9 ± 2.9 kcal/mol (0.56 ± 0.13 eV) using experimental *E*°s (*vide supra*), which further indicates that differential oxidation state stabilization can affect the correlation between *E*° and ln(τ), and thus the entatic energy.

The differential oxidation state interactions can be evaluated by including the effects of a weakly coordinating ligand interaction (H_2O) in Cu bis-phen, -mmp, and -dmp complexes (denoted bis-phen*, -mmp*, and -dmp*). Note the Cu(II)–OH_2 bond in bis-phen* is weak (~2.4 and ~2.5 Å in the oxidized and ^{3}MLCT states, respectively) and significantly weaker in bis-mmp* (~2.9 and ~3.0 Å in bis-mmp*). Water does not bond to Cu(II) in bis-dmp*. Differential oxidation

state stabilization in bis-phen* lowers the calculated $E°$ (BP86) from 1.07 to 0.77 V vs. NHE (Table 4.1), in better agreement with experiment. Additionally, including the oxidation state selective interactions in bis-mmp* and -dmp* lowers the calculated $E°$s to 1.048 and 1.201 V, respectively, both improved relative to experiment. Lastly, correlating the calculated $E°$s and ln(τ) using these values for bis-phen*, -mmp*, and -dmp* gives entatic energies of 3.3 ± 0.9 (0.14 ± 0.04 eV) and 13.1 ± 3.6 kcal/mol (0.57 ± 0.16 eV) for one and four orders of magnitude change in τ, respectively, in excellent agreement with values from purely experimental $E°$s (*vide supra*).

In addition to sterics, the difference in electron-donating ability of the 2,9-alkyl substituents relative to –H can contribute to $E°$ by preferentially stabilizing the oxidized over the reduced state. Here steric vs. electronic contributions can be decomposed using "H–capped" versions of the 2,9-alkyl substituents, which involve replacing the 2,9-alkyl group with an H atom and keeping the geometry completely unperturbed otherwise. Indeed, calculated $E°$s are sensitive to H–capping. For example, for bis-dtbp, -dsbp, and -dmp, the difference in calculated $E°$ between H–capped and uncapped structures is 0.148, 0.040, and 0.013 V, respectively, showing a systematic decrease with increasing electron-donating ability across the series. These contributions can also affect the correlation between $E°$ and ln(τ). Using the calculated H–capped values and correlating with experimental ln(τ)s results in entatic contributions for one and four orders of magnitude change in τ of 2.2 ± 1.0 (0.10 ± 0.04 eV) and 8.8 ± 4.1 kcal/mol (0.38 ± 0.18 eV), respectively. While the correlation for the H–capped structures is not as tight, these results suggest that the entatic contribution for the H–capped structures is larger than for the uncapped structures and that the electron-donating ability of the alkyl group opposes the entatic state. For a clearer comparison, τ increases from 0.14 to 3260 ns going from bis-phen to bis-dtbp. The calculated $E°$s for these structures vary by 0.330 V (~7.6 kcal/mol) in the uncapped structures. This difference increases to

0.476 V (~11.0 kcal/mol) in the H–capped structures. Therefore, the intrinsic entatic energy from bis-phen to bis-dtbp is opposed by the electron-donating dtbp group, consistent with the analyses using the slope of $E°$ vs. ln(τ).

In summary, for this series of Cu photosensitizers, experimental $E°$s correlate linearly with τ over four orders of magnitude in lifetime. The slope of this correlation provides a potential quantitative estimate of the entatic contributions to τ. From experiment, the entatic energy is estimated to be 12.9 ± 2.9 kcal/mol (0.56 ± 0.13 eV) for a four order of magnitude increase in τ. However, differential oxidation state interactions over this series of complexes can affect the correlation and result in an overestimation of the entatic energy. This is exemplified by comparing the entatic energies from calculated $E°$s with and without differential oxidation state interactions (6.8 ± 2.1 kcal/mol (0.29 ± 0.09 eV) and 13.1 ± 3.6 kcal/mol (0.57 ± 0.16 eV), respectively, for a four order of magnitude increase in excited state lifetime). Additionally, steric and electronic contributions to the slope can be decomposed using H–capped vs. uncapped structures. Analyses of these structures indicate that the electron-donating ability of the 2,9-alkyl substituents oppose the entatic contributions to the potentials and lifetimes from sterics; this is exemplified by the bis-phen to bis-dtbp comparison described above, for which the entatic energy is opposed by electron-donation by ~3 kcal/mol (~0.1 eV).

Entatic Contributions and Cu(I/II) Reorganization Energies

Entatic states have been invoked to rationalize the small reorganization energies of biological electron transfer active sites, which for T1 Cu active sites (e.g., plastocyanin, azurin) range from 0.7–1.2 eV.[40,41] This value contains contributions from outer sphere reorganization as well, and the inner sphere contribution is thought to be ~0.4 eV. Here we use λ_is as an alternative

means of quantifying entatic contributions to excited state processes, as they better capture the relative curvatures of the potential energy surfaces involved in redox and photophysical processes.

The approach described by Ryde et al.[42,43] has been applied successfully in calculating the λ_is for a wide-range of Cu complexes. Here λ_is have been calculated for a series of bis-phen and 2,9-alkyl Cu(I) complexes (Table 4.2). λ_i for bis-phen is calculated to be 1.06 eV (BP86). For comparison, this value is lower than that reported by Ryde et al. for Cu(I/II)$(NH_3)_4$ (1.40 eV),[42] which reflects the increased steric constraints provided by the phen ligand relative to NH_3. Note the majority of λ_i for Cu(I/II)$(NH_3)_4$ derives from the tetragonal distortion.[41,42] Beyond $E°$, additional insights regarding entatic contributions, including potential energy surfaces and their curvatures, can be determined from ground state λ_is.

As discussed above, a correlation can be drawn between the calculated ground state λ_is and the experimental ln(τ)s. This correlation, given in Figure 4.8A, is also linear and provides entatic contributions for one and four orders of magnitude change in τ of 4.3 ± 0.6 and 17.3 ± 2.2 kcal/mol. These calculated λ_is are free from differential oxidation state contributions, as was evaluated above for redox potentials. For comparison, using bis-phen*, -mmp*, and -dmp* in the correlation provides entatic contributions for one and four orders of magnitude change in τ of 5.4 ± 0.5 and 21.7 ± 2.0 kcal/mol.

Table 4.2 Comparisons between excited state lifetimes and calculated ground state reorganization energies, excited state relaxation energies, and energy gaps for 2,9-alkyl substituted bis-phen complexes.[a]

Ligand	τ (ns)	ln(τ)	λ (eV)[b]	λ (eV)[c]	γ (eV)[b]	γ (eV)[c]	EG (eV)[b]	EG (eV)[c]

phen	0.14	-1.97	0.994 (22.9)	1.064 (24.5)	1.434 (33.1)	1.428 (32.9)	0.778 (17.9)	0.767 (17.7)
phen*			1.067 (24.6)	1.222 (28.2)	1.391 (32.1)	1.411 (32.5)	0.655 (15.1)	0.627 (14.5)
mmp	2[d]	0.69	0.706 (16.3)	0.763 (17.6)	1.114 (25.7)	1.112 (25.6)	1.044 (24.1)	1.029 (23.7)
mmp*			0.802 (18.5)	0.922 (21.3)	1.202 (27.7)	1.202 (27.7)	0.944 (21.8)	0.932 (21.5)
dmp	90	4.50	0.484 (11.2)	0.521 (12.0)	0.910 (21.0)	0.890 (20.5)	1.377 (31.8)	1.360 (31.4)
dmp*			0.481 (11.1)	0.526 (12.1)	0.865 (19.9)	0.867 (20.0)	1.330 (30.7)	1.321 (30.5)
dbp	150	5.01	0.445 (10.3)	0.458 (10.6)	0.747 (17.2)	0.725 (16.7)	1.507 (34.8)	1.507 (34.8)
dnpp	260	5.56	0.388 (9.0)	0.393 (9.1)	0.665 (15.3)	0.664 (15.3)	1.418 (32.7)	1.423 (32.8)
dsbp	400	5.99	0.397 (9.2)	0.407 (9.4)	0.715 (16.5)	0.716 (16.5)	1.511 (34.8)	1.515 (34.9)

dmp-dtbp	730[e]	6.59	0.383 (8.8)	0.381 (8.8)	0.616 (14.2)	0.621 (14.3)	1.658 (38.2)	1.649 (38.0)
dtbp	3260	8.09	0.176 (4.1)	0.183 (4.2)	0.312 (7.2)	0.312 (7.2)	1.896 (43.7)	1.894 (43.7)

*Optimized structure includes a weak H_2O interaction as discussed in the text.

[a] Unless indicated, lifetimes were taken from Table 1 of Ref 21 and references cited therein. Parenthetical values in kcal/mol.

[b] Gas phase.

[c] CPCM corrected.

[d] This work.

[e] Ref 38.

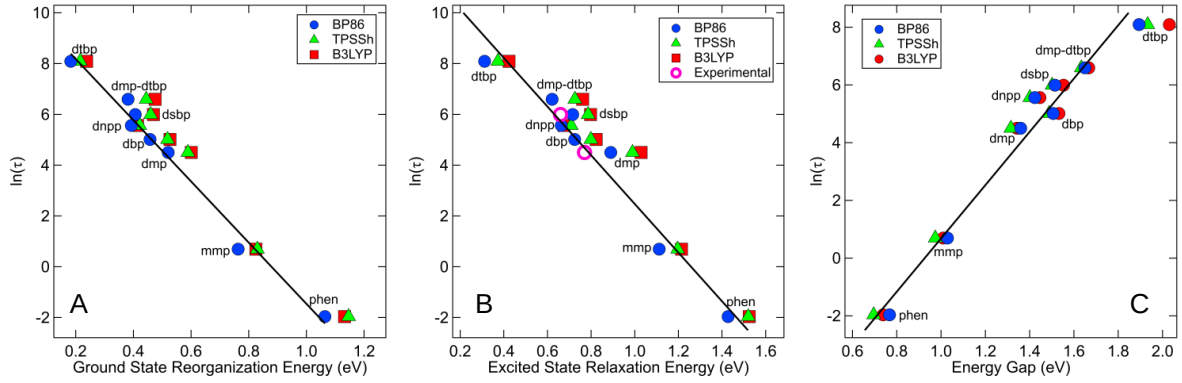

Figure 4.8 Correlations between ln(τ)s and (**A**) ground state reorganization energies, (**B**) excited state relaxation energies, and (**C**) energy gaps for bis-phen and the 2,9-alkyl substituted Cu(I) complexes. The linear fit (black line) is shown for BP86. For A, the fit has R^2 = 0.984 and the equation y = (-12.06 eV^{-1})x + 10.59. For B, R^2 = 0.956 and the equation y = (-9.58 eV^{-1})x + 12.05. For C, R^2 = 0.965 and the equation y = (9.23 eV^{-1})x + 8.55.

As presented above for ground state redox, the λ_is can be corrected for electron-donating effects of the 2,9-alkyl substituents to decompose the steric and electronic contributions to λ_i by analyzing the H-capped structures. The H–capped results provide entatic contributions for one and four orders of magnitude in τ of 4.4 ± 0.7 and 17.7 ± 3.0 kcal/mol. These values are similar to those obtained from uncapped structures, indicating that, unlike *E*°s, electron-donating effects are minimized in the evaluation of λ_i. Thus, the entatic contributions estimated using λ_i are largely due to sterics and further suggest sterics play a more significant role in excited state lifetimes than electron-donating contributions. This is corroborated below using excited state relaxation energies.

Lastly, entatic contributions estimated for over four orders of magnitude change in τ are similar between gas phase and CPCM solvation approaches (15.7 ± 2.4 and 17.3 ± 2.2 kcal/mol, respectively). This observation further supports that λ_is more so reflect geometric/steric contributions as opposed to solvation and/or electron-donating effects.

In summary, for this series of Cu(I) photosensitizers, the calculated λ_is correlate linearly with ln(τ) over four orders of magnitude in τ. The slope of this correlation provides a potential quantitative estimate of the entatic contributions to the excited state lifetimes. The entatic energy using this method is estimated to be 17.3 ± 2.2 kcal/mol for a four order of magnitude increase in τ. In contrast to *E*°s, differential oxidation state interactions over this series of complexes has a significantly smaller effect on the correlation between energetics and ln(τ). Furthermore, electron-donating effects, estimated using the comparison between H–capped and uncapped structures, are minimized in λ_is, which results in similar estimates of entatic contributions.

Entatic Contributions and Cu(I/II) Metal-to-Ligand Charge Transfer Relaxation

In addition to λ_is, the same methodology can be translated to estimate excited state ^{3}MLCT relaxation energies (γ_is). The calculated γ_is are given in Table 4.2, and their correlation with experimental ln(τ) is given in Figure 4.8B. This correlation provides entatic contributions of 5.3 ± 1.1 and 21.2 ± 4.5 kcal/mol, respectively, for one and four orders of magnitude change in τ.

To provide an experimental calibration, 77 K emission spectra were collected on $[Cu(dsbp)_2][PF_6]$ and $[Cu(dmp)_2][PF_6]$ complexes in 1:1 toluene/DCM glasses, and experimental bandwidths and fittings provide γ_is of 0.66 and 0.77 eV, respectively.[44] These values are in fair agreement with those calculated for bis-dsbp and -dmp complexes (0.715 and 0.910 eV, respectively) and are in good agreement with the overall correlation between ln(τ) and γ_i for bis-phen and the 2,9-alkyl complexes (Figure 4.8B, pink circles).

As done above, the potential role of differential solvation can be evaluated using the γ_is estimated for bis-phen*, -mmp*, and -dmp*. Using these structures in the correlation, entatic energies for one and four orders of magnitude in τ are estimated to be 5.5 ± 1.0 and 21.8 ± 4.1 kcal/mol, respectively. Furthermore, the role of electron-donation can be evaluated using the H–capped and uncapped structures. Using the H–capped structures gives entatic contributions of 5.2 ± 1.4 and 20.8 ± 5.5 kcal/mol, respectively, for one and four orders of magnitude change in τ. As with λ_is, γ_is provide very similar entatic contributions using H–capped vs. uncapped structures, both suggesting that excited state lifetimes are largely governed by sterics, and electron-donating contributions from the 2,9-alkyl groups are minimal. Furthermore, entatic contributions over four orders of magnitude in τ are similar between gas phase and PCM solvation approaches (21.3 ± 4.8 and 21.2 ± 4.5 kcal/mol, respectively). This further supports the observation that the calculated γ_is purely reflect geometric and steric contributions to the relaxation energy.

In summary, for this series of Cu photosensitizers, the calculated γ_is correlate linearly with ln(τ) over four orders of magnitude in τ. The slope of this correlation provides a potential quantitative estimate of the entatic contributions. The entatic energy estimated for four orders of magnitude in τ using the uncapped structures (21.2 ± 4.5 kcal/mol) is essentially identical to those determined using H–capped structures (20.8 ± 5.5 kcal/mol) or those accounting for differential oxidation state stabilization (21.8 ± 4.1 kcal/mol). Additionally, gas phase and PCM corrected calculations provide essentially identical entatic contributions. Thus, correlating γ_is and experimental τs provides a robust means to quantify purely geometric and steric contributions from the entatic state. As discussed below, we therefore use this correlation to provide a comparison to a variety of classes of Cu-based photosensitizers reported in the literature.

Entatic Contributions and the Cu(I/II) Metal-to-Ligand Charge Transfer Energy Gap

In addition to λ_is and γ_is, we can apply the same correlation between ln(τ) and the calculated energy gap between the ^{3}MLCT excited state and the reduced ground state in the equilibrium structure of the ^{3}MLCT excited. These energies are reported in Table 2 and are correlated with ln(τ) in Figure 4.8C. This correlation provides entatic contributions of 5.6 ± 1.0 and 22.2 ± 4.2 kcal/mol, respectively, for one and four orders of magnitude change in τ. This is in good agreement with entatic estimates using γ_is.

As done above, the potential role of differential solvation can be evaluated using the energy gaps for bis-phen*, -mmp*, and -dmp*. Using these structures in the correlation, entatic energies for one and four orders of magnitude in τ are estimated to be 6.4 ± 0.9 and 25.6 ± 3.8 kcal/mol, respectively. Furthermore, using the H–capped structures gives entatic contributions of 5.5 ± 1.6

and 22.1 ± 6.2 kcal/mol, respectively, for one and four orders of magnitude change in τ. As with λ_is and γ_is, energy gaps provide very similar entatic contributions using H–capped vs. uncapped structures, both suggesting that excited state lifetimes are largely governed by sterics, and electron-donating contributions from the 2,9-alkyl groups are minimal. Furthermore, entatic contributions over four orders of magnitude in τ are similar between gas phase and PCM solvation approaches (21.9 ± 4.3 and 22.2 ± 4.2 kcal/mol, respectively). This further supports the observation that the calculated λ_is, γ_is, and energy gaps purely reflect geometric and steric contributions to the relaxation energy.

In summary, similar to λ_is and $E°$s, the entatic energetics from the energy gap are somewhat sensitive to differential solvation, whereas γ_is appear to provide entatic energies that reflect steric contributions over this series of Cu bis-phen-based complexes. From these data, the entatic state can provide a strong influence over dynamics that can be described by the energy gap law.

Discussion

Photosensitizers have a broad range of applications, including solar electricity generation, solar fuels catalysis, photoredox catalysis, and OLEDs. Their applicability hinges on excited state lifetimes and excited state redox potentials. In terms of the former, much discussion has revolved around sterics and increasing structural rigidity. For Cu-based photosensitizers, the direct correlation between their excited state structural changes and the ground state redox properties of electron transfer active sites of metalloproteins has inspired an extension of the entatic/rack-induced state to photosensitizer dynamics.[39,45] While a core concept in bioinorganic chemistry and a powerful way to inspire new ligand design, the entatic state is difficult to quantify, and there are only a few examples in the literature where this has been accomplished.[46–50] Here we have leveraged correlations between ^{3}MLCT excited state lifetimes of Cu(I) bis-phen complexes and

their corresponding $E°$s, λ_is, γ_is, and energy gaps (Figures 4.8A/B/C, respectively). These linear correlations are observed for over four orders of magnitude change in τ and provide a direct means to quantify entatic state contributions to the excited state dynamics of a broad range of Cu(I)-based photosensitizers.

There can be differences in the quantified entatic energies, however, depending on which correlation is used. A summary of values for different approaches is given in Table 4. When using $E°$s, there can be significant contributions from differential oxidation state stabilization, which, for Cu(I) bis-phen complexes, stabilizes the oxidized over the reduced state and lowers the redox potential. This can affect the correlation between ln(τ) and redox potential. For example, from Table 4, the correlation between ln(τ) and experimental redox potential provides an estimate of an entatic contribution of 12.9 ± 2.9 kcal/mol for a four order of magnitude change in τ, while the same correlation using calculated values of redox potentials gives 6.8 ± 2.1 kcal/mol. The difference between these values largely derives from the overestimation of the calculated $E°$s of bis-phen, -mmp, and -dmp complexes. This overestimation decreases the slope of the ln(τ)/$E°$ correlation and gives rise to a lower value of entatic energy. Above, it was shown that accounting for the differential oxidation state stabilization for the three complexes (using bis-phen*, -mmp*, and -dmp*) results in a slope of 13.1 ± 3.6 kcal/mol, in much better agreement with experiment. Lastly, by using H–capped structures, it was demonstrated that electron donating effects of the 2,9-alkyl substituents can oppose the entatic state contributions (e.g., by ~3 kcal/mol for bis-phen vs. bis-dtbp).

Table 4.3. Entatic state analyses.[a]

Method	**R^2**	**slope (eV)**	**y-int (eV)**	**Entatic (kcal/mol)[b]**	**Entatic (kcal/mol)[c]**
E° (1)[d]	0.963	0.0606	0.9616	3.2 ± 0.7	12.9 ± 2.9
E° (2)[e]	0.935	0.0322	1.1264	1.7 ± 0.5	6.8 ± 2.1
E° (3)[f]	0.946	0.0616	0.9440	3.3 ± 0.9	13.1 ± 3.6
E° (4)[g]	0.857	0.0414	1.1243	2.2 ± 1.0	8.8 ± 4.1
λ_i (1)[h]	0.984	-0.0816	0.0873	4.3 ± 0.6	17.3 ± 2.2
λ_i (2)[i]	0.992	-0.1020	1.0010	5.4 ± 0.5	21.7 ± 2.0
λ_i (3)[j]	0.972	-0.0832	0.8817	4.4 ± 0.7	17.7 ± 3.0
λ_i (4)[k]	0.977	-0.0740	0.8156	3.9 ± 0.6	15.7 ± 2.4
γ_i (1)[h]	0.956	-0.0998	1.2383	5.3 ± 1.1	21.2 ± 4.5
γ_i (2)[i]	0.966	-0.1027	1.2571	5.5 ± 1.0	21.8 ± 4.1
γ_i (3)[j]	0.934	-0.0979	1.2378	5.2 ± 1.4	20.8 ± 5.5
γ_i (4)[k]	0.952	-0.1002	1.2461	5.3 ± 1.2	21.3 ± 4.8
EG (1)[h]	0.965	0.1046	0.9424	5.6 ± 1.0	22.2 ± 4.2
EG (2)[i]	0.978	0.1205	0.8395	6.4 ± 0.9	25.6 ± 3.8
EG (3)[j]	0.926	0.1043	0.9172	5.5 ± 1.6	22.1 ± 6.2

EG (4)[k]	0.962	0.1032	0.9539	5.5 ± 1.1	21.9 ± 4.3

[a] Error analyses conducted at the 95% confidence interval.

[b] One order of magnitude change in τ.

[c] Four orders of magnitude change in τ.

[d] Using experimental *E*°s.

[e] Using calculated *E*°s (uncapped).

[f] Using calculated *E*°s with differential oxidation state stabilization (bis-phen*, -mmp*, and -dmp*). *Optimized structure includes a weak H_2O interaction as discussed in the text.

[g] Using calculated *E*°s (H–capped).

[h] Using calculated energies (uncapped).

[i] Using calculated energies with differential oxidation state stabilization (bis-phen*, -mmp*, and -dmp*).

[j] Using calculated energies (H–capped).

[k] Using calculated energies (uncapped, gas phase).

Overall, the sensitivity to differential oxidation state contributions, largely stemming from the fact that the total oxidation state changes during redox (i.e. Cu(I/II)), in addition to contributions from electron-donating/-withdrawing effects of the 2,9-alkyl groups, suggests that using the correlation between *E*° and ln(τ) is not an ideal way to quantify entatic states in photophysical processes. This is perhaps not surprising given that ground state potentials are thermodynamic quantities and do not take into account important contributions from shifts and changes in curvature of the excited state potential energy surfaces when an entatic state is present.

The extension of the correlation to λ_is alleviates some of the issues presented using *E*°s. The entatic energies estimated using the correlations with calculated λ_is are also given in Table 4. Here the correlation provides an entatic energy of 17.3 ± 2.2 kcal/mol, and differential oxidation state stabilization using bis-phen*, -mmp*, and -dmp* provides an entatic energy that varies less relative to the same comparison using redox potentials (21.7 ± 2.0). Additionally, the entatic

energy is not sensitive to electron-donating/-withdrawing effects (i.e. H–capped vs. capped, 17.3 ± 2.2 vs. 17.7 ± 3.0 kcal/mol, respectively). These observations are also mirrored by the use of calculated γ_is, which provide an entatic energy of 21.2 ± 4.5 kcal/mol for a four order of magnitude change in τ. This value is similar when incorporating differential oxidation state stabilization, H–capped vs. uncapped structures, or gas phase vs. PCM calculations (Table 4.3), which indicates it is a robust, general means to estimate entatic contributions to photophysical processes. This correlation is used below to quantify entatic energies across other types of Cu(I)-based photosensitizers.

Conclusion

This study has developed a combined experimental and computational methodology to quantify entatic contributions to photophysical processes, with specific applications to a broad range of Cu-based photosensitizers and luminescent complexes. This methodology is based on the observation that experimental ^{3}MLCT excited state lifetimes for a range of Cu(I) bis-phen complexes correlate with redox potentials, ground state inner sphere reorganization energies, and excited state relaxation energies and energy gaps over four orders in magnitude in time. These correlations provide a means to directly quantify entatic contributions to the ^{3}MLCT excited state lifetimes over an entire class of photoactive metal complexes. Furthermore, the correlations in Figure 4.8 provide a means to benchmark the potential performance characteristics of new complexes before embarking on their syntheses. Lastly, within Cu(I)-based photosensitizers, entatic states are found here to reach ~20 kcal/mol relative to the conformationally flexible $[Cu(phen)_2]^+$. Being the largest entatic states yet quantified, these energetics are significant relative to typical chemical driving forces and barriers, suggesting entatic state descriptors will be valuable to extend to new classes of molecules and materials with interesting functional properties involving

the coupling between electron and vibrational dynamics. Our laboratory is currently extending these analyses to quantifying entatic states in (photo)catalytic and (photo)magnetic materials.

Citations

(1) Lumry, R.; Eyring, H. Conformation Changes of Proteins. *J. Phys. Chem.* **1954**, *58* (2), 110–120. https://doi.org/10.1021/j150512a005.

(2) Vallee, B. L.; Williams, R. J. Metalloenzymes: The Entatic Nature of Their Active Sites. *Proceedings of the National Academy of Sciences* **1968**, *59* (2), 498–505. https://doi.org/10.1073/pnas.59.2.498.

(3) Williams, R. J. P. Energised (Entatic) States of Groups and of Secondary Structures in Proteins and Metalloproteins. *European Journal of Biochemistry* **1995**, *234* (2), 363–381. https://doi.org/10.1111/j.1432-1033.1995.363_b.x.

(4) Gray, H. B.; Malmström, Bo. G. On the Relationship between Protein-Forced Ligand Fields and the Properties of Blue Copper Centers. *Comments on Inorganic Chemistry* **1983**, *2* (5), 203–209. https://doi.org/10.1080/02603598308078118.

(5) Malmström, B. G. Rack-Induced Bonding in Blue-Copper Proteins. In *EJB Reviews 1994*; Christen, P., Hofmann, E., Eds.; Springer: Berlin, Heidelberg, 1995; pp 157–164. https://doi.org/10.1007/978-3-642-79502-2_12.

(6) Gray, H. B.; Malmström, B. G.; Williams, R. J. P. Copper Coordination in Blue Proteins. *J. Biol. Inorg. Chem.* **2000**, *5* (5), 551–559. https://doi.org/10.1007/s007750000146.

(7) Ghosh, S.; Xie, X.; Dey, A.; Sun, Y.; Scholes, C. P.; Solomon, E. I. Thermodynamic Equilibrium between Blue and Green Copper Sites and the Role of the Protein in Controlling Function. *Proceedings of the National Academy of Sciences* **2009**, *106* (13), 4969–4974. https://doi.org/10.1073/pnas.0900995106.

(8) Mara, M. W.; Hadt, R. G.; Reinhard, M. E.; Kroll, T.; Lim, H.; Hartsock, R. W.; Alonso-Mori, R.; Chollet, M.; Glownia, J. M.; Nelson, S.; Sokaras, D.; Kunnus, K.; Hodgson, K. O.; Hedman, B.; Bergmann, U.; Gaffney, K. J.; Solomon, E. I. Metalloprotein Entatic Control of Ligand-Metal Bonds Quantified by Ultrafast x-Ray Spectroscopy. *Science* **2017**, *356* (6344), 1276–1280. https://doi.org/10.1126/science.aam6203.

(9) Solomon, E. I.; Hadt, R. G. Recent Advances in Understanding Blue Copper Proteins. *Coordination Chemistry Reviews* **2011**, *255* (7), 774–789. https://doi.org/10.1016/j.ccr.2010.12.008.

(10) Hadt, R. G.; Xie, X.; Pauleta, S. R.; Moura, I.; Solomon, E. I. Analysis of Resonance Raman Data on the Blue Copper Site in Pseudoazurin: Excited State π and σ Charge Transfer Distortions and Their Relation to Ground State Reorganization Energy. *Journal of Inorganic Biochemistry* **2012**, *115*, 155–162. https://doi.org/10.1016/j.jinorgbio.2012.03.006.

(11) Rorabacher, D. B. Electron Transfer by Copper Centers. *Chem. Rev.* **2004**, *104* (2), 651–698. https://doi.org/10.1021/cr020630e.

(12) Chaka, G.; Sonnenberg, J. L.; Schlegel, H. B.; Heeg, M. J.; Jaeger, G.; Nelson, T. J.; Ochrymowycz, L. A.; Rorabacher, D. B. A Definitive Example of a Geometric "Entatic State" Effect: Electron-Transfer Kinetics for a Copper(II/I) Complex Involving A

Quinquedentate Macrocyclic Trithiaether−Bipyridine Ligand. *J. Am. Chem. Soc.* **2007**, *129* (16), 5217–5227. https://doi.org/10.1021/ja068960u.
(13) Xie, B.; Elder, T.; Wilson, L. J.; Stanbury, D. M. Internal Reorganization Energies for Copper Redox Couples: The Slow Electron-Transfer Reactions of the [CuII/I(Bib)2]2+/+ Couple. *Inorg. Chem.* **1999**, *38* (1), 12–19. https://doi.org/10.1021/ic980926w.
(14) Comba, P. Coordination Compounds in the Entatic State. *Coordination Chemistry Reviews* **2000**, *200–202*, 217–245. https://doi.org/10.1016/S0010-8545(00)00265-4.
(15) Comba, P. Strains and Stresses in Coordination Compounds. *Coordination Chemistry Reviews* **1999**, *182* (1), 343–371. https://doi.org/10.1016/S0010-8545(98)00199-4.
(16) Lazorski, M. S.; Castellano, F. N. Advances in the Light Conversion Properties of Cu(I)-Based Photosensitizers. *Polyhedron* **2014**, *82*, 57–70. https://doi.org/10.1016/j.poly.2014.04.060.
(17) Lockard, J. V.; Kabehie, S.; Zink, J. I.; Smolentsev, G.; Soldatov, A.; Chen, L. X. Influence of Ligand Substitution on Excited State Structural Dynamics in Cu(I) Bisphenanthroline Complexes. *J. Phys. Chem. B* **2010**, *114* (45), 14521–14527. https://doi.org/10.1021/jp102278u.
(18) Mara, M. W.; Fransted, K. A.; Chen, L. X. Interplays of Excited State Structures and Dynamics in Copper(I) Diimine Complexes: Implications and Perspectives. *Coordination Chemistry Reviews* **2015**, *282–283*, 2–18. https://doi.org/10.1016/j.ccr.2014.06.013.
(19) Capano, G.; Milne, C. J.; Chergui, M.; Rothlisberger, U.; Tavernelli, I.; Penfold, T. J. Probing Wavepacket Dynamics Using Ultrafast X-Ray Spectroscopy. *J. Phys. B: At. Mol. Opt. Phys.* **2015**, *48* (21), 214001. https://doi.org/10.1088/0953-4075/48/21/214001.
(20) Iwamura, M.; Takeuchi, S.; Tahara, T. Real-Time Observation of the Photoinduced Structural Change of Bis(2,9-Dimethyl-1,10-Phenanthroline)Copper(I) by Femtosecond Fluorescence Spectroscopy: A Realistic Potential Curve of the Jahn−Teller Distortion. *J. Am. Chem. Soc.* **2007**, *129* (16), 5248–5256. https://doi.org/10.1021/ja069300s.
(21) Khnayzer, R. S.; McCusker, C. E.; Olaiya, B. S.; Castellano, F. N. Robust Cuprous Phenanthroline Sensitizer for Solar Hydrogen Photocatalysis. *J. Am. Chem. Soc.* **2013**, *135* (38), 14068–14070. https://doi.org/10.1021/ja407816f.
(22) Kohler, L.; Hadt, R. G.; Hayes, D.; Chen, L. X.; Mulfort, K. L. Synthesis, Structure, and Excited State Kinetics of Heteroleptic Cu(I) Complexes with a New Sterically Demanding Phenanthroline Ligand. *Dalton Trans.* **2017**, *46* (38), 13088–13100. https://doi.org/10.1039/C7DT02476B.
(23) Shaw, G. B.; Grant, C. D.; Shirota, H.; Castner, E. W.; Meyer, G. J.; Chen, L. X. Ultrafast Structural Rearrangements in the MLCT Excited State for Copper(I) Bis-Phenanthrolines in Solution. *J. Am. Chem. Soc.* **2007**, *129* (7), 2147–2160. https://doi.org/10.1021/ja067271f.
(24) McCullough, B. J.; Neyhouse, B. J.; Schrage, B. R.; Reed, D. T.; Osinski, A. J.; Ziegler, C. J.; White, T. A. Visible-Light-Driven Photosystems Using Heteroleptic Cu(I) Photosensitizers and Rh(III) Catalysts To Produce H2. *Inorg. Chem.* **2018**, *57* (5), 2865–2875. https://doi.org/10.1021/acs.inorgchem.7b03273.
(25) Dicke, B.; Hoffmann, A.; Stanek, J.; Rampp, M. S.; Grimm-Lebsanft, B.; Biebl, F.; Rukser, D.; Maerz, B.; Göries, D.; Naumova, M.; Biednov, M.; Neuber, G.; Wetzel, A.; Hofmann, S. M.; Roedig, P.; Meents, A.; Bielecki, J.; Andreasson, J.; Beyerlein, K. R.; Chapman, H. N.; Bressler, C.; Zinth, W.; Rübhausen, M.; Herres-Pawlis, S. Transferring

the Entatic-State Principle to Copper Photochemistry. *Nature Chem* **2018**, *10* (3), 355–362. https://doi.org/10.1038/nchem.2916.
(26) Robinson, G. W.; Frosch, R. P. Theory of Electronic Energy Relaxation in the Solid Phase. *J. Chem. Phys.* **1962**, *37* (9), 1962–1973. https://doi.org/10.1063/1.1733413.
(27) Jortner, J. Radiationless Transitions. *Pure and Applied Chemistry* **1971**, *27* (3), 389–420. https://doi.org/10.1351/pac197127030389.
(28) Pallenberg, A. J.; Koenig, K. S.; Barnhart, D. M. Synthesis and Characterization of Some Copper(I) Phenanthroline Complexes. *Inorg. Chem.* **1995**, *34* (11), 2833–2840. https://doi.org/10.1021/ic00115a009.
(29) Ruthkosky, M.; Castellano, F. N.; Meyer, G. J. Photodriven Electron and Energy Transfer from Copper Phenanthroline Excited States. *Inorg. Chem.* **1996**, *35* (22), 6406–6412. https://doi.org/10.1021/ic960503z.
(30) Desvergnes-Breuil, V.; Hebbe, V.; Dietrich-Buchecker, C.; Sauvage, J.-P.; Lacour, J. NMR Evaluation of the Configurational Stability of Cu(I) Complexes. *Inorg. Chem.* **2003**, *42* (2), 255–257. https://doi.org/10.1021/ic0259890.
(31) Scaltrito, D. V.; Thompson, D. W.; O'Callaghan, J. A.; Meyer, G. J. MLCT Excited States of Cuprous Bis-Phenanthroline Coordination Compounds. *Coordination Chemistry Reviews* **2000**, *208* (1), 243–266. https://doi.org/10.1016/S0010-8545(00)00309-X.
(32) Elgrishi, N.; Rountree, K. J.; McCarthy, B. D.; Rountree, E. S.; Eisenhart, T. T.; Dempsey, J. L. A Practical Beginner's Guide to Cyclic Voltammetry. *J. Chem. Educ.* **2018**, *95* (2), 197–206. https://doi.org/10.1021/acs.jchemed.7b00361.
(33) Noviandri, I.; Brown, K. N.; Fleming, D. S.; Gulyas, P. T.; Lay, P. A.; Masters, A. F.; Phillips, L. The Decamethylferrocenium/Decamethylferrocene Redox Couple: A Superior Redox Standard to the Ferrocenium/Ferrocene Redox Couple for Studying Solvent Effects on the Thermodynamics of Electron Transfer. *J. Phys. Chem. B* **1999**, *103* (32), 6713–6722. https://doi.org/10.1021/jp991381+.
(34) Eggleston, M. K.; McMillin, D. R.; Koenig, K. S.; Pallenberg, A. J. Steric Effects in the Ground and Excited States of Cu(NN)2+ Systems. *Inorg. Chem.* **1997**, *36* (2), 172–176. https://doi.org/10.1021/ic960698a.
(35) Cunningham, C. T.; Cunningham, K. L. H.; Michalec, J. F.; McMillin, D. R. Cooperative Substituent Effects on the Excited States of Copper Phenanthrolines. *Inorg. Chem.* **1999**, *38* (20), 4388–4392. https://doi.org/10.1021/ic9906611.
(36) Ichinaga, A. K.; Kirchhoff, J. R.; McMillin, D. R.; Dietrich-Buchecker, C. O.; Marnot, P. A.; Sauvage, J. P. Charge-Transfer Absorption and Emission of Cu(NN)2+ Systems. *Inorg. Chem.* **1987**, *26* (25), 4290–4292. https://doi.org/10.1021/ic00272a030.
(37) Vögtle, F.; Lüer, I.; Balzani, V.; Armaroli, N. Endoreceptors with Convergent Phenanthroline Units: A Molecular Cavity for Six Guest Molecules. *Angewandte Chemie International Edition in English* **1991**, *30* (10), 1333–1336. https://doi.org/10.1002/anie.199113331.
(38) Green, O.; Gandhi, B. A.; Burstyn, J. N. Photophysical Characteristics and Reactivity of Bis(2,9-Di-Tert-Butyl-1,10-Phenanthroline)Copper(I). *Inorg. Chem.* **2009**, *48* (13), 5704–5714. https://doi.org/10.1021/ic802361q.
(39) Kohler, L.; Hadt, R. G.; Hayes, D.; Chen, L. X.; Mulfort, K. L. Synthesis, Structure, and Excited State Kinetics of Heteroleptic Cu(I) Complexes with a New Sterically Demanding Phenanthroline Ligand. *Dalton Trans.* **2017**, *46* (38), 13088–13100. https://doi.org/10.1039/C7DT02476B.

(40) Di Bilio, A. J.; Hill, M. G.; Bonander, N.; Karlsson, B. G.; Villahermosa, R. M.; Malmström, B. G.; Winkler, J. R.; Gray, H. B. Reorganization Energy of Blue Copper: Effects of Temperature and Driving Force on the Rates of Electron Transfer in Ruthenium- and Osmium-Modified Azurins. *J. Am. Chem. Soc.* **1997**, *119* (41), 9921–9922. https://doi.org/10.1021/ja971518e.
(41) Solomon, E. I.; Szilagyi, R. K.; DeBeer George, S.; Basumallick, L. Electronic Structures of Metal Sites in Proteins and Models: Contributions to Function in Blue Copper Proteins. *Chem. Rev.* **2004**, *104* (2), 419–458. https://doi.org/10.1021/cr0206317.
(42) Olsson, M. H. M.; Ryde, U.; Roos, B. O. Quantum Chemical Calculations of the Reorganization Energy of Blue-Copper Proteins. *Protein Science* **1998**, *7* (12), 2659–2668. https://doi.org/10.1002/pro.5560071220.
(43) Ryde, U.; Olsson, M. H. M. Structure, Strain, and Reorganization Energy of Blue Copper Models in the Protein. *International Journal of Quantum Chemistry* **2001**, *81* (5), 335–347. https://doi.org/10.1002/1097-461X(2001)81:5<335::AID-QUA1003>3.0.CO;2-Q.
(44) Murtaza, Z.; Graff, D. K.; Zipp, A. P.; Worl, L. A.; Jones, W. E. Jr.; Bates, W. D.; Meyer, T. J. Energy Transfer in the Inverted Region: Calculation of Relative Rate Constants by Emission Spectral Fitting. *J. Phys. Chem.* **1994**, *98* (41), 10504–10513. https://doi.org/10.1021/j100092a020.
(45) Dicke, B.; Hoffmann, A.; Stanek, J.; Rampp, M. S.; Grimm-Lebsanft, B.; Biebl, F.; Rukser, D.; Maerz, B.; Göries, D.; Naumova, M.; Biednov, M.; Neuber, G.; Wetzel, A.; Hofmann, S. M.; Roedig, P.; Meents, A.; Bielecki, J.; Andreasson, J.; Beyerlein, K. R.; Chapman, H. N.; Bressler, C.; Zinth, W.; Rübhausen, M.; Herres-Pawlis, S. Transferring the Entatic-State Principle to Copper Photochemistry. *Nature Chemistry* **2018**, *10* (3), 355–362. https://doi.org/10.1038/nchem.2916.
(46) Ghosh, S.; Xie, X.; Dey, A.; Sun, Y.; Scholes, C. P.; Solomon, E. I. Thermodynamic Equilibrium between Blue and Green Copper Sites and the Role of the Protein in Controlling Function. *PNAS* **2009**, *106* (13), 4969–4974. https://doi.org/10.1073/pnas.0900995106.
(47) Tsai, M.-L.; Hadt, R. G.; Marshall, N. M.; Wilson, T. D.; Lu, Y.; Solomon, E. I. Axial Interactions in the Mixed-Valent CuA Active Site and Role of the Axial Methionine in Electron Transfer. *PNAS* **2013**, *110* (36), 14658–14663. https://doi.org/10.1073/pnas.1314242110.
(48) Mara, M. W.; Hadt, R. G.; Reinhard, M. E.; Kroll, T.; Lim, H.; Hartsock, R. W.; Alonso-Mori, R.; Chollet, M.; Glownia, J. M.; Nelson, S.; Sokaras, D.; Kunnus, K.; Hodgson, K. O.; Hedman, B.; Bergmann, U.; Gaffney, K. J.; Solomon, E. I. Metalloprotein Entatic Control of Ligand-Metal Bonds Quantified by Ultrafast x-Ray Spectroscopy. *Science* **2017**, *356* (6344), 1276–1280. https://doi.org/10.1126/science.aam6203.
(49) Metz, M.; Solomon, E. I. Dioxygen Binding to Deoxyhemocyanin: Electronic Structure and Mechanism of the Spin-Forbidden Two-Electron Reduction of O2. *J. Am. Chem. Soc.* **2001**, *123* (21), 4938–4950. https://doi.org/10.1021/ja004166b.
(50) Hadt, R. G.; Xie, X.; Pauleta, S. R.; Moura, I.; Solomon, E. I. Analysis of Resonance Raman Data on the Blue Copper Site in Pseudoazurin: Excited State π and σ Charge Transfer Distortions and Their Relation to Ground State Reorganization Energy. *Journal of Inorganic Biochemistry* **2012**, *115*, 155–162. https://doi.org/10.1016/j.jinorgbio.2012.03.006.

Chapter V

Time-Resolved Electron Paramagnetic Resonance Spectroscopy on HDPP-Pent, Li_2(DPP-Pent)$_2$, and KDPP-Pent

Introduction

Singlet fission is a multiexciton generating process by which two triplets may be generated from one singlet exciton.[1] This process proceeds through a correlated triplet pair state ^{M}(TT). Although the singlet character of the ^{M}(TT) state provides a spin-allowed pathway between singlet and triplet manifolds, the coupling of two triplets gives rise to nine states of different spin multiplicities.[2–4] In the high-field limit, these sublevels will approach the eigenstates of the $\hat{S}^2$ and $\hat{S}_z$ operators and represent states of singlet, triplet, and quintet multiplicity. Recent reports using time-resolved electron paramagnetic resonance (TREPR) spectroscopy have elucidated the formation of quintet states via singlet fission in material and molecular systems. The features of these TREPR spectra often suggest that the quintet is generated in a strongly exchange coupled triplet pair (J >> D), such that the eigenstates are roughly of pure spin multiplicity.[5–13]

The triplet pair states play a vital role in the singlet fission conversion process from singlet to free triplets that might be harvested in a solar energy device. Additionally, recent interest has been given to the triplet pair state for quantum information science because the triplet pair represents a maximally entangled state.[5,14,15] Ideally, in quantum information science, one can initialize the system with a high degree of polarization, which is possible for the triplet pair states. Recent investigations have demonstrated that the spin polarization of the quintet observed by TREPR is highly dependent on the relative orientation of the chromophores and their relative orientation with the applied magnetic field. Strict alignment of the molecular axes with each other and with the field produces maximal spin polarization, largely in the $M_s = 0$ sublevel.[15]

As this example shows, it is critically important to be able to understand the structural and electronic properties of singlet fission systems that give rise to different properties of the triplet pair states if we are to rationally design and apply them. To that end, molecular bipentacenes can

be very useful to study and compare with respect to their TREPR data to trace polarization and time evolution of the quintet triplet pair states and uncorrelated triplet features. In this chapter we present results and preliminary analysis regarding the TREPR spectra collected on HDPP-Pent, Li_2(DPP-Pent)$_2$, and KDPP-Pent. Appendix C contains the theoretical framework in the construction of triplet pair spin operators and spin Hamiltonians.

Time-Resolved EPR Spectroscopy

In time-resolved EPR (TREPR), a laser flash is applied to the sample and an EPR signal can be collected at certain time delays after the flash (DAFs). As a result, high-spin excited states may be probe by EPR even if the system is diamagnetic in its ground state. TREPR can be done in continuous wave (CW) mode or in pulsed mode. In CW mode, the laser flash is applied to the sample while the microwave radiation is continuously applied to the cavity, and the EPR spectrum can be read at a particular time by sweeping the magnetic field. This mode of collection has certain drawbacks, as the continuously applied microwave field can induce spin relaxation within the sample, decreasing the lifetime of the signal. In pulsed mode, the EPR signal intensity at a given time after the laser flash is read out by a Hahn echo sequence.

The pulsed detection has certain advantages over the CW detection scheme. As the microwave radiation is not applied continuously, the pulsed detection reduces microwave-driven spin relaxation. Additionally, pulsed detection makes possible the selective detection of transitions arising from specific spin states. The Hahn echo sequence reads out the net magnetization in the transverse plane of the rotating reference frame. The magnetic moments of the spin, initially aligned with the externally applied field along the z-axis, are rotated into the transverse plane by the pulsed application of the $\boldsymbol{B_1}$ field. As the magnetic moment of a spin system is proportional to its total spin angular momentum, systems with higher total spin angular momentum S will

generally exhibit greater magnitude magnetic moments μ. The perpendicularly applied $\boldsymbol{B_1}$ field imposes a torque on the magnetic moment of the spin system. The greater the magnitude of the magnetic moment of the spin system, the greater the torque and thus the greater the angular velocity with which the magnetic moment rotates. As such, the Rabi nutation frequency of a given spin packet will be dependent on the spin angular momentum quantum number S and the magnetic sublevel quantum number M_s. This is given in the expression below in which $\Omega_{M_s,M_s\pm1}$ represents the nutation frequency of a given spin packet and ω_1 is the $\boldsymbol{B_1}$ magnetic field strength in angular frequency units.[16]

$$\Omega_{M_s,M_s\pm1} = \omega_1\sqrt{S(S+1) - M_s(M_s \pm 1)} \qquad Eq.\,5.1$$

In standard EPR spectroscopy, the spin sublevels follow a Boltzmann distribution of the populations. As such, the population of the lower energy sublevel of a given transition (P_l) is greater than the population of the upper energy sublevel (P_u), which results in a net absorptive signal for each transition. In TREPR, the laser flash generates a nonequilibrium population distribution among the spin states. As a result, TREPR spectra can feature both net absorptive and net emissive signals.

As written out explicitly in Appendix C, we derive the spin Hamiltonian for the triplet pair state from the individual triplet spin operators. We follow in the vein of past triplet pair descriptions including recent work such as the JDE model.[14,17] We consider only intratriplet dipolar interactions and intertriplet exchange when including the zero-field splitting and exchange Hamiltonians, respectively. We include only the isotropic component of the exchange as this is generally the dominant exchange interaction in molecular organic electron spin systems.[18] This gives a spin Hamiltonian $\hat{H}$ of the form below:

$$\hat{H} = \hat{H}_{zee} + \hat{H}_{zfs} + \hat{H}_{ex}$$

$$\hat{H}_{zee} = \hat{H}^{A}_{zee} \otimes I_3 + I_3 \otimes \hat{H}^{B}_{zee}$$

$$\hat{H}^{A,B}_{zee} = \mu_B \boldsymbol{B^T} \cdot \boldsymbol{g^{A,B}} \cdot \boldsymbol{S^{A,B}}$$

$$\hat{H}_{zfs} = \hat{H}^{A}_{zfs} \otimes I_3 + I_3 \otimes \hat{H}^{B}_{zfs}$$

$$\hat{H}^{A,B}_{zfs} = \boldsymbol{S^{A,B^T}} \cdot \boldsymbol{D^{A,B}} \cdot \boldsymbol{S^{A,B}}$$

$$\hat{H}_{ex} = J(\hat{S}^{A}_{x} \otimes \hat{S}^{B}_{x} + \hat{S}^{A}_{y} \otimes \hat{S}^{B}_{y} + \hat{S}^{A}_{z} \otimes \hat{S}^{B}_{z}) \qquad Eq. 5.2A - F$$

$\hat{H}^{A,B}_{zee}$ and $\hat{H}^{A,B}_{zfs}$ represent the Zeeman and zero-field splitting Hamiltonians for individual triplets A or B and $\hat{H}_{ex}$ represents the exchange interaction between triplets A and B.[9,14,17,19–21]

In collaboration with Drs. Jens Niklas and Oleg Poluektov, we collected TREPR data on Li_2(DPP-Pent)$_2$, HDPP-Pent, and KDPP-Pent. The compounds were synthesized at Caltech. The data collection was performed at Argonne National Laboratory. EPR simulations were run using the EasySpin package developed for MATLAB.[22] Simulation of the ^{5}(TT) spectra using polarization in the spin basis was performed using an additional script for EasySpin developed by Dr. Matthew Krzyaniak.

Results

Li_2(DPP-Pent)$_2$

TREPR data was collected on 2 mM frozen glass solution samples of Li_2(DPP-Pent)$_2$. We collected EDFS spectra at microwave power attenuations of 17 and 12 dB to measure quintet- and triplet-selective spectra, respectively shown in Figure 5.1. As can be seen, the EDFS spectra collected at 17 dB, although predominately featuring quintet transitions, does have some intensity

coming from triplet transitions on the wings. The absolute signal intensity rises going from 300 ns to 5 μs and then is largely decayed by 70 μs. When normalized, the spectral features at 300 ns and 5 μs are consistent with each other. However, by 70 μs, the quintet features have largely decayed while the triplet features persist.

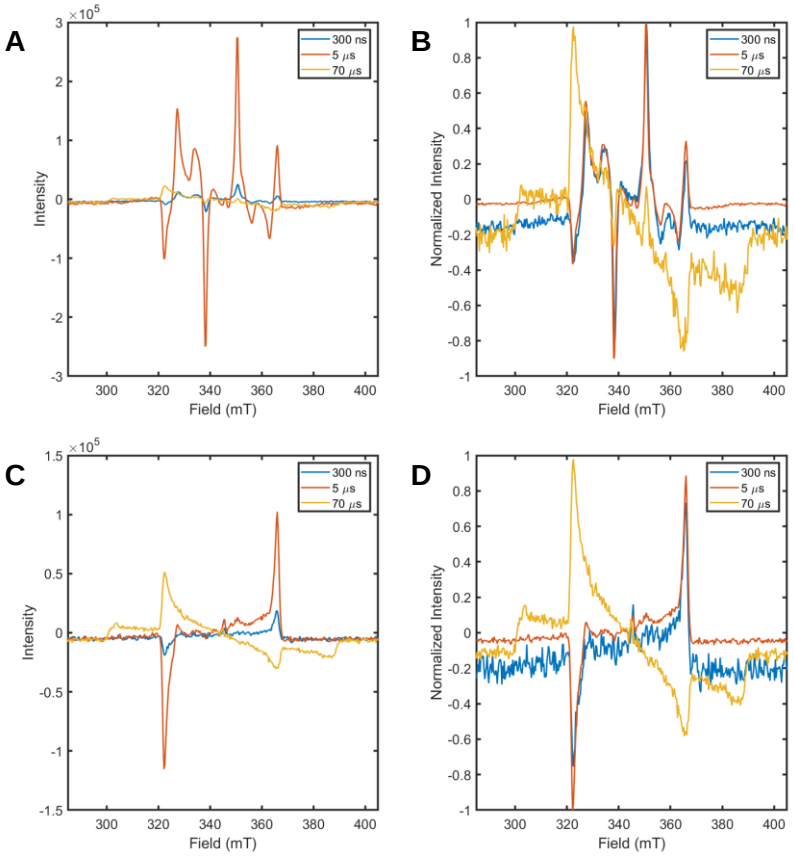

Figure 5.1 EDFS of $Li_2(DPP\text{-}Pent)_2$ at 17 dB microwave power attenuation (quintet-selective) collected at 300 ns, 5 μs, and 70 μs at absolute (**A**) and normalized (**B**) intensity. EDFS at 12 dB microwave power attenuation (triplet-selective) collected at 300 ns, 5 μs, and 70 μs at absolute (**C**) and normalized (**D**) intensity.

The triplet-selective EDFS collected at 12 dB microwave attenuation is dominated by the triplet features. These also rise going from 300 ns to 5 μs before decaying slightly in intensity

toward 70 μs as seen in Figure 5.1C. The polarization pattern of the triplet begins in a *eeaa* pattern where *a* stands for absorptive and *e* for emissive and the four positions correspond to parallel, perpendicular, perpendicular, parallel orientations of the spin packets involved in the two transitions observed in this region. At long DAFs, the polarization pattern changes to *aaee*, suggesting a redistribution of the population density among the magnetic sublevels of the triplet.

The quintet spectrum could be simulated using the triplet pair Hamiltonian above as shown in Figure 5.2. The eigenenergies and states are solved in the uncoupled basis, so the initial population is set to be the ^{1}(TT) projected into the uncoupled basis. This gives rise to quintet features via the off-diagonal elements of the spin Hamiltonian arising from the dipolar interactions. The spectrum was simulated using a g value of 2.0023, D value of 1250 MHz, E value of 10 MHz, and J value of 20 GHz (as per the convention used in EasySpin, the positive exchange coupling constant places the low spin multiplicity states lowest in energy).

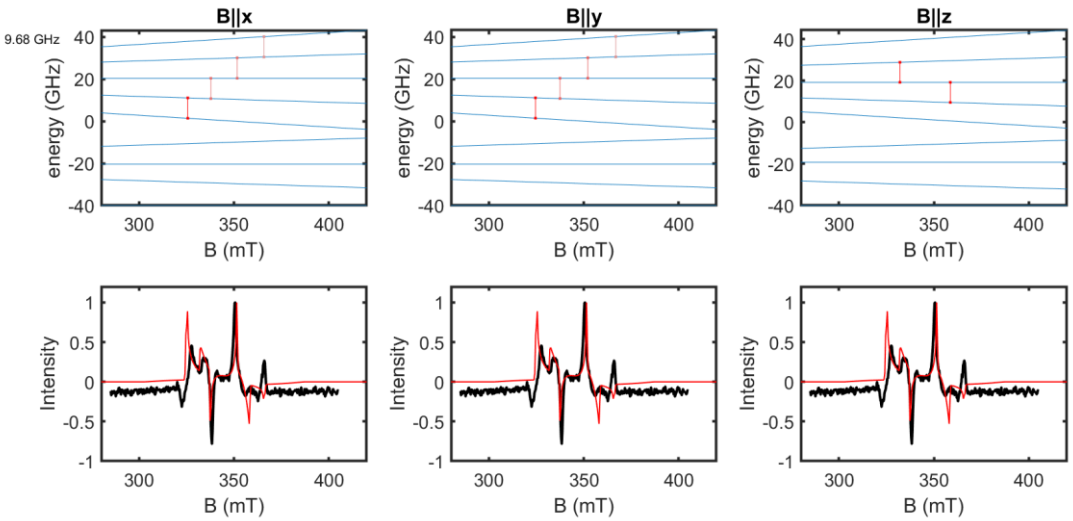

Figure 5.2 Simulated ^{5}(TT) TREPR spectrum (red lines in lower plots) overlaid on the EDFS spectrum of Li_2(DPP-Pent)$_2$ collected at 300 ns DAF and at 20 K, 9.68 GHz microwave frequency.

The levelsplot at each canonical orientation is shown above – the system is largely axial, so the x and y orientations are nearly identical (the rhombicity parameter is not well distinguished from linewidth effects).

The triplet spectrum could be well simulated with the inclusion of the Zeeman and zero-field splitting Hamiltonians in the spin Hamiltonian using a g value of 2.0023, D value of 1250 MHz, and an E value of 10 MHz. The simulated results are overlayed on the triplet spectrum at 5 μs in Figure 5.3.

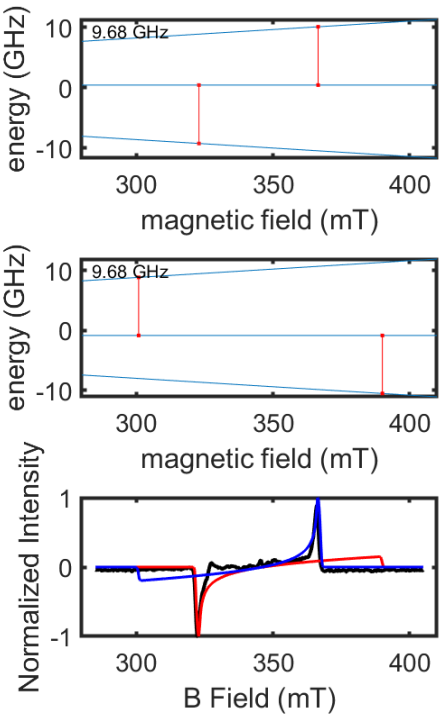

Figure 5.3 Simulated triplet TREPR spectrum (red and blue lines in lower plots) overlaid on the EDFS spectrum of Li_2(DPP-Pent)$_2$ collected at 5 μs DAF and at 20 K, 9.68 GHz microwave frequency. The top levelsplot shows the perpendicular orientations (x and y) and the middle levelsplot shows the parallel orientations (z) of the spin system with respect to the magnetic field.

The time traces of the quintet features at 338.0 and 350.4 mT are shown in Figure 5.4. These traces could be fit with a biexponential function which is shown overlaid over the data in Figure 6.4C. At 338.0 mT, we obtain time constants τ_1 = 1.84 μs and τ_2 = 19.4 μs reflecting the rise and decay times of the signal, respectively. At 350.4 mT, we obtain time constants τ_1 = 1.43 μs and τ_2 = 19.3 μs reflecting the rise and decay times of the signal, respectively.

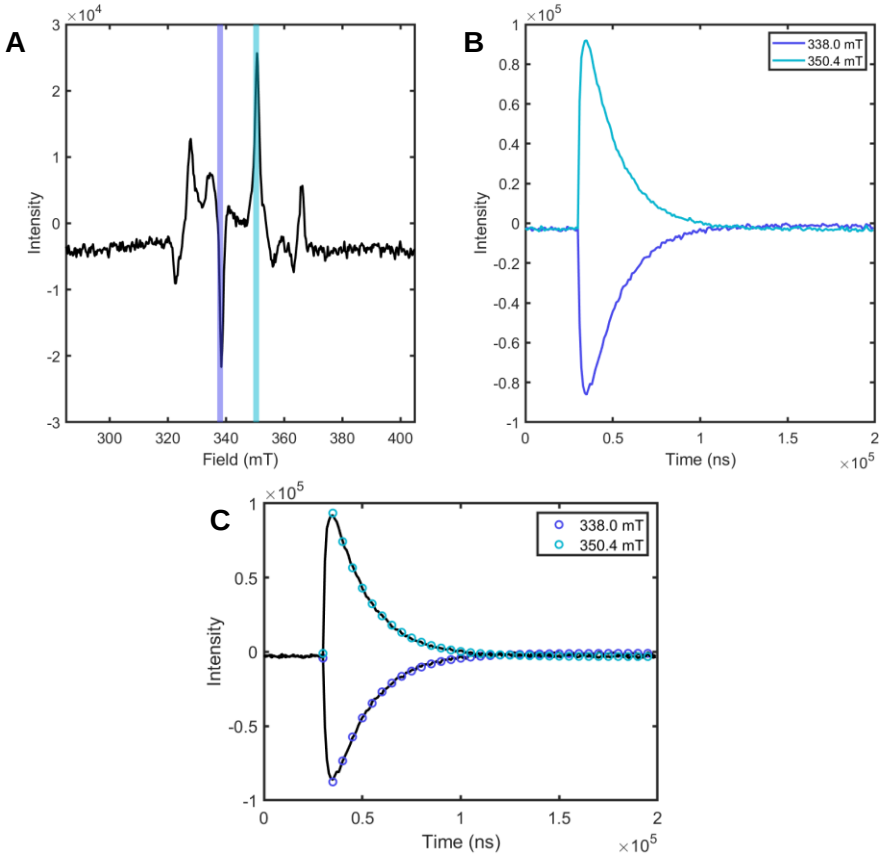

Figure 5.4 (**A**) Quintet spectrum at 5 μs of Li_2(DPP-Pent)$_2$ with field positions 338.0 mT and 350.4 mT highlighted. (**B**) The kinetic traces of the amplitude observed at 338.0 and 350.4 mT in purple and teal, respectively, where the time axis represents the DAF time. (**C**) The time traces overlaid with the results of a biexponential fit.

As previously mentioned, the polarization pattern of the triplet features changes over the times observed. This is shown more explicitly in the time traces collected at 322.2 and 366.0 mT in Figure 5.5.

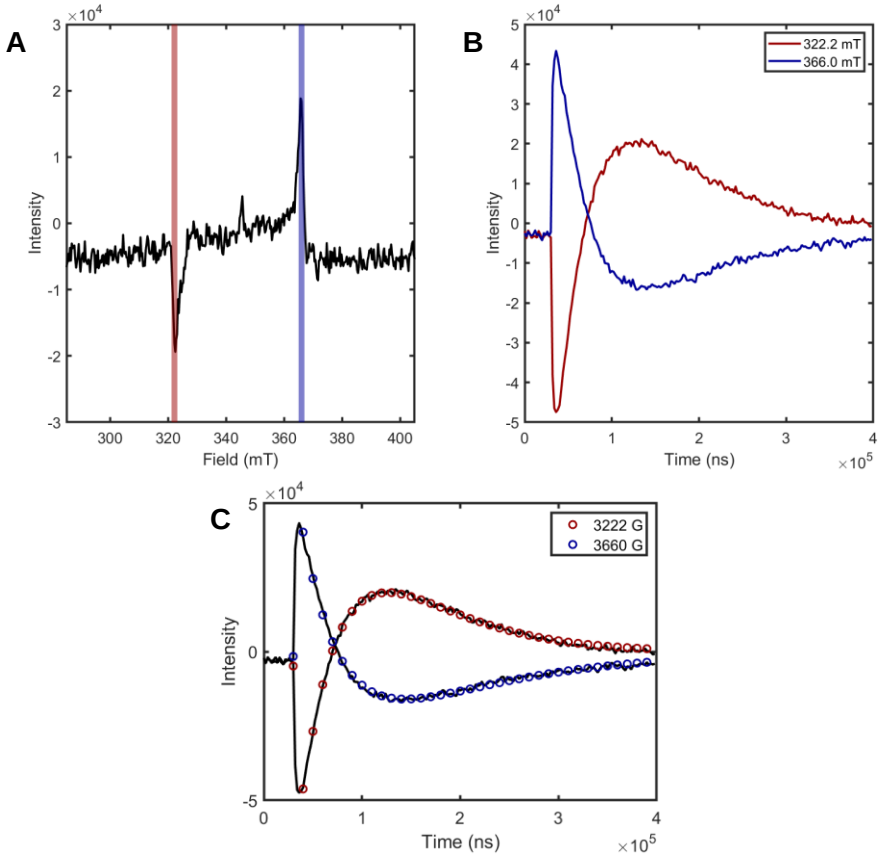

Figure 5.5 (**A**) Triplet spectrum at 300 ns of $Li_2(DPP\text{-}Pent)_2$ with field positions 322.2 and 366.0 mT highlighted. (**B**) The kinetic traces of the amplitude observed at 322.2 and 366.0 mT in red and blue, respectively, where the time axis represents the DAF time. (**C**) The time traces overlaid with the results of a triexponential fit.

The kinetic traces could be fit with a triexponential function, yielding time constants at 322.2 mT of τ_1 = 2.87 μs, τ_2 = 52.49 μs, τ_3 = 60.73 μs and time constants at 366.0 mT of τ_1 = 2.224 μs, τ_2 = 40.52 μs, τ_3 = 131.2 μs. The change in polarization pattern has been observed in correlated

radical pairs as well and arises due to spin-selective intersystem crossing back to the ground state from the triplet sublevels.[9]

A radical standard was added to the sample containing Li_2(DPP-Pent)$_2$ and used to reference the phasing of the data – the radical, which is not affected by the laser flash and exhibits Boltzmann population of its magnetic sublevels, should exhibit a net absorptive feature around the free electron g value ~2.0023. The radical also acts as a reference for Rabi nutation experiments at fixed microwave drive power and varied field position. Observing the ratio of the obtained nutation frequencies can corroborate the assignment of transitions within the S = 1 and S = 2 manifolds.

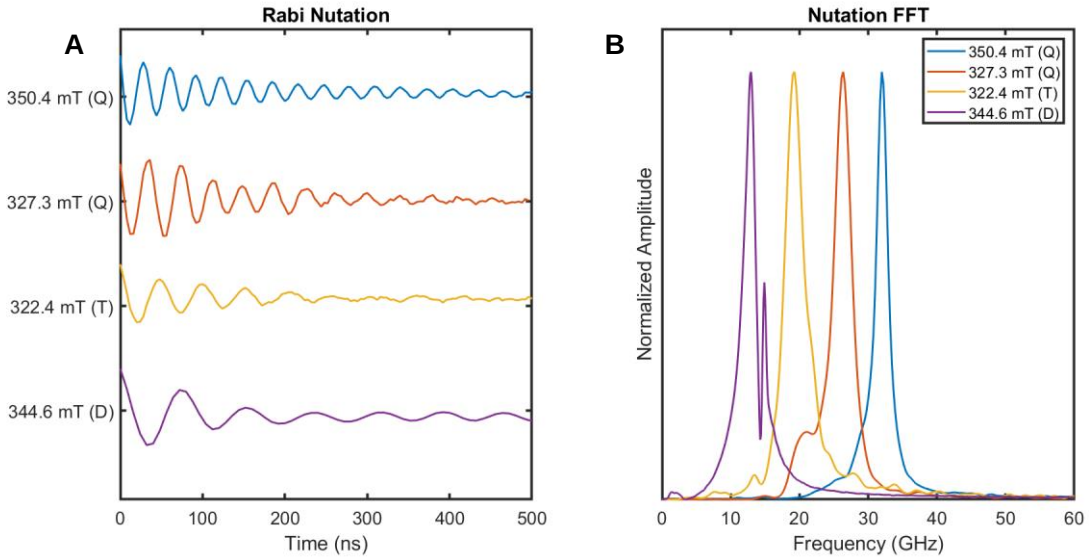

Figure 5.6 Rabi nutation experiments collected on the Li_2(DPP-Pent)$_2$ sample with added reference radical species at 14 dB microwave attenuation at 20 K observed at 350.4 mT (Quintet ~M_s = 0 ↔ +1, perpendicular, 5 μs DAF), 327.3 mT (Quintet ~M_s = -2 ↔ -1, perpendicular, 5 μs

DAF), 322.4 mT (Triplet ~ M_s = -1 ↔ 0, perpendicular, 90 μs DAF), and 344.6 mT (Doublet ~ M_s = -1/2 ↔ +1/2, 90 μs DAF).

As shown in Figure 5.6, Rabi nutation experiments were collected at 350.4, 327.3, 322.4, and 344.6 mT which correspond to quintet (~M_s = 0 ↔ +1, perpendicular), quintet (~M_s = -2 ↔ -1, perpendicular), triplet (~M_s = -1 ↔ 0, perpendicular), and the stable radical (M_s = -1/2 ↔ +1/2) transitions, respectively. The fast Fourier transform of the data provides nutation frequencies of 32.2 GHz (at 350.4 mT), 26.6 GHz (at 327.3 mT), 19.5 GHz (at 322.4 mT), and 13.1 GHz (at 344.6 mT). We can determine the expected ratios of the Rabi nutation frequencies for each given transition from Eq. 6.1. We expect $\frac{\Omega_{Q(0\leftrightarrow+1)}}{\Omega_{Q(-2\leftrightarrow-1)}} = \sqrt{\frac{3}{2}} \approx 1.22, \frac{\Omega_{Q(0\leftrightarrow+1)}}{\Omega_{T(-1\leftrightarrow0)}} = \sqrt{3} \approx 1.73, \frac{\Omega_{Q(0\leftrightarrow+1)}}{\Omega_{D(-1/2\leftrightarrow+1/2)}} = \sqrt{6} \approx 2.45$. Taking the ratio of the experimentally derived nutation frequencies we get $\frac{\Omega_{Q(0\leftrightarrow+1)}}{\Omega_{Q(-2\leftrightarrow-1)}} = 1.21$, $\frac{\Omega_{Q(0\leftrightarrow+1)}}{\Omega_{T(-1\leftrightarrow0)}} = 1.65$, and $\frac{\Omega_{Q(0\leftrightarrow+1)}}{\Omega_{D(-1/2\leftrightarrow+1/2)}} = 2.47$, which is consistent with our expectations.

HDPP-Pent

TREPR was collected on 2 mM glassed solutions of HDPP-Pent. The EDFS collected at 17 dB are shown in Figures 6.7A and 6.7B from 5 to 70 μs. The contribution of the triplet features is significantly reduced compared to the data acquired on Li_2(DPP-Pent)$_2$. In fact, the EDFS collected at 12 dB, which should be dominated by pure triplet features, is largely noise as shown in Figures 6.7C and 6.7D. This as well stands in stark contrast to the evident triplet features that dominate the EDFS at this drive power in Li_2(DPP-Pent)$_2$. There is a small radical impurity observed in the EDFS centered at 345.2 mT.

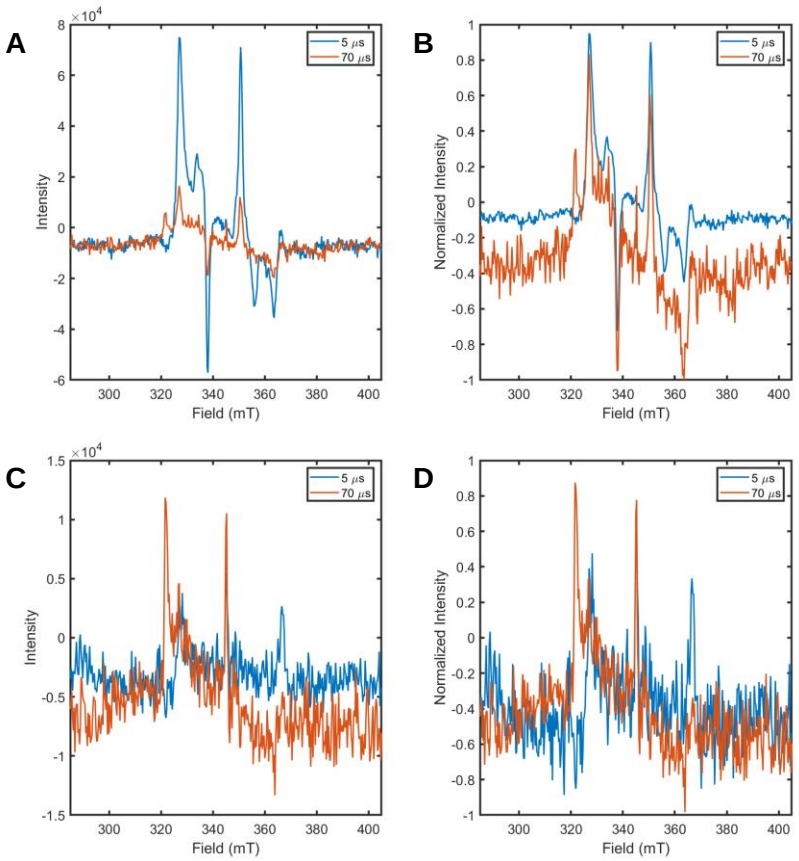

Figure 5.7 EDFS of HDPP-Pent at 17 dB microwave power attenuation (quintet-selective) collected at 5 and 70 μs at absolute (**A**) and normalized (**B**) intensity. EDFS at 12 dB microwave power attenuation (triplet-selective) collected at 5 and 70 μs at absolute (**C**) and normalized (**D**) intensity.

The quintet features from the EDFS of HDPP-Pent could be simulated with our spin Hamiltonian. The spectrum was reasonably simulated using a g value of 2.0023, D value of 1050 MHz, E value of 10 MHz, and J value of 20 GHz. The simulations are overlaid on the data in Figure 5.8 with accompanying levelsplots at perpendicular (only x-direction shown) and parallel (z) orientations.

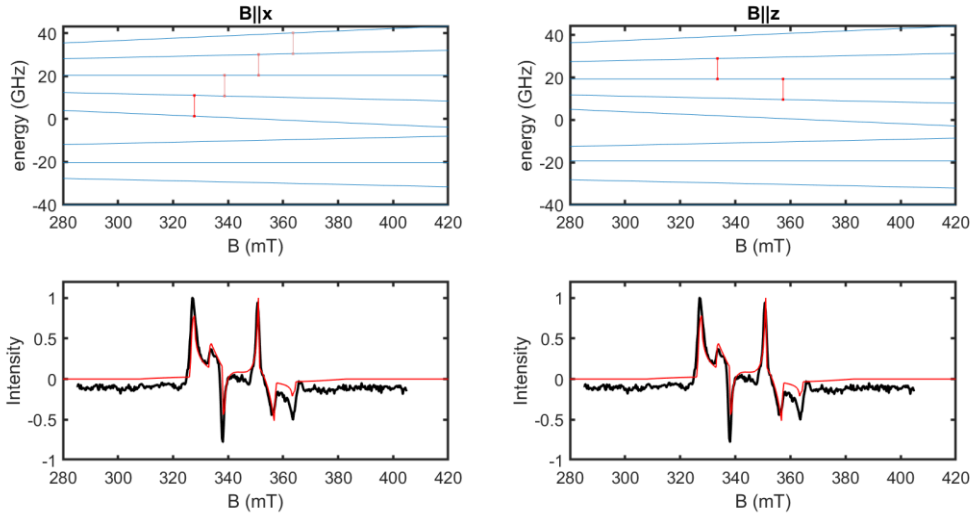

Figure 5.8 Simulated ^{5}(TT) TREPR spectrum (red lines in lower plots) overlaid on the EDFS spectrum of HDPP-Pent collected at 5 μs DAF and at 20 K, 9.68 GHz microwave frequency. The levelsplot at each perpendicular (x) and parallel (z) orientations are shown above.

The kinetic traces acquired on the quintet spectrum are shown in Figure 5.9. Following the kinetics at 338.0 and 350.8 mT, which correspond to ~M_s = -1 ↔0 and ~M_s = 0 ↔ +1 transitions, respectively, we can fit the evolution of these features to a biexponential. At 338.0 mT, we obtain time constants of τ_1 = 7.28 μs and τ_2 = 32.5 μs corresponding to rise and decay of the signal, respectively. At 350.8 mT, we obtain time constants of τ_1 = 5.15 μs and τ_2 = 37.1 μs corresponding to rise and decay of the signal, respectively. These fits are overlaid on the kinetic traces in Figure 5.9C.

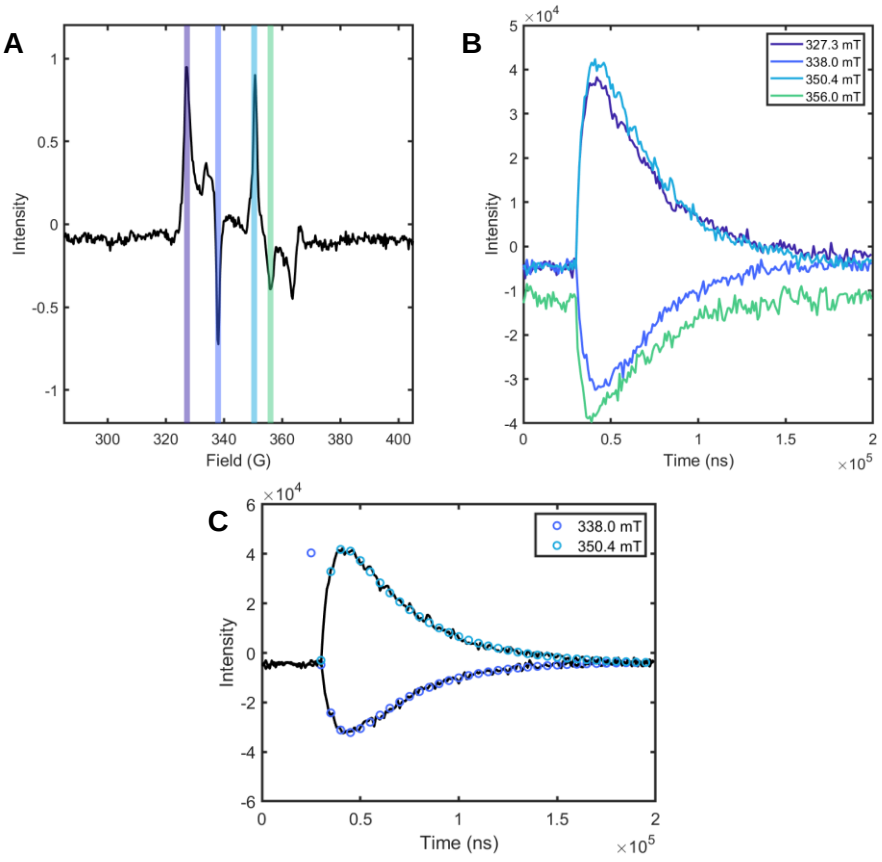

Figure 5.9 (**A**) Quintet spectrum at 5 μs of HDPP-Pent with field positions 338.0 mT and 350.8 mT highlighted. (**B**) The kinetic traces of the amplitude observed at 338.0 and 350.8 mT in purple and light blue, respectively, where the time axis represents the DAF time. (**C**) The time traces overlaid with the results of a biexponential fit.

Rabi nutation experiments were carried out at 5 μs DAF at field positions 350.4, 327.3, and 345.2 mT, which correspond to quintet ~$M_s = 0 \leftrightarrow +1$ transitions at perpendicular orientations, quintet ~$M_s = -2 \leftrightarrow -1$ transitions at perpendicular orientations, and radical impurity $M_s = -1/2 \leftrightarrow +1/2$ transitions. The data is summarized in Figure 5.10. The ratio of the nutation frequencies are

$\frac{\Omega_{Q(0\leftrightarrow+1)}}{\Omega_{Q(-2\leftrightarrow-1)}} = 1.21$ and $\frac{\Omega_{Q(0\leftrightarrow+1)}}{\Omega_{D(-1/2\leftrightarrow+1/2)}} = 2.56$, which is consistent with the expected values of $\sqrt{\frac{3}{2}} \approx 1.22$ and $\sqrt{6} \approx 2.45$.

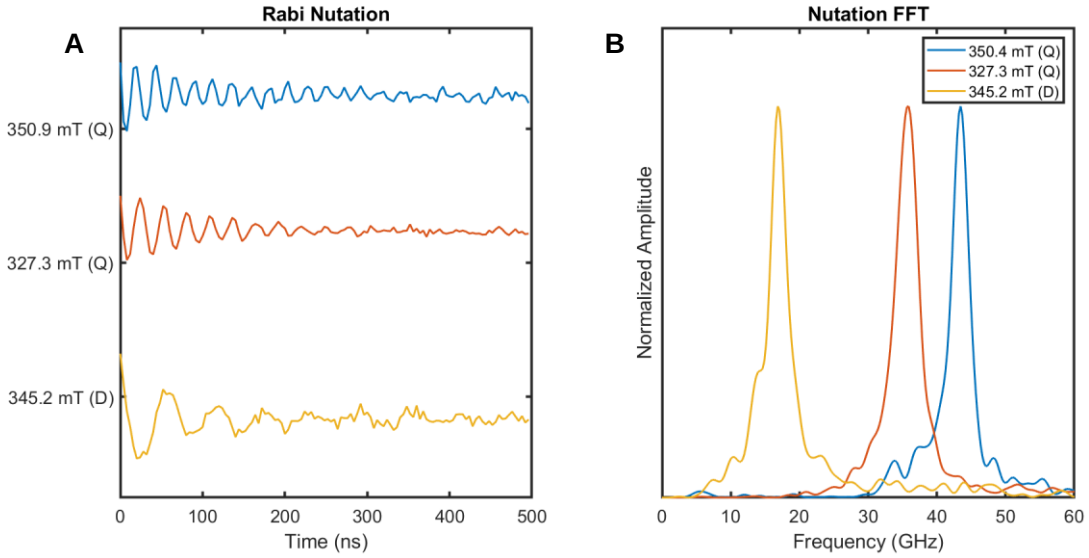

Figure 5.10 Rabi nutation experiments collected on the HDPP-Pent sample at 14 dB microwave attenuation at 20 K observed at 350.8 mT (Quintet ~$M_s = 0 \leftrightarrow +1$, perpendicular, 5 μs DAF), 327.3 mT (Quintet ~$M_s = -2 \leftrightarrow -1$, perpendicular, 5 μs DAF), and 354.2 mT (Doublet impurity ~ $M_s = -1/2 \leftrightarrow +1/2$, 5 μs DAF).

KDPP-Pent

TREPR was collected on 2 mM glassed solutions of KDPP-Pent. The EDFS collected at 20 dB are shown in Figures 5.11A and 5.11B from 5 to 100 μs. The contribution of the triplet features is substantial at this power attenuation. The triplet optimized EDFS collected at 14 dB are shown in shown in Figures 5.11C and 5.11D. The triplet spectrum, even at early times, demonstrates the opposite polarization pattern than that observed for Li_2(DPP-Pent)$_2$ at early times

and is rather similar to the long-time triplet spectra observed for Li_2(DPP-Pent)$_2$. The polarization pattern is similar to that observed for intersystem crossing-populated triplets.

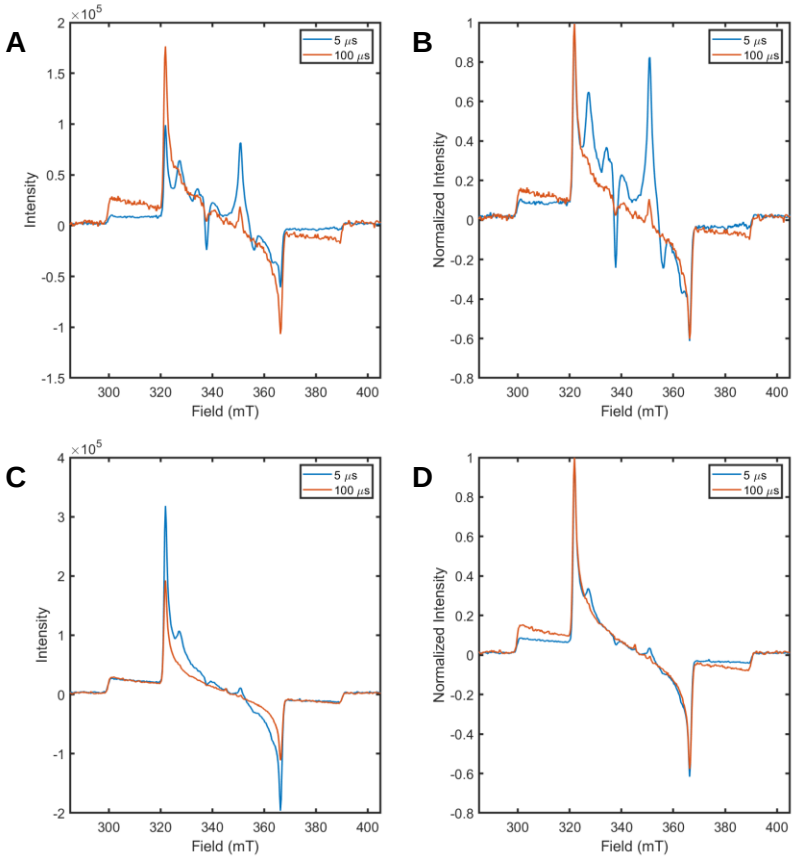

Figure 5.11 EDFS of KDPP-Pent at 20 dB microwave power attenuation (quintet-selective) collected at 5 and 100 μs at absolute (**A**) and normalized (**B**) intensity. EDFS at 14 dB microwave power attenuation (triplet-selective) collected at 5 and 100 μs at absolute (**C**) and normalized (**D**) intensity.

The quintet features from the EDFS of KDPP-Pent could be reasonably simulated using a g value of 2.0023, D value of 1050 MHz, E value of 10 MHz, and J value of 20 GHz. The simulations are overlaid on the data in Figure 5.12 with accompanying levelsplots at perpendicular (only x-direction shown) and parallel (z) orientations.

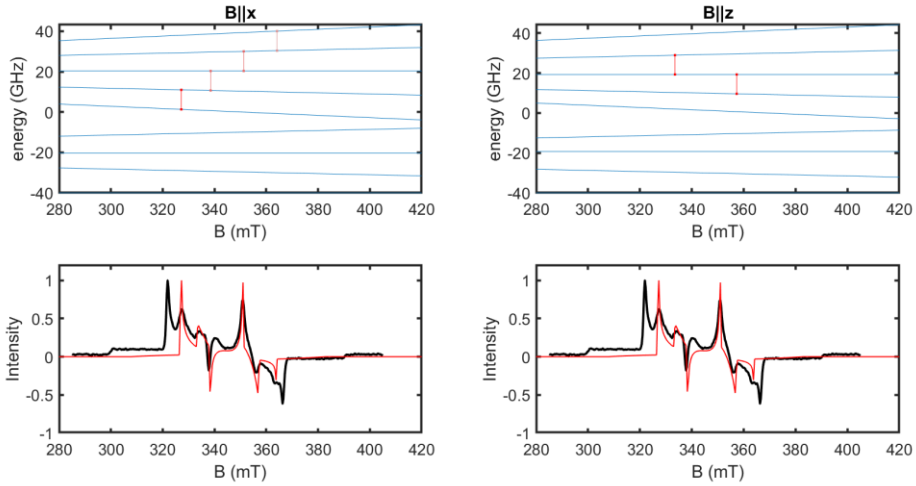

Figure 5.12 Simulated ^{5}(TT) TREPR spectrum (red lines in lower plots) overlaid on the EDFS spectrum of KDPP-Pent collected at 5 μs DAF and at 20 K, 9.68 GHz microwave frequency. The levelsplot at each perpendicular (x) and parallel (z) orientations re shown above.

The kinetic traces acquired at 327.3, 337.8, 350.9, and 356.0 mT are shown in Figure 5.13B. We fit the traces at 337.8 and 350.9 mT to a biexponential function. At 337.8 mT, we obtain time constants of τ_1 = 9.82 μs and τ_2 = 26.3 μs corresponding to rise and decay of the signal, respectively. At 350.9 mT, we obtain time constants of τ_1 = 3.93 μs and τ_2 = 31.0 μs corresponding to rise and decay of the signal, respectively. These fits are overlaid on the kinetic traces in Figure 5.13C.

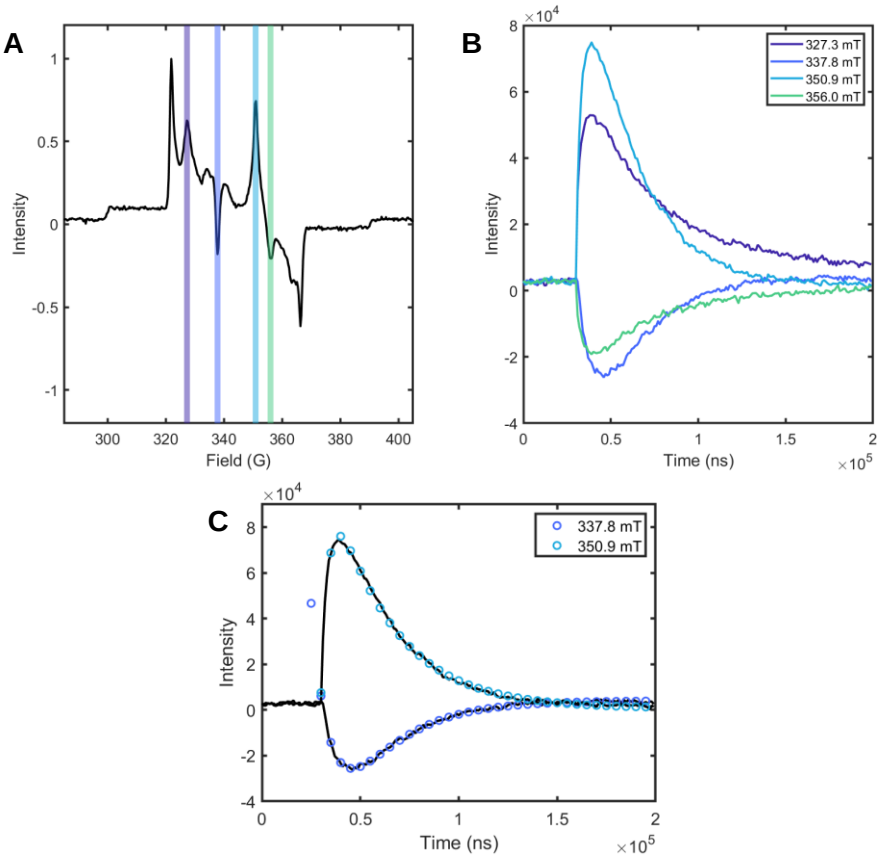

Figure 5.13 (**A**) Quintet spectrum at 5 μs of KDPP-Pent with field positions 337.8 mT and 350.9 mT highlighted. (**B**) The kinetic traces of the amplitude observed at 337.8 and 350.9 mT in purple and light blue, respectively, where the time axis represents the DAF time. (**C**) The time traces overlaid with the results of a biexponential fit.

The kinetic traces of the triplet optimized TREPR spectrum of KDPP-Pent at 321.9 and 366.0 mT, corresponding to the perpendicular extrema of the -1 ↔ 0 and 0 ↔ +1 transitions respectively, are shown in Figure 5.14. Notably, the triplet features appear within the instrument response time. This is unlike $Li_2(DPP\text{-}Pent)_2$ where they grow in roughly on the same timescale as the quintet features (several microseconds).

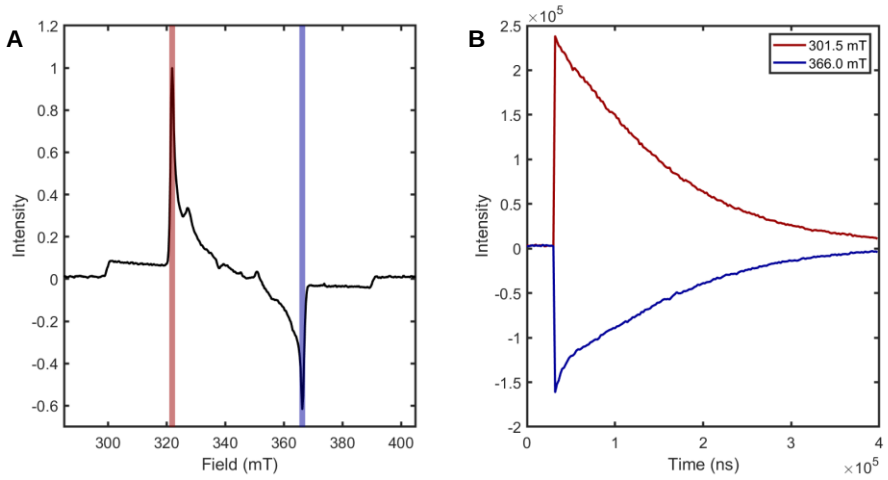

Figure 5.14 (**A**) The triplet optimized TREPR spectrum of KDPP-Pent at 5 μs DAF, 14 dB attenuation with 321.9 and 366.0 mT highlighted in red and blue, respectively. (**B**) The kinetic traces collected at 321.9 and 366.0 mT.

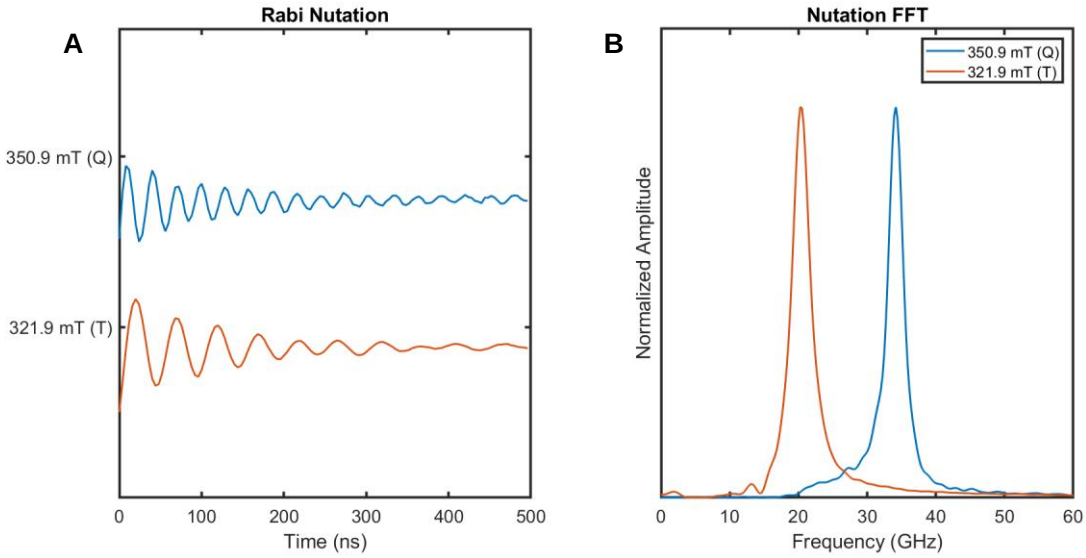

Figure 5.15 Rabi nutation experiments collected on the KDPP-Pent sample at 14 dB microwave attenuation at 20 K observed at 350.8 mT (Quintet ~$M_s = 0 \leftrightarrow +1$, perpendicular, 5 μs DAF) and 321.9 mT (Triplet ~$M_s = -1 \leftrightarrow 0$, perpendicular, 5 μs DAF).

Rabi nutation experiments were carried out at 350.9 mT (quintet, ~M_s = 0 ↔ +1, perpendicular) and 321.9 mT (triplet, ~M_s = -1 ↔ 0) and are shown in Figure 5.15. The nutation frequencies obtained from fast Fourier transform were 34.4 GHz (350.9 mT) and 20.5 GHz (321.9 mT). The ratio of these two gives $\frac{\Omega_{Q(0\leftrightarrow+1)}}{\Omega_{T(-1\leftrightarrow0)}} = 1.68$ which is consistent with the expected ratio of $\sqrt{3} \approx 1.73$ and corroborates our assignment of these features.

Discussion and Summary

In summary, we have examined the TREPR data for Li_2(DPP-Pent)$_2$, HDPP-Pent, and KDPP-Pent. Discussion in the literature has suggested that the quintet states may play a role in the dephasing of the triplet pair state, giving rise to free triplets. Alternatively, they may help ultimately populate overall S = 1 pair states that can undergo triplet-triplet annihilation to provide a sole triplet state. Li_2(DPP-Pent)$_2$ exhibits a dataset most in line with expectations from other TREPR studies on singlet fission systems wherein the quintet and triplet features rise within the microsecond timescale. HDPP-Pent, however, features no substantial signal arising from free triplets in the timescales observed here. KDPP-Pent as well strays from the pack by exhibiting strong triplet features that rise within the instrument response, preceding the rise of the quintet features. KDPP-Pent also exhibits a polarization pattern that is most consistent with a triplet populated by intersystem crossing, or the polarization pattern observed in the triplet spectra at long DAFs in Li_2(DPP-Pent)$_2$. The investigation into the origin of these differences between the DPP-Pent series is ongoing.

Citations

(1) Smith, M. B.; Michl, J. Singlet Fission. *Chem. Rev.* **2010**, *110* (11), 6891–6936. https://doi.org/10.1021/cr1002613.

(2) Merrifield, R. E. Magnetic Effects on Triplet Exciton Interactions. *Pure and Applied Chemistry* **1971**, *27* (3), 481–498. https://doi.org/10.1351/pac197127030481.
(3) Benk, H.; Sixl, H. Theory of Two Coupled Triplet States. *Molecular Physics* **1981**, *42* (4), 779–801. https://doi.org/10.1080/00268978100100631.
(4) Piland, G. B.; Burdett, J. J.; Dillon, R. J.; Bardeen, C. J. Singlet Fission: From Coherences to Kinetics. *J. Phys. Chem. Lett.* **2014**, *5* (13), 2312–2319. https://doi.org/10.1021/jz500676c.
(5) Weiss, L. R.; Bayliss, S. L.; Kraffert, F.; Thorley, K. J.; Anthony, J. E.; Bittl, R.; Friend, R. H.; Rao, A.; Greenham, N. C.; Behrends, J. Strongly Exchange-Coupled Triplet Pairs in an Organic Semiconductor. *Nature Phys* **2017**, *13* (2), 176–181. https://doi.org/10.1038/nphys3908.
(6) Tayebjee, M. J. Y.; Sanders, S. N.; Kumarasamy, E.; Campos, L. M.; Sfeir, M. Y.; McCamey, D. R. Quintet Multiexciton Dynamics in Singlet Fission. *Nature Phys* **2017**, *13* (2), 182–188. https://doi.org/10.1038/nphys3909.
(7) Basel, B. S.; Zirzlmeier, J.; Hetzer, C.; Reddy, S. R.; Phelan, B. T.; Krzyaniak, M. D.; Volland, M. K.; Coto, P. B.; Young, R. M.; Clark, T.; Thoss, M.; Tykwinski, R. R.; Wasielewski, M. R.; Guldi, D. M. Evidence for Charge-Transfer Mediation in the Primary Events of Singlet Fission in a Weakly Coupled Pentacene Dimer. *Chem* **2018**, *4* (5), 1092–1111. https://doi.org/10.1016/j.chempr.2018.04.006.
(8) Lubert-Perquel, D.; Salvadori, E.; Dyson, M.; Stavrinou, P. N.; Montis, R.; Nagashima, H.; Kobori, Y.; Heutz, S.; Kay, C. W. M. Identifying Triplet Pathways in Dilute Pentacene Films. *Nat Commun* **2018**, *9* (1), 4222. https://doi.org/10.1038/s41467-018-06330-x.
(9) Bayliss, S. L.; Weiss, L. R.; Kraffert, F.; Granger, D. B.; Anthony, J. E.; Behrends, J.; Bittl, R. Probing the Wave Function and Dynamics of the Quintet Multiexciton State with Coherent Control in a Singlet Fission Material. *Phys. Rev. X* **2020**, *10* (2), 021070. https://doi.org/10.1103/PhysRevX.10.021070.
(10) Chen, M.; Krzyaniak, M. D.; Nelson, J. N.; Bae, Y. J.; Harvey, S. M.; Schaller, R. D.; Young, R. M.; Wasielewski, M. R. Quintet-Triplet Mixing Determines the Fate of the Multiexciton State Produced by Singlet Fission in a Terrylenediimide Dimer at Room Temperature. *Proceedings of the National Academy of Sciences* **2019**, *116* (17), 8178–8183. https://doi.org/10.1073/pnas.1820932116.
(11) Bayliss, S. L.; Weiss, L. R.; Mitioglu, A.; Galkowski, K.; Yang, Z.; Yunusova, K.; Surrente, A.; Thorley, K. J.; Behrends, J.; Bittl, R.; Anthony, J. E.; Rao, A.; Friend, R. H.; Plochocka, P.; Christianen, P. C. M.; Greenham, N. C.; Chepelianskii, A. D. Site-Selective Measurement of Coupled Spin Pairs in an Organic Semiconductor. *Proceedings of the National Academy of Sciences* **2018**, *115* (20), 5077–5082. https://doi.org/10.1073/pnas.1718868115.
(12) Nagashima, H.; Kawaoka, S.; Akimoto, S.; Tachikawa, T.; Matsui, Y.; Ikeda, H.; Kobori, Y. Singlet-Fission-Born Quintet State: Sublevel Selections and Trapping by Multiexciton Thermodynamics. *J. Phys. Chem. Lett.* **2018**, *9* (19), 5855–5861. https://doi.org/10.1021/acs.jpclett.8b02396.
(13) Basel, B. S.; Zirzlmeier, J.; Hetzer, C.; Phelan, B. T.; Krzyaniak, M. D.; Reddy, S. R.; Coto, P. B.; Horwitz, N. E.; Young, R. M.; White, F. J.; Hampel, F.; Clark, T.; Thoss, M.; Tykwinski, R. R.; Wasielewski, M. R.; Guldi, D. M. Unified Model for Singlet Fission within a Non-Conjugated Covalent Pentacene Dimer. *Nat Commun* **2017**, *8* (1), 15171. https://doi.org/10.1038/ncomms15171.

(14) Smyser, K. E.; Eaves, J. D. Singlet Fission for Quantum Information and Quantum Computing: The Parallel JDE Model. *Sci Rep* **2020**, *10* (1), 18480. https://doi.org/10.1038/s41598-020-75459-x.
(15) Lewis, S. G.; Smyser, K. E.; Eaves, J. D. Clock Transitions Guard against Spin Decoherence in Singlet Fission. *J. Chem. Phys.* **2021**, *155* (19), 194109. https://doi.org/10.1063/5.0069344.
(16) Stoll, S.; Jeschke, G.; Willer, M.; Schweiger, A. Nutation-Frequency Correlated EPR Spectroscopy: The PEANUT Experiment. *Journal of Magnetic Resonance* **1998**, *130* (1), 86–96. https://doi.org/10.1006/jmre.1997.1285.
(17) Collins, M. I.; McCamey, D. R.; Tayebjee, M. J. Y. Fluctuating Exchange Interactions Enable Quintet Multiexciton Formation in Singlet Fission. *J. Chem. Phys.* **2019**, *151* (16), 164104. https://doi.org/10.1063/1.5115816.
(18) Bencini, A.; Gatteschi, D. *EPR of Exchange Coupled Systems*; Courier Corporation, 2012.
(19) Weil, J. A.; Bolton, J. R. Basic Principles of Paramagnetic Resonance. In *Electron Paramagnetic Resonance*; John Wiley & Sons, Ltd, 2006; pp 1–35. https://doi.org/10.1002/9780470084984.ch1.
(20) McWeeny, R. *Spins in Chemistry*; Dover Publications, 2004.
(21) Yunusova, K. M.; Bayliss, S. L.; Chanelière, T.; Derkach, V.; Anthony, J. E.; Chepelianskii, A. D.; Weiss, L. R. Spin Fine Structure Reveals Biexciton Geometry in an Organic Semiconductor. *Phys. Rev. Lett.* **2020**, *125* (9), 097402. https://doi.org/10.1103/PhysRevLett.125.097402.
(22) Stoll, S.; Schweiger, A. EasySpin, a Comprehensive Software Package for Spectral Simulation and Analysis in EPR. *Journal of Magnetic Resonance* **2006**, *178* (1), 42–55. https://doi.org/10.1016/j.jmr.2005.08.013.

Chapter VI

Ultrafast Transient Absorption Spectroscopy on Ni 2,2'-bipyridine Aryl Halide Complexes

Introduction

In recent decades, photoredox catalysis involving first-row transition metals has proliferated. Of particular interest is photoredox involving nickel catalysts, which has been demonstrated to provide access to C-C and C-heteroatom bond forming methodologies toward high-value synthetic products.[1–9] In some cases, these photoredox systems can perform couplings that are otherwise challenging for thermally driven Ni catalysis. Although some of these methodologies employ exogeneous photocatalysts such as Ir photosensitizers, recent reports have found that photoredox catalysis can be promoted using only Ni catalyst. As such, Ni complex excited states may play a significant role in the mechanisms of these photoredox cycles. This highlights the importance of understanding the relevant excited states and photodynamics of these Ni complexes.

Many of the relevant Ni catalysts that have been studied utilize 2,2'-bipyridine (bpy) and other bidentate diimine-type ligands. Recent work by the Doyle, Scholes, and Castellano groups have examined the transient absorption (TA) spectroscopy of various Ni(bpy)ArX complexes in which the bpy may be functionalized at the 4 and 4' positions.[10–12] The aryl group Ar may similarly be varied with substituents, but it is common to utilize kinetically stabilized variants that are functionalized in the *ortho*-position relative to the Ni-Ar bond. Finally, the X ligand can be varied between halides such as Cl and Br and O-atom ligating groups such as acetate (OAc). It was proposed that the initially excited ^{1}MLCT state quickly undergoes intersystem crossing within 5 – 10 ps followed by relaxation into a triplet ligand field [^{3}(d-d)] state. It was further proposed that Ni-C bond homolysis occurs from the transiently generated ^{3}(d-d) state as a part of the mechanistic cycle for these photocatalytic systems.

Recent reports have suggested from multireference *ab initio* calculations that the thermal barrier for bond homolysis is large (~70 kcal) from the ^{3}(d-d) minimum energy point and proposed that higher lying repulsive potential energy surfaces may be involved in the bond homolysis.[13,14] A series of the Ni(bpy)ArX complexes were synthesized and studied with respect to their wavelength-dependent photodecomposition. We continue the characterization of some of these compounds here by fsTA to compare the relative rates of the photodynamic processes observed. We compare as well to the previous literature regarding the photophysics of these complexes and speak to some differences in the fittings we have obtained.

Results

Ni(tBu-bpy)(o-tolyl)Cl

We will begin with the discussion of the femtosecond transient absorption spectra of Ni(tBu-bpy)(*o*-tolyl)Cl (**1B**) and compare it to the previously reported spectra and fitted time constants. Selected time traces are shown in Figure 6.1.

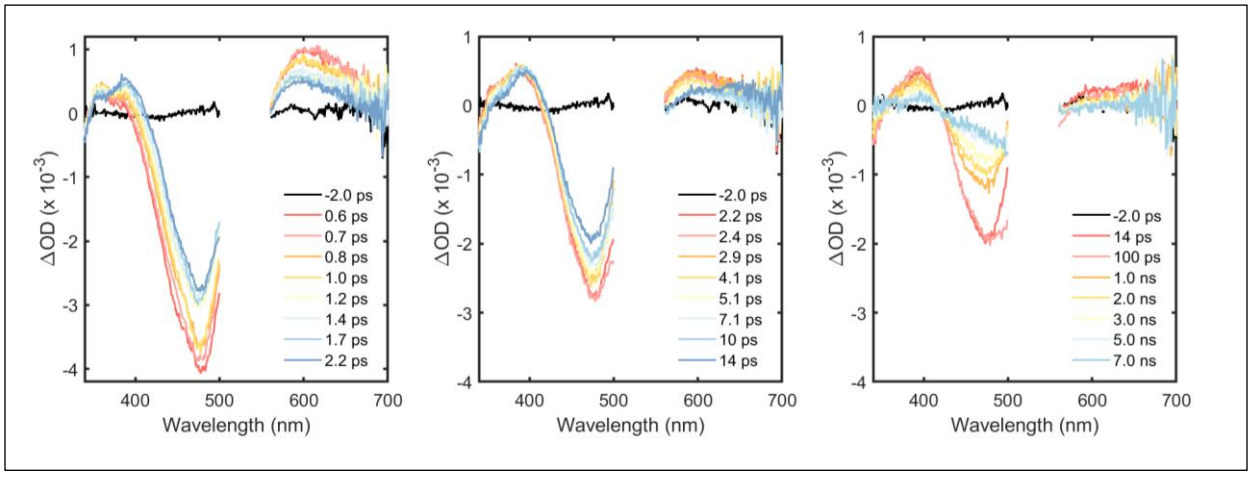

Figure 6.1 Transient absorption time traces of Ni(tBu-bpy)(*o*-tolyl)Cl across various time scales (left) 0.6 – 2.2 ps, (center) 2.2 – 14 ps, (right) 14 ps – 7 ns.

The initial transient features observed in the difference spectra of Ni(tBu-bpy)(*o*-tolyl)Cl after excitation with 530 nm light include a large bleach signal (GSB) centered around 480 nm near the maximum of the steady-state visible absorption spectrum flanked by excited state absorption (ESA) features in the 350 – 400 nm and 580 – 700 nm regions. Over the first 2.2 ps, the GSB feature decreases in intensity while the ESA features exhibit a time-dependent spectral shift. The 580 – 700 nm ESA decreases and blue shifts over the wavelength range, whereas the 350 – 400 nm ESA feature maximum around 360 nm decreases in intensity while the difference absorption (ΔA or ΔOD) increases at longer wavelengths around 380 nm, a red shift in ΔA maximum. In the time from 2.2 – 14 ps, the spectral shapes change little and we observe a monotonic decrease in the ΔA signals. By 14 ps, the 580 – 700 nm ESA signal has largely been reduced to zero. The transient spectrum continues to decay back to zero from 14 ps out to 7 ns.

The fsTA data matrix can be fit using global and target kinetic analysis. We fit the data using a four-component sequential model including a coherent artifact (CA) that persists around time zero. The evolution associated difference spectra (EADS) and weighted amplitudes of the fitted spectra are shown in Figure 6.2.

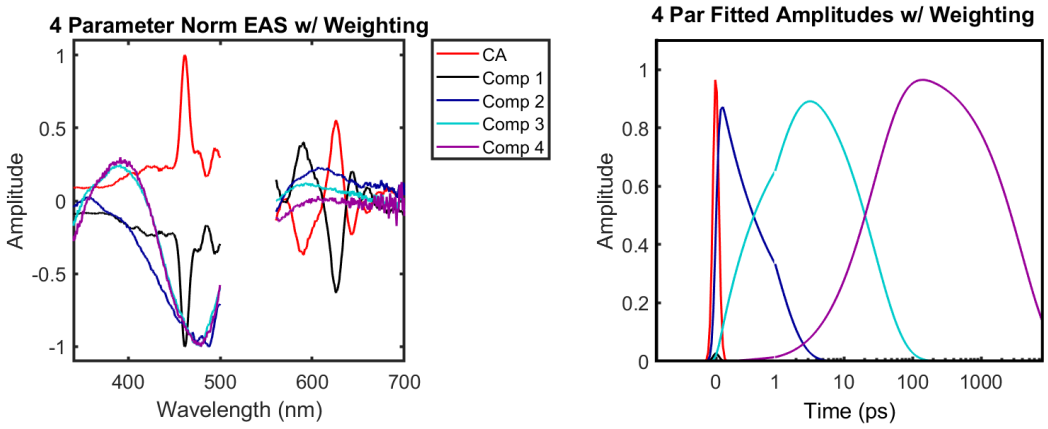

Figure 6.2 The EADS from fitting the Ni(tBu-bpy)(*o*-tolyl)Cl fsTA data matrix with a four-component sequential model (left) and the associated amplitude vectors (right).

As can be observed in the results of the fit, the first fitted component (Comp 1) has very little intensity and only persists around time zero. Additionally, the EADS of Comp 1 largely reflect the features in the fitted CA, which contains contributions from both oscillatory cross-phase modulation (XPM) as well as multiphoton coherent artifacts (large positive feature around 460 nm in CA, the position of this artifact is dependent on λ_{ex}). As such, this component does not realistically represent signal from the sample. However, attempts to fit with a three-component model generally led to bleed over of these coherent artifact features into the first component. The four-component model gave the best separation of these artifacts and the signal arising from the sample.

Components 2, 3, and 4 (Comp 2, Comp 3, Comp 4) reflect well the differences we observed across the various time scales of the data. For example, all three components share a negative feature around 480 nm consistent with the GSB observed in the time cuts. Comp 2 exhibits the ESA features on either side of the bleach, the higher energy ESA in Comp 2 has a

maximum near 360 nm, and the lower energy ESA a maximum near 620 nm. Comp 3, on the other hand, exhibits the higher energy ESA as having a maximum around 380 nm and the lower energy ESA having a maximum around 580 nm. This is consistent with the red and blue shifts observed in the higher energy and lower energy ESA features of the dataset over the first tens of picoseconds. Finally, Comp 4 is very similar to Comp 3 except with negligible ESA intensity in the 580 – 700 nm range, which is also consistent with what we observed in the 14 ps – 7 ns range. We plot the overlay of various time traces with the fits in Figure 6.3 as a means of assessing the quality of the fit. As observed, the fit is reasonably good across the time scales observed with some minor differences in intensity at early times.

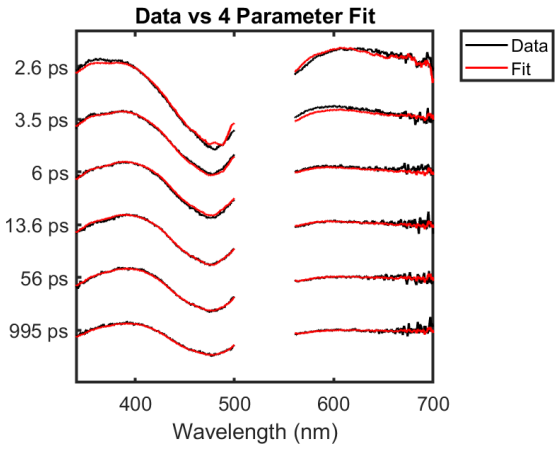

Figure 6.3 An overlay of the time cuts from the Ni(tBu-bpy)(*o*-tolyl)Cl fsTA dataset with time cuts of the fitted data matrix at 2.6, 3.5, 6, 13.6, 56, and 995 ps.

Finally, we compare the fitted rates and time constants with that reported by Doyle et al. In that report, the authors use a three-component sequential model to fit the data. As mentioned, the first component of our four-component model does not reflect signal arising from the sample,

so we compare time constants associated with Comps 2, 3, and 4 with the time constants of the previous report τ_1, τ_2, and τ_3. The results are listed in Table 6.1.

Table 6.1. Comparison of the rate and time constants obtained by fitting the Ni(tBu-bpy)(*o*-tolyl)Cl fsTA data with the previous report by Doyle et al.

	Our Experiment	Doyle et al. 2020		Our Experiment	Doyle et al. 2020
$k_1 (ps^{-1})$	1.1	1.5	τ_1 (ps)	0.91	0.66
$k_2 (ps^{-1})$	0.036	0.145	τ_2 (ps)	28.0	6.89
$k_3 (ps^{-1})$	0.000257	0.00025	τ_3 (ps)	3900	4000

Our results compare favorably to the previous report. The first fitted time constant is around 1 ps in both cases (our experiment: 0.91 ps, Doyle et al. 2020: 0.66 ps). The second time constant displays the largest difference (our experiment: 28.0 ps, Doyle et al 2020: 6.89 ps). Finally, the third time constant is very similar (our experiment: 3900 ps, Doyle et al. 2020: 4000 ps). The second time constant seems to be closely associated with the loss of the low energy ESA feature in the spectrum. It is possible that better signal-to-noise in this region for our data (either by averaging or changing to a different probe beam) may improve the agreement between our data modeling and the reported values.

*Ni(COOCH$_3$-bpy)(*o*-tolyl)Cl*

The next compound we will discuss is Ni(COOCH$_3$-bpy)(*o*-tolyl)Cl. Here, the bipyridine is substituted by methyl ester in the 4 and 4' positions, which is more electron withdrawing relative to the *tert*-butyl substituents in the previous example. In the case of Ni(COOCH$_3$-bpy)(*o*-tolyl)Cl,

we chose to run successive experiments with increasing excitation energy as high energy excitation of the samples by LED lamps in prior photolysis studies exhibit greater product formation than low energy excitation. The steady-state absorption spectrum of Ni(COOCH$_3$-bpy)(*o*-tolyl)Cl along with a guide of the various excitation wavelengths is shown in Figure 6.4. In this trial, we ran the successive excitation wavelength experiments on the same sample, but further studies will probe the fsTA at each excitation wavelength on independent samples to remove any possible effects of prior photodegradation in the laser beam.

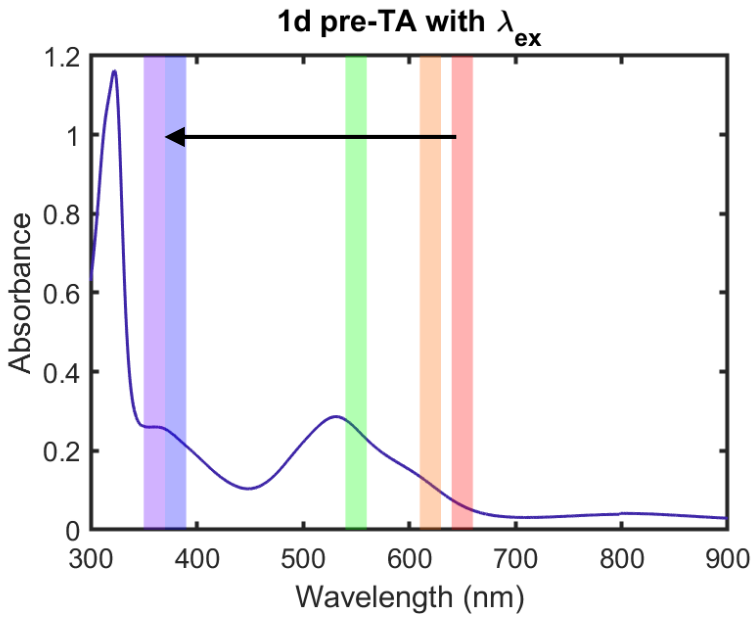

Figure 6.4 Steady-state absorption spectrum (pre-TA) of Ni(COOCH$_3$-bpy)(*o*-tolyl)Cl. The successive excitation wavelengths (λ_{ex}) examined are also denoted by color: 650, 620, 550, 380, 360 nm. Two runs were carried out at 650 nm, the first at 50 nJ/pulse and the second at 100 nJ/pulse. The rest of the experiments were carried out at 100 nJ/pulse save for the 380 nm experiment where the maximum power we were able to obtain at the sample was 80 nJ/pulse.

We will first show the fitting process and time cuts for the λ_{ex} = 650 nm dataset before comparing the results across the datasets collected. Initially we show the fsTA data at selected time cuts overlayed against a single component fit in Figure 6.5 along with the decay associated difference spectra (DADS) and associated fitted amplitudes.

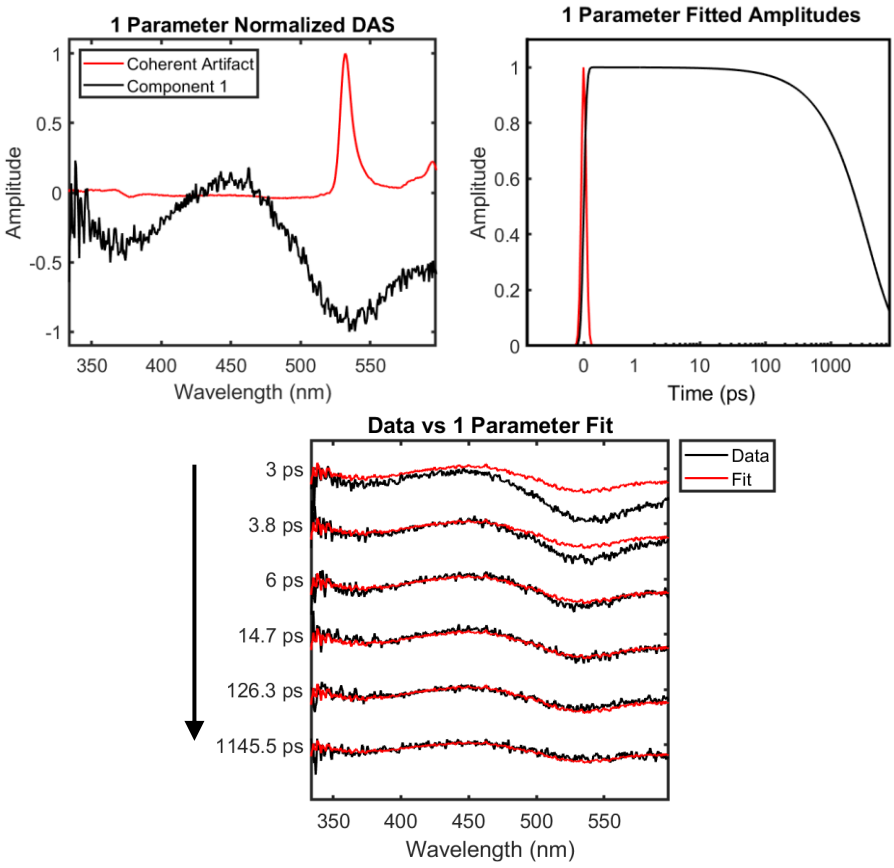

Figure 6.5 (Top left) The normalized DADS and (top right) associated amplitudes of the results from the one component global fitting of the data with a fitted coherent artifact. (Bottom) Overlay of the fsTA data with fitted data matrix time cuts at 3, 3.8, 6, 14.7, 126.3, and 1145.5 ps.

As seen in the time cuts of Figure 6.5, the major features of the fsTA spectra of Ni(COOCH$_3$-bpy)(*o*-tolyl)Cl include a negative GSB feature around 540 nm consistent with the

maximum of the MLCT transitions in the steady-state absorption spectrum. There is a slight positive feature around 450 nm observed as well and an additional bleach feature around 360 nm. The shape of the difference spectrum is consistent over the time scales observed. The single component global fit of the data yields a time constant for Component 1 of 3,750 ps. Although the DAS captures the spectrum at long times, as observed in the overlay, the single component model poorly fits the early time cuts of the dataset, particularly in the intensity of the GSB around 540 nm. This suggests that additional components are required to fit the data.

The results of a two-component sequential model fit are shown in Figure 6.6. Here, the data was weighted by a factor of 0.2 in the region from 2.3 to 2.7 ps and 520 to 585 nm, which covers the time and wavelength region of the sharp coherent artifact centered around 530 nm. Without this weighting factor, the first component DADS contained contribution from this coherent feature.

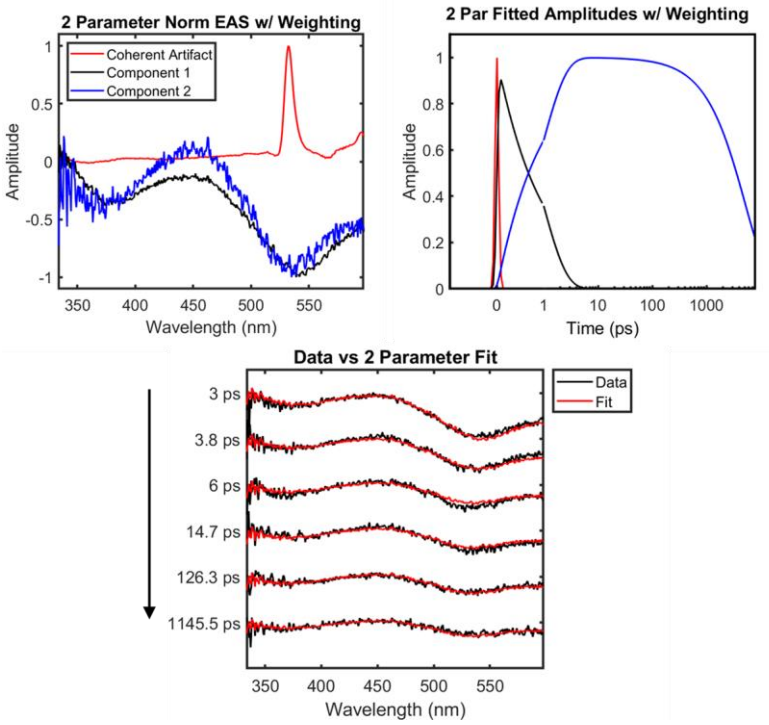

Figure 6.6 (Top left) The normalized EADS and (top right) associated amplitudes of the results from the fit of the data to a two-component sequential model with a fitted coherent artifact. (Bottom) Overlay of the fsTA data with fitted data matrix time cuts at 3, 3.8, 6, 14.7, 126.3, and 1145.5 ps.

As observed in the overlays, the two-component model provides a better fit of the data across all time scales. The time constants associated with components 1 and 2 are 0.972 and 5,130 ps, respectively. We repeated this fitting process for all of the datasets taken on the Ni($COOCH_3$-bpy)(*o*-tolyl)Cl sample. We summarize and compare the results in Table 6.2 and Figure 6.7.

Table 6.2. Comparison of the two-component sequential model fits of the various λ_{ex} experiments on Ni(COOCH$_3$-bpy)(*o*-tolyl)Cl.

	k_1 (ps^{-1})	k_1 error	k_2 (ps^{-1})	k_2 error	τ_1 (ps)	τ_2 (ps)
650 nm, 50 µW	0.75232	0.01434	0.000148093	0.000002584	1.32922	6752.51
650 nm, 100 µW	0.817024	0.009809	0.000219954	0.00000251	1.22395	4546.41
620 nm, 100 µW	1.02869	0.00621	0.000195029	0.000001227	0.972107	5127.44
550 nm, 100 µW	1.29303	0.00625	0.000187795	0.000001051	0.773375	5324.96
380 nm, 80 µW	1.01451	0.006165	0.000196895	8.041E-07	0.9857	5078.85
360 nm, 100 µW	0.311567	0.001667	0.000152447	7.499E-07	3.20959	6559.68
Average	0.869524		0.000183369		1.415657	5564.975
Std. Dev.	0.332722		2.78479E-05		0.900727	885.7216

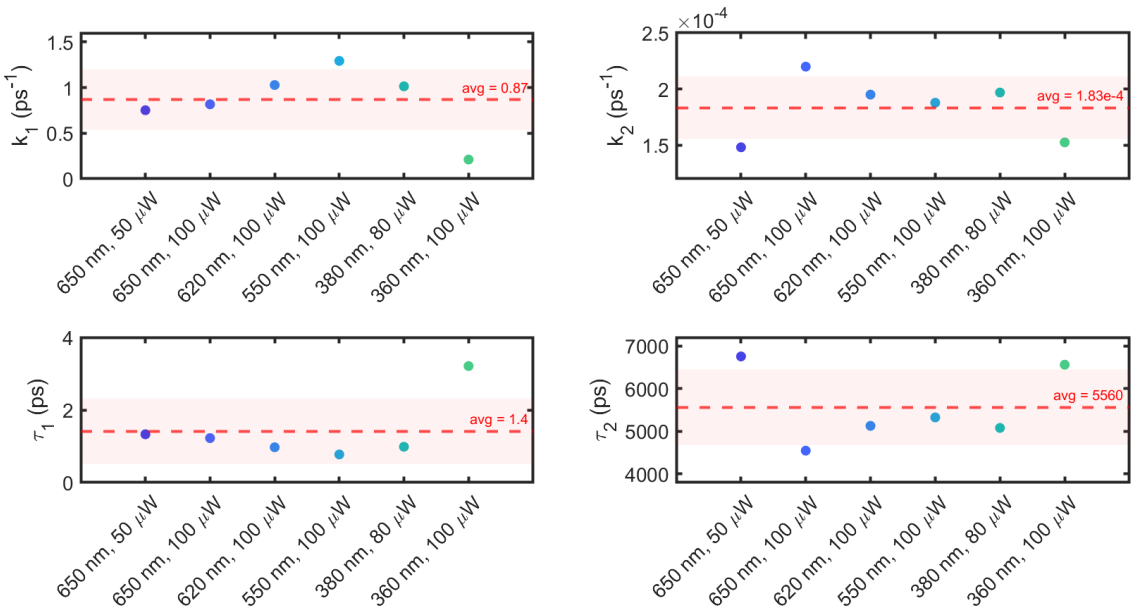

Figure 6.7 Comparison of the rate and time constants detailed in Table 7.2. The average and single standard deviation are denoted by the dashed red line and shaded red area respectively.

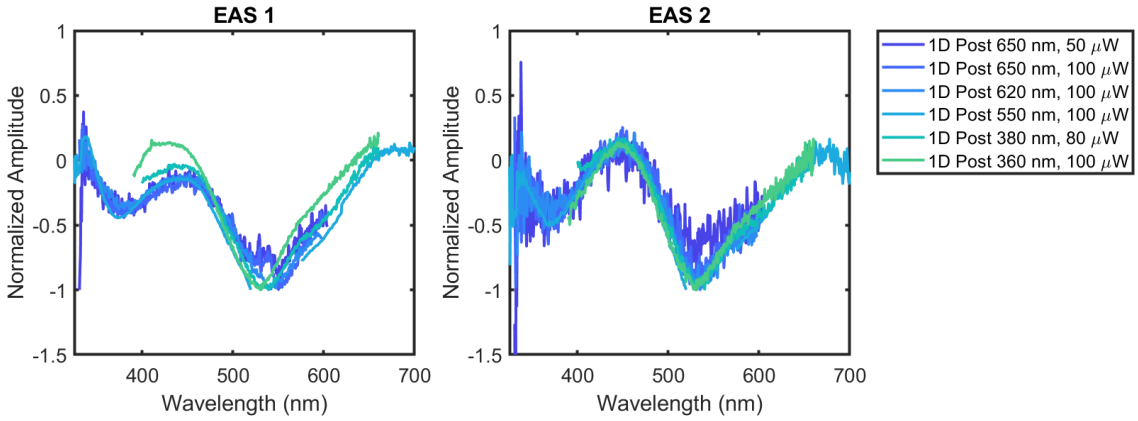

Figure 6.8 Overlay of the EADS 1 and 2 for each of the λ_{ex} experiments carried out on Ni(COOCH$_3$-bpy)(*o*-tolyl)Cl.

As can be seen in Table 6.2, Figure 6.7 and Figure 6.8, the fitted rate constants are consistent across the collected datasets. The main outlier is that collected at 360 nm. Nevertheless, the EADS are all consistent with each other. Attempts to fit the datasets to three-component models were unsuccessful. This contrasts with the Ni(tBu-bpy)(*o*-tolyl)Cl fsTA data, which required a three-component model. Assuming that the excited state relaxation processes are the same between the two Ni-bipyridine complexes, it is possible that the fastest relaxation process is too fast to observe in Ni($COOCH_3$-bpy)(*o*-tolyl)Cl given the time resolution of our instrument (~100 fs).

Power titrations were collected at λ_{ex} = 550 and 380 nm. At 550 nm, the powers investigated were 50, 100, 250, 500, and 800 μW (or nJ/pulse). The ΔA values collected at four wavelength positions across the spectrum around 2 ps time delay are plotted versus applied power in Figure 7.X. The trend in ΔA values with power confirms that our studies fall within the linear regime.

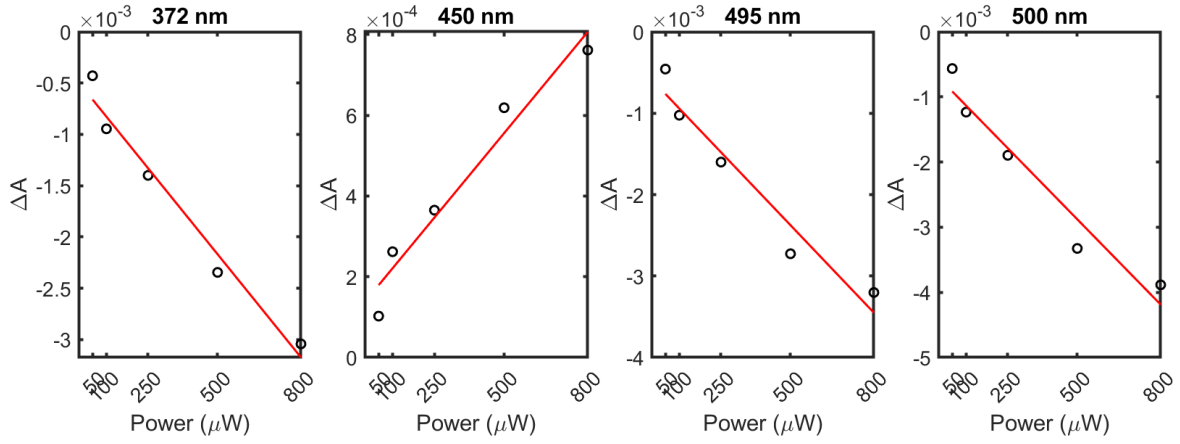

Figure 6.9 Power dependence of the Ni($COOCH_3$-bpy)(*o*-tolyl)Cl ΔA signal at 372, 450, 495, and 500 nm. The red line represents the linear fit of the data points.

To examine the time traces and general kinetics at each power, we overlay the normalized time traces observed at 450 nm in Figure 7.X and show that the kinetics do not diverge significantly with changing power.

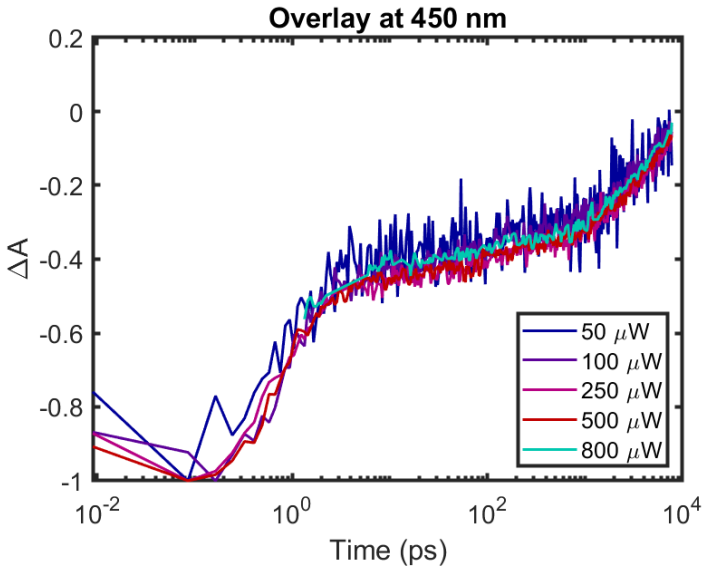

Figure 6.10 Overlay of the time traces observed at 450 nm collected for the Ni($COOCH_3$-bpy)(*o*-tolyl)Cl fsTA data at each power.

Ni(tBu-bpy)(mesityl)Br

We also examined the more sterically encumbered complex Ni(*t*Bu-bpy)(mesityl)Br. The fitting results and time cuts for a 3 parameter sequential model are shown in Figure 6.11. As with Ni(*t*Bu-bpy)(*o*-tolyl)Cl, the first time component only has small amplitude within the instrument response and contains mostly features associated with coherent artifacts around time zero. The inclusion of this additional component helped to separate these coherent artifact features from the other fitted components.

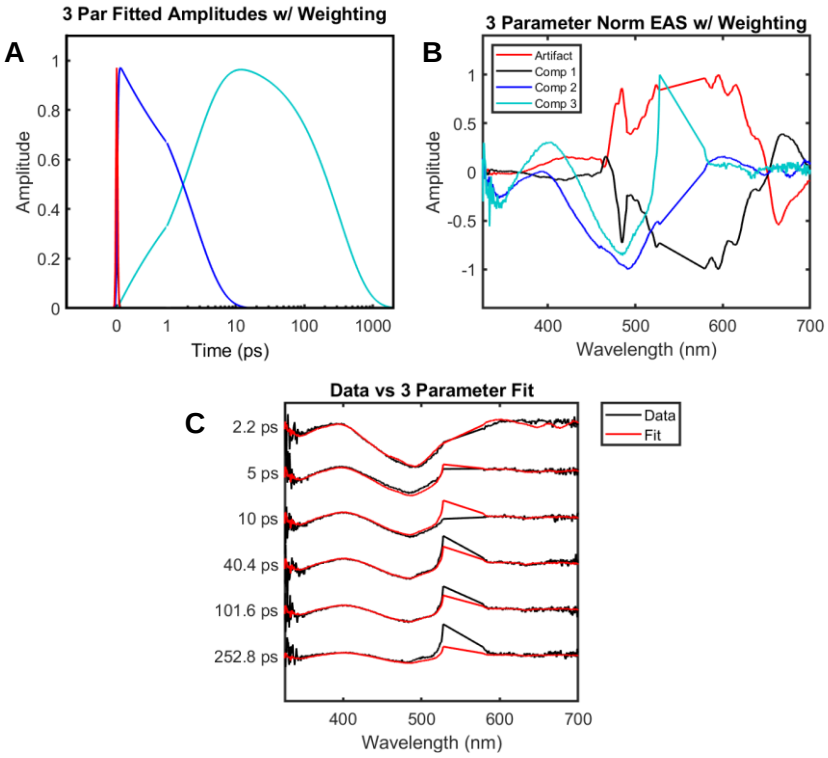

Figure 6.11 The results of a three-component sequential model fit to the Ni(*t*Bu-bpy)(mesityl)Br fsTA dataset. (**A**) The amplitudes of the fitted components along with a fitted coherent artifact (in red) (**B**) The normalized EADS of the fitted components along with a fitted coherent artifact (**C**) An overlay of the three-component model fit (in red) over spectral traces of the data (in black).

The results of the three-component fitting yield time constants τ_1 = 10.5 fs, τ_2 = 2.44 ps, and τ_3 = 323 ps. As mentioned, we take the first time component to be unrelated to the dynamics of the complex. The other two time components are reasonable given the dataset. We note that the low energy region of the spectrum is still not fit well at the earliest times (see 2.2 ps in Figure 6.11C). As previously discussed with respect to this region, further averaging or a different probe could improve the signal-to-noise in this region, which could help better fit it. This could be a result of oscillatory features in the cross phase modulation bleeding over into Comp 2 of the fit.

The first time component (2.44 ps) is consistent with the fast decay component observed in the fsTA datasets of the previous Ni complexes. The second time component (323 ps) is, however, significantly faster than those observed in the other complexes (typically the signal persists out to several nanoseconds). In the case of Ni(*t*Bu-bpy)(mesityl)Br, the transient signal is fully decayed by 2 ns.

Discussion and Summary

We have reported here the fsTA data for three Ni(bpy)ArX complexes: Ni(*t*Bu-bpy)(*o*-tolyl)Cl, Ni($COOCH_3$-bpy)(*o*-tolyl)Cl, and Ni(*t*Bu-bpy)(mesityl)Br. The general features observed in the difference spectra are similar with a prominent ground state bleach signal in the 450 – 550 nm region flanked by weaker excited state absorptions on the low and high energy sides. The datasets were fitted with target kinetic analyses, yielding rate constants comparable to those reported for related complexes. In general, there is a faster time component on the order of ~1 ps, a middle time component on the order of 5 – 10 ps, which have been difficult to accurately fit, and a longer lived time component that spans out to several nanoseconds.

Ni(*t*Bu-bpy)(mesityl)Br stands in contrast as the excited state population decays much more quickly back to the ground state and is fully returned by 2 ns. This could potentially arise from the mesityl group that may restrict conformational changes in the molecule. For example, we expect that relaxation into a metal-centered ^{3}(d-d) state would encourage a square planar to tetrahedral distortion in the ligand coordination geometry. The mesityl group may prohibit the rotation required to achieve this. Potential agostic interactions between the Ni and methyl C-H bonds may also stabilize the ^{3}(d-d) relative to the singlet ground state, promoting faster nonradiative decay.

Citations

(1) Twilton, J.; Le, C. (Chip); Zhang, P.; Shaw, M. H.; Evans, R. W.; MacMillan, D. W. C. The Merger of Transition Metal and Photocatalysis. *Nat Rev Chem* **2017**, *1* (7), 1–19. https://doi.org/10.1038/s41570-017-0052.

(2) Milligan, J. A.; Phelan, J. P.; Badir, S. O.; Molander, G. A. Alkyl Carbon–Carbon Bond Formation by Nickel/Photoredox Cross-Coupling. *Angewandte Chemie International Edition* **2019**, *58* (19), 6152–6163. https://doi.org/10.1002/anie.201809431.

(3) Narayanam, J. M. R.; Stephenson, C. R. J. Visible Light Photoredox Catalysis: Applications in Organic Synthesis. *Chem. Soc. Rev.* **2010**, *40* (1), 102–113. https://doi.org/10.1039/B913880N.

(4) Prier, C. K.; Rankic, D. A.; MacMillan, D. W. C. Visible Light Photoredox Catalysis with Transition Metal Complexes: Applications in Organic Synthesis. *Chem. Rev.* **2013**, *113* (7), 5322–5363. https://doi.org/10.1021/cr300503r.

(5) Koike, T.; Akita, M. Visible-Light Radical Reaction Designed by Ru- and Ir-Based Photoredox Catalysis. *Inorg. Chem. Front.* **2014**, *1* (8), 562–576. https://doi.org/10.1039/C4QI00053F.

(6) Shaw, M. H.; Twilton, J.; MacMillan, D. W. C. Photoredox Catalysis in Organic Chemistry. *J. Org. Chem.* **2016**, *81* (16), 6898–6926. https://doi.org/10.1021/acs.joc.6b01449.

(7) Heitz, D. R.; Tellis, J. C.; Molander, G. A. Photochemical Nickel-Catalyzed C–H Arylation: Synthetic Scope and Mechanistic Investigations. *J. Am. Chem. Soc.* **2016**, *138* (39), 12715–12718. https://doi.org/10.1021/jacs.6b04789.

(8) Welin, E. R.; Le, C.; Arias-Rotondo, D. M.; McCusker, J. K.; MacMillan, D. W. C. Photosensitized, Energy Transfer-Mediated Organometallic Catalysis through Electronically Excited Nickel(II). *Science* **2017**, *355* (6323), 380–385. https://doi.org/10.1126/science.aal2490.

(9) Kudisch, M.; Lim, C.-H.; Thordarson, P.; Miyake, G. M. Energy Transfer to Ni-Amine Complexes in Dual Catalytic, Light-Driven C–N Cross-Coupling Reactions. *J. Am. Chem. Soc.* **2019**, *141* (49), 19479–19486. https://doi.org/10.1021/jacs.9b11049.

(10) Shields, B. J.; Kudisch, B.; Scholes, G. D.; Doyle, A. G. Long-Lived Charge-Transfer States of Nickel(II) Aryl Halide Complexes Facilitate Bimolecular Photoinduced Electron Transfer. *J. Am. Chem. Soc.* **2018**, *140* (8), 3035–3039. https://doi.org/10.1021/jacs.7b13281.

(11) Ting, S. I.; Garakyaraghi, S.; Taliaferro, C. M.; Shields, B. J.; Scholes, G. D.; Castellano, F. N.; Doyle, A. G. 3d-d Excited States of Ni(II) Complexes Relevant to Photoredox Catalysis: Spectroscopic Identification and Mechanistic Implications. *J. Am. Chem. Soc.* **2020**, *142* (12), 5800–5810. https://doi.org/10.1021/jacs.0c00781.

(12) Yang, L.; Lu, H.-H.; Lai, C.-H.; Li, G.; Zhang, W.; Cao, R.; Liu, F.; Wang, C.; Xiao, J.; Xue, D. Light-Promoted Nickel Catalysis: Etherification of Aryl Electrophiles with Alcohols Catalyzed by a NiII-Aryl Complex. *Angewandte Chemie International Edition* **2020**, *59* (31), 12714–12719. https://doi.org/10.1002/anie.202003359.

(13) Cagan, D. A.; Stroscio, G. D.; Cusumano, A. Q.; Hadt, R. G. Multireference Description of Nickel–Aryl Homolytic Bond Dissociation Processes in Photoredox Catalysis. *J. Phys. Chem. A* **2020**, *124* (48), 9915–9922. https://doi.org/10.1021/acs.jpca.0c08646.
(14) Cagan, D. A.; Bím, D.; Silva, B.; Kazmierczak, N. P.; McNicholas, B. J.; Hadt, R. G. Elucidating the Mechanism of Excited-State Bond Homolysis in Nickel–Bipyridine Photoredox Catalysts. *J. Am. Chem. Soc.* **2022**. https://doi.org/10.1021/jacs.2c01356.

Appendix A:

Experimental Methods and Supplementary Figures for Chapter II: Singlet Fission in HDPP-Pent, Li_2(DPP-Pent)$_2$, and KDPP-Pent

Methods

Rotating Frame Nuclear Overhauser Spectroscopy

ROESY, like standard nuclear Overhauser enhancement spectroscopy (NOESY), probes through-space dipolar couplings between nuclear spins. NOESY effectively operates by saturating the transition of a particular nuclear spin and observing changes in intensity of the rest of the spectrum. As the saturated spin undergoes relaxation toward thermal equilibrium, dipolar interactions with another nearby nuclear spin can give rise to relaxation pathways that perturb the population distribution of this second unsaturated spin system, leading to a change in signal intensity for this other transition. Two major pathways for this perturbation exist: zero-quantum and double-quantum transitions. In a magnetic field, the nuclear Zeeman states are split with α spin states lower in energy than the β states. Zero-quantum transitions ($\alpha_I\beta_S \leftrightarrow \beta_I\alpha_S$), or flip-flop transitions, preserve the total M_I of the two-spin system but exchange the individual spin states of spins I and S. Double-quantum transitions, on the other hand, change the total M_I by ±2 ($\alpha_I\alpha_S \leftrightarrow \beta_I\beta_S$).

If we saturate spin S, we will overpopulate the higher energy β_S state and relaxation will favor transitions that lead from β_S to α_S to restore the equilibrium populations. We can see that zero-quantum transitions $\alpha_I\beta_S \rightarrow \beta_I\alpha_S$, will lead to a simultaneous increase in the β_I population, which decreases the population difference between α_I and β_I, leading to a decrease in absorption intensity for spin I. For double-quantum transitions $\beta_I\beta_S \rightarrow \alpha_I\alpha_S$, the population difference between α_I and β_I will on average increase, leading to an increase in the absorption signal intensity for spin I. This leads to two different relaxation mechanisms that will impact the sign of the observed change in signal intensity.

These transitions require exchange of energy between the spin system and the environment. For the zero-quantum transition, the energy required is proportional only to the difference in transition frequency for the two spins I and S, whereas for double-quantum transitions, it is proportional to the sum of the transition frequencies. As a result, double quantum transitions require greater energetic exchange with the environment. The zero- and double-quantum transitions may couple to molecular motions on the frequency scale of the transitions. In this case, rotational motion from molecular tumbling in solution gives rise to the appropriate spectral density function covering these transitions. Because double-quantum transitions require greater energy, higher frequency rotational motion is required for this relaxation pathway to be efficient. As a result, the double-quantum transition is dominant in small molecules with fast rotational tumbling, leading to positive NOE signals. As the average molecular size increases, the rotational motion slows and the double-quantum transition becomes inefficient, allowing the zero-quantum transition to dominate NOE relaxation in large molecules, such as proteins, which gives negative NOE signals.

This trend necessarily means that there is an intermediate regime for molecular size in which the double- and zero-quantum transitions are equally efficient, giving rise to a null NOE signal intensity. As the size (taken as a sphere) and molecular weight can be connected via the Stokes-Einstein equation, the molecular weight for this null region is typically given around 1 kDa. The DPP-Pent subunit stands at molecular weight of 1124, and as a result, we were unable to resolve NOE cross-correlation signals even for through-space interactions that should be inherent to the pentacene moiety (i.e. H_aH_b).

These same relaxation pathways are present in ROESY experiments. However, ROESY differs from NOESY in the pulse sequency. In NOESY, spin mixing is allowed to occur while

polarized along the z-axis of the laboratory frame (along the external magnetic field where α and β are reasonable eigenstates). In ROESY, after the initial π/2 pulse, an effectively continuous-wave RF pulse is applied along the direction of the magnetization in the transverse plane, which effectively holds the magnetization in the XY plane, a process known as spin-locking. The spin mixing now occurs between dressed states of the system that are quantized against the B_1 field of the RF spin-locking pulse. This B_1 field is significantly weaker in magnitude than the external magnetic field B_0, and as a result the transition frequencies between the dressed states are significantly reduced. The result of this is that the double-quantum transition is effectively always operative and dominant even for large molecules, and the ROE signal intensity is always positive with respect to molecular weight/size. This has the advantage of allowing resolution of the NOE signal even when NOESY pulse sequences provide a null cross-correlation intensity. ROESY was therefore utilized for Li_2(DPP-Pent)$_2$ and KDPP-Pent in this study.

Steady-State Emission Spectroscopy

Corrected room temperature emission spectra were collected in the Beckman Institute Laser Resource Center using a modified Jobin Yvon Spec Fluorolog-3 instrument. Samples were excited with a xenon arc lamp, employing a monochromator for wavelength selection, and emission was detected at 90° using two Ocean Optics EQDPro CCD spectrometers spanning 300 to 930 nm.

Fluorescence quantum yields were determined via the comparative method in which the experimental quantum yields were measured relative to a known standard under the same excitation conditions. Rhodamine-6G in EtOH was used as a standard (Φ_S = 0.95). All samples

were diluted such that the maximum absorbance values were less than 0.1. Pentacene samples of unknown quantum yield were prepared in toluene and added to 1 cm glass emission cuvettes and sealed with a Kontes plug under $N_{2(g)}$ atmosphere. Samples were excited at λ_{ex} = 530 nm. The unknown quantum yields (Φ_X) were calculated with Equation 1 using the absorbance values $A(\lambda_{ex})$, the integrated fluorescence intensities $F(\lambda_{ex})$, and correcting for the differing indices of refraction between EtOH and toluene.

$$\Phi_X = \frac{A_S(\lambda_{ex})}{A_X(\lambda_{ex})} \cdot \frac{F_X(\lambda_{ex})}{F_S(\lambda_{ex})} \cdot \frac{n_X^2}{n_S^2} \cdot \Phi_S \qquad Eq\ (1)$$

Time-Resolved Luminescence Spectroscopy

The 1064 nm output of a Nd:YAG laser (Spectra Physics Vanguard) was regeneratively amplified (Continuum) and frequency doubled using a potassium dihydrogen phosphate (KDP) crystal to 532 nm excitation pulses (~10 ps, 10 Hz). Luminescence was collected 90° from the excitation, passed through a polarizer oriented at the magic angle, then directed onto the entrance slit of a monochromator for wavelength selection. Detection was achieved using a streak camera (Hamamatsu C5680) in photon-counting mode, and data were collected over a 50 ns time window. Samples were prepared in sealed 1 cm quartz cuvettes under $N_{2(g)}$ and were stirred during data acquisition.

Transient Absorption Spectroscopy

The 800 nm output of a 5 W, 1 kHz pulsed Ti:sapphire amplifier (Coherent Astrella) was partitioned with a 50:50 beamsplitter. One half was fed into an OPerA Solo optical parametric

amplifier tuned to 550 nm output, which was used as the excitation pump and routed through a chopper and into a joint femtosecond and nanosecond HELIOS FIRE / EOS transient absorption (TA) spectrometer (Ultrafast Systems). For femtosecond experiments, a small portion of the other half of the Ti:sapphire output was routed into the spectrometer and used to generate broadband probe light of the appropriate wavelength region (visible or near-infrared). For nanosecond experiments, a separate white light fiber laser was employed as the probe light. Samples were prepared in sealed 2 mm glass cuvettes under $N_{2(g)}$ and were stirred during data acquisition. Data were processed using Ultrafast Systems Surface Xplorer software for chirp and time zero corrections. The rest of the data workup was performed in MATLAB. For fsTA datasets, pre-time zero spectral vectors were averaged and subtracted from the rest of the dataset to remove background pump scatter. Pre-time zero spectral vectors were similarly averaged in the nsTA datasets and then subtracted up to 20 μs delay times as pump scatter is not detected beyond this threshold by the EOS.

I. Experimental Considerations

General Information

Air- and moisture-sensitive compounds were handled with standard Schlenk line techniques or in a $N_{2(g)}$ atmosphere glove box. When air- and moisture-free techniques were required, dry solvents were acquired from an alumina solvent still. No unexpected or unusually high safety hazards were encountered. 2,6-dibromopyridine was purchased from Combi-Blocks Inc. and used without further purification. Tin (II) dichloride dihydrate was purchased from Matrix Scientific and used without further purification. $Pd(PPh_3)_4$ was purchased from Oakwood Chemicals, stored under inert atmosphere, and used without further purification. Lithium hexamethyldisilazide and potassium hexamethyl disilazide were purchased from Sigma Aldrich, stored in an inert atmosphere glovebox, and used without further purification. 13-hydroxy-13-[(triisopropylsilyl)ethynyl]pentacen-6(13H)-one (Ketone 1, Figure S1)[1] and 2,5-bis(pinacolatoboranyl)pyrrole[2] were synthesized according to previous reports. ^{1}H, ^{13}C, and 2D NMR spectra were collected on a 400 MHz Varian spectrometer. All pentacene solution-state samples for optical spectroscopy were prepared in an inert-atmosphere glovebox using solvents dried and purified on an alumina drying column and degassed prior to being brought into the glovebox. Steady-state absorption spectra were collected using a Varian Cary 500 Scan spectrophotometer. Glotaran (http://glotaran.org), a user interface for the R-based time-resolved fitting software TIMP, was used for kinetic modeling of the transient absorption data.[3]

II. Synthetic Procedures

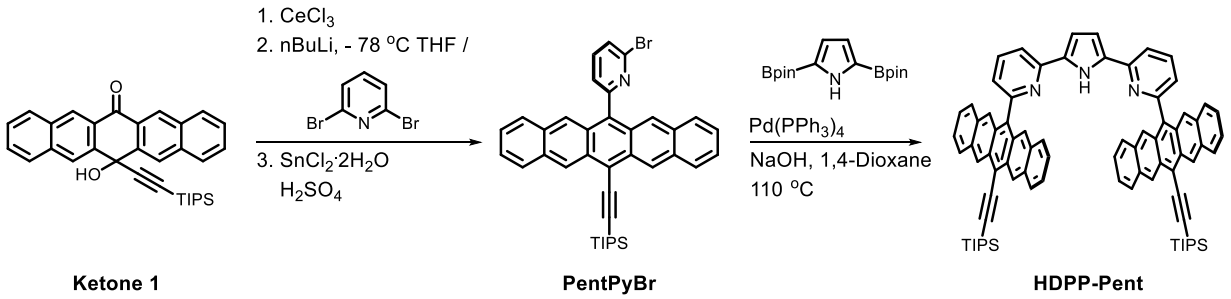

Figure A.1 Synthetic scheme for HDPP-Pent. Ketone 1 is activated with $CeCl_3$ then converted into PentPyBr by deprotonation and nucleophilic attack by monolithiated 2,6-dibromopyridine at -78 °C, followed by reductive aromatization with $SnCl_2 \cdot 2H_2O$. HDPP-Pent is then furnished after a double-Suzuki-Miyaura coupling of PentPyBr with 2,5-bis(pinacolatoboranyl)pyrrole using catalytic $Pd(PPh_3)_4$.

Synthesis of PentPyBr

Ketone 1 (10 mmol) was dissolved in THF in an oven-dried flask under inert conditions. $CeCl_3$ (20 mmol) was added under positive $N_{2(g)}$ pressure and the mixture was stirred for 1 h at room temperature. In a separate flask under nitrogen atmosphere, dibromopyridine (30 mmol) was dissolved in THF and cooled to -78 °C. nBuLi (1.6M solution in hexanes, 30 mmol) was then added slowly to the pyridine solution, which was stirred for 30 min to achieve monolithiation. The solution of Ketone 1 was cooled to -78 °C and the lithiated pyridine solution was slowly cannula transferred under positive nitrogen pressure with stirring. The mixture was warmed to room temperature and stirred for 15 h. Aqueous ammonium chloride solution was slowly added to quench. The brown solution was filtered through a pad of celite to remove salts. The organics were taken up in dichloromethane and washed with brine (2x), dried over Mg_2SO_4, and concentrated to an oily solid. This material was taken up in THF (80 mL) and transferred to a three-neck roundbottom flask. The solution was sparged with $N_{2(g)}$ and $SnCl_2 \cdot 2H_2O$ (20 mmol) was added followed by slow addition of 10% H_2SO_4 (3 mL). The solution was sparged again and stirred for 3 h under nitrogen atmosphere at room temperature. The reaction was neutralized with $K_2CO_{3(aq)}$ and the reaction mixture was filtered through celite. The product was extracted with dichloromethane and dried over Mg_2SO_4. The mixture was concentrated, and the target compound was crashed from methanol to give a dark blue powder. ^{1}H NMR (400 MHz, $CDCl_3$, 25 ºC): δ 9.37 (s, 2H), 8.16 (s, 2H), 7.96 (d, J = 8.5 Hz, 2H), 7.93 – 7.89 (m, 1H), 7.81 (dd, J = 8.0, 1.0 Hz, 1H), 7.77 (d, J = 8.5 Hz, 2H), 7.60 (dd, J = 7.4, 1.0 Hz, 1H), 7.40 – 7.29 (m, 5H), 1.39 (s, 21H). ^{13}C NMR (101 MHz, $CDCl_3$, 25 ºC): δ 159.7, 142.7, 139.0, 134.0, 132.0, 130.9, 128.8, 128.7, 128.3, 127.5, 126.5, 126.2, 126.1, 125.9, 125.1, 119.2, 106.4, 104.7, 19.2, 11.8. HRMS (FAB+) Calcd. For $C_{38}H_{36}NSiBr$: 615.1780. Found: 615.1770.

Synthesis of HDPP-Pent

PentPyBr (2.5 g), 2,5-bis(pinacolatoboranyl)pyrrole (0.65 mg), and NaOH (8.7 mg) were added to an oven-dried Schlenk flask under nitrogen atmosphere and a degassed 9:1 1,4-dioxane/H_2O solution (100 mL) was added. $Pd(PPh_3)_4$ (5 mol%) was added under a counter-flow of $N_{2(g)}$ and the reaction mixture was heated to 110 °C for 5 h. Volatiles were removed under vacuum pressure and the organics were taken up in dichloromethane, washed with brine (2x), dried over Mg_2SO_4, filtered, and concentrated to dryness. HDPP-Pent was obtained as a blue solid by silica-column chromatography (3 : 1 Hexanes/CH_2Cl_2, followed by 5 : 1 Hexanes/THF, then 5:1:1 Hexanes/CH_2Cl_2/Toluene with 1% MeOH). ^{1}H NMR (400 MHz, CD_2Cl_2, 25 ºC): δ 10.39 (s, 1H), 8.48 (br s, 4H), 7.64 – 7.58 (m, 5H), 7.48 (d, 5H), 7.43 (br s, 4H), 7.07 (d, 2H), 6.95 (dd, J = 6.2, 2.1 Hz, 2H), 6.84 – 6.73 (m, 9H), 1.46 (br s, 42H). ^{13}C NMR (101 MHz, CD_2Cl_2, 25 ºC): δ 158.1, 149.7, 136.0, 135.8, 133.3, 130.7, 130.0, 129.6, 127.7, 127.2, 127.0, 125.0, 124.6, 124.5, 124.0, 123.6, 117.2, 116.9, 109.3, 105.4, 103.4, 19.3, 12.0.

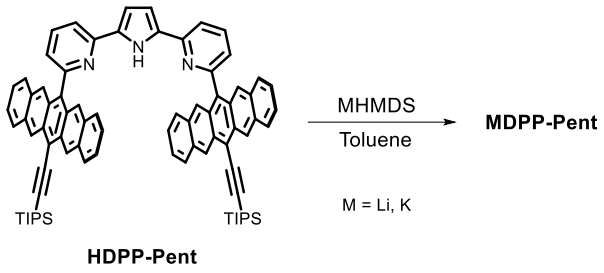

Figure A.2 Synthetic scheme for MDPP-Pent (M = Li, K). HDPP-Pent is deprotonated with the appropriate alkali metal hexamethyldisilazide (MHMDS).

Synthesis of Li_2(DPP-Pent)$_2$

HDPP-Pent (0.1 mmol) was dissolved in toluene (3 mL) and a solution of lithium hexamethyldisilazide (0.1 mmol) in toluene (2 mL) was added, and the mixture was stirred for 20 min. The solution quickly turned from blue to blue-green. Volatiles were removed via vacuum pressure and the desired product was obtained as a blue-green powder. ^{1}H NMR (400 MHz, CD_2Cl_2, 25 °C): δ 9.10 (s, 4H), δ 7.84 (d, 4H), δ 7.75 (s, 4H), δ 7.51 (d, 4H), δ 7.23 (dd, 4H), δ 6.93 (dd, 4H), δ 6.04 (m, 4H), δ 5.12 (d, 2H), δ 4.36 (s, 2H), δ 1.53 (m, 42H).

Synthesis of KDPP-Pent

HDPP-Pent (0.1 mmol) was dissolved in toluene (3 mL) and a solution of potassium hexamethyldisilazide (0.1 mmol) in toluene (2 mL) was added, and the mixture was stirred for 20 min. The solution quickly turned from blue to blue-green. Volatiles were removed via vacuum pressure and the desired product was obtained as a blue-green powder. ^{1}H NMR (400 MHz, CD_2Cl_2, 25 °C): δ 9.13 (s, 4H), δ 8.15 (s, 4H), δ 7.80 (m, 8H), δ 7.59 (d, 4H), δ 7.24 (m, 4H), δ 7.15 (m, 4H), δ 7.01 (s, 2H), δ 6.96 (d, 2H), δ 1.35 (m, 42H).

Synthesis of NaDPP-Pent

HDPP-Pent (0.1 mmol) was dissolved in toluene (3 mL) and a solution of sodium hexamethyldisilazide (0.1 mmol) in toluene (2 mL) was added, and the mixture was stirred for 20 min. The solution quickly turned from blue to blue-green. Volatiles were removed via vacuum pressure and the desired product was obtained as a blue-green powder. ^{1}H NMR (400 MHz, CD_2Cl_2, 25 °C): δ 9.07 (s, 4H), δ 8.09 (s, 4H), δ 7.79 (m, 8H), δ 7.59 (d, 4H), δ 7.24 (m, 4H), δ 7.15 (m, 4H), δ 7.04 (s, 2H), δ 6.94 (d, 2H), δ 1.36 (m, 42H).

III. 2D Rotating Frame Overhauser Effect Spectroscopy (ROESY)

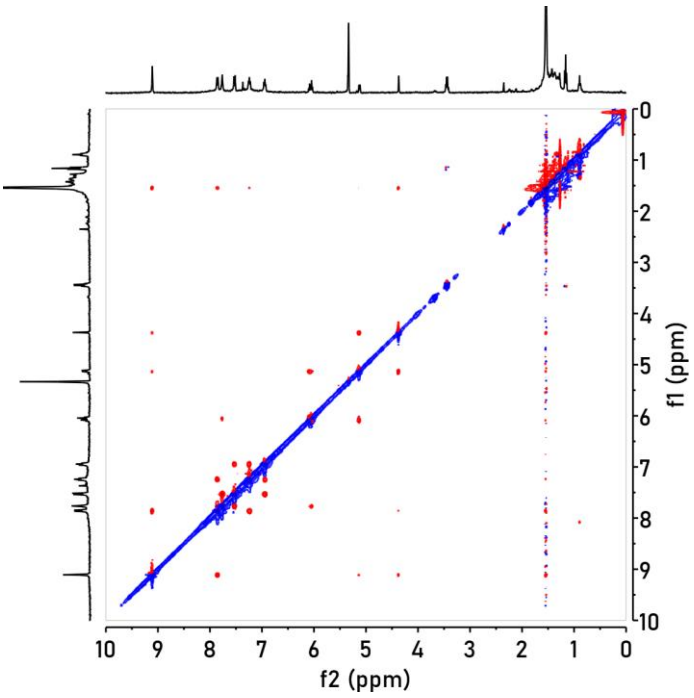

Figure A.3 2D ROESY spectrum of $Li_2(DPP\text{-}Pent)_2$ (400 MHz, CD_2Cl_2).

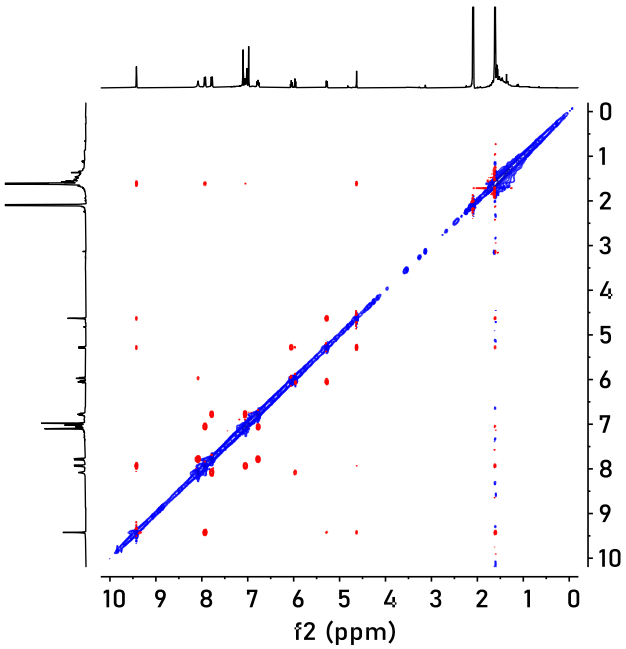

Figure A.4 2D ROESY spectrum of $Li_2(DPP\text{-}Pent)_2$ (400 MHz, toluene-d8).

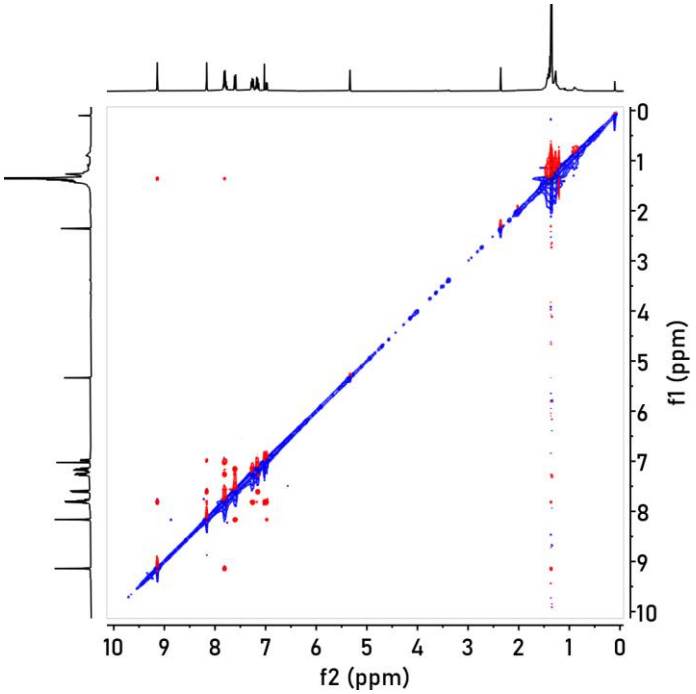

Figure A.5 2D ROESY spectrum of KDPP-Pent (400 MHz, CD_2Cl_2).

IV. Steady-State Absorption and Emission Spectroscopy

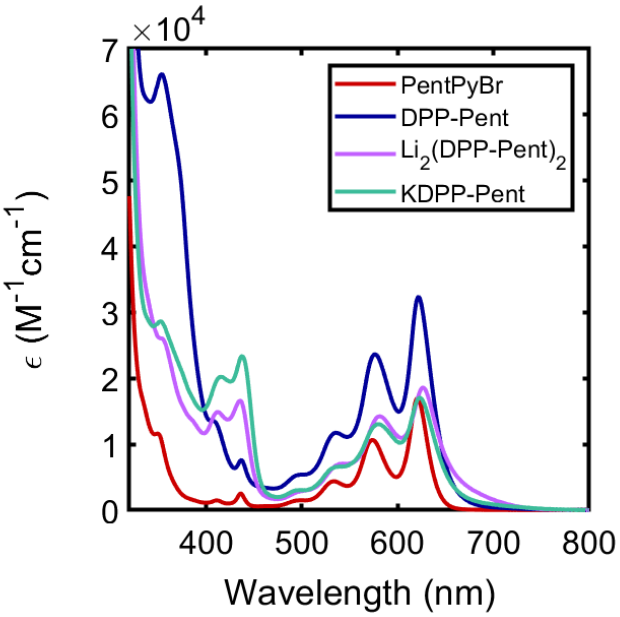

Figure A.6 Visible absorption spectra of PentPyBr (red), HDPP-Pent (blue), $Li_2(DPP\text{-}Pent)_2$ (purple), and KDPP-Pent (teal) in toluene.

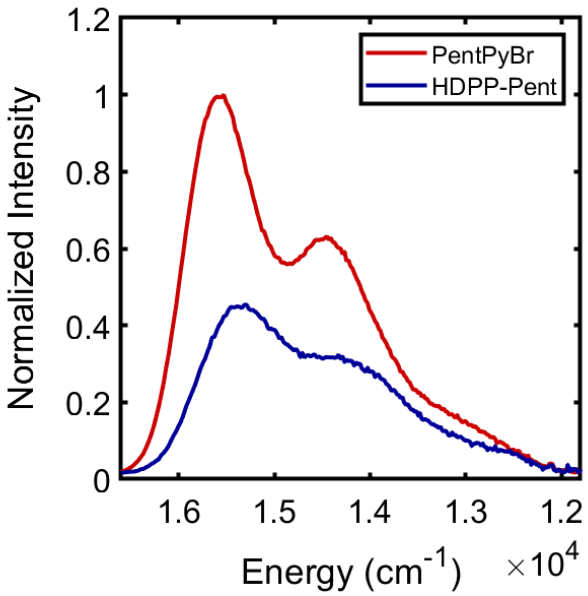

Figure A.7 Emission spectra of PentPyBr (red) and HDPP-Pent (blue). The PentPyBr maximum signal intensity was normalized to one, and the HDPP-Pent spectrum was scaled such that the integrated intensity of the samples reflected their relative estimated quantum yields.

V. Time-Resolved Luminescence Spectroscopy

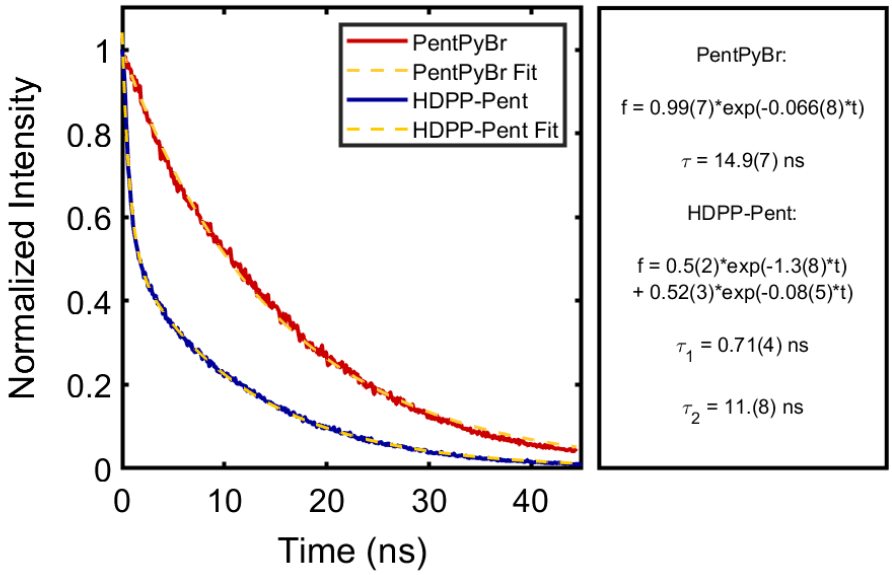

Figure A.8 Time-resolved luminescence spectra of PentPyBr (λ_{obs} = 640 nm) and HDPP-Pent (λ_{obs} = 650 nm) after excitation at 532 nm. The spectra were normalized to a maximum of 1. The fluorescence decay of PentPyBr was fit to a monoexponential function (τ = 15 ns), whereas the decay of HDPP-Pent had to be fit biexponentially (τ_1 = 0.71 ns, τ_2 = 11.8 ns).

VI. Transient Absorption Spectroscopy

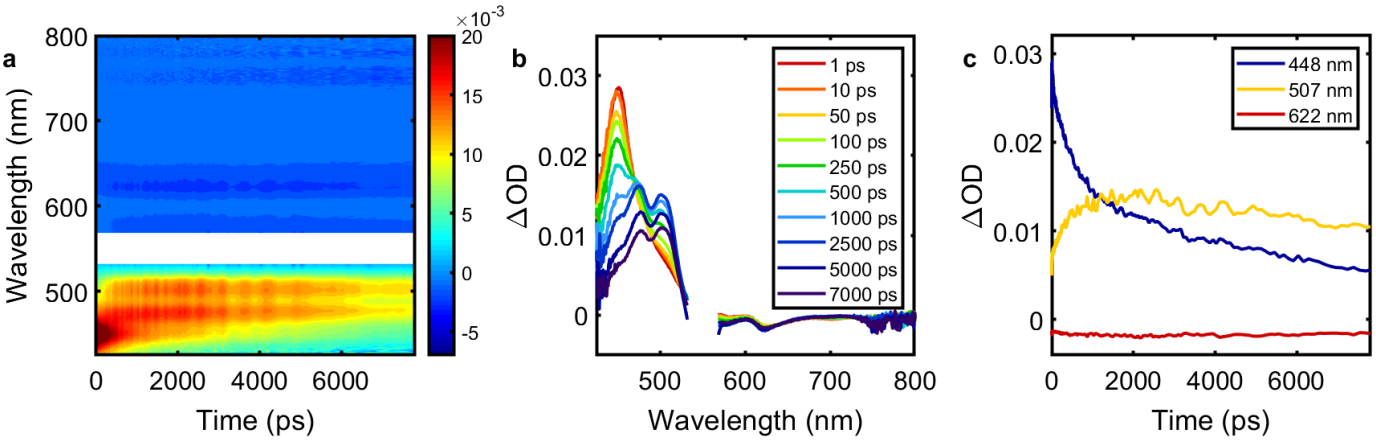

Figure A.9 Femtosecond visible transient absorption spectra of HDPP-Pent (50 μM, toluene) after excitation at 550 nm (0.100 μJ/pulse): (a) contour plot, (b) spectral traces at various time delays, (c) selected time traces at 448, 507, and 622 nm.

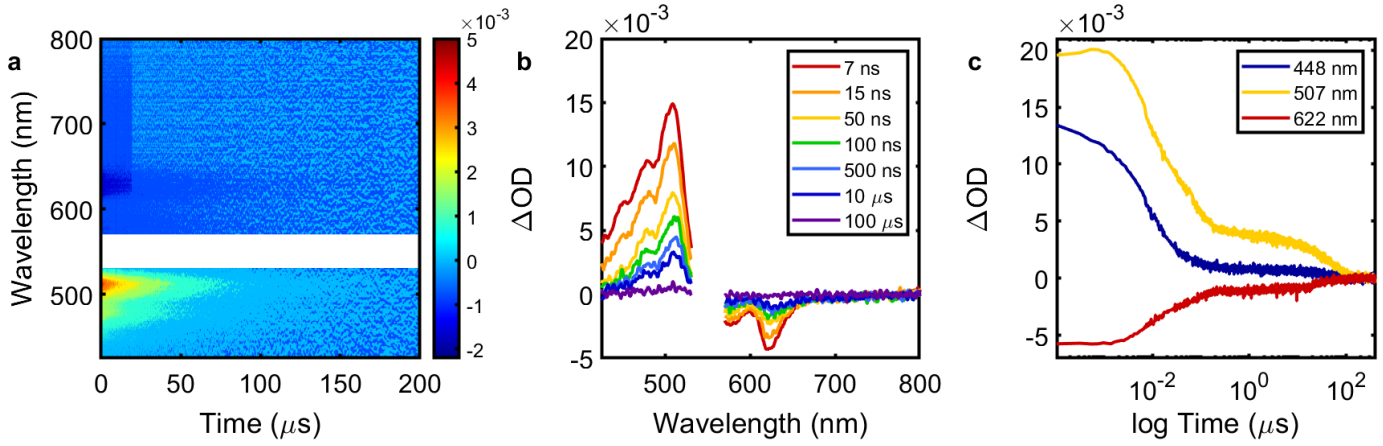

Figure A.10 Nanosecond visible transient absorption spectra of HDPP-Pent (50 μM, toluene) after excitation at 550 nm (0.100 μJ/pulse): (a) contour plot, (b) spectral traces at various time delays, (c) selected time traces at 448, 507, and 622 nm.

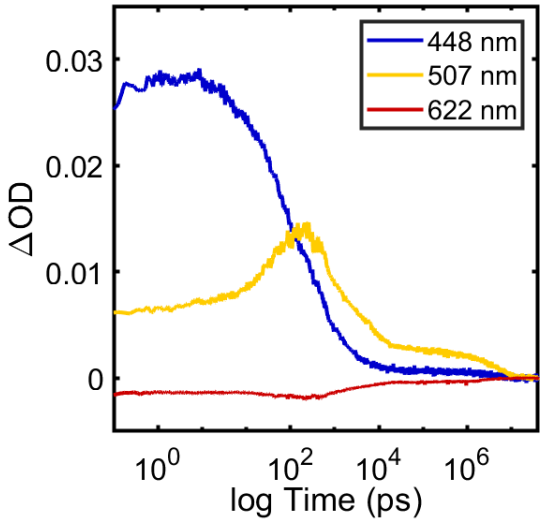

Figure A.11 Combined visible fs and ns TA spectra of HDPP-Pent (50 μM, toluene) after excitation at 550 nm (0.100 μJ/pulse); time traces selected at 448, 507, and 622 nm.

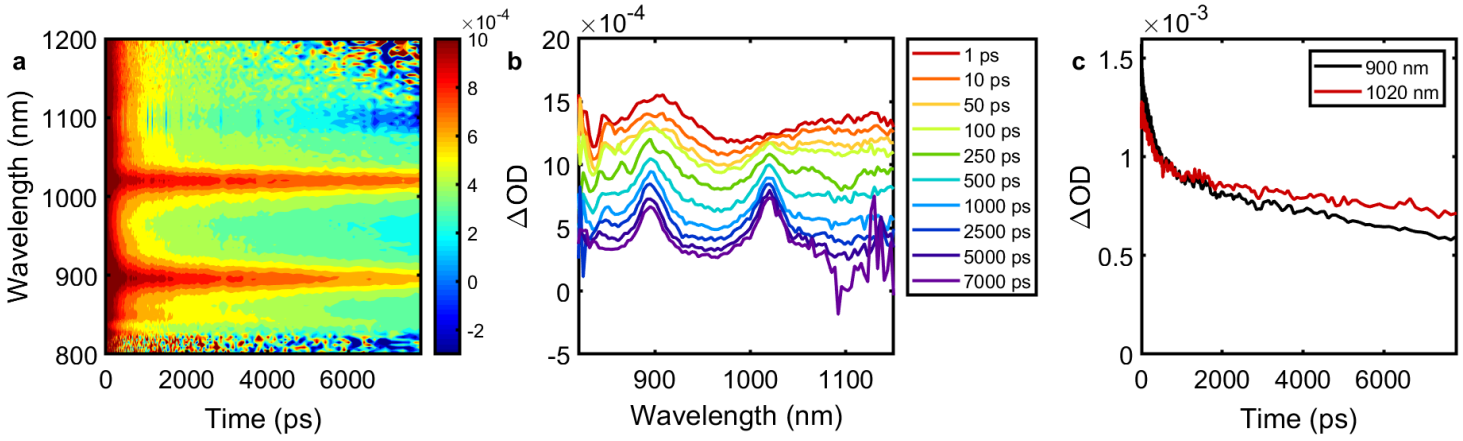

Figure A.12 Near-IR fsTA spectra of HDPP-Pent (50 μM, toluene) after excitation at 550 nm (0.100 μJ/pulse): (a) contour plot, (b) spectral traces at various time delays, (c) selected time traces at 900 and 1020 nm.

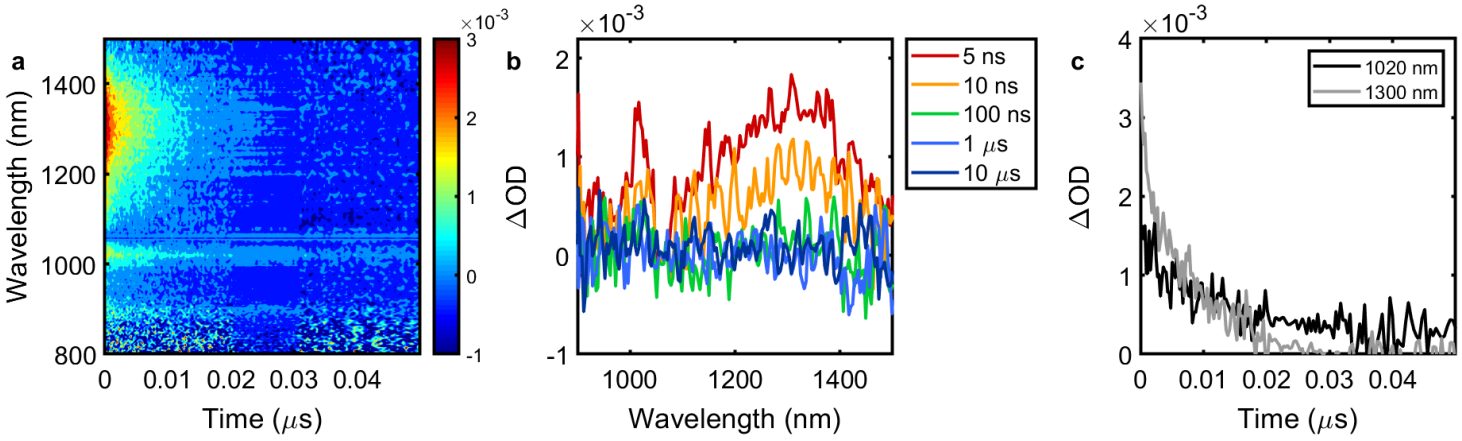

Figure A.13 Near-IR nsTA spectra of HDPP-Pent (50 μM, toluene) after excitation at 550 nm (0.100 μJ/pulse): (a) contour plot, (b) spectral traces at various time delays, (c) selected time traces at 900 and 1020 nm.

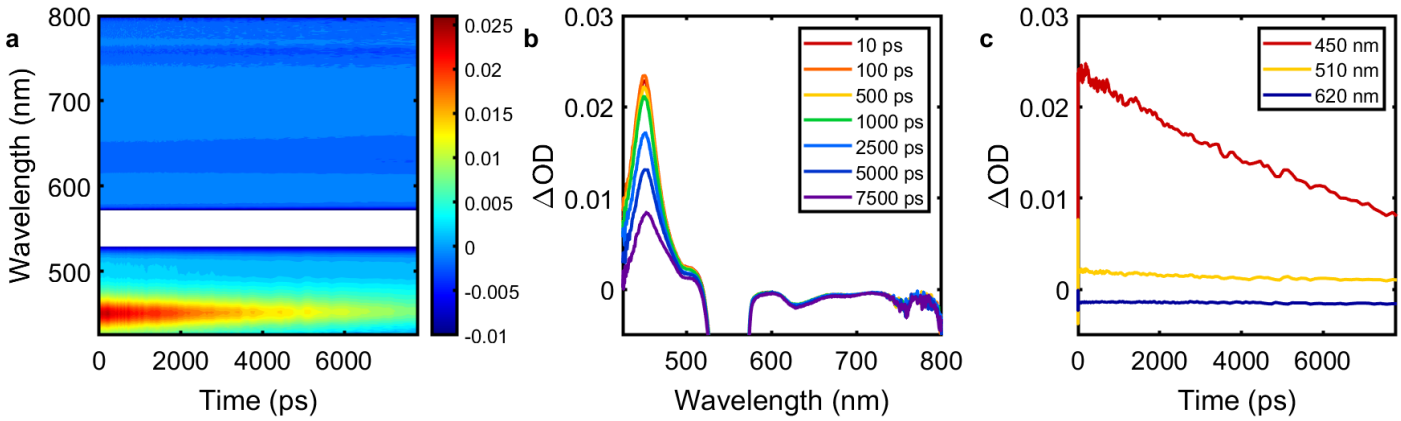

A.14 Visible fsTA spectra of PentPyBr (80 μM, toluene) after excitation at 550 nm (0.100 μJ/pulse): (a) contour plot, (b) spectral traces at various time delays, (c) selected time traces at 900 and 1020 nm.

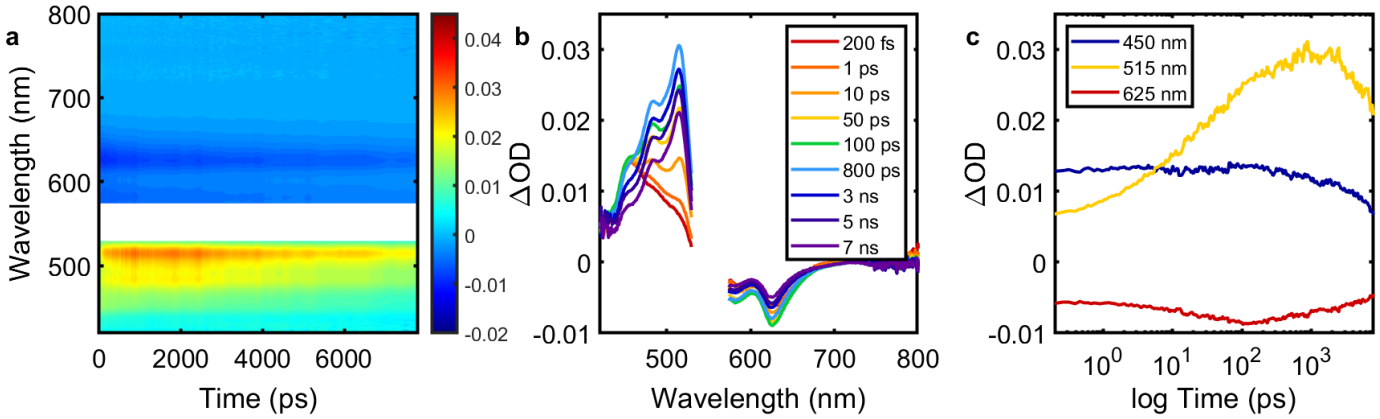

Figure A.15 Visible fsTA spectra of $Li_2(DPP\text{-}Pent)_2$ (50 μM, toluene) after excitation at 550 nm (0.100 μJ/pulse): (a) contour plot, (b) spectral traces at various time delays, (c) selected time traces at 450, 515, and 625 nm.

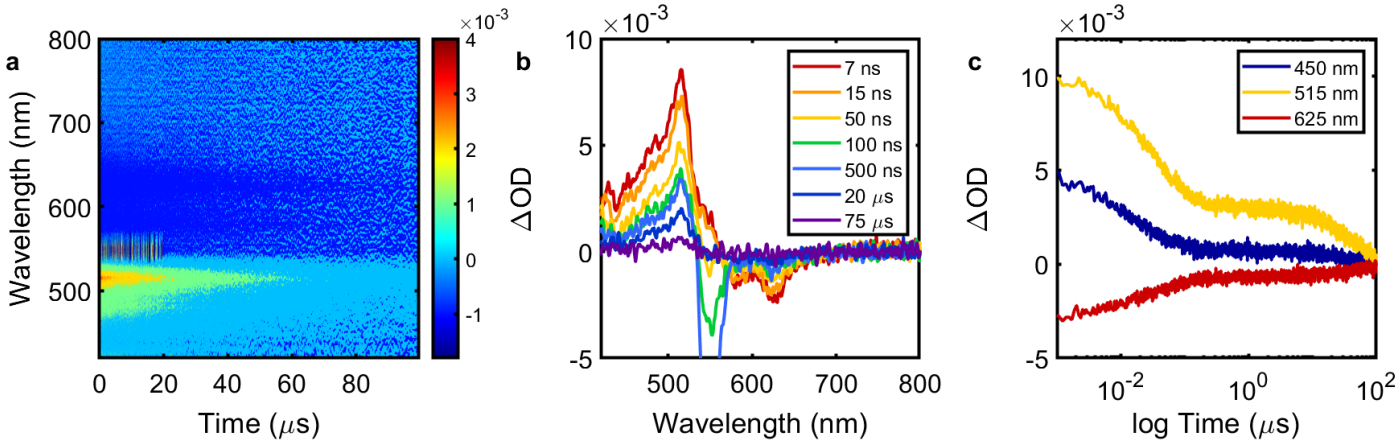

Figure A.16 Visible nsTA spectra of Li_2(DPP-Pent)$_2$ (50 μM, toluene) after excitation at 550 nm (0.100 μJ/pulse): (a) contour plot, (b) spectral traces at various time delays, (c) selected time traces at 450, 515, and 625 nm.

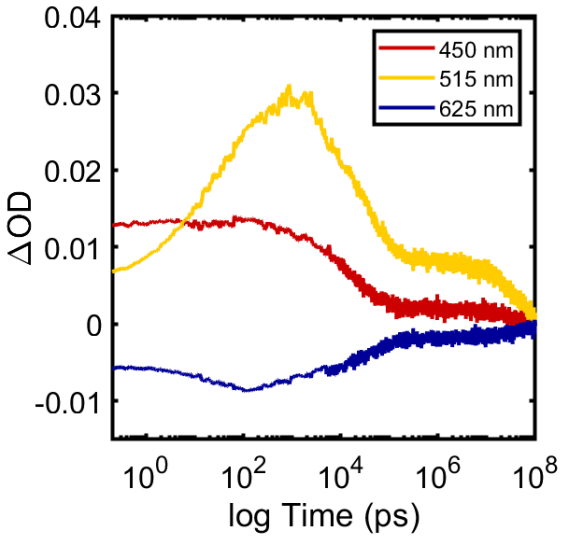

Figure A.17 Combined visible fs and ns TA spectra of $Li_2(DPP\text{-}Pent)_2$ (50 μM, toluene) after excitation at 550 nm (0.100 μJ/pulse); time traces selected at 450, 515, and 625 nm.

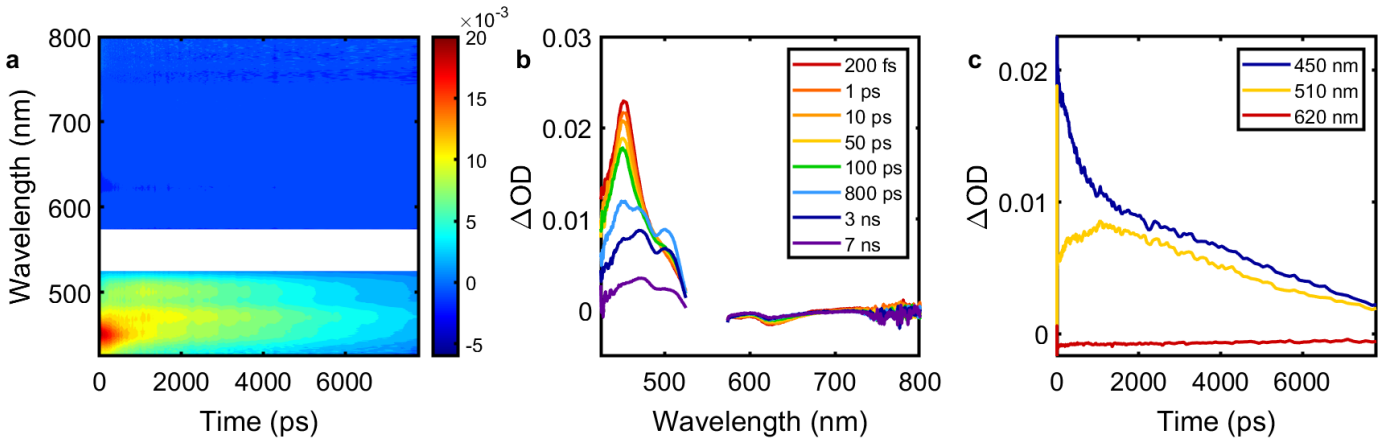

Figure A.18 Visible fsTA spectra of KDPP-Pent (50 μM, toluene) after excitation at 550 nm (0.100 μJ/pulse): (a) contour plot, (b) spectral traces at various time delays, (c) selected time traces at 450, 510, and 620 nm.

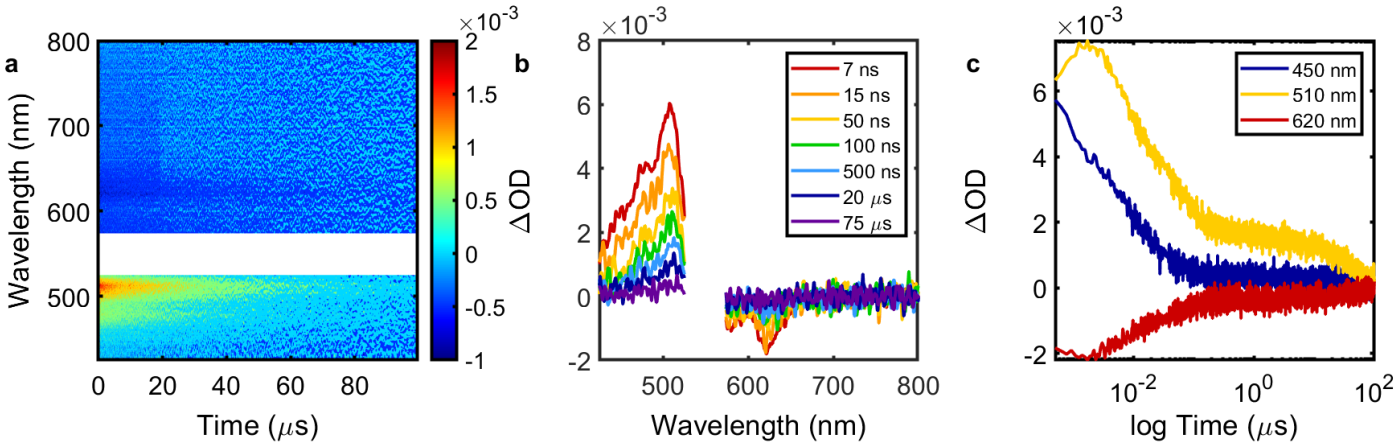

Figure A.19 Visible nsTA spectra of KDPP-Pent (50 μM, toluene) after excitation at 550 nm (0.100 μJ/pulse): (a) contour plot, (b) spectral traces at various time delays, (c) selected time traces at 450, 510, and 620 nm.

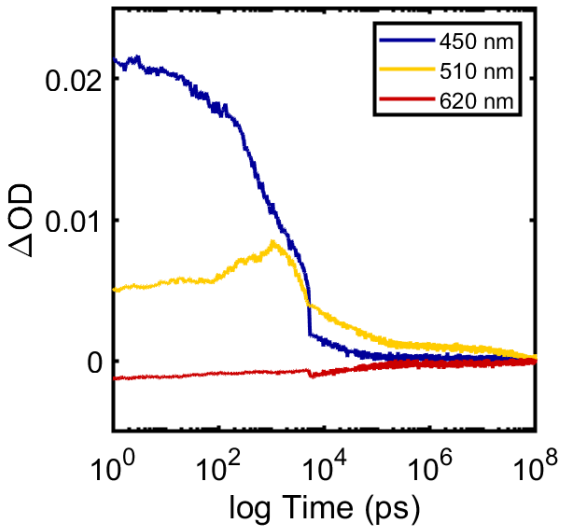

Figure A.20 Combined visible fs and ns TA spectra of KDPP-Pent (50 μM, toluene) after excitation at 550 nm (0.100 μJ/pulse); time traces selected at 450, 510, and 620 nm.

VII. Target Kinetic Analysis

HDPP-Pent

For HDPP-Pent, the time-resolved luminescence data provide information solely on the dynamics of the S_1 state independent of the TA spectroscopy. The results of the emission experiment may therefore be appropriately applied to a kinetic model for fitting the composite TA data. Our model assumes the decay of the ^{1}ESA feature should mirror the biexponential decay observed in the time-resolved emission data, as both reflect the dynamics of the S_1 state. Thus, we require terms that account for both the radiative and nonradiative relaxation pathways. Initial attempts to fit single wavelength decay curves of the ^{3}ESA feature from the nsTA data to an exponential function clearly indicated the triplet decay required at least a biexponential. In fact, attempts to model the kinetics with only a monoexponential triplet decay produced results that exhibited significant intensity of the triplet feature in the singular value decomposition (SVD) of the residual data matrix, highlighting that the monoexponential decay model does not adequately describe the decay of the ^{3}ESA feature. This is consistent with other reports of multiexponential decays in the ^{3}ESA feature reflecting geminate recombination of the triplet pair on a faster timescale than uncorrelated triplet decay.

In order to accommodate the biexponential decay of the ^{1}ESA, components 1 and 2 are set to equally reflect the ^{1}ESA spectrum and are weighted equally in initial intensity to reflect the weighting coefficients from the time-resolved fluorescence results (Supplementary Table S1). Components 3 and 4 are allowed to vary spectrally, but ultimately both reflect the ^{3}ESA feature. Component 1 decays into components 3 and 4 equally with a rate constant k_1, component 2 decays to the ground state with rate constant k_2, and components 3 and 4 decay to the ground state with rate constants k_3 and k_4 respectively.

Table A.1 HDPP-Pent visible fs and ns TA target analysis; no parameters fixed

	k (s^{-1})	Standard Error
k_1	1.3(4) x 10^9	1.07 x 10^7
k_2	2.0(2) x 10^8	2.31 x 10^6
k_3	2.6(6) x 10^7	1.72 x 10^5
k_4	2.8(1) x 10^4	3.32 x 10^2

	τ (ps)
τ_1	7.4(6) x 10^2
τ_2	4.9(5) x 10^3
τ_3	3.7(6) x 10^4
τ_4	3.5(6) x 10^7

	1	2	3	4
1				
2		k_2		
3	k_1		k_3	
4	k_1			k_4

Fitted kinetic parameters obtained from a four-component model of the composite visible fs and ns TA data of HDPP-Pent: components 1 and 2 equally correspond to ^{1}ESA vectors (reflecting the biexponential decay observed from the time-resolved fluorescence measurements); components 3 and 4 similarly reflect the short- and long-lived ^{3}ESA vectors. Component 1 decays equally into components 3 and 4 with a rate k_1; components 2, 3, and 4 decay with a rate of k_2, k_3, k_4 respectively. Residual standard error 0.00175329.

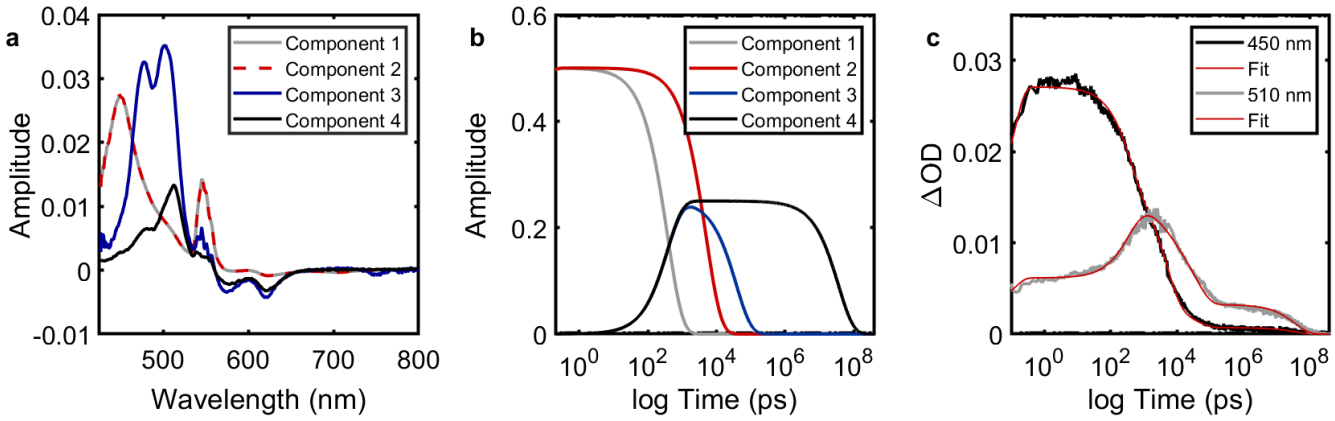

Figure A.21 Glotaran target analysis (Table A.1) of HDPP-Pent (50 μM, toluene) visible fs and ns TA data; no parameters fixed: (a) species associated spectra, (b) kinetic traces of fitted components, and (c) kinetic fits overlaying experimental data at 450 and 510 nm.

Table A.2 HDPP-Pent visible fs and ns TA target analysis; k_1 and k_2 fixed

	k (s^{-1})	Standard Error
k_1	1.3(8) x 10^9	-
k_2	8.5(0) x 10^8	-
k_3	2.6(7) x 10^7	1.98 x 10^5
k_4	2.8(7) x 10^4	3.37 x 10^2
	τ (ps)	
τ_1	7.2(5) x 10^2	
τ_2	1.1(8) x 10^4	
τ_3	3.7(5) x 10^4	
τ_4	3.4(8) x 10^7	

	1	2	3	4
1				
2		k_2		
3	k_1		k_3	
4	k_1			k_4

Fitted kinetic parameters obtained from a four-component model of the composite visible fs and ns TA data of HDPP-Pent: components 1 and 2 equally correspond to ^{1}ESA vectors (reflecting the biexponential decay observed from the time-resolved fluorescence measurements), components 3 and 4 similarly reflect the short- and long-lived ^{3}ESA vectors. Component 1 decays equally into components 3 and 4 with a rate k_1; components 2, 3, and 4 decay with a rate of k_2, k_3, k_4 respectively. k_1 and k_2 have been fixed given the rates from time-resolved fluorescence measurements. Residual standard error: 0.00176051.

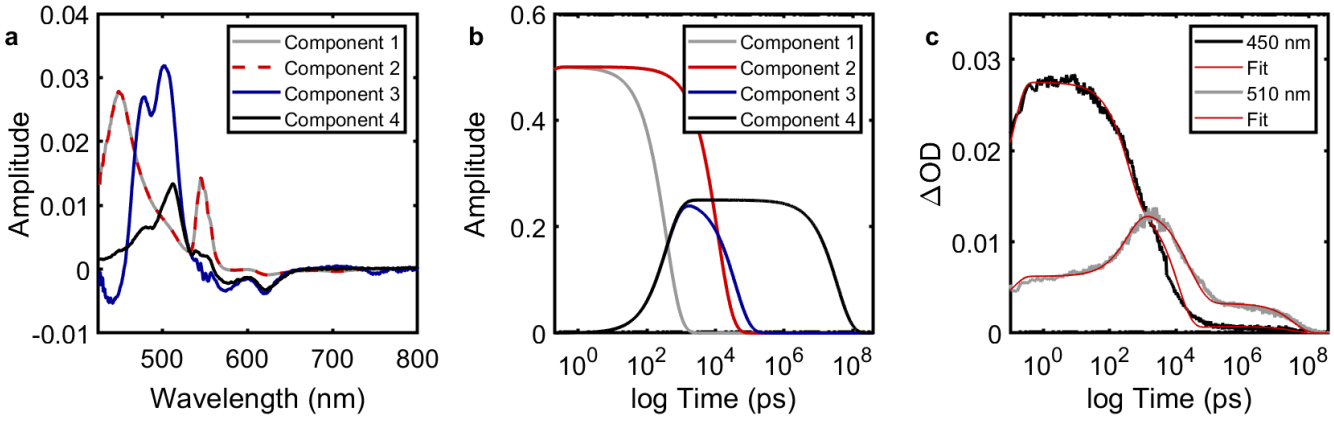

Figure A.22 Glotaran target analysis (Table A.2) of HDPP-Pent (50 μM, toluene) visible fs and ns TA data, k_1 and k_2 fixed: (a) species associated spectra, (b) kinetic traces of fitted components, and (c) kinetic fits overlaying experimental data at 450 and 510 nm.

Table A.3 HDPP-Pent visible fsTA target analysis

	k (s^{-1})	Standard Error
k_1	2.5(6) x 10^9	3.86 x 10^7
k_2	1.7(2) x 10^8	5.20 x 10^6
k_3	1.(8) x 10^7	1.72 x 10^6
	τ (ps)	
τ_1	3.9(1) x 10^2	
τ_2	5.8(1) x 10^3	
τ_3	5.(6) x 10^4	

	1	2	3
1			
2		k_2	
3	k_1		k_3

Fitted kinetic parameters obtained from a three-component model of the fsTA data of HDPP-Pent: components 1 and 2 equally correspond to ^{1}ESA vectors (reflecting the biexponential decay observed from the time-resolved fluorescence measurements); component 3 reflects the decay of the ^{3}ESA vector. Component 1 decays into component 3 with a rate k_1; components 2 and 3 decay with a rate of k_2 and k_3 respectively. Residual standard error: 0.00249052.

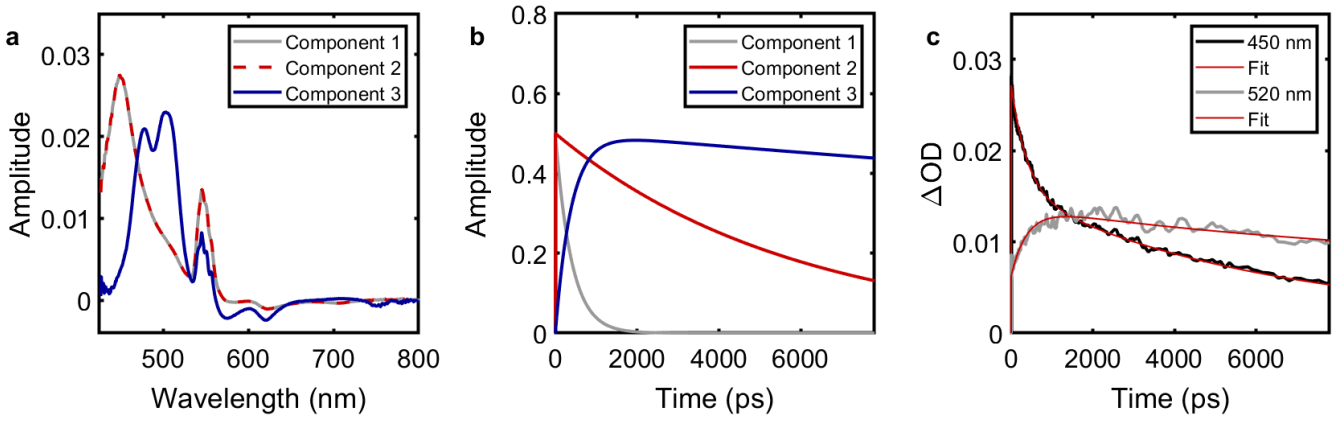

Figure A.23 Glotaran target analysis (Table A.3) of HDPP-Pent (50 μM, toluene) visible fsTA data: (a) species associated spectra, (b) kinetic traces of fitted components, and (c) kinetic fits overlaying experimental data at 450 and 510 nm.

Table A.4 HDPP-Pent nsTA target analysis

	k (s^{-1})	Standard Error
k_1	3.5(5) x 10^7	1.76 x 10^5
k_2	2.9(4) x 10^4	2.74 x 10^2
	τ (ns)	
τ_1	2.8(2) x 10^1	
τ_2	3.4(0) x 10^4	

	1	2
1	k_1	
2		k_2

Fitted kinetic parameters obtained from a three-component model of the nsTA data of HDPP-Pent: components 1 and 2 correspond to ^{3}ESA vectors representing the biexponential decay in the feature. Components 1 and 2 decay with rate constants k_1 and k_2 respectively. Residual standard error: 0.00197139.

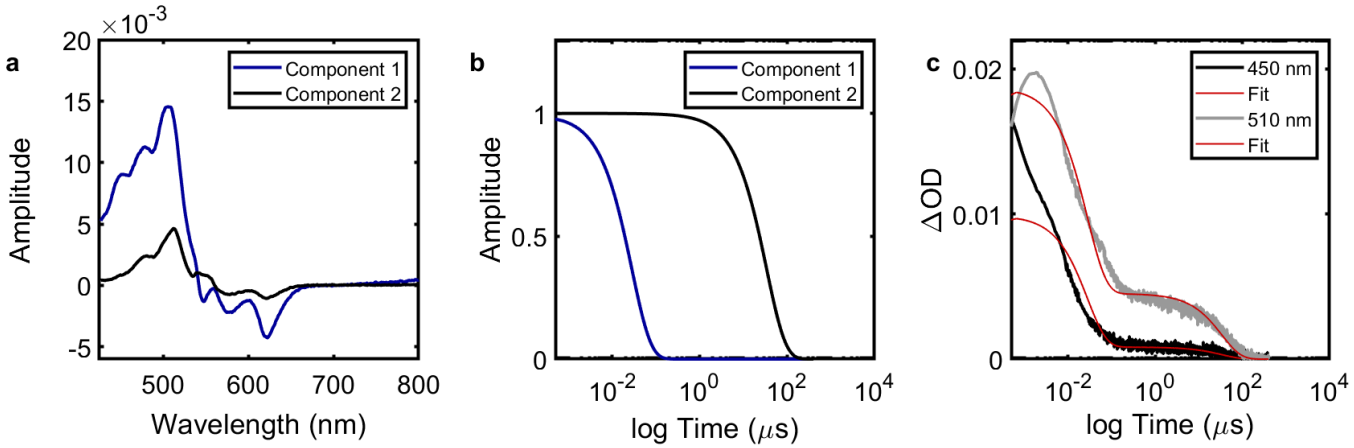

Figure A.24 Glotaran target analysis (Table A.4) of HDPP-Pent (50 μM, toluene) visible nsTA data: (a) species associated spectra, (b) kinetic traces of fitted components, and (c) kinetic fits overlaying experimental data at 450 and 510 nm.

$Li_2(DPP\text{-}Pent)_2$

Table A.5 $Li_2(DPP\text{-}Pent)_2$ visible fs and ns TA target analysis; 3-component model

	k (s^{-1})	Standard Error
k_1	1.0(4) x 10^{10}	1.47 x 10^8
k_2	4.3(0) x 10^7	2.44 x 10^4
k_3	2.8(6) x 10^4	2.84 x 10^2
	τ (ps)	
τ_1	96.(2)	
τ_2	2.3(3) x 10^4	
τ_3	3.5(0) x 10^7	

	1	2	3
1			
2	k_1	k_2	
3	k_1		k_3

Fitted kinetic parameters obtained from a three-component model of the composite fs and ns TA data of $Li_2(DPP\text{-}Pent)_2$: component 1 corresponds to a ^{1}ESA; components 2 and 3 reflect the short- and long-lived ^{3}ESA vectors. Component 1 decays equally into components 2 and 3 with a rate k_1; components 2 and 3 decay with a rate of k_2 and k_3 respectively. The final fits reported are averaged over two datasets. Residual standard error 0.00167259.

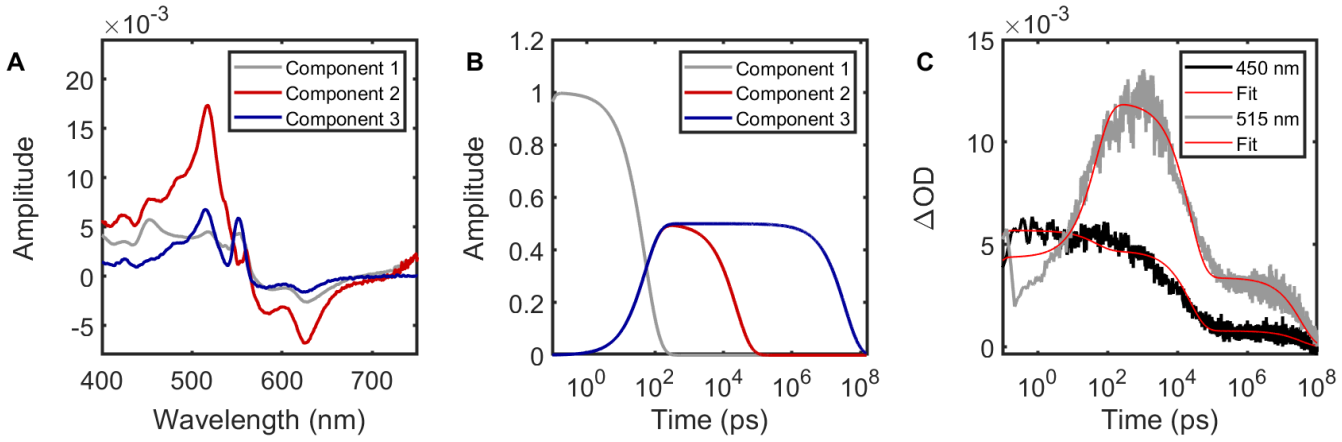

Figure A.25 Glotaran target analysis (Table A.5) of $Li_2(DPP\text{-}Pent)_2$ (50 μM, toluene) visible fs and ns TA data with a three-component model: (a) species associated spectra, (b) kinetic traces of fitted components, and (c) kinetic fits overlaying experimental data at 450 and 515 nm. The rapid rise of the triplet feature causes a slight deviation for the fits at these early times as seen in the intensity at 515 nm in the species associated spectra of component 1.

Table A.6 Li_2(DPP-Pent)$_2$ visible fs and ns TA target; 4-component model

	k (s^{-1})	Standard Error
k_1	9.0(4) x 10^9	9.66 x 10^7
k_2	9.3(9) x 10^7	2.75 x 10^5
k_3	7.(8) x 10^6	1.4 x 10^5
k_4	1.9(9) x 10^4	2.72 x 10^2

	τ (ps)
τ_1	1.1(1) x 10^2
τ_2	1.0(7) x 10^4
τ_3	1.(3) x 10^5
τ_4	5.0(3) x 10^7

	1	2	3	4
1				
2	k_1	k_2		
3	k_1		k_3	
4	k_1			k_4

Fitted kinetic parameters obtained from a four-component model of the composite fs and ns TA data of Li_2(DPP-Pent)$_2$: component 1 corresponds to a ^{1}ESA; components 2, 3, and 4 reflect short-, intermediate-, and long-lived ^{3}ESA vectors. Component 1 decays equally into components 2, 3, and 4 with a rate k_1; components 2, 3, and 4 decay with a rate of k_2, k_3, and k_4 respectively. The final fits reported are averaged over two datasets. Residual standard error 0.00167048.

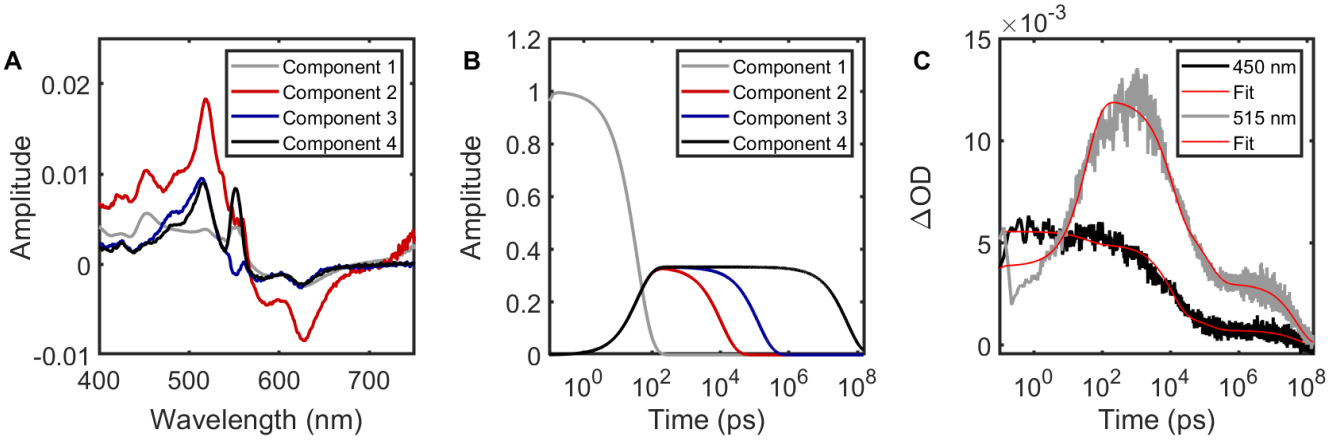

Figure A.26 Glotaran target analysis (Table A.6) of Li_2(DPP-Pent)$_2$ (50 μM, toluene) visible fs and ns TA data with a four-component model: (a) species associated spectra, (b) kinetic traces of fitted components, and (c) kinetic fits overlaying experimental data at 450 and 515 nm. The rapid rise of the triplet feature causes a slight deviation for the fits at these early times as seen in the intensity at 515 nm in the species associated spectra of component 1.

Table A.7 $Li_2(DPP\text{-}Pent)_2$ visible fsTA target analysis

	k (s^{-1})	Standard Error
k_1	1.44(0) x 10^{10}	8.786 x 10^7
k_2	2.8(6) x 10^7	3.25 x 10^5
	τ (ps)	
τ_1	6.94(4) x 10^1	
τ_2	2.51(1) x 10^4	

	1	2
1		
2	k_1	k_2

Fitted kinetic parameters obtained from a two-component, sequential model of the fsTA data of $Li_2(DPP\text{-}Pent)_2$: component 1 corresponds to a ^{1}ESA, and component 2 reflects the ^{3}ESA vector. Residual standard error 0.00211332.

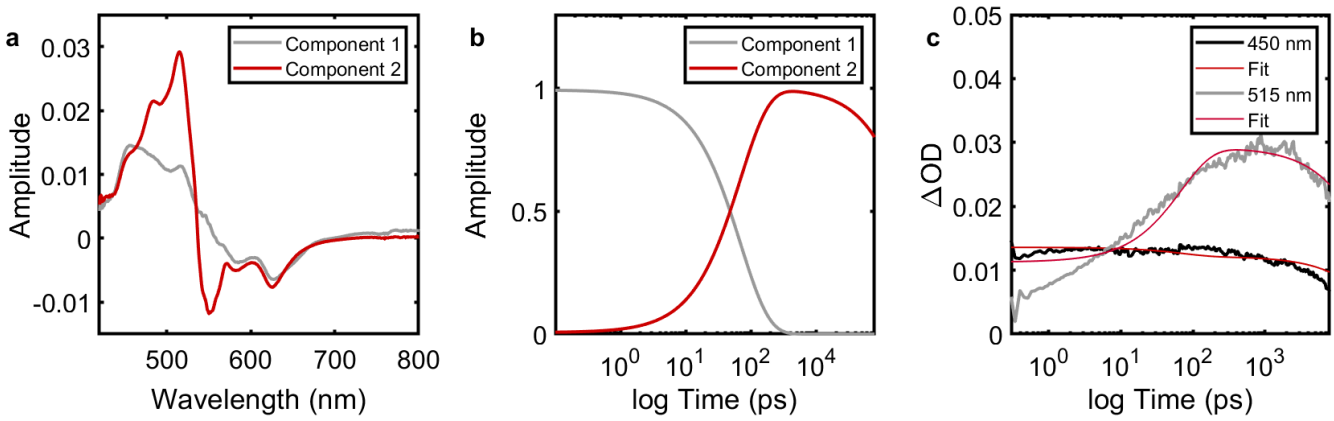

Figure A.27 Glotaran target analysis (Table A.7) of $Li_2(DPP\text{-}Pent)_2$ (50 μM, toluene) visible fsTA data: (a) evolution associated spectra, (b) kinetic traces of fitted components, and (c) kinetic fits overlaying experimental data at 450 and 510 nm. The rapid rise of the triplet feature causes a slight deviation for the fits at these early times as seen in the intensity at 515 nm in the species associated spectra of component 1.

Table A.8 $Li_2(DPP\text{-}Pent)_2$ visible nsTA target analysis

	k (s^{-1})	Standard Error
k_1	2.60(2) x 10^7	7.978 x 10^4
k_2	2.19(1) x 10^4	9.291 x 10^1
	τ (ns)	
τ_1	3.84(3) x 10^1	
τ_2	4.56(4) x 10^4	

	1	2
1	k_1	
2		k_2

Fitted kinetic parameters obtained from a two-component, sequential model of the nsTA data of $Li_2(DPP\text{-}Pent)_2$: components 1 and 2 correspond to the ^{3}ESA vector, reflecting a biexponential decay. Residual standard error 0.000664370.

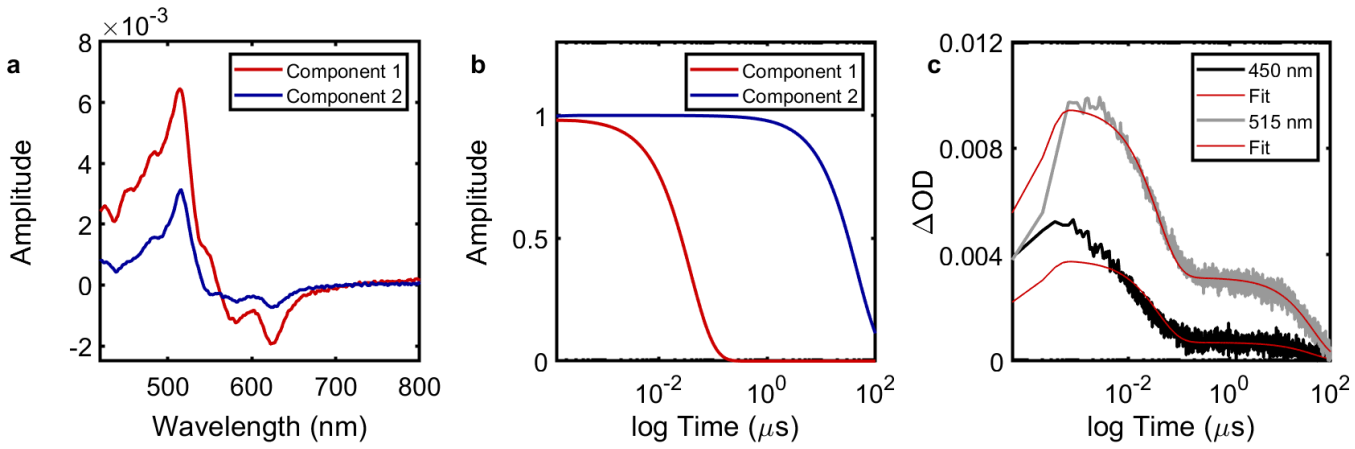

Figure A.28 Glotaran target analysis (Table A.8) of $Li_2(DPP\text{-}Pent)_2$ (50 μM, toluene) visible nsTA data: (a) species associated spectra, (b) kinetic traces of fitted components, and (c) kinetic fits overlaying experimental data at 450 and 510 nm.

KDPP-Pent

Table A.9 KDPP-Pent visible fs and ns TA target analysis – 3 components

	k (s^{-1})	Standard Error
k_1	1.60(0) x 10^9	9.897 x 10^6
k_2	1.75(3) x 10^8	5.121 x 10^5
k_3	6.0(5) x 10^4	1.6(5) x 10^2
	τ (ps)	
τ_1	6.25(0) x 10^2	
τ_2	5.70(5) x 10^4	
τ_3	1.6(5) x 10^7	

	1	2	3
1			
2	k_1	k_2	
3	k_1		k_3

Fitted kinetic parameters obtained from a three-component model of the composite fs and ns TA data of KDPP-Pent: component 1 corresponds to a ^{1}ESA; components 2 and 3 reflect the short- and long-lived ^{3}ESA vectors. Component 1 decays equally into components 2 and 3 with a rate k_1; components 2 and 3 decay with a rate of k_2 and k_3 respectively. Residual standard error 0.000864311.

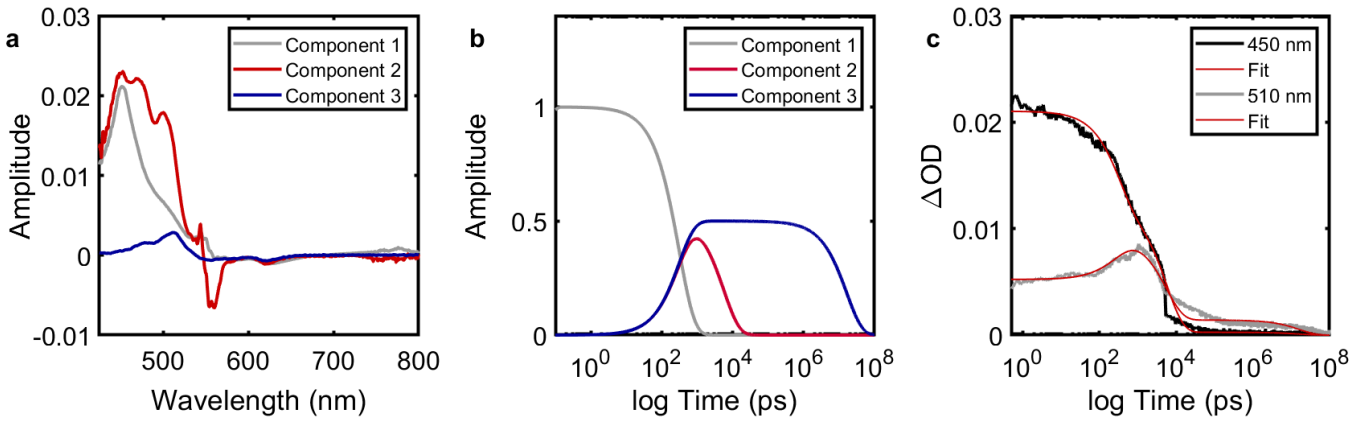

Figure A.29 Glotaran target analysis (Table A.9) of KDPP-Pent (50 μM, toluene) visible fs and nsTA data – three-component fit: (a) species associated spectra, (b) kinetic traces of fitted components, and (c) kinetic fits overlaying experimental data at 450 and 510 nm.

Table A.10 KDPP-Pent visible fs and ns TA target analysis – 4 components

	k (s^{-1})	Standard Error
k_1	2.2(5) x 10^9	1.71 x 10^7
k_2	2.7(5) x 10^8	2.14 x 10^6
k_3	8.7(1) x 10^7	4.85 x 10^5
k_4	3.7(2) x 10^4	4.85 x 10^2

	τ (ps)
τ_1	4.4(4) x 10^2
τ_2	3.6(4) x 10^4
τ_3	1.1(5) x 10^5
τ_4	2.6(9) x 10^7

	1	2	3	4
1				
2		k_2		
3	k_1		k_3	
4	k_1			k_4

Fitted kinetic parameters obtained from a four-component model of the composite fs and ns TA data of KDPP-Pent: components 1 and 2 equally correspond to ^{1}ESA vectors; components 3 and 4 similarly reflect the short- and long-lived ^{3}ESA vectors. Component 1 decays equally into components 3 and 4 with a rate k_1; components 2, 3, and 4 decay with a rate of k_2, k_3, k_4 respectively. Residual standard error 0.000862214. k_1 and k_2 have been fixed given the rates from time-resolved fluorescence measurements.

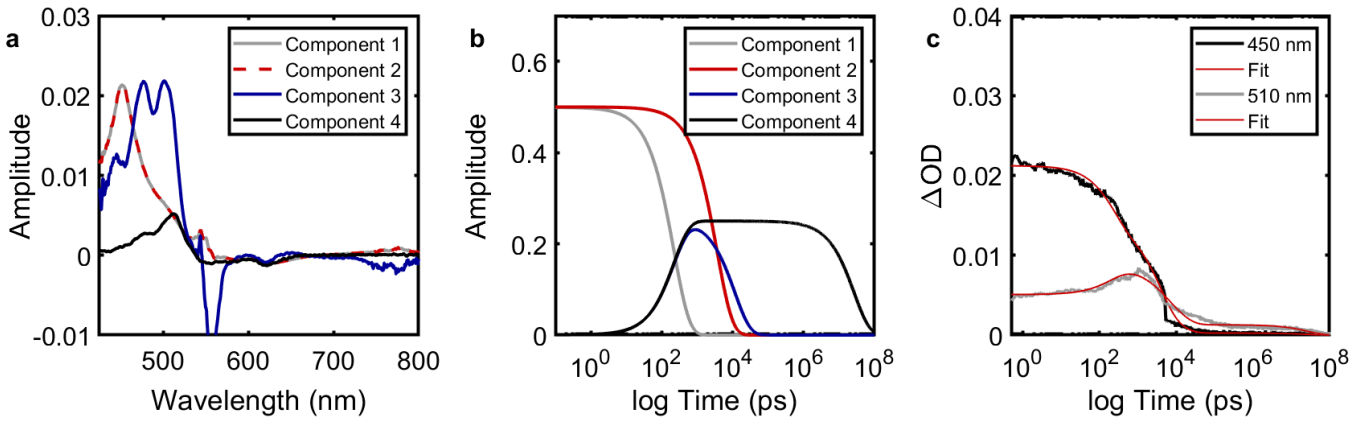

Figure A.30 Glotaran target analysis (Table A.10) of KDPP-Pent (50 μM, toluene) visible fs and nsTA data – four-component fit: (a) species associated spectra, (b) kinetic traces of fitted components, and (c) kinetic fits overlaying experimental data at 450 and 510 nm.

Table A.11 KDPP-Pent visible fsTA target analysis

	k (s^{-1})	Standard Error
k_1	2.2(7) x 10^9	2.86 x 10^7
k_2	1.4(4) x 10^8	1.14 x 10^6
	τ (ps)	
τ_1	4.4(1) x 10^2	
τ_2	6.9(4) x 10^3	

	1	2
1		
2	k_1	k_2

Fitted kinetic parameters obtained from a two-component, sequential decay model of the fsTA data of KDPP-Pent: components 1 and 2 correspond to the ^{1}ESA and ^{3}ESA vectors, respectively. Residual standard error 0.00179745.

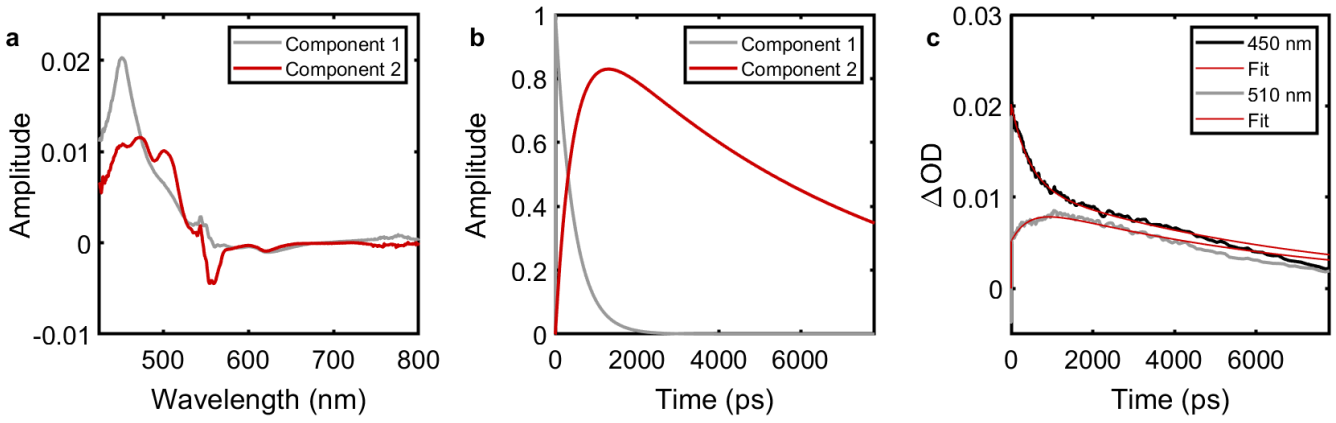

Figure A.31 Glotaran target analysis (Table A.11) of KDPP-Pent (50 μM, toluene) visible fsTA data: (a) evolution associated spectra, (b) kinetic traces of fitted components, and (c) kinetic fits overlaying experimental data at 450 and 510 nm.

Table A.12 KDPP-Pent visible nsTA target analysis

	k (s^{-1})	Standard Error
k_1	3.1(6) x 10^7	1.27 x 10^5
k_2	2.7(3) x 10^4	1.14 x 10^2
	τ (ns)	
τ_1	3.1(6) x 10^1	
τ_2	3.6(6) x 10^4	

	1	2
1	k_1	
2		k_2

Fitted kinetic parameters obtained from a two-component, parallel decay model of the nsTA data of KDPP-Pent: components 1 and 2 correspond to the ^{3}ESA vectors. Residual standard error 0.000674488.

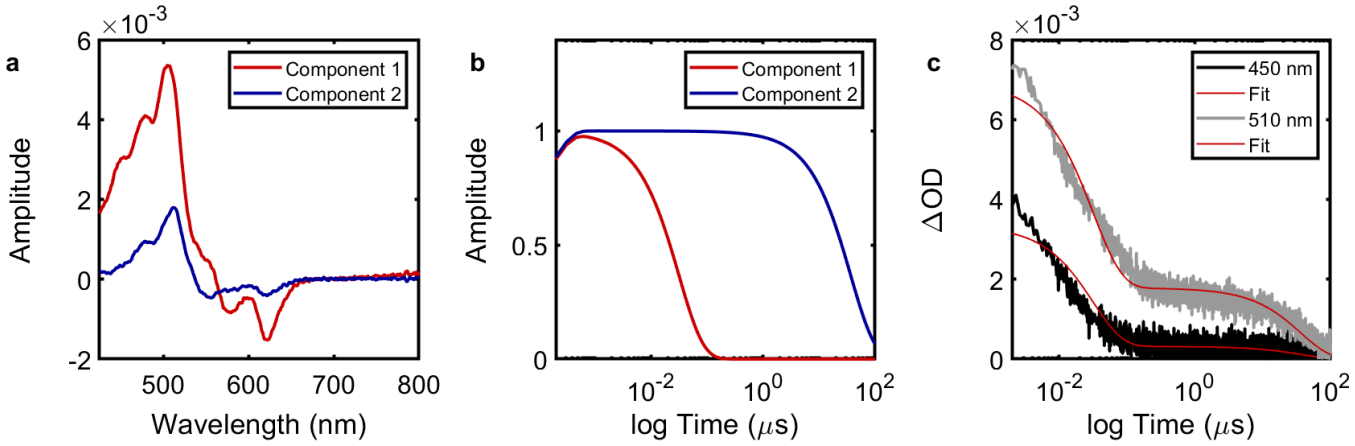

Figure A.32 Glotaran target analysis (Table A.12) of KDPP-Pent (50 μM, toluene) visible nsTA data: (a) evolution associated spectra, (b) kinetic traces of fitted components, and (c) kinetic fits overlaying experimental data at 450 and 510 nm.

VIII. HDPP-Pent: Triplet Extinction Coefficient Estimation

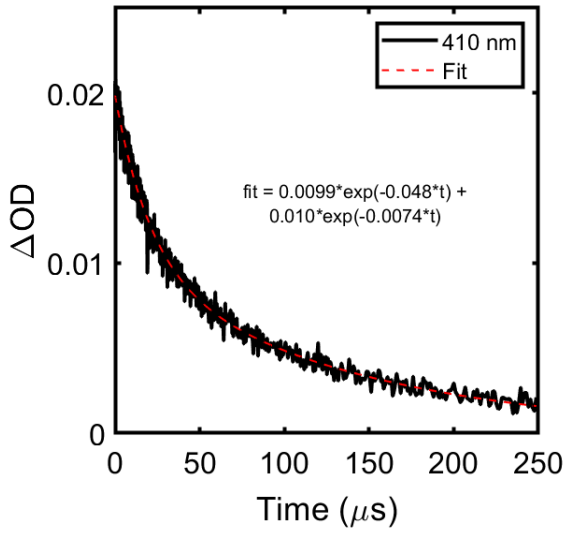

Figure A.33 Anthracene (500 μM, toluene) ^{3}ESA ns transient absorption trace at 410 nm.

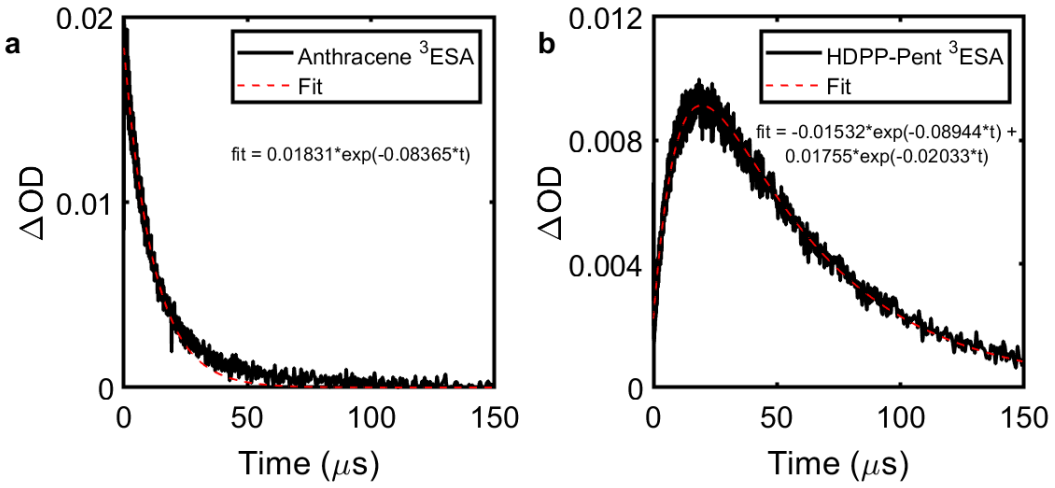

Figure A.34 Photosensitization experiment (500 μM Anthracene, 10 μM HDPP-Pent in toluene): (a) Anthracene ^{3}ESA nsTA kinetic trace at 410 nm, (b) HDPP-Pent ^{3}ESA nsTA kinetic trace at 510 nm.

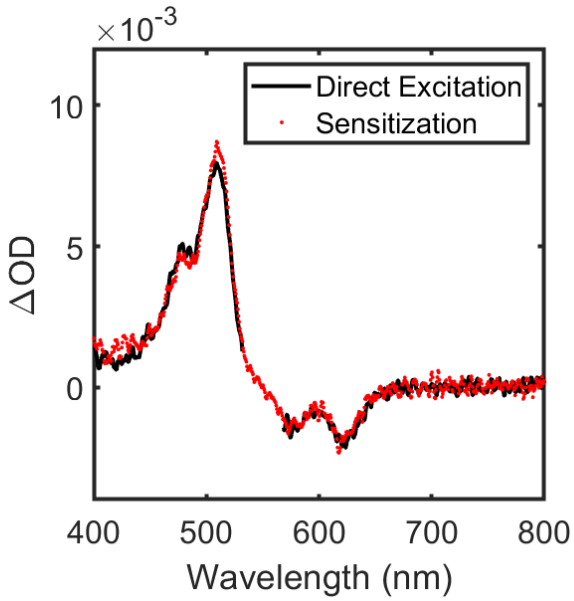

Figure A.35 Comparison between the transient absorption spectrum of HDPP-Pent at long delay times (50 ns) after direct photosensitization with 550 nm light and the transient absorption spectrum of the photosensitized anthracene (500 μM) and HDPP-Pent (10 μM) after exciting anthracene at 360 nm at delay times (35 μs) past the decay of the anthracene triplet ESA. In the photosensitization experiment, we expect the anthracene triplet to be transferred to HDPP-Pent, resulting in the observation of the triplet transient absorption spectrum of HDPP-Pent at long delay times. This same spectrum is observed in the direct excitation experiment at long delay times, indicating that these spectral features are indeed associated with the HDPP-Pent T_1 state. The residual pump scatter at 550 nm was excised from the direct excitation spectrum.

The Anthracene (500 μM) and HDPP-Pent (10 μM) photosensitization experiment will be used to demonstrate the calculation of the HDPP-Pent ^{3}ESA extinction coefficient given the reported Anthracene ^{3}ESA molar absorptivity (42,000 M^{-1} cm^{-1}).[4–7] This is accomplished by setting the concentrations of Anthracene and HDPP-Pent triplets to be equal in the Beer-Lambert regime and solving for ^{3}HDPP-Pent ε as in Equation 2:

$$c_{^3Anth} = c_{^3HDPP-Pent}$$

$$\frac{\Delta OD_{^3Anth}}{\varepsilon_{^3Anth} \cdot l} = \frac{\Delta OD_{^3HDPP-Pent}}{\varepsilon_{^3HDPP-Pent} \cdot l}$$

$$\varepsilon_{^3HDPP-Pent} = \frac{\Delta OD_{^3HDPP-Pent}}{\Delta OD_{^3Anth}} \cdot \varepsilon_{^3Anth} \qquad Eq\ (2)$$

The assumption underlying this equation is that the energy transfer efficiency is near unity – that the concentration of anthracene triplets fully transfers into HDPP-Pent triplets. In order to fulfill this estimation, corrections must be made to the ^{3} HDPP-Pent ΔOD to account for triplet transfer efficiency (Φ_{ET}) and the relative rate of the rise and decay of the HDPP-Pent ^{3}ESA ($\Phi_{T(decay)}$).

$$\Phi_{ET} = \frac{k_{sens}}{k_{sens} + k_{intrinsic}}$$

$$\Phi_{ET} = \frac{0.08365}{0.08365 + 0.048} = 0.64$$

$$\Phi_{T(decay)} = \frac{k_{T(rise)}}{k_{T(rise)} + k_{T(decay)}}$$

$$\Phi_{T(decay)} = \frac{0.08944}{0.08944 + 0.02033} = 0.81$$

The corrected ^{3}HDPP-Pent ΔOD (ΔOD_{corr}) can thus be estimated and the HDPP-Pent ^{3}ESA extinction coefficient can be calculated as in Equation 2:

$$\Delta OD_{corr} = \frac{\Delta OD\ {}^3{}_{HDPP-Pent}}{\Phi_{ET} \cdot \Phi_{T(decay)}} = \frac{0.0091}{0.64 \cdot 0.81}$$

$$\Delta OD_{corr} = 0.0176$$

$$\varepsilon\ {}^3{}_{HDPP-Pent} = \frac{0.0176}{0.0183} \cdot (42{,}000\ M^{-1}cm^{-1})$$

$$\varepsilon\ {}^3{}_{HDPP-Pent} = 40{,}393\ M^{-1}cm^{-1}$$

This process is repeated for each concentration of HDPP-Pent (10, 20, 50, 100 μM) and the results are compiled in Figure S35. As can be seen, the calculated ^{3}HDPP-Pent extinction coefficient approaches a limit of ~ 49,000 M^{-1} cm^{-1} as the concentration of HDPP-Pent is increased (i.e. the triplet energy transfer efficiency approaches unity).

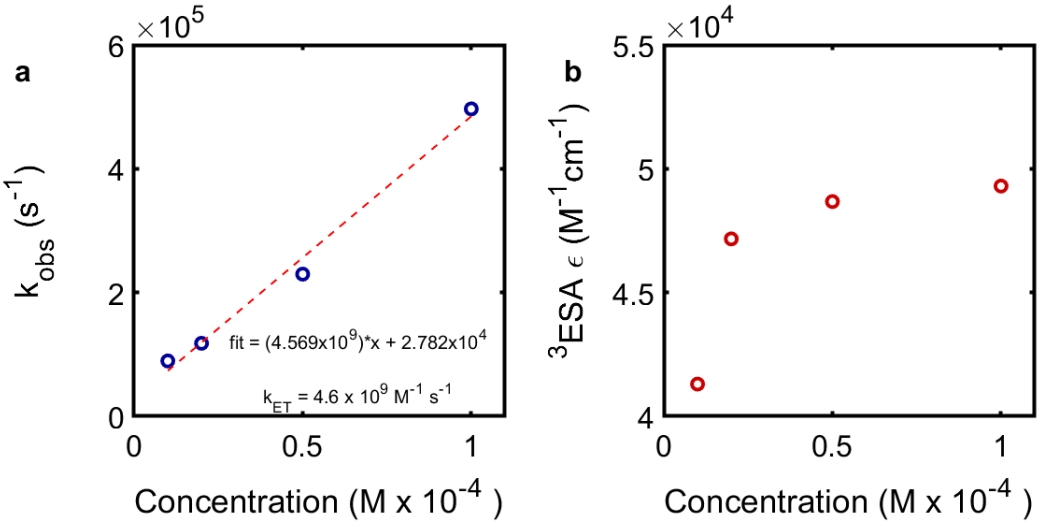

Figure A.36 Concentration-dependent photosensitization experiments between Anthracene (500 μM) and HDPP-Pent (X μM, X = 10, 20, 50, 100): (a) observed energy transfer rate (k_{obs}) vs. HDPP-Pent concentration, fitted to a linear function, the slope of which gives the bimolecular rate constant (k_{ET}); (b) calculated HDPP-Pent ^{3}ESA extinction coefficient vs. HDPP-Pent concentration.

IX. HDPP-Pent: Triplet Yield Estimation

In order to estimate the triplet yield, we can use Equation 3. As a note, we refer to $[T_1]$ as the concentration of excited triplet states without differentiation between triplet pair (T_1T_1) and free triplet (T_1) states.

$$Triplet\ \%\ Yield = \frac{[T_1]}{[S_1]} \cdot 100 \qquad Eq\ (3)$$

i. Concentration of Excited Singlets

Let us first consider the maximum concentration of excited singlets generated. This has been previously estimated using the ground state bleach (GSB) feature. However, it must be noted in the case of HDPP-Pent that the shape and intensity of the GSB changes over the course of the transient absorption experiment in a way that suggests there is a complex overlap of GSB and ESA features in the spectrum. This makes the GSB unreliable in the evaluation of the triplet yield. The concentration of excited singlets may alternatively be estimated as the product of the number of photons per pulse and the ratio of pump intensity before and after the sample (I/I_0) divided by the product of Avogadro's number (N_A) and the excitation volume (V):[8]

$$[\boldsymbol{S_1}] = \frac{\left(\frac{\boldsymbol{photons}}{\boldsymbol{pulse}}\right) \cdot \left(\frac{\boldsymbol{I}}{\boldsymbol{I_0}}\right)}{\boldsymbol{N_A \cdot V}}$$

$$\left(\frac{photons}{pulse}\right) = \frac{power}{(rep\ rate) \cdot \left(\frac{energy}{photon}\right)}$$

$$\left(\frac{I}{I_0}\right) = 1 - 10^{-A}$$

$$V = \pi r^2 l$$

Each component may be first evaluated individually. The photons per pulse can be derived from the excitation power (100 μW), the laser repetition rate (1000 s^{-1}), and the energy per photon (as calculated by the product of Planck's constant h and the frequency of 550 nm light). I/I_0 can be calculated as the difference from unity of ten raised to the negative power of the sample absorbance at 550 nm (0.11). The excitation volume is assumed to be cylindrical using the radius of the excitation spot (0.013 cm) and the path length of the sample (0.2 cm).

$$\left(\frac{photons}{pulse}\right) = \frac{1 \times 10^{-4}\ W}{(1{,}000\ s^{-1}) \cdot (3.61 \times 10^{-19}\ J)} = 2.77 \times 10^{11}\ pulse^{-1}$$

$$\left(\frac{I}{I_0}\right) = 1 - 10^{-0.11} = 0.2238$$

$$V = \pi \cdot (1.30 \times 10^{-2}\ cm)^{2} \cdot (0.2\ cm) \cdot (0.001\ L\ cm^{-3}) = 1.06 \times 10^{-7}\ L$$

$$[S_1] = \frac{(2.77 \times 10^{11}) \cdot (0.2238)}{(6.022 \times 10^{23}) \cdot (1.06 \times 10^{-7})} = 9.7 \times 10^{-7}\ M$$

ii. Concentration of Excited Triplets

The concentration of HDPP-Pent triplets may be estimated from the extinction coefficient of the ^{3}ESA at 510 nm as derived above and the maximum ΔOD value at 510 nm from the experimental transient absorption data. However, from the time-resolved luminescence data and the target fitting, it is apparent that when the TA ^{3}ESA at 510 nm reaches its maximum intensity (t ~ 1.4 ns), there is contribution to this intensity from the ^{1}ESA. The fit may be used to decompose the ΔOD at 510 nm to its contributions from the ^{1}ESA and ^{3}ESA, and the triplet contribution may be used to estimate the corrected triplet yield.

The target fitting as shown in Figure S21 gives a maximum ΔOD_{510nm} of 0.0128. The contributions of the different component vectors to the target fit can be decomposed from the kinetic traces (Figure S21b), which provides a weighting coefficient or effective concentration for each vector at 1.4 ns. The SAS (Figure S21a) provides the relative molar extinction of each vector at 510 nm. Taking the weighted sum of the first and second vectors gives the ΔOD contribution of the ^{1}ESA at 510 nm. Likewise, taking the weighted sum of the third and fourth vectors gives the relative ΔOD contribution of the ^{3}ESA. These values are collected in Table S12.

Table A.13 Estimation of ^{1}ESA and ^{3}ESA ΔOD contributions at 510 nm in the transient absorption spectrum of HDPP-Pent (50 μM, toluene).

component	1	2	3	4
Relative contribution at 1.4 ns	0.0103	0.4437	0.2379	0.2448
Intensity of SAS at 510 nm	0.0062	0.0062	0.0285	0.0180
	^{1}ESA		^{3}ESA	
ΔOD_{510nm} contribution at 1.4 ns	0.0028		0.010	

The maximum concentration of triplets can then be estimated in the Beer-Lambert regime and the triplet yield can be thus calculated.

$$[T_1] = \frac{\Delta OD_{510nm}}{\varepsilon\,{}^{3}{}_{DPP-Pent} \cdot l}$$

$$[T_1] = \frac{0.010}{(49{,}000) \cdot (0.2)} = 1.0 \times 10^{-6}\ M$$

$$Triplet\ Yield = \frac{[T_1]}{[S_1]} \cdot 100 = \frac{1.0 \times 10^{-6}\ M}{9.7 \times 10^{-7}\ M} \cdot 100$$

$$Triplet\ Yield \sim 100\ \%$$

X. $Li_2(DPP\text{-}Pent)_2$: Triplet Extinction Coefficient Estimation

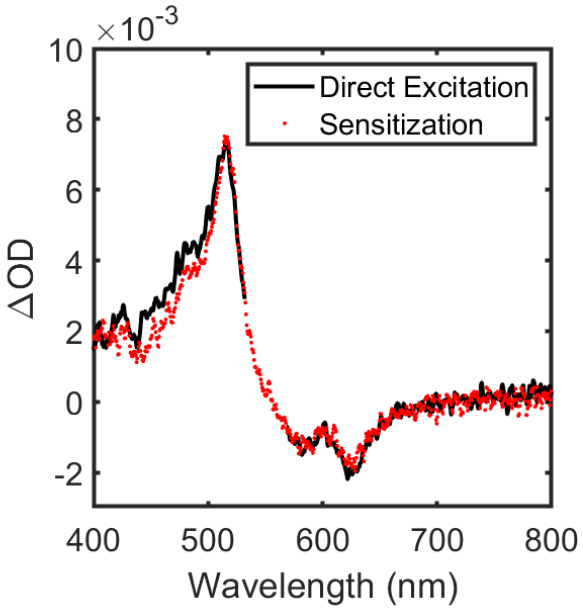

Figure A.37 Comparison between the transient absorption spectrum of $Li_2(DPP\text{-}Pent)_2$ at long delay times (20 ns) after direct photosensitization with 550 nm light and the transient absorption spectrum of the photosensitized anthracene (500 μM) and $Li_2(DPP\text{-}Pent)_2$ (50 μM) after exciting anthracene at 360 nm at delay times (100 μs) past the decay of the anthracene triplet ESA. In the photosensitization experiment, we expect the anthracene triplet to be transferred to $Li_2(DPP\text{-}Pent)_2$, resulting in the observation of the triplet transient absorption spectrum of $Li_2(DPP\text{-}Pent)_2$ at long delay times. This same spectrum is observed in the direct excitation experiment at long delay times, indicating that these spectral features are indeed associated with the $Li_2(DPP\text{-}Pent)_2$ T_1 state. The residual pump scatter at 550 nm was excised from the direct excitation spectrum.

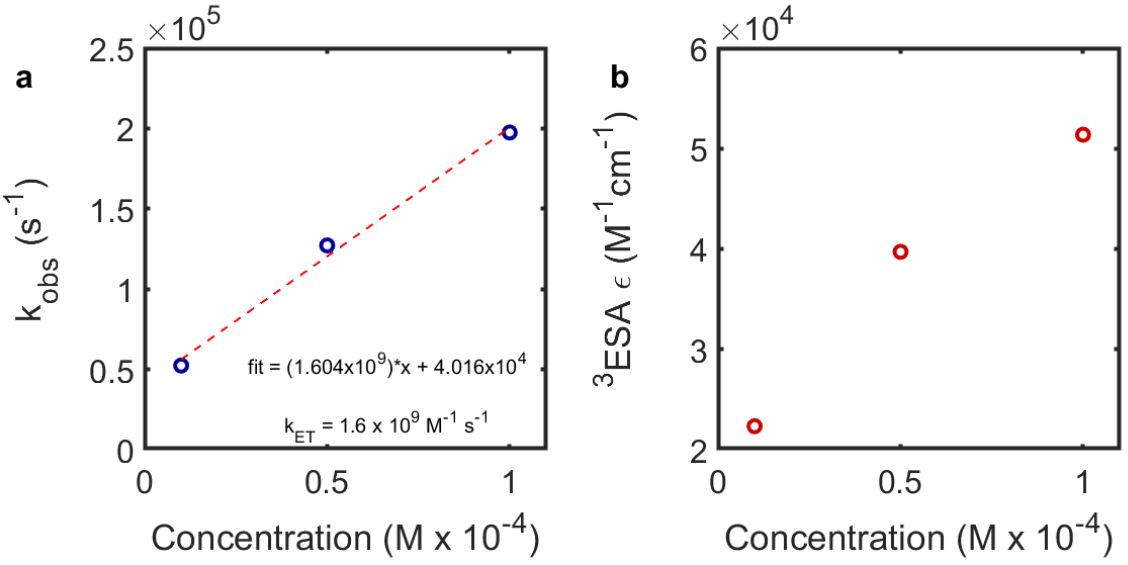

Figure A.38 Concentration-dependent photosensitization experiments between Anthracene (500 μM) and Li_2(DPP-Pent)$_2$ (X μM, X = 10, 50, 100): (a) observed energy transfer rate (k_{obs}) vs. Li_2(DPP-Pent)$_2$ concentration (based on formula weight), fitted to a linear function, the slope of which gives the bimolecular rate constant (k_{ET}); (b) calculated Li_2(DPP-Pent)$_2$ ^{3}ESA extinction coefficient vs. Li_2(DPP-Pent)$_2$ concentration.

XI. $Li_2(DPP\text{-}Pent)_2$: Triplet Yield Estimation

i. Method: extinction coefficient

As with HDPP-Pent, the concentration of excited singlets is first estimated using the energy of the 550 nm pump excitation, the absorbance of the sample at 550 nm (0.0711), and the excitation volume (1.06×10^{-7} L).

$$[S_1] = \frac{(2.77 \times 10^{11}) \cdot (0.1489)}{(6.022 \times 10^{23}) \cdot (1.06 \times 10^{-7})} = 6.5 \times 10^{-7}\ M$$

As we do not have evidence to suggest there is significant singlet population overlapped with the triplet ESA at its maximum in the TA data of $Li_2(DPP\text{-}Pent)_2$, we directly estimate the triplet yield without correction from the fitted data.

$$[T_1] = \frac{\Delta OD_{510nm}}{\varepsilon\,{}^3{}_{LiDPP-Pent} \cdot l}$$

$$[T_1] = \frac{0.013}{(52{,}000) \cdot (0.2)} = 1.27 \times 10^{-6}\ M$$

$$Triplet\ Yield = \frac{[T_1]}{[S_1]} \cdot 100 = \frac{1.27 \times 10^{-6}\ M}{9.7 \times 10^{-7}\ M} \cdot 100$$

$$Triplet\ Yield \sim 195\ \%$$

ii. Method: ground state bleach

We can estimate the triplet yield in Li_2(DPP-Pent)$_2$ via the ground state bleach in the method of Eaton et al.[9] The percentage of excited molecules estimated from the energy density of the 550 nm pump is approximately 1.1%, and using the ground state absorbance at 625 nm (0.2), we can estimate the expected ground state bleach intensity of -0.0022. From this we can estimate a triplet yield of ~ 186%.

$$Predicted\ Max\ \Delta OD_{625\ nm} = -2.2\ mOD$$

$$Experimental\ Max\ \Delta OD_{625\ nm} = -4.1\ mOD$$

$$Triplet\ Yield = \frac{-4.1}{-2.2} \cdot 100 \sim 186\ \%$$

XII. Comparison Between Singlet Fission Rates and Triplet Lifetimes

Table A.14 Comparison between singlet fission (τ_{SF}) and triplet lifetimes (τ_T) for HDPP-Pent, Li_2(DPP-Pent)$_2$, KDPP-Pent, and previously reported bipentacene systems *ortho*-**2**, *meta*-**2**, and *para*-**2** (in benzonitrile),[10] BP0, BP1, BP2,[11] TFM, BCO, Spi, and EBD (in chloroform),[12] PD, and PT.[13] The compounds are referenced using the moniker given in their respective texts, and structures are provided for each following the table. Here, τ_T is used generally for the fitted lifetimes of the triplet features in the transient absorption spectrum, encompassing both ^{M}(TT) – the shorter lifetime(s) – and uncorrelated triplet lifetimes where applicable. A comprehensive review of lifetimes in covalently linked dimers appears in Korovina et al.[14]

	τ_{SF}	τ_T
ortho-**2**	500 fs	12 ps
meta-**2**	63 ps	2.2 ns
para-**2**	2.7 ps	17.3 ps
BP0	760 fs	450 ps
BP1	20 ps	16.5 ns
BP2	220 ps	270 ns (1)
TFM	49.7 ps	531 ns (1), 23.0 μs (2)
BCO	20 ns	1.8 μs (1), 18.0 μs (2)
Spi	54.5 ps	705 ns (1), 19.6 μs (2)
EBD	10.4 ps	174 ns (1), 24.3 μs (2)
PD	435 ps	8.3 ns (1); 87 ns (2); 25 μs (3)
PT	147 ps	12 ns (1); 70 ns (2); 32 μs (3)
HDPP-Pent	730 ps	38 ns (1); 36 μs (2)
Li_2(DPP-Pent)$_2$	100 ps	23 ns (1); 35 μs (2)
KDPP-Pent	400 – 600 ps	12 ns (1); 27 μs (2)

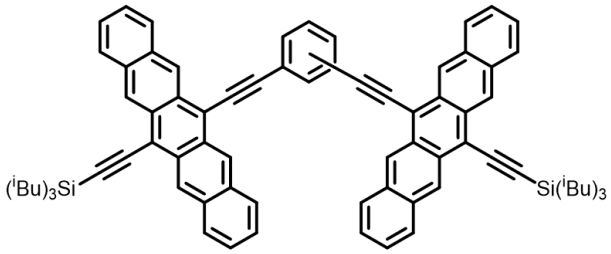

*ortho-, meta-, and para-***1**

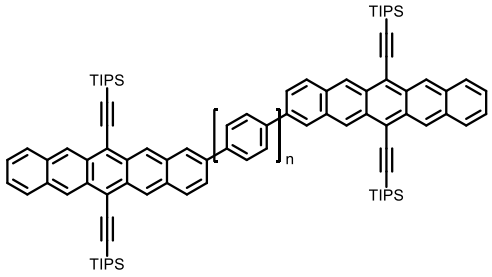

BPn (n=0,1,2)

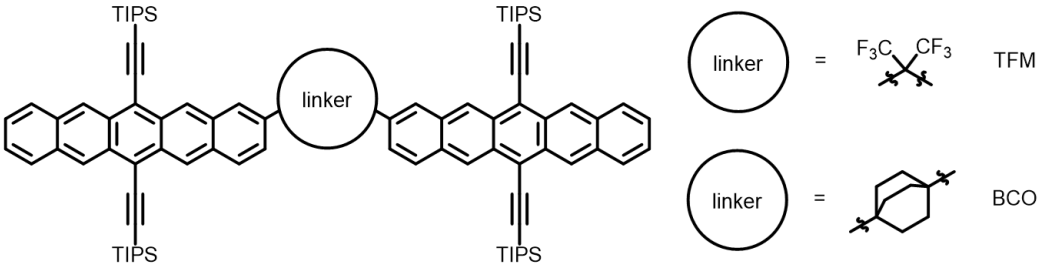

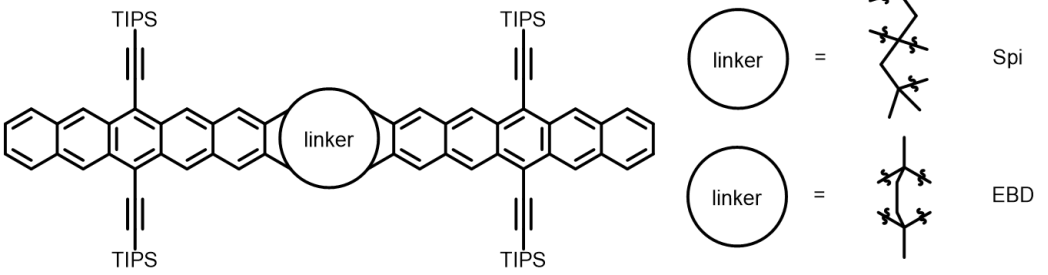

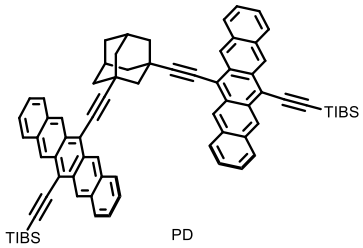

PD

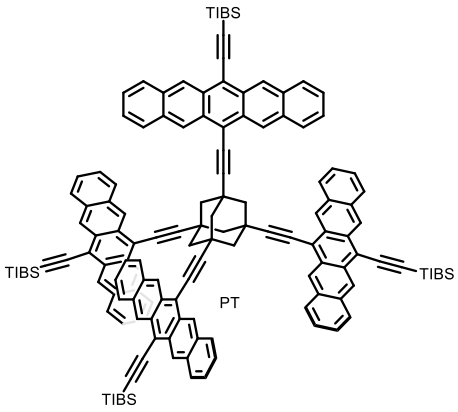

PT

XIII. ^{1}H and ^{13}C NMR

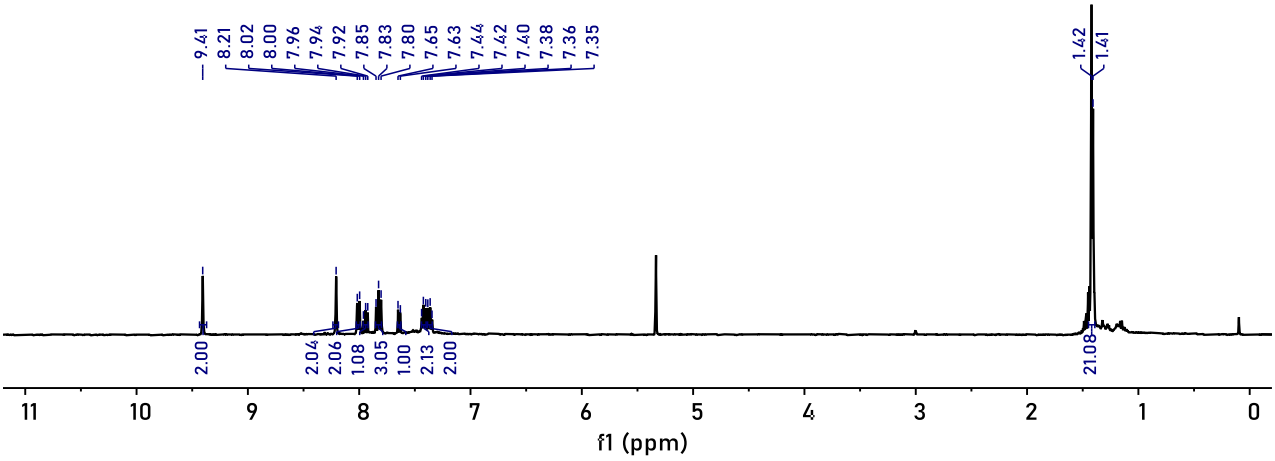

Figure A.39 ^{1}H NMR spectrum of PentPyBr (400 MHz, $CDCl_3$).

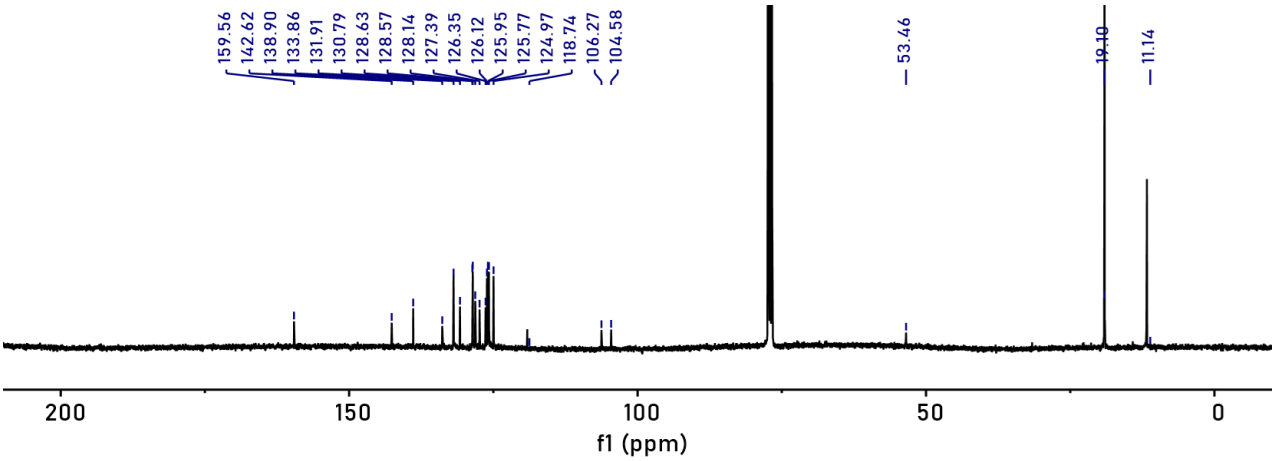

Figure A.40 ^{13}C NMR spectrum of PentPyBr (400 MHz, $CDCl_3$).

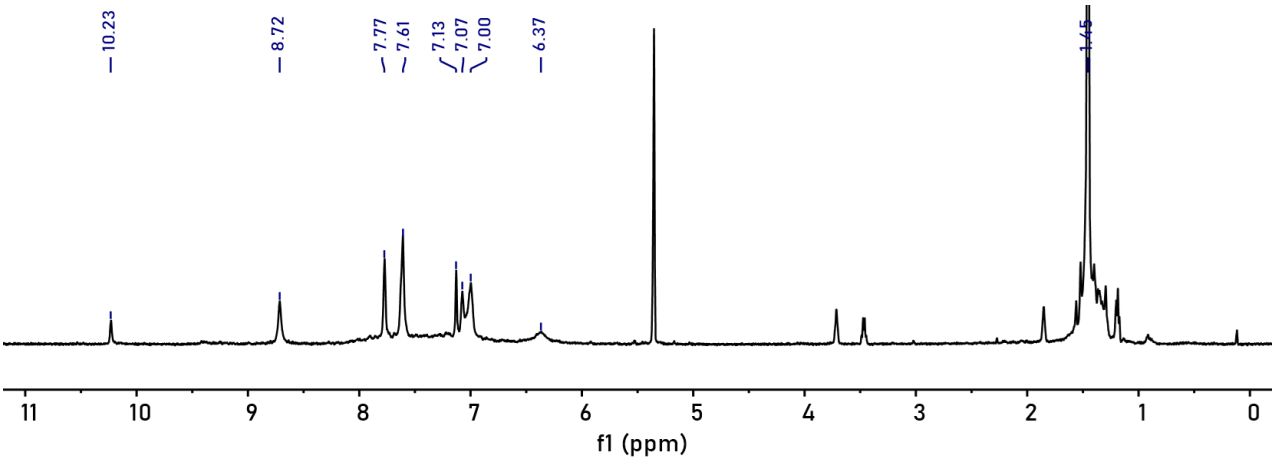

Figure A.41 ^{1}H NMR spectrum of HDPP-Pent (400 MHz, CD_2Cl_2).

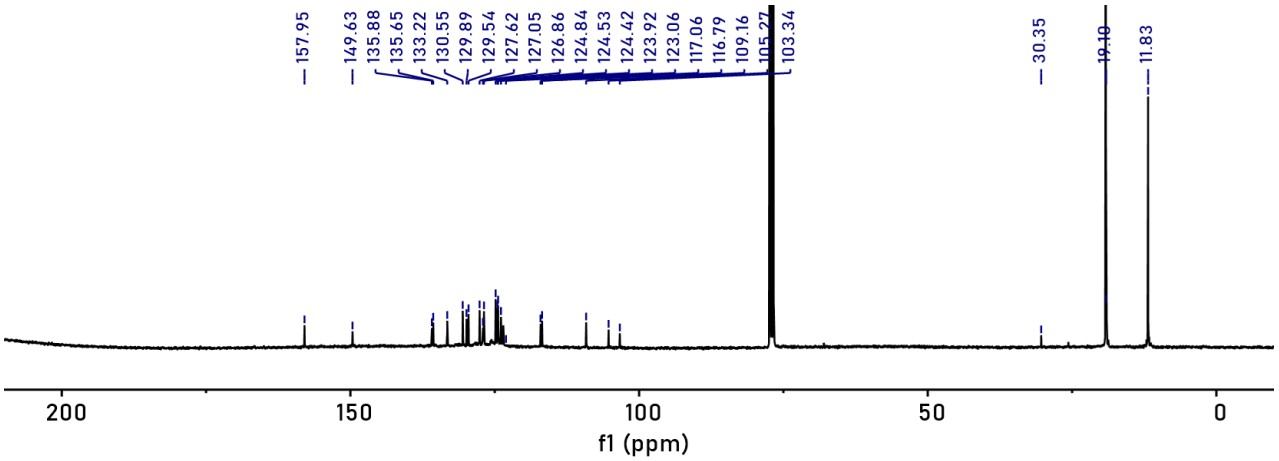

Figure A.42 ^{13}C NMR spectrum of HDPP-Pent (400 MHz, $CDCl_3$).

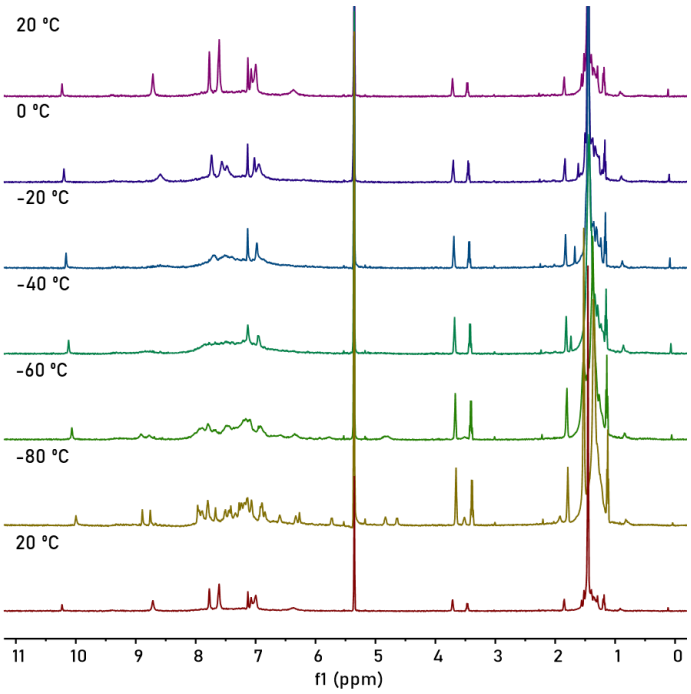

Figure A.43 Variable temperature ^{1}H NMR spectra of HDPP-Pent (400 MHz, CD_2Cl_2).

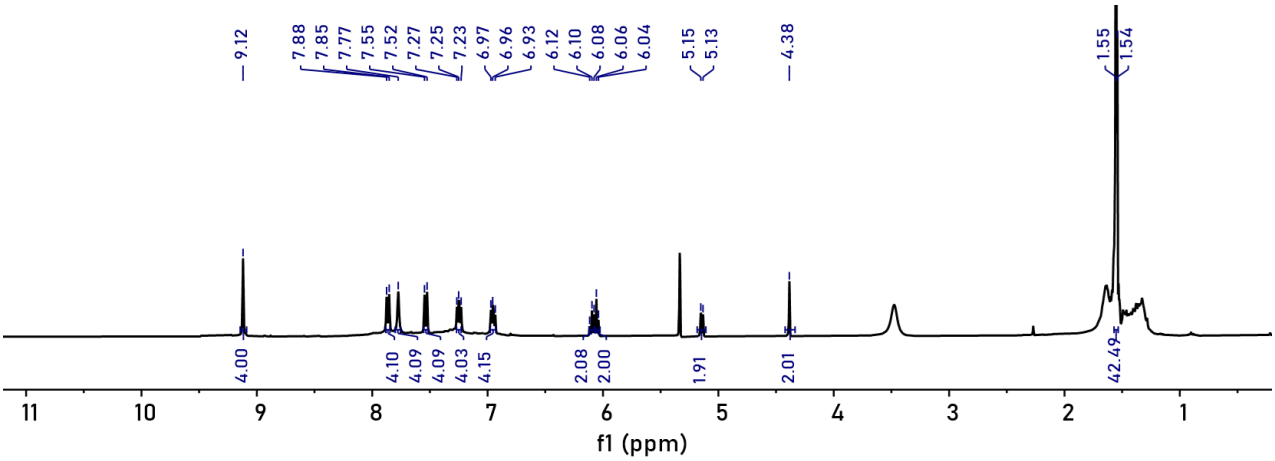

Figure A.44 ^{1}H NMR spectrum of $Li_2(DPP\text{-}Pent)_2$ (400 MHz, CD_2Cl_2).

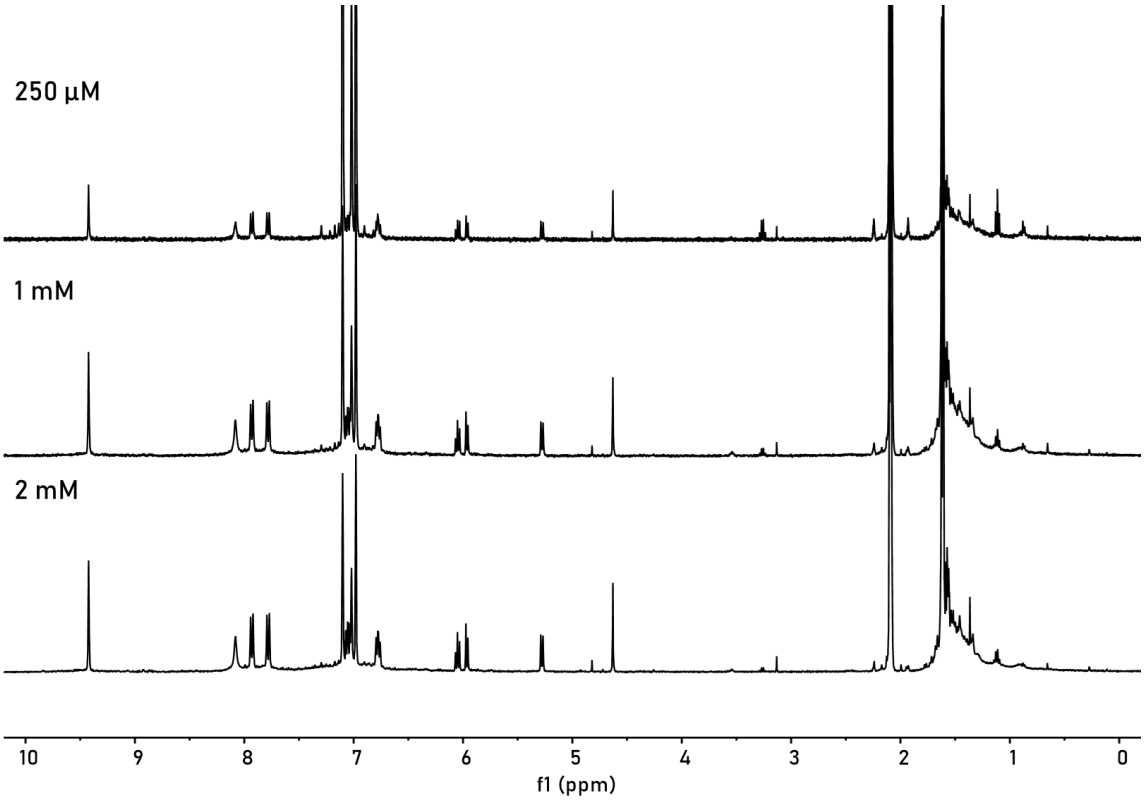

Figure A.45 ^{1}H NMR spectrum of $Li_2(DPP\text{-}Pent)_2$ at different concentrations in toluene-d8 (400 MHz, toluene-d8).

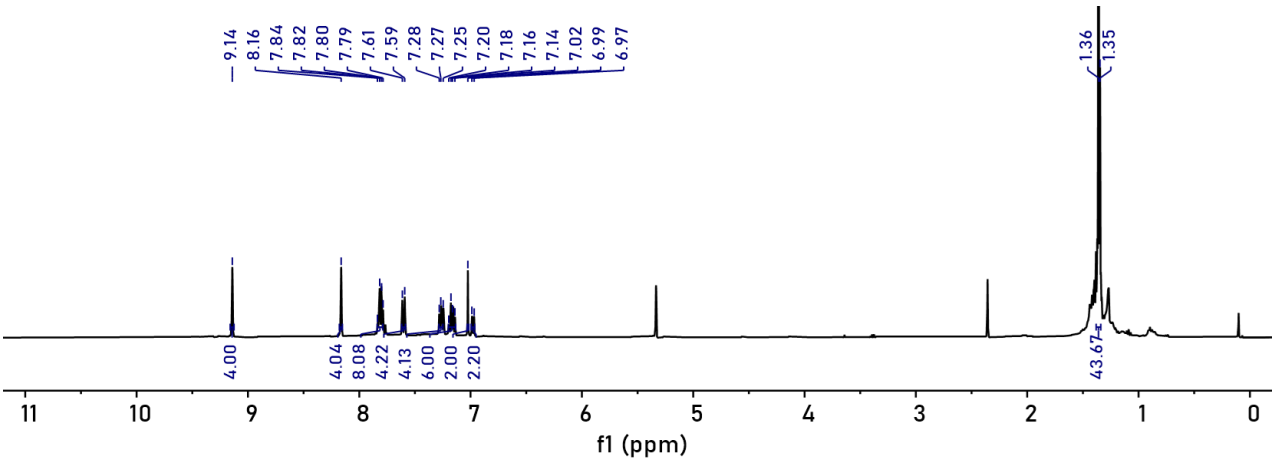

Figure A.46 ^{1}H NMR spectrum of KDPP-Pent (400 MHz, CD_2Cl_2).

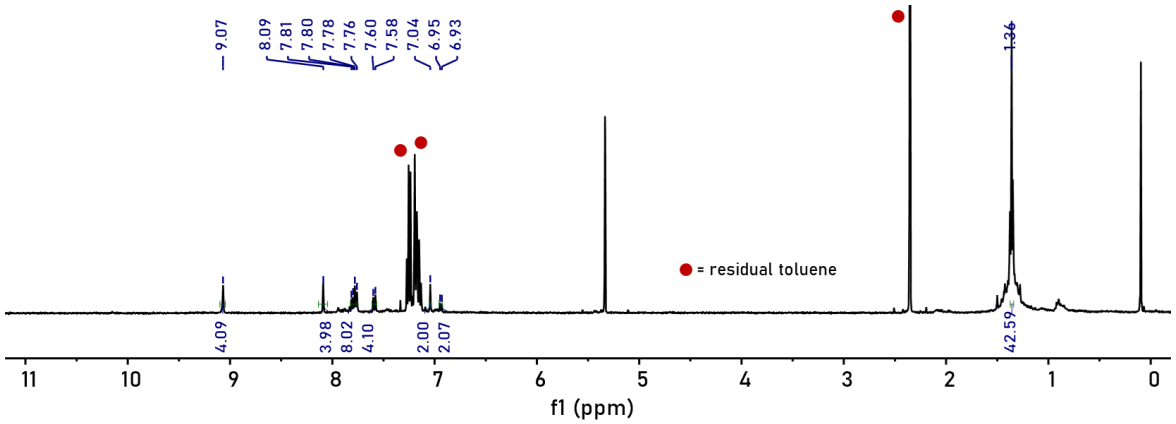

Figure A.47 ^{1}H NMR spectrum of NaDPP-Pent (400 MHz, CD_2Cl_2). A significant amount of toluene (peaks at 2.34, 7.14, 7.24 ppm) remained in the sample post-synthesis despite extensive drying *in vacuo*. Further handling and attempts to fully remove the toluene led to a small degree of decomposition. The toluene multiplets in the aromatic region mask three peaks expected in the compound but can be inferred from cross peaks detected in the COSY and ROESY experiments.

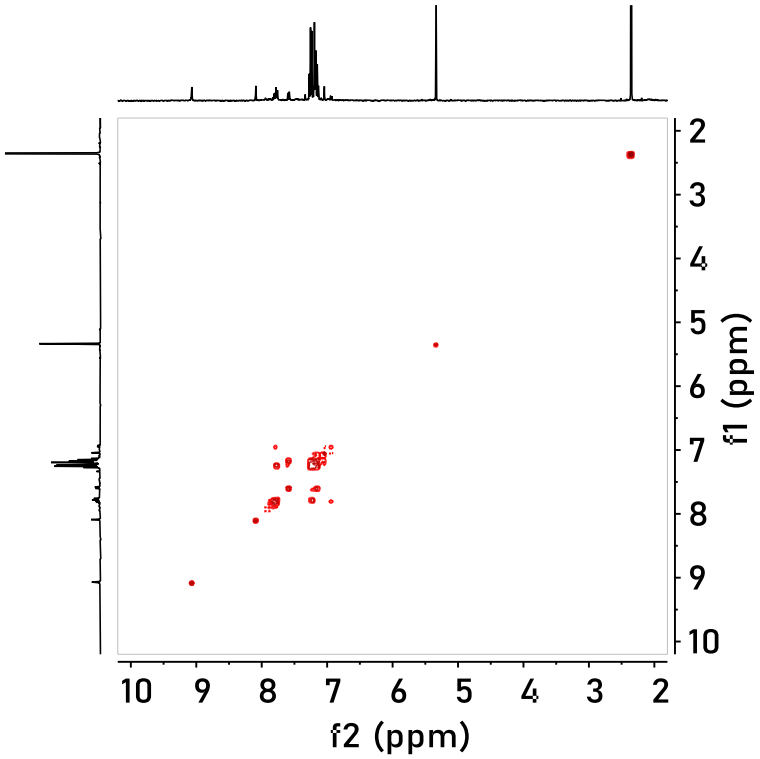

Figure A.48 Gradient COSY spectrum of NaDPP-Pent (400 MHz, CD_2Cl_2).

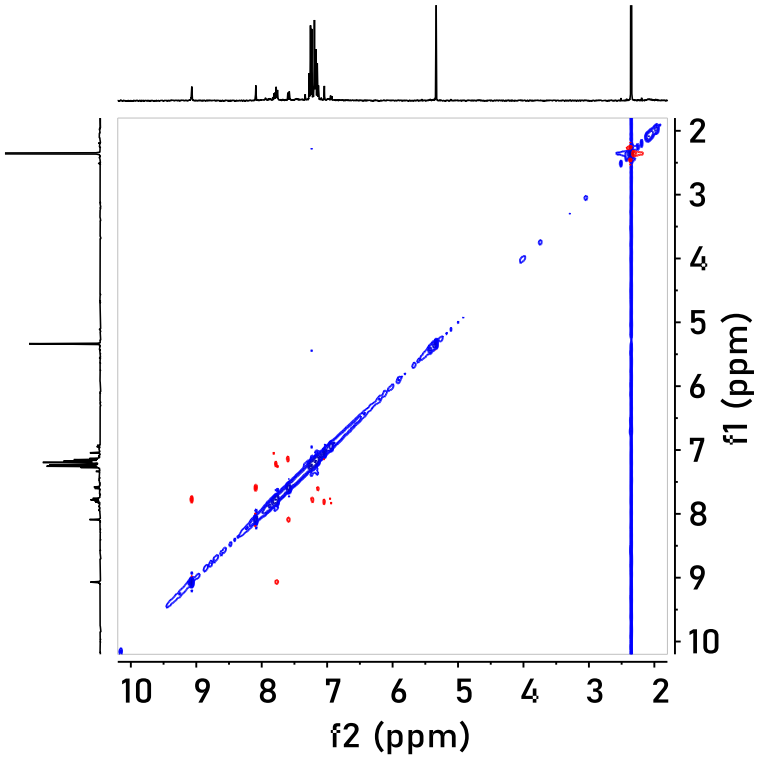

Figure A.49 2D ROESY spectrum of NaDPP-Pent (400 MHz, CD_2Cl_2).

XIV. $Li_2(DPP\text{-}Anth)_2$ Crystallographic Information

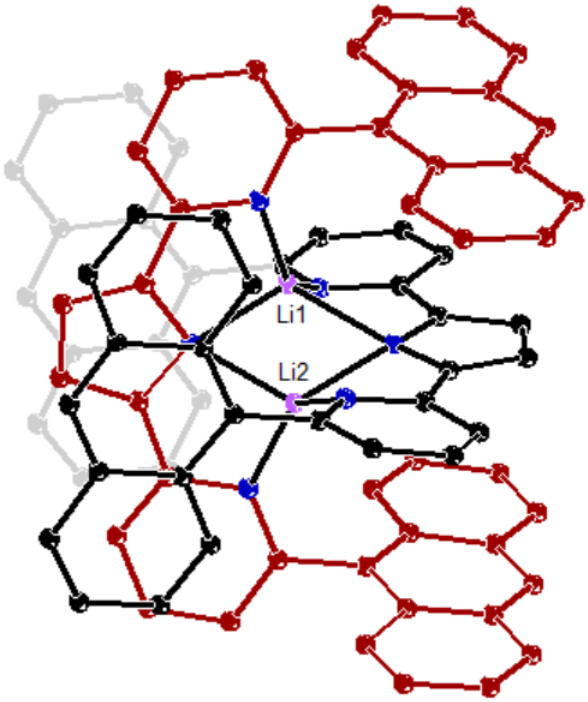

Figure A.50 X-ray crystal structure of $Li_2(DPP\text{-}Anth)_2$. The DPP-Anth ligand 1 and 2 are coded as black and red, respectively. Ellipsoids are drawn at the 50% probability level.

Table A.14 Crystal and refinement data for $Li_2(DPP\text{-}Anth)_2$

	$Li_2(DPP\text{-}Anth)_2$
CCDC	2031858
Empirical formula	$C_{84}H_{52}Li_2N_6$
Formula weight	1158.46
Temperature/K	100
Crystal System	Triclinic
Space group	P -1
a/Å	14.6365(8)
b/Å	15.1790(7)
c/Å	16.9748(11)
α/°	69.030(4)
β/°	68.970(5)
γ/°	70.059(4)
Volume/Å^3	3187.6
Z	2
ρ_{calc}g/cm^3	1.296
μ/mm^{-1}	1.331
F(000)	1297.0
Radiation	Cu Kα (λ = 1.54178)
2θ range for data collection	5.8 to 158.22
Index ranges	$-16 \leq h \leq 18$, $-18 \leq k \leq 14$, $-8 \leq l \leq 20$
Reflection collected	9802
Independent reflections	7982 [R_{int} = 0.0820, R_{sigma} = 0.1123]
Data/restraints/parameters	7982/0/856
Goodness-of-fit on F^2	1.081
Final R indexes [I>=2σ (I)]	R_1 = 0.0991, wR_2 = 0.2473
Final R indexes [all data]	R_1 = 0.1716, wR_2 = 0.2991
Largest diff. peak/hole/e Å^{-3}	1.16/-1.09

1. Lehnherr, D., McDonald, R. & Tykwinski, R. R. Exploring Electronically Polarized Pentacenes. *Org. Lett.* **10**, 4163–4166 (2008).
2. Seechurn, C. C. C. J., Sivakumar, V., Satoskar, D. & Colacot, T. J. Iridium-Catalyzed C–H Borylation of Heterocycles Using an Overlooked 1,10-Phenanthroline Ligand: Reinventing the Catalytic Activity by Understanding the Solvent-Assisted Neutral to Cationic Switch. *Organometallics* **33**, 3514–3522 (2014).
3. Snellenburg, J. J., Laptenok, S., Seger, R., Mullen, K. M. & Stokkum, I. H. M. van. Glotaran: A Java-Based Graphical User Interface for the R Package TIMP. *Journal of Statistical Software* **49**, 1–22 (2012).
4. Bensasson, R. & Land, E. J. Triplet-triplet extinction coefficients via energy transfer. *Trans. Faraday Soc.* **67**, 1904–1915 (1971).
5. Amand, B. & Bensasson, R. Determination of triplet quantum yields by laser flash absorption spectroscopy. *Chemical Physics Letters* **34**, 44–48 (1975).
6. Compton, R. H., Grattan, K. T. V. & Morrow, T. Extinction coefficients and quantum yields for triplet—triplet absorption using laser flash photolysis. *Journal of Photochemistry* **14**, 61–66 (1980).
7. Nielsen, B. R., Jørgensen, K. & Skibsted, L. H. Triplet—triplet extinction coefficients, rate constants of triplet decay and rate constant of anthracene triplet sensitization by laser flash photolysis of astaxanthin, β-carotene, canthaxanthin and zeaxanthin in deaerated toluene at 298 K. *Journal of Photochemistry and Photobiology A: Chemistry* **112**, 127–133 (1998).
8. Walker, B. J., Musser, A. J., Beljonne, D. & Friend, R. H. Singlet exciton fission in solution. *Nature Chemistry* **5**, 1019–1024 (2013).

9. Eaton, S. W. *et al.* Singlet Exciton Fission in Polycrystalline Thin Films of a Slip-Stacked Perylenediimide. *J. Am. Chem. Soc.* **135**, 14701–14712 (2013).
10. Zirzlmeier, J. *et al.* Singlet fission in pentacene dimers. *PNAS* **112**, 5325–5330 (2015).
11. Sanders, S. N. *et al.* Quantitative Intramolecular Singlet Fission in Bipentacenes. *J. Am. Chem. Soc.* **137**, 8965–8972 (2015).
12. Kumarasamy, E. *et al.* Tuning Singlet Fission in π-Bridge-π Chromophores. *J. Am. Chem. Soc.* **139**, 12488–12494 (2017).
13. Hetzer, C. *et al.* Chromophore Multiplication To Enable Exciton Delocalization and Triplet Diffusion Following Singlet Fission in Tetrameric Pentacene. *Angewandte Chemie International Edition* **58**, 15263–15267 (2019).
14. Korovina, N. V., Pompetti, N. F. & Johnson, J. C. Lessons from intramolecular singlet fission with covalently bound chromophores. *J. Chem. Phys.* **152**, 040904 (2020).

Appendix B:

Experimental Methods and Supplementary Figures for Chapter 3: Magnetic Relaxation in CuPc and VOPc

Methods

B.1 Synthesis and Sample Preparation

Copper phthalocyanine (CuPc), zinc phthalocyanine (ZnPc), titanyl phthalocyanine (TiOPc, Type IV), and vanadyl phthalocyanine (VOPc) were purchased from Sigma Aldrich and used without further purification.

CuPc:ZnPc 1:1000

CuPc:ZnPc 1:1000 was prepared by a modification of previously reported preparations[1] of α-CuPc. CuPc (0.5 mg) and ZnPc (498.7 mg) were added to a 50 mL Erlenmeyer flask with a magnetic stir bar. Concentrated H_2SO_4 (10 mL) was added, dissolving the materials, and the dark green solution was stirred for 15 min. The solution was then poured onto DI H_2O ice (previously prepared) to cause precipitation of a dark green solid. The precipitate was filtered, washed with DI H_2O, and dried overnight under vacuum on a Schlenk line.

CuPc:ZnPc 1:100

CuPc:ZnPc 1:100 was prepared analogously to the 1:1000 sample. CuPc (2.0 mg), ZnPc (196.5 mg), and H_2SO_4 (5 mL) were used for the appropriate ratios.

VOPc:TiOPc 1:1000

VOPc:TiOPc 1:1000 was prepared via an established method.[2] VOPc (Type II, 0.5 mg) and TiOPc (Type IV, 497.0 mg) were added to a 250 mL Erlenmeyer flask with a magnetic stir bar. A mixture of trifluoroacetic acid (11 mL) and dichloromethane (DCM) (44 mL) was then added to dissolve the reagents. The dark blue-green solution was stirred for 15 min and then poured into isopropyl alcohol (IPA) (460 mL) causing the precipitation of a fine bright blue precipitate. The mixture was stirred for an additional 15 min. Fractions were centrifuged and the blue residue was washed with IPA and recentrifuged. IPA was used to transfer the remaining blue residue to a 100 mL round-bottom flask, and the solvent was removed via rotary evaporation. The sample was then rigorously dried overnight under vacuum on a Schlenk line.

VOPc:TiOPc 1:100

VOPc:TiOPc 1:100 was prepared analogously to the 1:1000 sample as above. VOPc (Type II, 1.7 mg), TiOPc (Type IV, 172.9 mg), trifluoroacetic acid (4 mL), DCM (16 mL), and IPA (200 mL) were used for the appropriate ratios.

B.2 EPR Spectroscopy

Continuous wave (CW) X-Band EPR spectra were acquired on a Brucker EMX spectrometer. All pulse X- and Q-band EPR experiments were performed using a Bruker ELEXSYS E580 pulse EPR Spectrometer. X-band measurements were performed using a Bruker MS-5 Resonator. Simulations of all CW and pulse EPR data were achieved using the EasySpin simulation toolbox (release 5.2.25) with MATLAB 2019b.[3] Q-band measurements were performed using a Bruker MD-4 X-band Resonator. Temperature control was achieved using an Oxford Instruments CF935 cryogen flow cryostat using liquid helium (5 -100 K) or liquid nitrogen (>100 K) and a Mercury ITC temperature controller. Pulse electron spin-echo detected EPR (ESE-EPR) field-swept spectra were acquired using the 2-pulse "Hahn-echo" sequence ($\pi/2 - \tau - \pi -$ echo). T_m measurements were performed using the same Hahn echo sequence ($\pi/2 - \tau - \pi -$ echo) at fixed magnetic fields, with τ varied at regular intervals to measure the decay in echo intensity. T_1 measurements were performed using the inversion recovery pulse sequence (π - T - $\pi/2 - \tau - \pi$ – echo), where T is a variable delay and τ is a fixed delay of 200 ns.

Inversion recovery and echo decay experiments were fit using stretched-exponential Equation S1 and Equation S2, respectively.

Equation S1.

$$I = I_0 + k_1 \exp\left[-\left(\frac{\tau}{T_1}\right)^{\beta_1}\right]$$

Equation S2.

$$I = I_0 + k_m \exp\left[-\left(\frac{2\tau}{T_m}\right)^{\beta_m}\right]$$

The temperature dependence of T_1 was modeled for 1:1000 CuPc:ZnPc and VOPc:TiOPc samples using the equation below, which includes direct, Raman, and local mode-mediated processes. As the electronic excited states in CuPc and VOPc are estimated to be much higher in energy than the Debye temperature, we do not expect an Orbach mechanism to be operative in these systems, consistent with another report.[4]

$$\frac{1}{T_1} = A_{dir} \cdot T + B_{ram} \cdot \left(\frac{T}{\theta_D}\right)^9 \cdot J_8\left(\frac{\theta_D}{T}\right) + C_{loc} \cdot \frac{e^{\Delta_{loc}/T}}{(e^{\Delta_{loc}/T} - 1)^2}$$

A_{dir}, B_{ram}, and C_{loc} represent the coefficients for the direct, Raman, and local mode processes, respectively, θ_D is the Debye temperature (K), Δ_{loc} is the local mode energy (K), and $J_8(\theta_D/T)$ represents the transport integral, shown below.

$$J_8\left(\frac{\theta_D}{T}\right) = \int_0^{\theta_D/T} x^8 \cdot \frac{e^x}{(e^x - 1)^2}\, dx$$

Here we approximate the solution of the transport integral as the n-power of θ_D/T, which leads to the following equation.[5]

$$\frac{1}{T_1} = A_{dir} \cdot T + B_{ram} \cdot \left(\frac{T}{\theta_D}\right)^n + C_{loc} \cdot \frac{e^{\Delta_{loc}/T}}{(e^{\Delta_{loc}/T} - 1)^2}$$

We acknowledge the limitations of this phenomenological fitting. As addressed by others previously, this equation is not well fit using a least-squares minimization procedure, as each process contributes differently at different temperatures and some parameters are correlated.[6] We begin by fitting the data to a Raman process. The power dependence of the Raman process may first be estimated from the slope of the log-log plot of the spin-lattice relaxation rates, using $\log(1/T_1) = n \cdot \log(T)$. A rough approximation of the Raman function was achieved by a least-squares minimization by manually adjusting parameters until a reasonable combination of Raman coefficient and Debye temperature was obtained. Debye temperatures for copper(II) and vanadyl complexes have typically been found to be less than 130 K.[4] The Raman parameters were then fixed, and the local mode function was added to the fit. The local mode coefficient and energy were then varied until a reasonable fit was achieved. This process of fixing the parameters of one process while adjusting the parameters of the other was iterated until an optimal fit was achieved. Finally, a direct process was added and the direct coefficient was manually increased until the low-temperature data points were fit.

B.3 Powder X-Ray Diffraction

All powder X-ray diffraction (PXRD) patterns were collected on an Analytical X'Pert Pro diffractometer with a Cu source at 40 kV and 40 mA. Data were collected from 5°-40° 2θ.

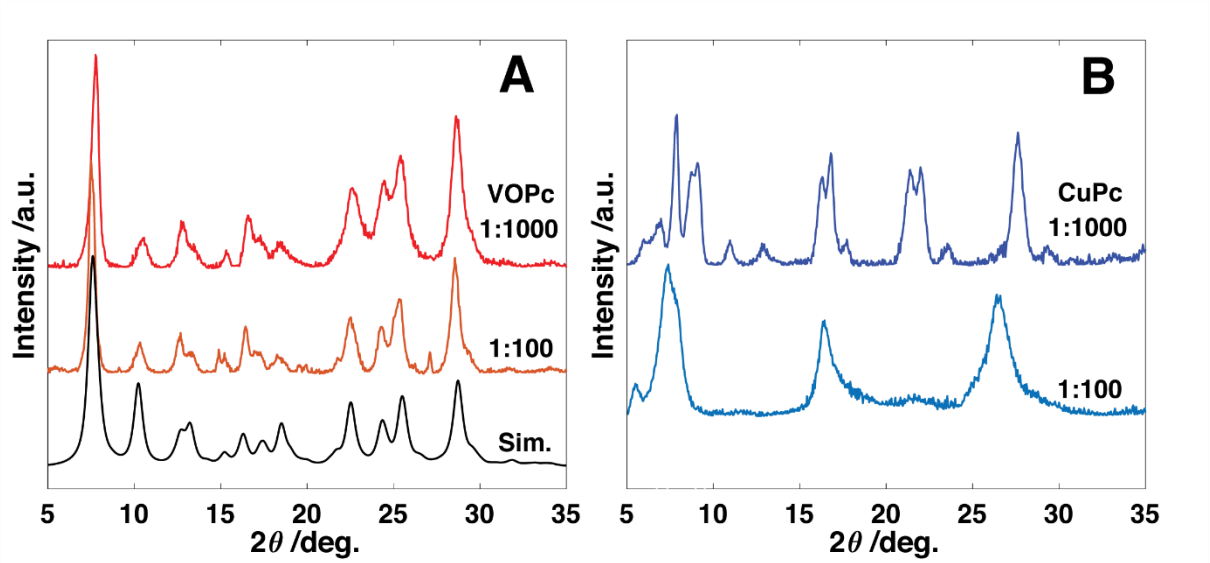

Figure B.1 (A) Comparison between PXRD patterns of VOPc:TiOPC at concentrations of 1:1000 (top), 1:100 (middle), and simulated Type II VOPc (bottom). **(B)** Comparison between the PXRD patterns of CuPc:ZnPc 1:1000 (top), 1:100 (middle), and simulated β-CuPc (bottom).

The PXRD patterns of both the 1:1000 and 1:100 VOPc:TiOPc mixtures shown in Figure S1 are consistent with previously reported diffraction data for the type-II polymorph and are well reproduced by simulation. This indicates structural phase homogeneity of the vanadyl samples. The PXRD patterns of the 1:1000 and 1:100 CuPc:ZnPc dispersions show distinct patterns between samples and do not strictly match either the reported α- or β-CuPc diffraction patterns.[7]

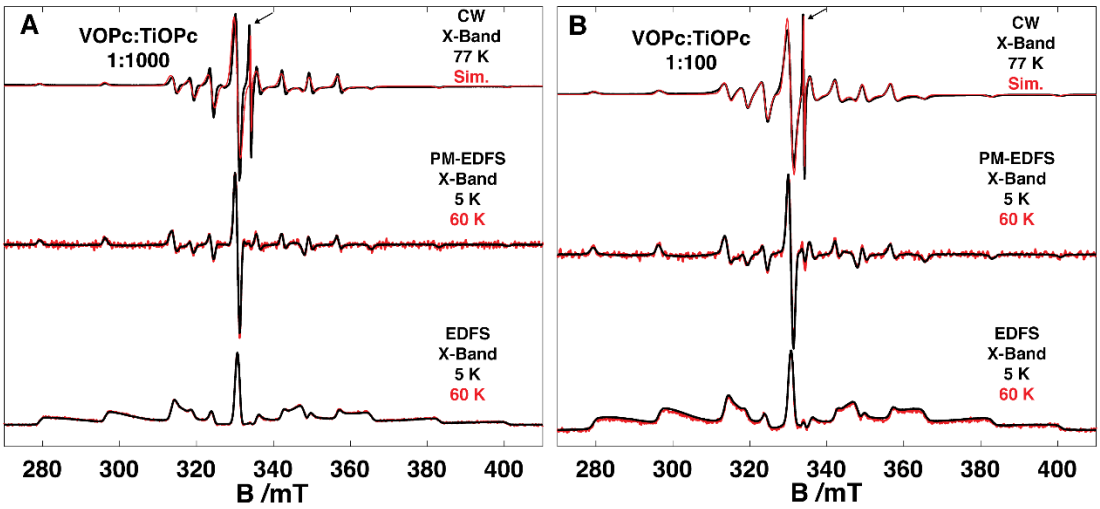

Figure B.2 Comparison between CW X-band EPR at 77 K to pseudo-modulated echo-detected field sweeps (PM-EDFSs) and the associated field sweeps at 5 K (black) and 60 K (red) of **(A)** VOPc 1:1000 and **(B)** 1:100. The additional radical species is indicated by an arrow.

	1:1000 VOPc:TiOPc	**1:100 VOPc:TiOPc**
$\mathbf{g_{\parallel}}$	1.968	1.968
$\mathbf{g_{\perp}}$	1.988	1.988
$\mathbf{A_{\parallel}}$ **(MHz)**	478.6	473.6
$\mathbf{A_{\parallel}}$ **(cm^{-1})**	160 x 10^{-4}	158 x 10^{-4}
$\mathbf{A_{\perp}}$ **(MHz)**	167.6	167.9
$\mathbf{A_{\perp}}$ **(cm^{-1})**	56 x 10^{-4}	56 x 10^{-4}

Table B.1 Best-fit parameters of the simulated EPR spectra in Figure S2 used to reproduce the EPR spectra T = 77 K.

The CW-EPR of the 1:1000 and 1:100 samples of VOPc are similar. The 1:100 sample exhibits slightly broader features, presumably due to increased dipolar interactions with other vanadyl species at this higher concentration. The EDFSs of the two dilutions at both 5 K and 60 K are similar and consistent with literature reports. The PM-EDFS spectra lack the sharp radical feature present in the CW EPR (although it may slightly appear in the 1:100 spectrum), indicating that the spins responsible for this signal relax significantly slower than the shot repetition time of the spin-echo detection experiment. This feature has previously been attributed to organic radical impurities that are consistently found even in diamagnetic phthalocyanine matrices.[2,8]

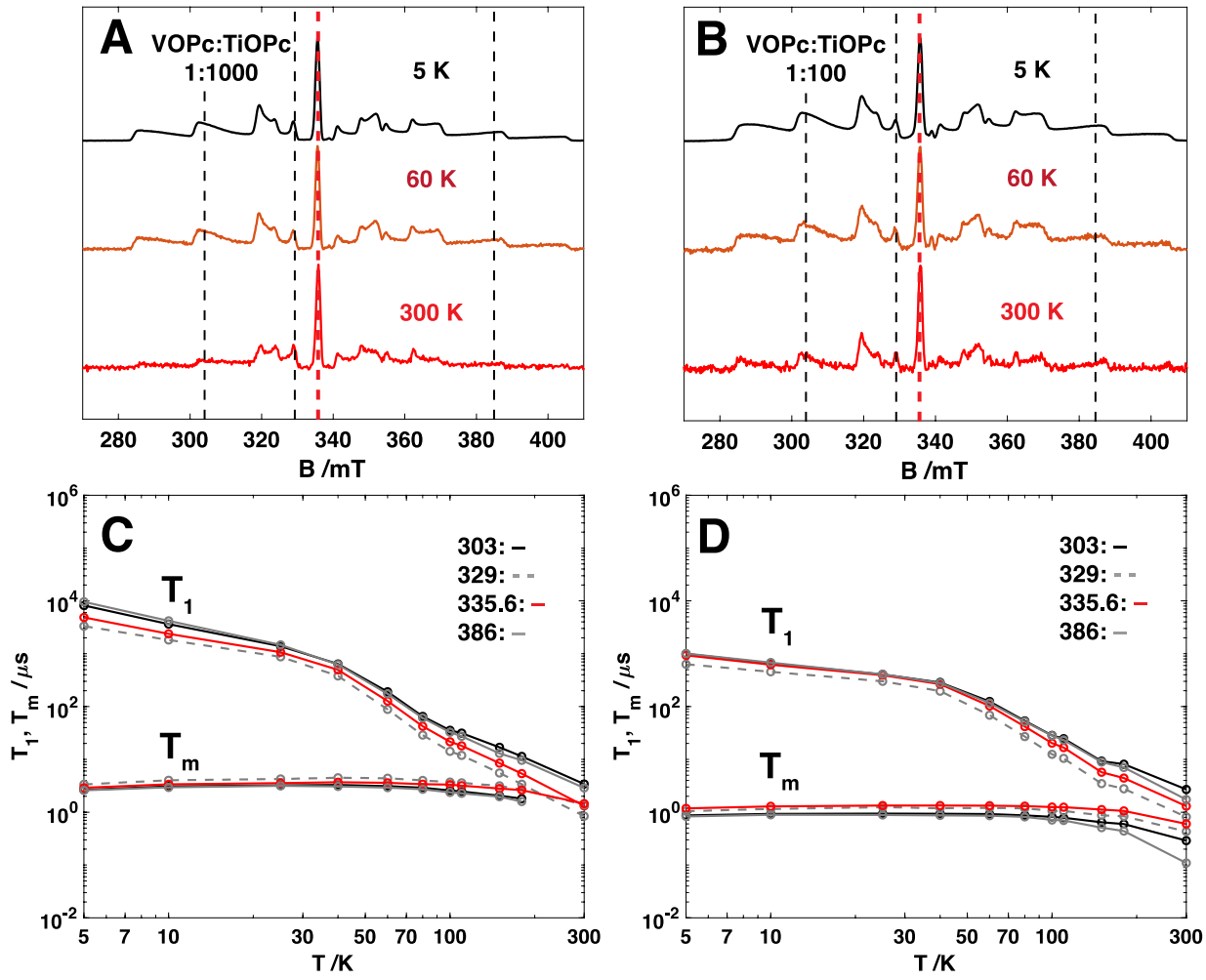

Figure B.3 Echo-detected EPR X-band field sweeps of **(A)** VOPc:TiOPc 1:1000 and **(B)** 1:100 at 5 K, 60 K, and 300 K. Dashed lines indicate field positions where relaxation data were collected. Comparison between the field position dependent behavior of the T_1 and T_m relaxation times from 5 to 300 K of VOPc:TiOPc **(C)** 1:1000 and **(D)** 1:100.

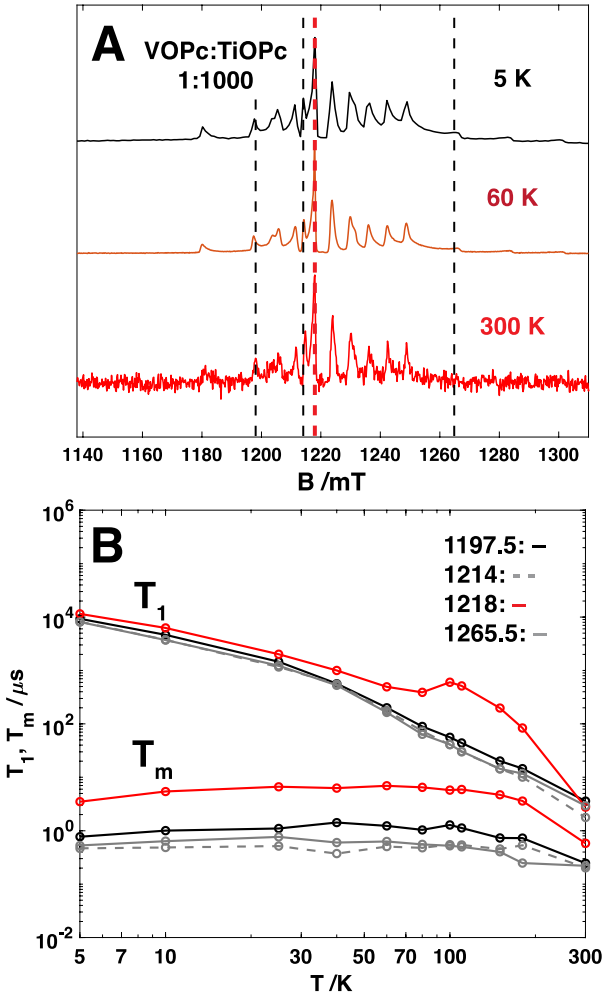

Figure B.4 EDFS EPR Q-band of **(A)** VOPc 1:1000 at 5 K, 10 K, and 60 K. Dashed lines indicate field positions where relaxation data was collected. Comparison of the field position dependent behavior of the T_1 and T_m relaxation times from 5 to 300 K of VOPc **(B)** 1:1000.

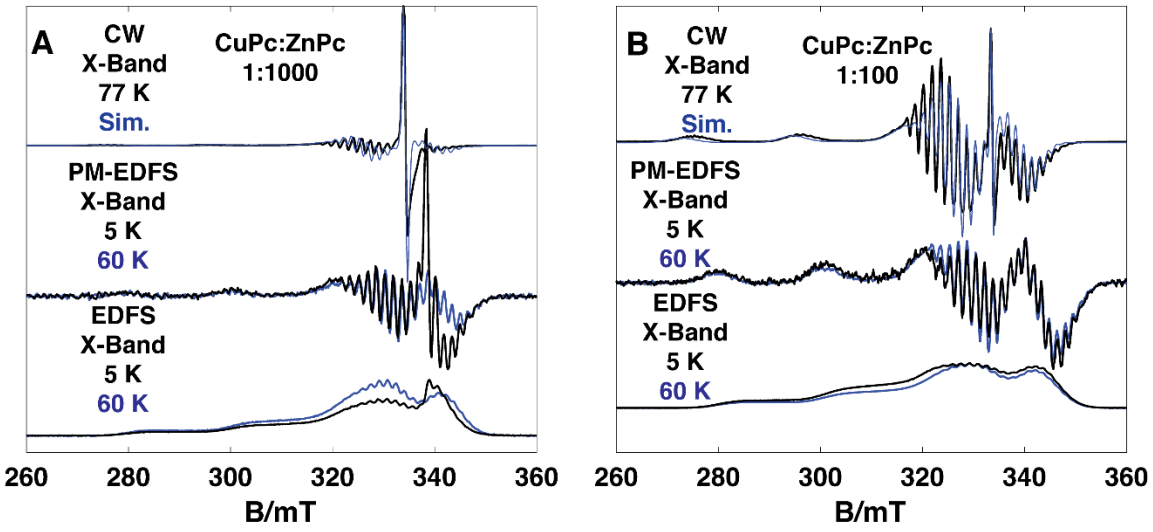

Figure B.5 Comparison between CW-EPR at 77 K to PM-EDFSs and the associated field sweeps at 5 K (black) and 60 K (blue) of **(A)** CuPc:ZnPc 1:1000 and **(B)** 1:100.

	1:1000 CuPc:ZnPc	**1:100 CuPc:ZnPc**
$\mathbf{g_{\parallel}}$	2.047	2.049
$\mathbf{g_{\perp}}$	2.185	2.172
$\mathbf{A_{Cu\parallel}}$ **(MHz)**	655.0	646.5
$\mathbf{A_{Cu\parallel}}$ **(cm^{-1})**	218 x 10^{-4}	216 x 10^{-4}
$\mathbf{A_{Cu\perp}}$ **(MHz)**	35.3	15.2
$\mathbf{A_{Cu\perp}}$ **(cm^{-1})**	12 x 10^{-4}	5 x 10^{-4}
$\mathbf{A_{N\perp}}$ **(MHz)**	45	45-50
$\mathbf{A_{N\perp}}$ **(cm^{-1})**	15 x 10^{-4}	15-17 x 10^{-4}
$\mathbf{A_{N\parallel}}$ **(MHz)**	45	40-48
$\mathbf{A_{N\parallel}}$ **(cm^{-1})**	15 x 10^{-4}	13-16 x 10^{-4}

Table B.2 Best-fit parameters of the simulated EPR spectra in Figure S5 used to reproduce the EPR spectra T = 77 K.

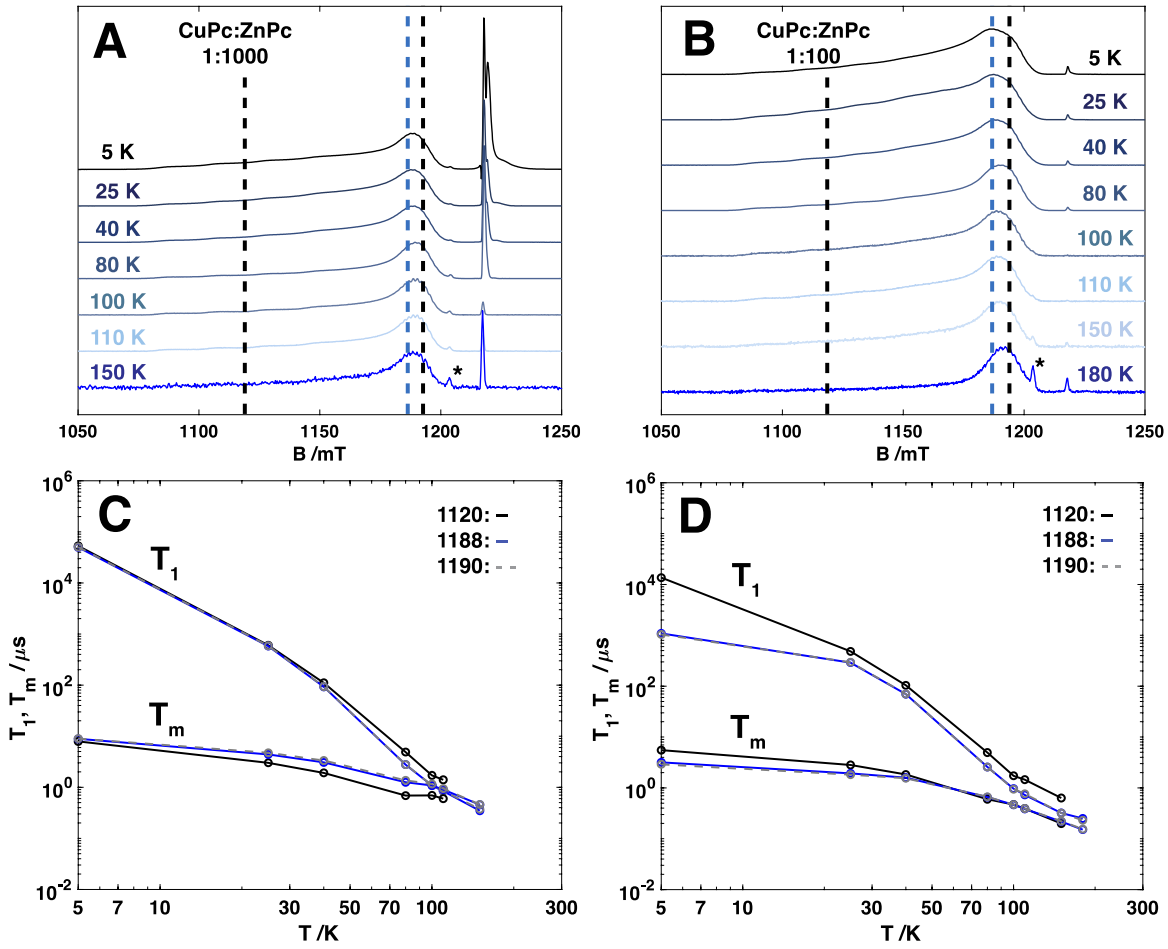

Figure B.6 Echo-detected EPR Q-band field sweeps of **(A)** CuPc 1:1000 and **(B)** 1:100 from 5 K to 180 K. Dashed lines indicate field positions where relaxation data were collected. Comparison between the field position dependent behavior of the T_1 and T_m relaxation times from 5 to 180 K of CuPc **(C)** 1:1000 and **(D)** 1:100. (*) denotes the sharp radical-like feature at 1204 mT is due to a background signal in the Q-band resonator.

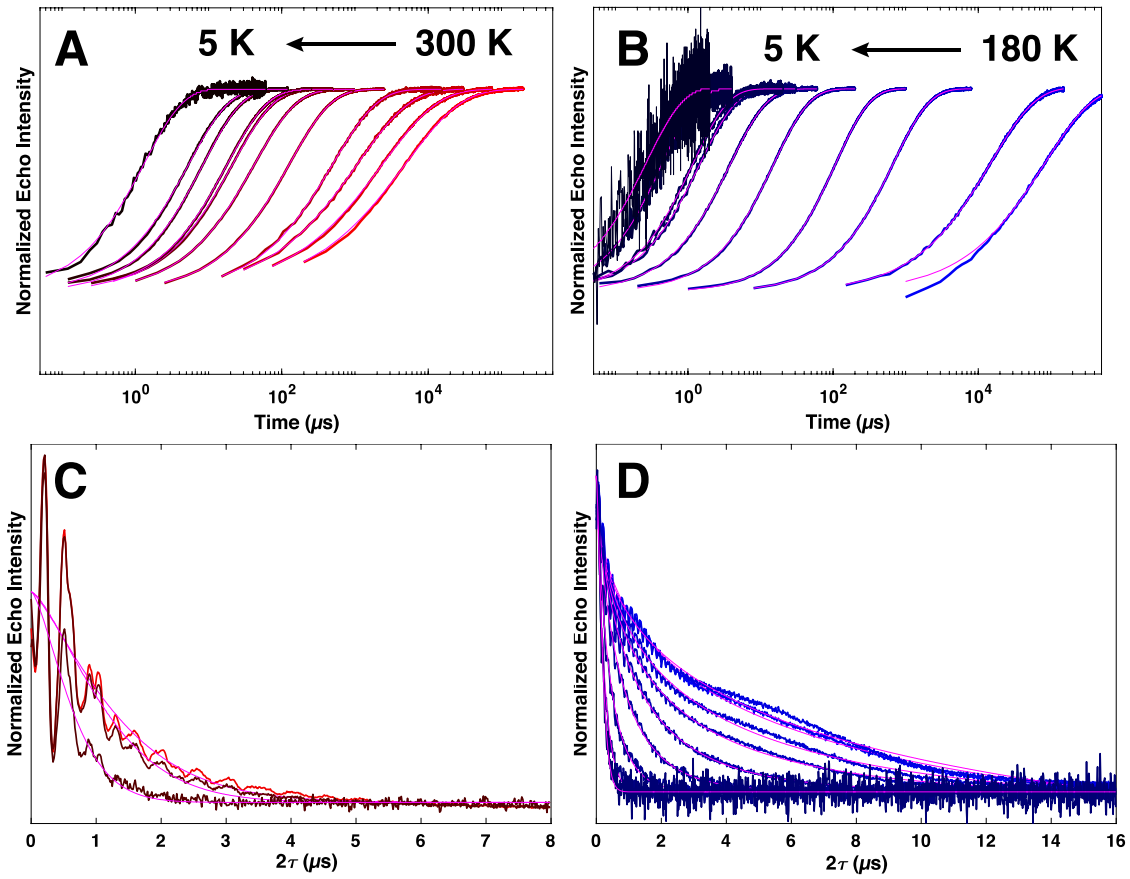

Figure B.7 Inversion recoveries and associated fits (pink) of **(A)** CuPc 1:1000 and **(B)** VOPc 1:1000 from at X-band. Hahn echo and associated fits (pink) of **(C)** CuPc 1:1000 and **(D)** VOPc 1:1000 from at X-band. Due to large ESEEM modulations in VOPc, we have only displayed 3 normalized traces: 5 K, 180 K, and 300K.

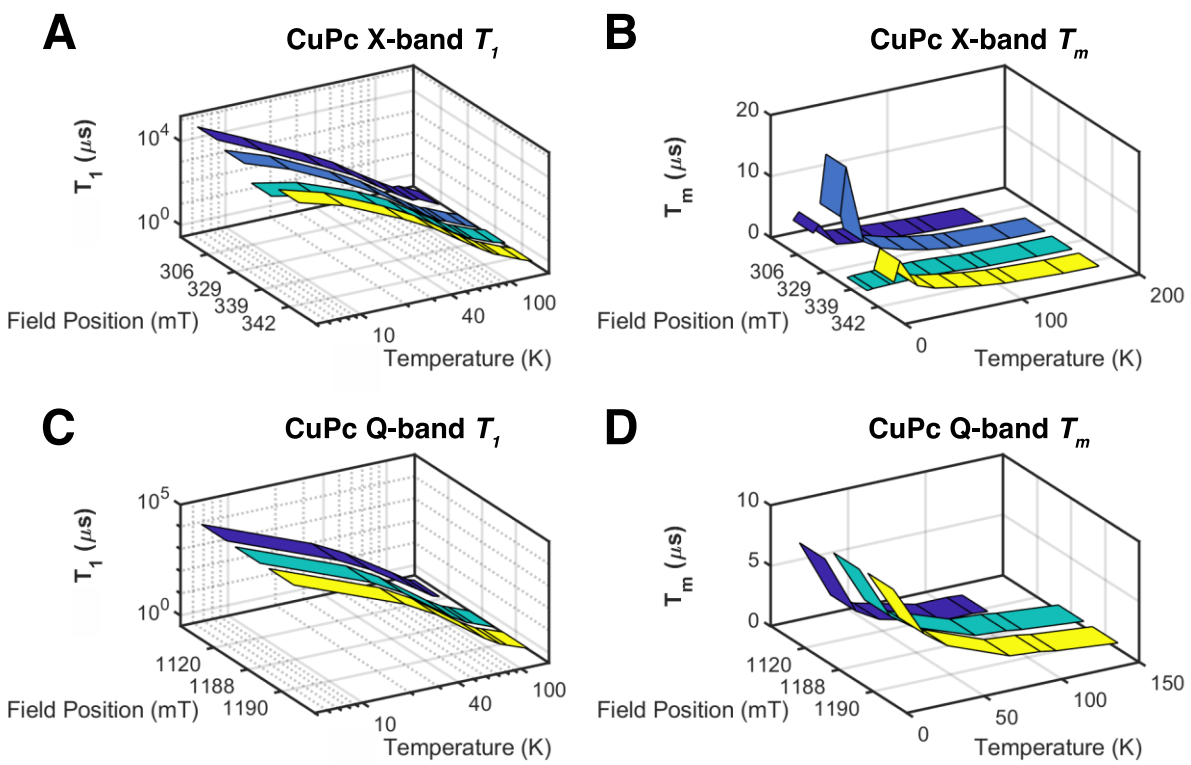

Figure B.8 3D-comparison between the field position dependent behavior of the CuPc 1:1000 T_1 and T_m relaxation times at X-**(A and B)** and Q- **(C and D)** band.

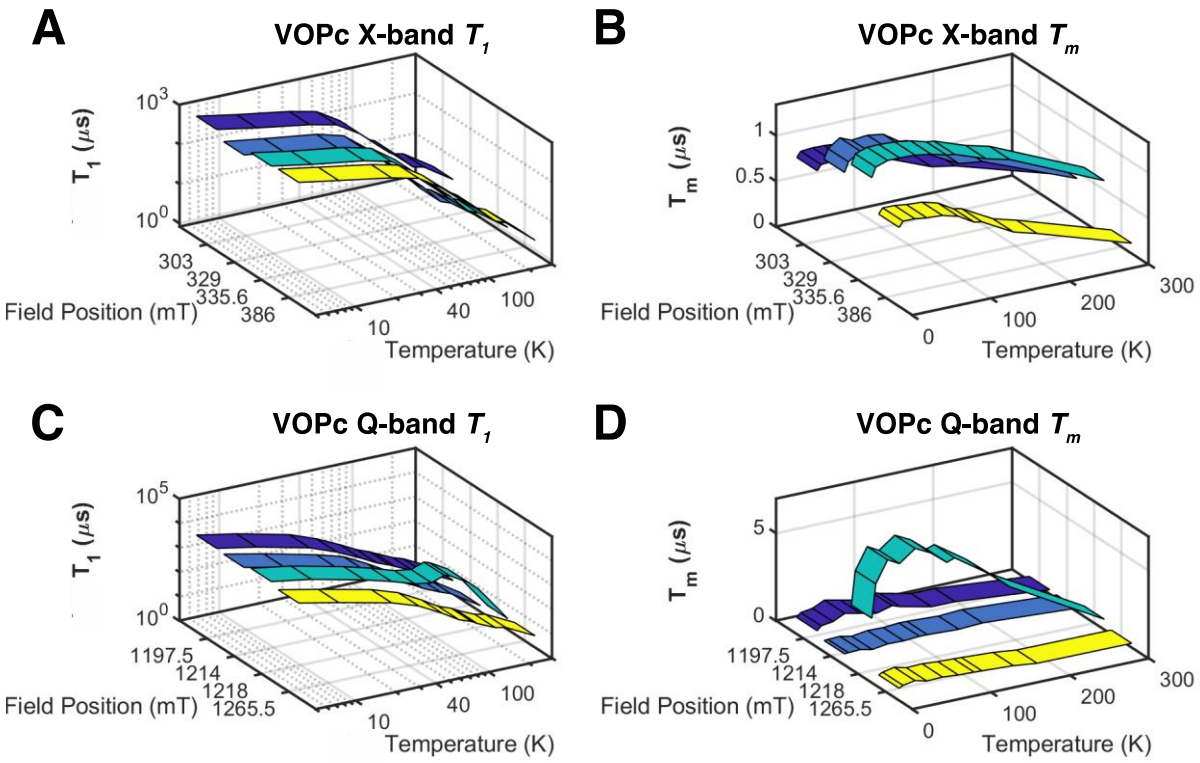

Figure B.9 3D-comparison between the field position dependent behavior of the VOPc 1:1000 T_1 and T_m relaxation times at X- **(A and B)** and Q- **(C and D)** band.

Table B.3 1:1000 VOPc:TiOPc temperature-dependent T_1 and T_m data collected at selected field positions at X-band.

VOPc 1:1000	*303 mT*		*329 mT*		*335.6 mT*		*386 mT*	
Temperature (K)	T_1 (µs)	T_m (µs)	T_1 (µs)	T_m (µs)	T_1 (µs)	T_m (µs)	T_1 (µs)	T_m (µs)
5	$8.2 \cdot 10^3$	2.7	$3.3 \cdot 10^3$	3.4	$4.9 \cdot 10^3$	2.9	$9.6 \cdot 10^3$	2.6
10	$3.6 \cdot 10^3$	3.1	$1.8 \cdot 10^3$	4.0	$2.4 \cdot 10^3$	3.4	$4.2 \cdot 10^3$	2.9
25	$1.4 \cdot 10^3$	3.2	$8.7 \cdot 10^2$	4.3	$1.1 \cdot 10^3$	3.6	$1.5 \cdot 10^3$	3.2
40	$6.4 \cdot 10^2$	3.2	$3.4 \cdot 10^2$	4.5	$5.0 \cdot 10^2$	3.7	$6.2 \cdot 10^2$	3.1
60	$1.9 \cdot 10^2$	3.1	$8.8 \cdot 10^1$	4.4	$1.3 \cdot 10^2$	3.6	$1.7 \cdot 10^2$	2.9
80	$6.5 \cdot 10^1$	2.9	$2.9 \cdot 10^1$	4.0	$4.2 \cdot 10^1$	3.4	$6.1 \cdot 10^1$	2.7
100	$3.5 \cdot 10^1$	2.6	$1.4 \cdot 10^1$	3.7	$2.1 \cdot 10^1$	3.3	$3.3 \cdot 10^1$	2.4
110	$3.1 \cdot 10^1$	2.5	$1.2 \cdot 10^1$	3.6	$1.8 \cdot 10^1$	3.2	$2.7 \cdot 10^1$	2.3
150	$1.7 \cdot 10^1$	2.1	5.5	3.1	8.5	2.8	$1.3 \cdot 10^1$	2.0
180	$1.1 \cdot 10^1$	1.8	3.4	2.7	5.4	2.6	9.6	1.6
300	3.4	–	0.8	1.4	1.3	1.5	2.9	–

Table B.4 1:1000 VOPc:TiOPc temperature-dependent T_1 and T_m data collected at selected field positions at Q-band.

VOPc 1:1000	*1197.5 mT*		*1214 mT*		*1218 mT*		*1265.5 mT*	
Temperature (K)	T_1 (µs)	T_m (µs)	T_1 (µs)	T_m (µs)	T_1 (µs)	T_m (µs)	T_1 (µs)	T_m (µs)
5	$9.3 \cdot 10^3$	0.8	$8.2 \cdot 10^3$	0.5	$1.2 \cdot 10^4$	3.5	$8.1 \cdot 10^3$	0.5
10	$4.7 \cdot 10^3$	1.0	$3.8 \cdot 10^3$	0.5	$6.3 \cdot 10^3$	5.4	$3.7 \cdot 10^3$	0.6
25	$1.5 \cdot 10^3$	1.1	$1.2 \cdot 10^3$	0.5	$2.0 \cdot 10^3$	6.6	$1.2 \cdot 10^3$	0.8
40	$5.7 \cdot 10^2$	1.4	$5.5 \cdot 10^2$	0.4	$1.0 \cdot 10^3$	6.3	$5.3 \cdot 10^3$	0.6
60	$2.0 \cdot 10^2$	1.2	$1.8 \cdot 10^2$	0.5	$4.9 \cdot 10^2$	7.0	$1.6 \cdot 10^2$	0.6
80	$9.0 \cdot 10^1$	1.0	$7.3 \cdot 10^1$	0.5	$3.9 \cdot 10^2$	6.5	$6.4 \cdot 10^2$	0.6
100	$5.6 \cdot 10^1$	1.3	$4.1 \cdot 10^1$	0.5	$6.0 \cdot 10^2$	5.8	$4.1 \cdot 10^2$	0.5
110	$4.4 \cdot 10^1$	1.1	$3.0 \cdot 10^1$	0.5	$5.1 \cdot 10^2$	6.0	$3.1 \cdot 10^1$	0.5
150	$2.0 \cdot 10^1$	0.7	$1.4 \cdot 10^1$	0.5	$2.0 \cdot 10^2$	4.7	$1.4 \cdot 10^1$	0.4
180	$1.5 \cdot 10^1$	0.7	$1.0 \cdot 10^1$	0.5	$8.4 \cdot 10^1$	3.6	$1.2 \cdot 10^2$	0.2
300	3.6	0.2	1.8	0.2	2.8	0.6	2.9	0.2

Table B.5 1:100 VOPc:TiOPc temperature-dependent T_1 and T_m data collected at selected field positions at X-band.

VOPc 1:100	*303 mT*		*329 mT*		*335.6 mT*		*386 mT*	
Temperature (K)	T_1 (µs)	T_m (µs)	T_1 (µs)	T_m (µs)	T_1 (µs)	T_m (µs)	T_1 (µs)	T_m (µs)
5	$1.0 \cdot 10^3$	0.9	$6.3 \cdot 10^2$	1.0	$9.3 \cdot 10^2$	1.2	$1.0 \cdot 10^3$	0.8
10	$6.6 \cdot 10^2$	0.9	$4.6 \cdot 10^2$	1.2	$6.2 \cdot 10^2$	1.3	$6.8 \cdot 10^2$	0.9
25	$4.1 \cdot 10^2$	0.9	$3.0 \cdot 10^2$	1.2	$3.9 \cdot 10^2$	1.3	$4.1 \cdot 10^2$	0.9
40	$2.9 \cdot 10^2$	0.9	$2.0 \cdot 10^2$	1.2	$2.7 \cdot 10^2$	1.3	$2.8 \cdot 10^2$	0.9
60	$1.3 \cdot 10^2$	0.9	$6.9 \cdot 10^1$	1.2	$1.0 \cdot 10^2$	1.3	$1.2 \cdot 10^2$	0.9
80	$5.4 \cdot 10^1$	0.9	$2.7 \cdot 10^1$	1.2	$4.2 \cdot 10^1$	1.3	$5.2 \cdot 10^1$	0.8
100	$2.8 \cdot 10^1$	0.8	$1.2 \cdot 10^1$	1.1	$2.0 \cdot 10^1$	1.3	$2.8 \cdot 10^1$	0.7
110	$2.5 \cdot 10^1$	0.8	$1.0 \cdot 10^1$	1.1	$1.7 \cdot 10^1$	1.2	$2.3 \cdot 10^1$	0.7
150	9.3	0.6	3.5	0.9	5.7	1.1	8.9	0.5
180	8.1	0.6	2.8	0.8	4.4	1.1	7.0	0.4
300	2.7	0.3	0.8	0.4	1.3	0.6	1.7	0.1

Table B.6 1:1000 CuPc:ZnPc temperature-dependent T_1 and T_m data collected at selected field positions at X-band.

CuPc 1:1000	*306 mT*		*329 mT*		*339 mT*		*342 mT*	
Temperature (K)	T_1 (µs)	T_m (µs)	T_1 (µs)	T_m (µs)	T_1 (µs)	T_m (µs)	T_1 (µs)	T_m (µs)
5	$1.6 \cdot 10^5$	4.4	$8.3 \cdot 10^4$	$1.0 \cdot 10^1$	$1.5 \cdot 10^4$	0.7	$5.1 \cdot 10^4$	5.0
10	$1.7 \cdot 10^4$	5.5	$1.5 \cdot 10^4$	$1.8 \cdot 10^1$	$5.6 \cdot 10^3$	0.8	$1.3 \cdot 10^4$	8.1
25	$7.4 \cdot 10^2$	1.8	$6.7 \cdot 10^2$	5.0	$5.0 \cdot 10^2$	0.9	$6.8 \cdot 10^2$	3.5
40	$1.3 \cdot 10^2$	1.4	$1{,}1 \cdot 10^2$	3.4	$9.7 \cdot 10^1$	1.0	$1.2 \cdot 10^2$	2.5
60	$1.9 \cdot 10^1$	1.1	$1.5 \cdot 10^1$	2.3	$1.5 \cdot 10^1$	1.0	$1.7 \cdot 10^1$	1.9
80	5.1	0.9	3.9	1.5	4.0	0.8	4.5	1.3
100	2.0	0.7	1.5	0.9	1.5	0.5	1.7	0.9
110	1.9	0.6	1.2	0.8	1.2	0.5	1.3	0.8
150	0.7	0.4	0.4	0.5	0.5	0.3	0.5	0.4
180	–	–	0.3	0.4	0.3	0.3	0.3	0.4

Table B.7 1:1000 CuPc:ZnPc temperature-dependent T_1 and T_m data collected at selected field positions at Q-band.

CuPc 1:1000	*1120 mT*		*1188 mT*		*1190 mT*	
Temperature (K)	T_1 (µs)	T_m (µs)	T_1 (µs)	T_m (µs)	T_1 (µs)	T_m (µs)
5	$5.3 \cdot 10^4$	7.9	$5.0 \cdot 10^4$	8.9	$5.1 \cdot 10^4$	9.0
25	$6.0 \cdot 10^2$	3.0	$5.8 \cdot 10^2$	4.4	$5.9 \cdot 10^2$	4.7
40	$1.1 \cdot 10^2$	1.9	$9.2 \cdot 10^1$	3.1	$9.3 \cdot 10^1$	3.3
80	4.9	0.7	2.8	1.3	2.8	1.4
100	1.7	0.7	1.1	1.1	1.1	1.2
110	1.4	0.6	0.8	0.9	0.8	0.9
150	–	–	0.3	0.5	0.4	0.5

Table B.8 1:100 CuPc:ZnPc temperature-dependent T_1 and T_m data collected at selected field positions at X-band.

CuPc 1:100	*306 mT*		*329 mT*		*339 mT*		*342 mT*	
Temperature (K)	T_1 (µs)	T_m (µs)	T_1 (µs)	T_m (µs)	T_1 (µs)	T_m (µs)	T_1 (µs)	T_m (µs)
5	$1.2 \cdot 10^4$	1.4	$2.7 \cdot 10^3$	1.1	$3.7 \cdot 10^3$	1.5	$5.6 \cdot 10^3$	1.5
10	$5.5 \cdot 10^3$	1.4	$1.9 \cdot 10^3$	1.2	$2.4 \cdot 10^3$	1.5	$3.7 \cdot 10^3$	1.5
25	$6.0 \cdot 10^2$	1.3	$4.0 \cdot 10^2$	1.2	$4.7 \cdot 10^2$	1.5	$5.6 \cdot 10^2$	1.5
40	$1.2 \cdot 10^2$	1.2	$8.9 \cdot 10^1$	1.1	$9.5 \cdot 10^1$	1.4	$1.1 \cdot 10^2$	1.3
60	$2.0 \cdot 10^1$	0.9	$1.4 \cdot 10^1$	0.9	$1.4 \cdot 10^1$	1.1	$1.5 \cdot 10^1$	1.0
80	5.3	0.7	3.9	0.7	3.7	0.7	4.1	0.7
100	2.5	0.5	1.7	0.5	1.6	0.5	1.8	0.5
110	1.7	0.4	1.2	0.4	1.2	0.5	1.3	0.5
150	0.8	0.3	0.5	0.3	0.5	0.3	0.5	0.3
180	–	–	0.3	0.2	0.3	0.2	0.3	0.2

Table B.9 1:100 CuPc:ZnPc temperature-dependent T_1 and T_m data collected at selected field positions at Q-band.

CuPc 1:100	*1120 mT*		*1188 mT*		*1190 mT*	
Temperature (K)	T_1 (µs)	T_m (µs)	T_1 (µs)	T_m (µs)	T_1 (µs)	T_m (µs)
5	$1.36 \cdot 10^4$	5.5	$1.1 \cdot 10^3$	3.2	$1.0 \cdot 10^3$	2.9
25	$4.8 \cdot 10^2$	2.8	$2.9 \cdot 10^2$	1.9	$3.0 \cdot 10^2$	1.8
40	$1.0 \cdot 10^2$	1.8	$7.0 \cdot 10^1$	1.6	$7.0 \cdot 10^1$	1.5
80	4.9	0.6	2.6	0.7	2.6	0.7
100	1.7	0.5	1.0	0.5	0.9	0.5
110	1.5	0.4	0.7	0.4	0.8	0.4
150	0.6	0.2	0.3	0.2	0.3	0.2
180	–	–	0.3	0.2	0.2	0.2

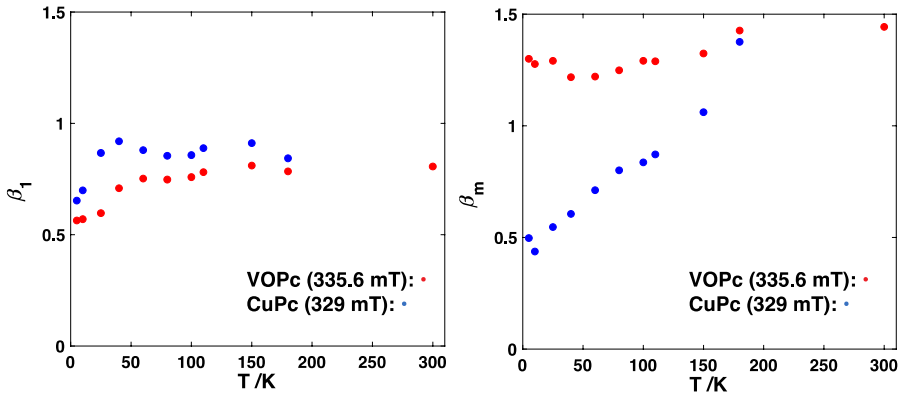

Figure B.10 Comparison stretching term, β, for VOPc 1:1000 at 335.6 mT (red) and CuPc 1:1000 at 329 mT (blue) **(A)** T_1 times (β_1) and **(B)** T_m times (β_m).

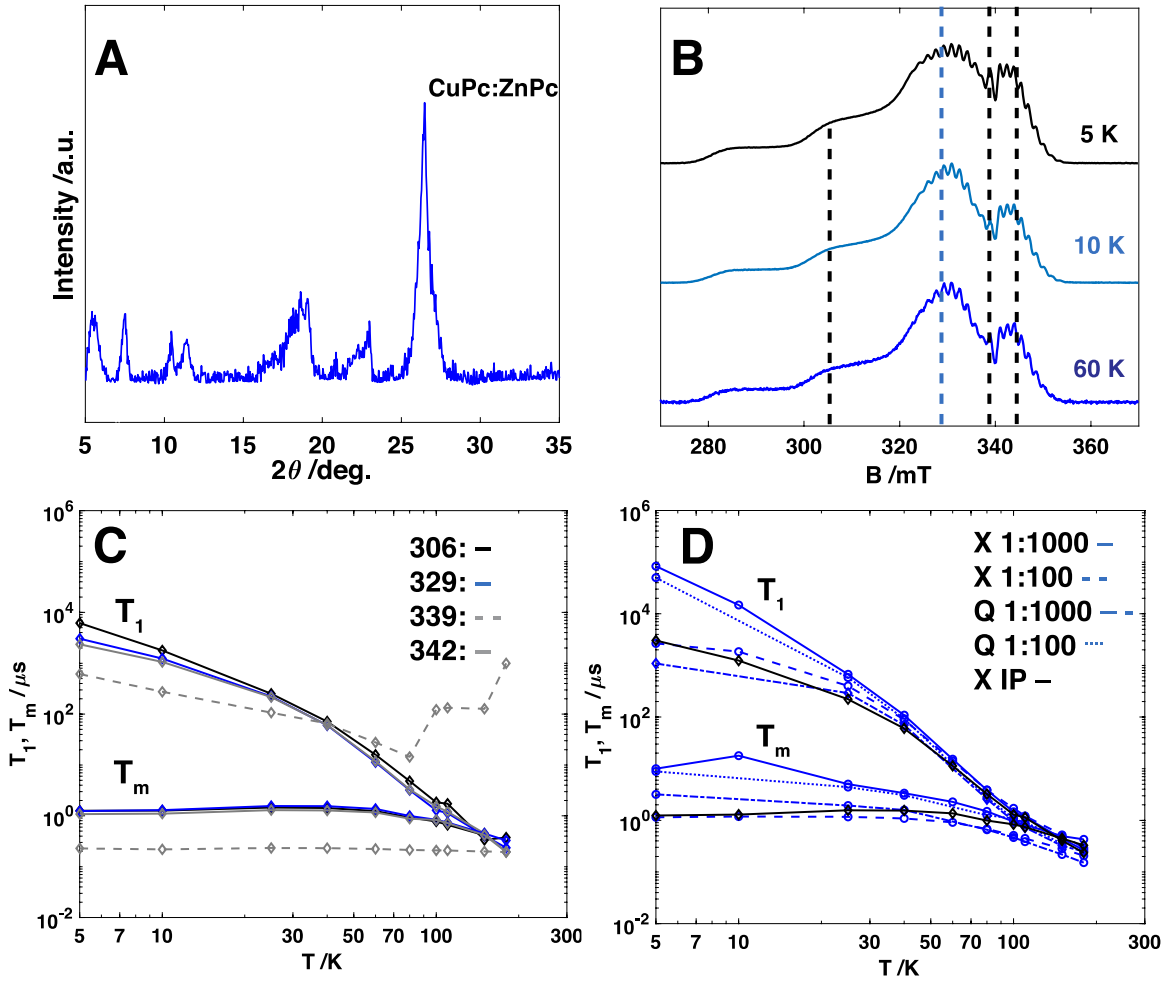

Figure B.11 (A) Comparison of the PXRD pattern of an independent preparation of CuPc:ZnPc. **(B)** Echo-detected EPR X-band field sweeps of CuPc at 5 K, 10 K, and 60 K. Dashed lines indicate field positions where relaxation data were collected. **(C)** Comparison of the field position dependent behavior of the T_1 and T_m relaxation times from 5–180 K of CuPc dilution. **(D)** Comparison between X-band T_1 and T_m times vs. temperature for the 329 mT features in CuPc at X- and Q-band for the 1:1000, 1:100 preparations and the independent preparation.

A CuPc:ZnPc sample was prepared to yield a final dilution of 1:1000 by an independent method analogous to the preparation for VOPc:TiOPc samples using DCM/CF_3CO_2H/IPA. Due to solubility issues in the preparation of this CuPc:ZnPc sample, the final concentration is unknown. The PXRD patterns are distinct from the 1:1000 and 1:100 previously prepared (Figure S11A). However, the CW-EPR spectrum shows similar copper features despite a significantly more intense radical signal (Figure S12). As well, the T_1 and T_m temperature-dependences observed for this sample were consistent with the other CuPc samples when measured at 306, 329,

and 342 mT (Figure S11). This preparation method did, however, display substantially different behavior with respect to the 339 mT field position. In the EDFS, there is a sharp signal at 339 mT. The T_1 times measured at this position remained significantly longer at higher temperatures than for other field positions, whereas the T_m times of this feature were found to be lower than at the other positions. These observations indicate that this signal arises from the organic radical. In contrast to the samples prepared by the sulfuric acid method, the EDFS spectra do not change much with increasing temperature. The distinct temperature dependences in the EDFS spectra, T_1, and T_m times between the various preparations indicate that the radical species may be delocalized in different ways in these two samples. When monitoring relaxation behavior at field positions not associated with the radical (e.g., 306, 329 mT at X-band), then similar temperature-dependent trends are observed regardless of sample preparation method or concentration (Figure S11D). This suggests that the radical is not the dominant feature contributing to the differences in relaxation times between VOPc and CuPc mixtures.

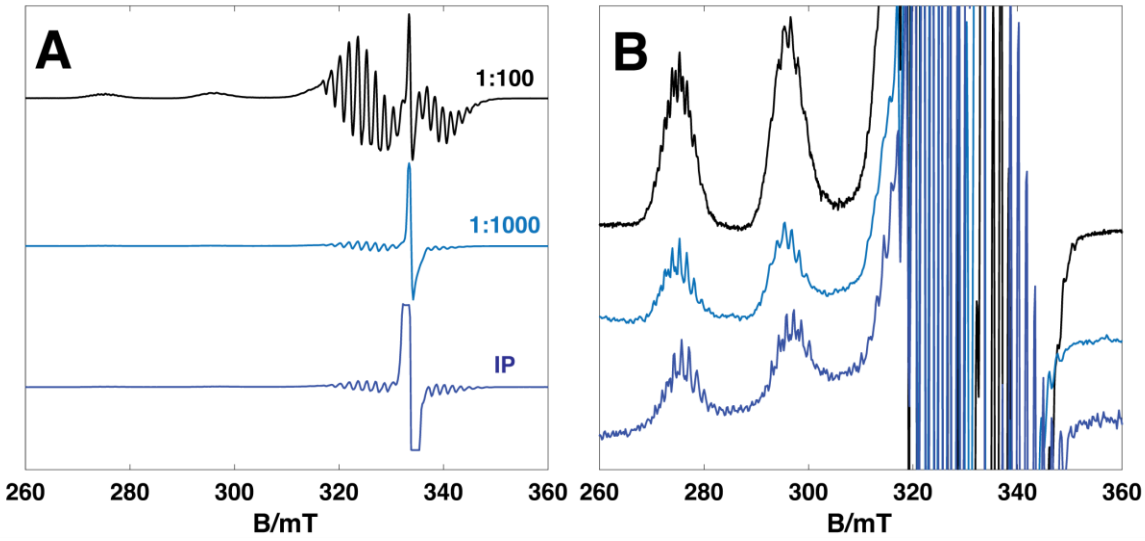

Figure B.12 (A) Comparison of CW-EPR at 77 K of the CuPc:ZnPc 1:100 and 1:1000 and independent preparations. **(B)** Zoom-in to show ^{14}N superhyperfine features.

References:

(1) Abkowitz, M.; Chen, I.; Sharp, J. H. Electron Spin Resonance of the Organic Semiconductor, α -Copper Phthalocyanine. *J. Chem. Phys.* **1968**, *48* (10), 4561–4567. https://doi.org/10.1063/1.1668028.

(2) Atzori, M.; Tesi, L.; Morra, E.; Chiesa, M.; Sorace, L.; Sessoli, R. Room-Temperature Quantum Coherence and Rabi Oscillations in Vanadyl Phthalocyanine: Toward Multifunctional Molecular Spin Qubits. *J. Am. Chem. Soc.* **2016**, *138* (7), 2154–2157. https://doi.org/10.1021/jacs.5b13408.

(3) Stoll, S.; Schweiger, A. EasySpin, a Comprehensive Software Package for Spectral Simulation and Analysis in EPR. *J. Magn. Reson.* **2006**, *178* (1), 42–55. https://doi.org/10.1016/j.jmr.2005.08.013.

(4) Zhou, Y.; Bowler, B. E.; Eaton, G. R.; Eaton, S. S. Electron Spin Lattice Relaxation Rates for S = 1/2 Molecular Species in Glassy Matrices or Magnetically Dilute Solids at Temperatures between 10 and 300 K. *J. Magn. Reson.* **1999**, *139* (1), 165–174. https://doi.org/10.1006/jmre.1999.1763.

(5) Abragam, A.; Bleaney, B. *Electron Paramagnetic Resonance of Transition Ions*; Clarendon P., 1970.

(6) Lin, C.-Y.; Ngendahimana, T.; Eaton, G. R.; Eaton, S. S.; Zadrozny, J. M. Counterion Influence on Dynamic Spin Properties in a V(IV) Complex. *Chem. Sci.* **2019**, *10* (2), 548–555. https://doi.org/10.1039/C8SC04122A.

(7) Schmidt, M. U. Industrial Organic Pigments; 2019; pp 834–842. https://doi.org/10.1107/97809553602060000984.

(8) Assour, J. M.; Harrison, S. E. On the Origin of Unpaired Electrons in Metal-Free Phthalocyanine. *J. Phys. Chem.* **1964**, *68* (4), 872–876. https://doi.org/10.1021/j100786a029.

Appendix C:

Triplet Pair Spin Operators and Spin Hamiltonian

Triplet Pair Spin Operators

The triplet pair eigenstates may be constructed by standard rules of angular momentum addition as we will show below. We first begin by defining the $|\alpha\rangle$ and $|\beta\rangle$ basis functions in matrix form in addition to the Pauli matrices for the Cartesian components of a single electron spin operator that operate on these basis functions.[1,2]

$$|\alpha\rangle = \begin{bmatrix} 1 \\ 0 \end{bmatrix}$$

$$|\beta\rangle = \begin{bmatrix} 0 \\ 1 \end{bmatrix}$$

$$\hat{S}_x = \frac{1}{2}\begin{bmatrix} 0 & 1 \\ 1 & 0 \end{bmatrix}$$

$$\hat{S}_y = \frac{1}{2}\begin{bmatrix} 0 & -i \\ i & 0 \end{bmatrix}$$

$$\hat{S}_z = \frac{1}{2}\begin{bmatrix} 1 & 0 \\ 0 & -1 \end{bmatrix}$$

From here, there are two potential routes to generating the triplet pair eigenstates. The first is the traditional route used by Merrifield by defining two sets of triplet eigenfunctions and corresponding spin operators and taking their tensor products to generate the nine triplet pair eigenstates.[3,4] The second was outlined by Scholes in 2015, by generating the spin operators for four electron basis functions and factoring the uncoupled basis into the triplet pair basis assuming the two triplets are distinguishable.[5]

To define the triplet pair states in the vein of Merrifield, we must first construct triplet eigenstates and spin operators in the coupled two-electron basis. For two electrons, we can define

the uncoupled set of basis states as the tensor (Kronecker) product, denoted by $\otimes$, of the individual $|\alpha\rangle$ and $|\beta\rangle$ basis functions:

$$|\alpha\alpha\rangle = |\alpha\rangle \otimes |\alpha\rangle = \begin{bmatrix}1\\0\end{bmatrix} \otimes \begin{bmatrix}1\\0\end{bmatrix} = \begin{bmatrix}1\\0\\0\\0\end{bmatrix}$$

$$|\alpha\beta\rangle = |\alpha\rangle \otimes |\beta\rangle = \begin{bmatrix}1\\0\end{bmatrix} \otimes \begin{bmatrix}0\\1\end{bmatrix} = \begin{bmatrix}0\\1\\0\\0\end{bmatrix}$$

$$|\beta\alpha\rangle = |\beta\rangle \otimes |\alpha\rangle = \begin{bmatrix}0\\1\end{bmatrix} \otimes \begin{bmatrix}1\\0\end{bmatrix} = \begin{bmatrix}0\\0\\1\\0\end{bmatrix}$$

$$|\beta\beta\rangle = |\beta\rangle \otimes |\beta\rangle = \begin{bmatrix}0\\1\end{bmatrix} \otimes \begin{bmatrix}0\\1\end{bmatrix} = \begin{bmatrix}0\\0\\0\\1\end{bmatrix}$$

The spin operators in the uncoupled basis are similarly constructed by summing over the following Kronecker products where $\mathbf{I_2}$ represents the 2x2 identity matrix, $\hat{S}_{x,y,z}$ represents the total two-electron spin operator for each Cartesian coordinate, and $\hat{S}_{1x,y,z}$ and $\hat{S}_{2x,y,z}$ represent the Cartesian spin operators for electron 1 and 2, respectively:

$$\hat{S}_{Tot\ x,y,z} = \hat{S}_{1x,y,z} \otimes \boldsymbol{I_2} + \boldsymbol{I_2} \otimes \hat{S}_{2x,y,z}$$

$$\hat{S}_x = \hat{S}_{1x} \otimes \boldsymbol{I_2} + \boldsymbol{I_2} \otimes \hat{S}_{2x} = \frac{1}{2}\begin{bmatrix}0 & 1\\1 & 0\end{bmatrix} \otimes \begin{bmatrix}1 & 0\\0 & 1\end{bmatrix} + \frac{1}{2}\begin{bmatrix}1 & 0\\0 & 1\end{bmatrix} \otimes \begin{bmatrix}0 & 1\\1 & 0\end{bmatrix}$$

$$\hat{S}_x = \frac{1}{2}\begin{bmatrix}0 & 0 & 1 & 0\\0 & 0 & 0 & 1\\1 & 0 & 0 & 0\\0 & 1 & 0 & 0\end{bmatrix} + \frac{1}{2}\begin{bmatrix}0 & 1 & 0 & 0\\1 & 0 & 0 & 0\\0 & 0 & 0 & 1\\0 & 0 & 1 & 0\end{bmatrix} = \frac{1}{2}\begin{bmatrix}0 & 1 & 1 & 0\\1 & 0 & 0 & 1\\1 & 0 & 0 & 1\\0 & 1 & 1 & 0\end{bmatrix}$$

$$\hat{S}_y = \hat{S}_{1y} \otimes \boldsymbol{I_2} + \boldsymbol{I_2} \otimes \hat{S}_{2y} = \frac{1}{2}\begin{bmatrix} 0 & -i \\ i & 0 \end{bmatrix} \otimes \begin{bmatrix} 1 & 0 \\ 0 & 1 \end{bmatrix} + \frac{1}{2}\begin{bmatrix} 1 & 0 \\ 0 & 1 \end{bmatrix} \otimes \begin{bmatrix} 0 & -i \\ i & 0 \end{bmatrix}$$

$$\hat{S}_y = \frac{1}{2}\begin{bmatrix} 0 & 0 & -i & 0 \\ 0 & 0 & 0 & -i \\ i & 0 & 0 & 0 \\ 0 & i & 0 & 0 \end{bmatrix} + \frac{1}{2}\begin{bmatrix} 0 & -i & 0 & 0 \\ i & 0 & 0 & 0 \\ 0 & 0 & 0 & -i \\ 0 & 0 & i & 0 \end{bmatrix} = \frac{1}{2}\begin{bmatrix} 0 & -i & -i & 0 \\ i & 0 & 0 & -i \\ i & 0 & 0 & -i \\ 0 & i & i & 0 \end{bmatrix}$$

$$\hat{S}_z = \hat{S}_{1z} \otimes \boldsymbol{I_2} + \boldsymbol{I_2} \otimes \hat{S}_{2z} = \frac{1}{2}\begin{bmatrix} 1 & 0 \\ 0 & -1 \end{bmatrix} \otimes \begin{bmatrix} 1 & 0 \\ 0 & 1 \end{bmatrix} + \frac{1}{2}\begin{bmatrix} 1 & 0 \\ 0 & 1 \end{bmatrix} \otimes \begin{bmatrix} 1 & 0 \\ 0 & -1 \end{bmatrix}$$

$$\hat{S}_z = \frac{1}{2}\begin{bmatrix} 1 & 0 & 0 & 0 \\ 0 & 1 & 0 & 0 \\ 0 & 0 & -1 & 0 \\ 0 & 0 & 0 & -1 \end{bmatrix} + \frac{1}{2}\begin{bmatrix} 1 & 0 & 0 & 0 \\ 0 & -1 & 0 & 0 \\ 0 & 0 & 1 & 0 \\ 0 & 0 & 0 & -1 \end{bmatrix} = \frac{1}{2}\begin{bmatrix} 2 & 0 & 0 & 0 \\ 0 & 0 & 0 & 0 \\ 0 & 0 & 0 & 0 \\ 0 & 0 & 0 & -2 \end{bmatrix} = \begin{bmatrix} 1 & 0 & 0 & 0 \\ 0 & 0 & 0 & 0 \\ 0 & 0 & 0 & 0 \\ 0 & 0 & 0 & -1 \end{bmatrix}$$

$$\hat{S}^2 = \hat{S}_x + \hat{S}_y + \hat{S}_z = \begin{bmatrix} 2 & 0 & 0 & 0 \\ 0 & 1 & 1 & 0 \\ 0 & 1 & 1 & 0 \\ 0 & 0 & 0 & 2 \end{bmatrix}$$

As can be seen, the $\hat{S}^2$ operator is not diagonal in the uncoupled basis. Specifically, $|\alpha\beta\rangle$ and $|\beta\alpha\rangle$ are not eigenstates, i.e. they are not states of pure spin multiplicity. The elements $\langle\alpha\alpha|\hat{S}^2|\alpha\alpha\rangle$ and $\langle\beta\beta|\hat{S}^2|\beta\beta\rangle$ are both 2, consistent with the expected eigenvalue S(S+1) for a triplet S = 1, and the corresponding matrix elements of the $\hat{S}_z$ operator give m_s values of +1 and -1, respectively. We can diagonalize the $\hat{S}^2$ matrix to retrieve the eigenvalues and associated eigenvectors:

$$\hat{S}^2 = \begin{bmatrix} 0 & 0 & 0 & 0 \\ 0 & 2 & 0 & 0 \\ 0 & 0 & 2 & 0 \\ 0 & 0 & 0 & 2 \end{bmatrix}$$

$$eigenvectors: \frac{1}{\sqrt{2}}\begin{bmatrix} 0 \\ 1 \\ -1 \\ 0 \end{bmatrix}, \begin{bmatrix} 1 \\ 0 \\ 0 \\ 0 \end{bmatrix}, \frac{1}{\sqrt{2}}\begin{bmatrix} 0 \\ 1 \\ 1 \\ 0 \end{bmatrix}, \begin{bmatrix} 0 \\ 0 \\ 0 \\ 1 \end{bmatrix}$$

This provides us a set of eigenvectors in the coupled spin basis $|S,M\rangle$ that are pure singlet and triplet functions (S = 0 and S=1 respectively):

$$|0,0\rangle = |S\rangle = \frac{1}{\sqrt{2}}(|\alpha\beta\rangle - |\beta\alpha\rangle)$$

$$|1,0\rangle = |T_0\rangle = \frac{1}{\sqrt{2}}(|\alpha\beta\rangle + |\beta\alpha\rangle)$$

$$|1,+1\rangle = |T_+\rangle = |\alpha\alpha\rangle$$

$$|1,-1\rangle = |T_-\rangle = |\beta\beta\rangle$$

From these eigenvectors we can construct a rotation matrix to transform the individual Cartesian spin operators into the coupled $|S,M\rangle$ basis; alternatively, we can directly construct the matrix from the Clebsch-Gordon coefficients:

$$R = \begin{bmatrix} 0 & 1 & 0 & 0 \\ {}^{1}/_{\sqrt{2}} & 0 & {}^{1}/_{\sqrt{2}} & 0 \\ {}^{-1}/_{\sqrt{2}} & 0 & {}^{1}/_{\sqrt{2}} & 0 \\ 0 & 0 & 0 & 1 \end{bmatrix}$$

$$\hat{S}_{x,y,z}^{|S,M\rangle} = R' * \hat{S}_{x,y,z} * R$$

$$\hat{S}_{x}^{|S,M\rangle} = \begin{bmatrix} 0 & 0 & 0 & 0 \\ 0 & 0 & {}^{1}/_{\sqrt{2}} & 0 \\ 0 & {}^{1}/_{\sqrt{2}} & 0 & {}^{1}/_{\sqrt{2}} \\ 0 & 0 & {}^{1}/_{\sqrt{2}} & 0 \end{bmatrix}$$

$$\hat{S}_y^{|S,M\rangle} = \begin{bmatrix} 0 & 0 & 0 & 0 \\ 0 & 0 & -i/\sqrt{2} & 0 \\ 0 & i/\sqrt{2} & 0 & -i/\sqrt{2} \\ 0 & 0 & i/\sqrt{2} & 0 \end{bmatrix}$$

$$\hat{S}_z^{|S,M\rangle} = \begin{bmatrix} 0 & 0 & 0 & 0 \\ 0 & 1 & 0 & 0 \\ 0 & 0 & 0 & 0 \\ 0 & 0 & 0 & -1 \end{bmatrix}$$

As can be seen, the spin operators in the coupled $|S, M\rangle$ basis are block diagonal – no matrix elements connect the singlet and triplet eigenfunctions. Furthermore, all elements associated with the $|S\rangle$ eigenstate are 0, which makes sense because all components of the net spin vector should sum to zero for a singlet. As a result, we will truncate the matrices to carry forward only the triplet eigenstates to generate the triplet pair functions:

$$\hat{S}_{Tx} = \begin{bmatrix} 0 & 1/\sqrt{2} & 0 \\ 1/\sqrt{2} & 0 & 1/\sqrt{2} \\ 0 & 1/\sqrt{2} & 0 \end{bmatrix}$$

$$\hat{S}_{Ty} = \begin{bmatrix} 0 & -i/\sqrt{2} & 0 \\ i/\sqrt{2} & 0 & -i/\sqrt{2} \\ 0 & i/\sqrt{2} & 0 \end{bmatrix}$$

$$\hat{S}_{Tz} = \begin{bmatrix} 1 & 0 & 0 \\ 0 & 0 & 0 \\ 0 & 0 & -1 \end{bmatrix}$$

$$basis\ functions: |1,+1\rangle = |+\rangle = \begin{bmatrix} 1 \\ 0 \\ 0 \end{bmatrix}, |1,0\rangle = |0\rangle = \begin{bmatrix} 0 \\ 1 \\ 0 \end{bmatrix}, |1,-1\rangle = |-\rangle = \begin{bmatrix} 0 \\ 0 \\ 1 \end{bmatrix}$$

We then take the Kronecker products of our triplet basis functions to generate uncoupled triplet pair basis states.

$$|+\,+\rangle = |+\rangle \otimes |+\rangle = \begin{bmatrix}1\\0\\0\end{bmatrix} \otimes \begin{bmatrix}1\\0\\0\end{bmatrix} = \begin{bmatrix}1\\0\\0\\0\\0\\0\\0\\0\\0\end{bmatrix}$$

$$|+0\rangle = |+\rangle \otimes |0\rangle = \begin{bmatrix}1\\0\\0\end{bmatrix} \otimes \begin{bmatrix}0\\1\\0\end{bmatrix} = \begin{bmatrix}0\\1\\0\\0\\0\\0\\0\\0\\0\end{bmatrix}$$

$$|+\,-\rangle = |+\rangle \otimes |-\rangle = \begin{bmatrix}1\\0\\0\end{bmatrix} \otimes \begin{bmatrix}0\\0\\1\end{bmatrix} = \begin{bmatrix}0\\0\\1\\0\\0\\0\\0\\0\\0\end{bmatrix}$$

$$|0\,+\rangle = |0\rangle \otimes |+\rangle = \begin{bmatrix}0\\1\\0\end{bmatrix} \otimes \begin{bmatrix}1\\0\\0\end{bmatrix} = \begin{bmatrix}0\\0\\0\\1\\0\\0\\0\\0\\0\end{bmatrix}$$

$$|00\rangle = |0\rangle \otimes |0\rangle = \begin{bmatrix}0\\1\\0\end{bmatrix} \otimes \begin{bmatrix}0\\1\\0\end{bmatrix} = \begin{bmatrix}0\\0\\0\\0\\1\\0\\0\\0\\0\end{bmatrix}$$

$$|0\,-\rangle = |0\rangle \otimes |-\rangle = \begin{bmatrix}0\\1\\0\end{bmatrix} \otimes \begin{bmatrix}0\\0\\1\end{bmatrix} = \begin{bmatrix}0\\0\\0\\0\\0\\1\\0\\0\\0\end{bmatrix}$$

$$|-\,+\rangle = |-\rangle \otimes |+\rangle = \begin{bmatrix}0\\0\\1\end{bmatrix} \otimes \begin{bmatrix}1\\0\\0\end{bmatrix} = \begin{bmatrix}0\\0\\0\\0\\0\\0\\1\\0\\0\end{bmatrix}$$

$$|-0\rangle = |-\rangle \otimes |0\rangle = \begin{bmatrix}0\\0\\1\end{bmatrix} \otimes \begin{bmatrix}0\\1\\0\end{bmatrix} = \begin{bmatrix}0\\0\\0\\0\\0\\0\\0\\1\\0\end{bmatrix}$$

$$|--\rangle = |-\rangle \otimes |-\rangle = \begin{bmatrix} 0 \\ 0 \\ 1 \end{bmatrix} \otimes \begin{bmatrix} 0 \\ 0 \\ 1 \end{bmatrix} = \begin{bmatrix} 0 \\ 0 \\ 0 \\ 0 \\ 0 \\ 0 \\ 0 \\ 0 \\ 1 \end{bmatrix}$$

We build triplet pair spin operators in analogous fashion by the following summation of Kronecker products:

$$\hat{S}_{TTx,y,z} = \hat{S}_{Tx,y,z} \otimes \boldsymbol{I}_3 + \boldsymbol{I}_3 \otimes \hat{S}_{Tx,y,z}$$

$$\hat{S}_{TTx} = \begin{bmatrix} 0 & {}^{1}/_{\sqrt{2}} & 0 & {}^{1}/_{\sqrt{2}} & 0 & 0 & 0 & 0 & 0 \\ {}^{1}/_{\sqrt{2}} & 0 & {}^{1}/_{\sqrt{2}} & 0 & {}^{1}/_{\sqrt{2}} & 0 & 0 & 0 & 0 \\ 0 & {}^{1}/_{\sqrt{2}} & 0 & 0 & 0 & {}^{1}/_{\sqrt{2}} & 0 & 0 & 0 \\ {}^{1}/_{\sqrt{2}} & 0 & 0 & 0 & {}^{1}/_{\sqrt{2}} & 0 & {}^{1}/_{\sqrt{2}} & 0 & 0 \\ 0 & {}^{1}/_{\sqrt{2}} & 0 & {}^{1}/_{\sqrt{2}} & 0 & {}^{1}/_{\sqrt{2}} & 0 & {}^{1}/_{\sqrt{2}} & 0 \\ 0 & 0 & {}^{1}/_{\sqrt{2}} & 0 & {}^{1}/_{\sqrt{2}} & 0 & 0 & 0 & {}^{1}/_{\sqrt{2}} \\ 0 & 0 & 0 & {}^{1}/_{\sqrt{2}} & 0 & 0 & 0 & {}^{1}/_{\sqrt{2}} & 0 \\ 0 & 0 & 0 & 0 & {}^{1}/_{\sqrt{2}} & 0 & {}^{1}/_{\sqrt{2}} & 0 & {}^{1}/_{\sqrt{2}} \\ 0 & 0 & 0 & 0 & 0 & {}^{1}/_{\sqrt{2}} & 0 & {}^{1}/_{\sqrt{2}} & 0 \end{bmatrix}$$

$$\hat{S}_{TTy} = \begin{bmatrix} 0 & -i/\sqrt{2} & 0 & -i/\sqrt{2} & 0 & 0 & 0 & 0 & 0 \\ i/\sqrt{2} & 0 & -i/\sqrt{2} & 0 & -i/\sqrt{2} & 0 & 0 & 0 & 0 \\ 0 & i/\sqrt{2} & 0 & 0 & 0 & -i/\sqrt{2} & 0 & 0 & 0 \\ i/\sqrt{2} & 0 & 0 & 0 & -i/\sqrt{2} & 0 & -i/\sqrt{2} & 0 & 0 \\ 0 & i/\sqrt{2} & 0 & i/\sqrt{2} & 0 & -i/\sqrt{2} & 0 & -i/\sqrt{2} & 0 \\ 0 & 0 & i/\sqrt{2} & 0 & i/\sqrt{2} & 0 & 0 & 0 & -i/\sqrt{2} \\ 0 & 0 & 0 & i/\sqrt{2} & 0 & 0 & 0 & -i/\sqrt{2} & 0 \\ 0 & 0 & 0 & 0 & i/\sqrt{2} & 0 & i/\sqrt{2} & 0 & -i/\sqrt{2} \\ 0 & 0 & 0 & 0 & 0 & i/\sqrt{2} & 0 & i/\sqrt{2} & 0 \end{bmatrix}$$

$$\hat{S}_{TTz} = \begin{bmatrix} 2 & 0 & 0 & 0 & 0 & 0 & 0 & 0 & 0 \\ 0 & 1 & 0 & 0 & 0 & 0 & 0 & 0 & 0 \\ 0 & 0 & 0 & 0 & 0 & 0 & 0 & 0 & 0 \\ 0 & 0 & 0 & 1 & 0 & 0 & 0 & 0 & 0 \\ 0 & 0 & 0 & 0 & 0 & 0 & 0 & 0 & 0 \\ 0 & 0 & 0 & 0 & 0 & -1 & 0 & 0 & 0 \\ 0 & 0 & 0 & 0 & 0 & 0 & 0 & 0 & 0 \\ 0 & 0 & 0 & 0 & 0 & 0 & 0 & -1 & 0 \\ 0 & 0 & 0 & 0 & 0 & 0 & 0 & 0 & -2 \end{bmatrix}$$

$$\hat{S}_{TT}^2 = \hat{S}_{TTx}^2 + \hat{S}_{TTy}^2 + \hat{S}_{TTz}^2 = \begin{bmatrix} 6 & 0 & 0 & 0 & 0 & 0 & 0 & 0 & 0 \\ 0 & 4 & 0 & 2 & 0 & 0 & 0 & 0 & 0 \\ 0 & 0 & 2 & 0 & 2 & 0 & 0 & 0 & 0 \\ 0 & 2 & 0 & 4 & 0 & 0 & 0 & 0 & 0 \\ 0 & 0 & 2 & 0 & 4 & 0 & 2 & 0 & 0 \\ 0 & 0 & 0 & 0 & 0 & 4 & 0 & 2 & 0 \\ 0 & 0 & 0 & 0 & 2 & 0 & 2 & 0 & 0 \\ 0 & 0 & 0 & 0 & 0 & 2 & 0 & 4 & 0 \\ 0 & 0 & 0 & 0 & 0 & 0 & 0 & 0 & 6 \end{bmatrix}$$

By diagonalizing the $\hat{S}_{TT}^2$ matrix, we retrieve the pure spin eigenvectors and eigenvalues:

$$\hat{S}_{TT}^2 = \begin{bmatrix} 0 & 0 & 0 & 0 & 0 & 0 & 0 & 0 & 0 \\ 0 & 2 & 0 & 0 & 0 & 0 & 0 & 0 & 0 \\ 0 & 0 & 2 & 0 & 0 & 0 & 0 & 0 & 0 \\ 0 & 0 & 0 & 2 & 0 & 0 & 0 & 0 & 0 \\ 0 & 0 & 0 & 0 & 6 & 0 & 0 & 0 & 0 \\ 0 & 0 & 0 & 0 & 0 & 6 & 0 & 0 & 0 \\ 0 & 0 & 0 & 0 & 0 & 0 & 6 & 0 & 0 \\ 0 & 0 & 0 & 0 & 0 & 0 & 0 & 6 & 0 \\ 0 & 0 & 0 & 0 & 0 & 0 & 0 & 0 & 6 \end{bmatrix}$$

$$eigenvectors\text{: } \frac{1}{\sqrt{3}}\begin{bmatrix} 0 \\ 0 \\ 1 \\ 0 \\ -1 \\ 0 \\ 1 \\ 0 \\ 0 \end{bmatrix}, \frac{1}{\sqrt{2}}\begin{bmatrix} 0 \\ 1 \\ 0 \\ -1 \\ 0 \\ 0 \\ 0 \\ 0 \\ 0 \end{bmatrix}, \frac{1}{\sqrt{2}}\begin{bmatrix} 0 \\ 0 \\ 1 \\ 0 \\ 0 \\ 0 \\ -1 \\ 0 \\ 0 \end{bmatrix}, \frac{1}{\sqrt{2}}\begin{bmatrix} 0 \\ 0 \\ 0 \\ 0 \\ 0 \\ 1 \\ 0 \\ -1 \\ 0 \end{bmatrix}, \begin{bmatrix} 1 \\ 0 \\ 0 \\ 0 \\ 0 \\ 0 \\ 0 \\ 0 \\ 0 \end{bmatrix}, \frac{1}{\sqrt{2}}\begin{bmatrix} 0 \\ 1 \\ 0 \\ 1 \\ 0 \\ 0 \\ 0 \\ 0 \\ 0 \end{bmatrix}, \frac{1}{\sqrt{6}}\begin{bmatrix} 0 \\ 0 \\ 1 \\ 0 \\ 2 \\ 0 \\ 1 \\ 0 \\ 0 \end{bmatrix}, \frac{1}{\sqrt{2}}\begin{bmatrix} 0 \\ 0 \\ 0 \\ 0 \\ 0 \\ 1 \\ 0 \\ 1 \\ 0 \end{bmatrix}, \begin{bmatrix} 0 \\ 0 \\ 0 \\ 0 \\ 0 \\ 0 \\ 0 \\ 0 \\ 1 \end{bmatrix}$$

We can rotate the $\hat{S}_{TTz}$ matrix into this new basis to specify the associated m_s values with each eigenvector, which leads to the following triplet pair eigenstates expanded in the basis of uncoupled triplet product states. As can be seen, we expect one state of pure singlet character, three of triplet character, and five of quintet character.

$$\left|\, {}^1TT\right\rangle = \frac{1}{\sqrt{3}}(|00\rangle - |+-\rangle - |-+\rangle)$$

$$\left|\, {}^3TT_{+1}\right\rangle = \frac{1}{\sqrt{2}}(|+0\rangle - |0+\rangle)$$

$$\left|\, {}^3TT_{0}\right\rangle = \frac{1}{\sqrt{2}}(|+-\rangle - |-+\rangle)$$

$$\left|\, {}^3TT_{-1}\right\rangle = \frac{1}{\sqrt{2}}(|0-\rangle - |-0\rangle)$$

$$\left|\, {}^5TT_{+2}\right\rangle = |++\rangle$$

$$\left|\,^5TT_{+1}\right\rangle = \frac{1}{\sqrt{2}}(|+0\rangle + |0+\rangle)$$

$$\left|\,^5TT_{0}\right\rangle = \frac{1}{\sqrt{6}}(2|00\rangle + |+-\rangle + |-+\rangle)$$

$$\left|\,^5TT_{-1}\right\rangle = \frac{1}{\sqrt{2}}(|0-\rangle + |-0\rangle)$$

$$\left|\,^5TT_{-2}\right\rangle = |--\rangle$$

Triplet Pair Spin Hamiltonian

We define the spin Hamiltonian similarly to previous reports.[6–9] In the conceptualization of the spin Hamiltonian, we consider the four unpaired electron spin system with electrons 1 and 2 localized on triplet A, and electrons 3 and 4 are localized on triplet B. At zero-field, we will consider the intratriplet magnetic dipolar interactions, $\widehat{H}_{zfs}$, and the intertriplet exchange interaction, $\widehat{H}_{ex}$. The intratriplet exchange, intertriplet dipolar interactions are excluded, and spin-orbit coupling, typically weak in these organic chromophores, is neglected.

The intratriplet exchange interaction serves to split the energies of the excited singlet S_1 and excited triplet T_1 states by a large energy – in pentacene around 1.2 eV – which is necessary for singlet fission to be thermodynamically accessible. When considering the triplet pair states, we make the assumption that the singly excited singlet state does not interact substantially with the triplets, an assumption that underlies our construction of the triplet pair spin operators when we carry forward only the triplet subspace from the individual triplet operators. For the intertriplet interactions, the exchange is typically dominant, so we disregard the magnetic dipolar interactions between electrons localized on separate chromophores, although these can be included as well.

We define the spin Hamiltonian below as a summation over the three interactions:

$$\hat{H} = \hat{H}_{zee} + \hat{H}_{zfs} + \hat{H}_{ex}$$

The total Zeeman Hamiltonian, $\hat{H}_{zee}$, can be constructed from the Kronecker product of the individual Zeeman Hamiltonians defined for triplets A and B that are expressed in terms of the triplet spin operators.

$$\hat{H}_{zee}^{A,B} = \mu_B \boldsymbol{B^T} \cdot \boldsymbol{g^{A,B}} \cdot \boldsymbol{S^{A,B}} = \mu_B \sum_{i,j=x,y,z} B_i g_{ij}^{A,B} \hat{S}_j^{A,B}$$

$$\hat{H}_{zee} = \hat{H}_{zee}^{A} \otimes I_3 + I_3 \otimes \hat{H}_{zee}^{B}$$

$$\boldsymbol{g^{A,B}} = R^{A,B} \boldsymbol{g} {R^{A,B}}^T$$

$$\boldsymbol{g} = \begin{bmatrix} g_x & 0 & 0 \\ 0 & g_y & 0 \\ 0 & 0 & g_z \end{bmatrix}$$

Here, μ_B is the Bohr magneton. $\boldsymbol{B^T}$ is the external magnetic field vector defined by the x-, y-, and z-components of the field. $\boldsymbol{g^{A,B}}$ is the g tensor defined for each triplet that describes the coupling between the spin angular momentum and the externally applied field. The g tensor can be defined in its principal frame $\boldsymbol{g}$. In general, the principal axes of the two spin systems will not be aligned with each other nor the externally applied field. As a result, the g tensor can be rotated using three Euler angles by the rotation matrices $R^{A,B}$.

The total zero-field splitting Hamiltonian $\hat{H}_{zfs}$ may similarly be constructed over the Kronecker sum of the individual triplet zero-field splitting Hamiltonians $\hat{H}_{zfs}^{A,B}$.

$$\hat{H}_{zfs}^{A,B} = \boldsymbol{S^{A,B^T}} \cdot \boldsymbol{D^{A,B}} \cdot \boldsymbol{S^{A,B}} = \sum_{i,j=x,y,z} \hat{S}_i^{A,B} \cdot D_{ij}^{A,B} \cdot \hat{S}_j^{A,B}$$

$$\widehat{H}_{zfs} = \widehat{H}_{zfs}^{A} \otimes I_3 + I_3 \otimes \widehat{H}_{zfs}^{B}$$

$$\boldsymbol{D^{A,B}} = R^{A,B}\boldsymbol{D}R^{A,B^T}$$

$$\boldsymbol{D} = \begin{bmatrix} D_x & 0 & 0 \\ 0 & D_y & 0 \\ 0 & 0 & D_z \end{bmatrix} = \begin{bmatrix} -\frac{1}{3}D + E & 0 & 0 \\ 0 & -\frac{1}{3}D - E & 0 \\ 0 & 0 & \frac{2}{3}D \end{bmatrix}$$

Here, $\boldsymbol{D^{A,B}}$ is the molecular D tensor for triplets A and B. Similarly, to the g tensor, the D tensor may be written in its principal frame as $\boldsymbol{D}$. The D tensor arising from magnetic dipolar coupling is traceless (i.e. $Tr(\boldsymbol{D}) = D_x + D_y + D_z = 0$) and as a result, the tensor can be parametrized using only two values: $D = \frac{3}{2}D_z$ and $E = \frac{1}{2}(D_x - D_y)$. As with the g tensor, the D tensor is defined in the molecular frame, and principal axes for each triplet may not be aligned with each other or the magnetic field. As a result, we can apply an arbitrary rotation $R^{A,B}$ to the D tensor to define a particular intertriplet orientation as well as the orientations with respect to the applied field.

To describe the exchange interaction between triplets A and B, we define the exchange Hamiltonian $\widehat{H}_{ex}$ as follows:[10]

$$\widehat{H}_{ex} = \widehat{\boldsymbol{S}}^{\boldsymbol{A^T}} \cdot \boldsymbol{J} \cdot \widehat{\boldsymbol{S}}^{\boldsymbol{B}} = \sum_{i,j=x,y,z} J_{ij}\hat{S}_i^A \otimes \hat{S}_j^B$$

In molecular systems, the isotropic exchange is typically the dominant portion of the exchange interaction. Accordingly, we can simplify the expression for $\widehat{H}_{ex}$ as follows where we define the scalar exchange coupling constant as $J_{iso} = J$.

$$\hat{H}_{ex} = J(\hat{S}_x^A \otimes \hat{S}_x^B + \hat{S}_y^A \otimes \hat{S}_y^B + \hat{S}_z^A \otimes \hat{S}_z^B)$$

We will provide an illustrative example of the construction of the spin Hamiltonian matrix representation under the assumption that the molecular axes of the two triplets, and their respective g and D tensor principal axes, are aligned with each other. We use a general magnetic field vector $\boldsymbol{B^T} = [B_x \quad B_y \quad B_z]$ and use the triplet Cartesian spin operators we defined previously.

$$\hat{H}_{zee}^{A,B} = \mu_B [B_x \quad B_y \quad B_z] \cdot \begin{bmatrix} g_x & 0 & 0 \\ 0 & g_y & 0 \\ 0 & 0 & g_z \end{bmatrix} \cdot \begin{bmatrix} \hat{S}_x^{A,B} \\ \hat{S}_y^{A,B} \\ \hat{S}_z^{A,B} \end{bmatrix} = \mu_B (B_x g_x \hat{S}_x^{A,B} + B_y g_y \hat{S}_y^{A,B} + B_z g_z \hat{S}_z^{A,B})$$

$$\hat{H}_{zee}^{A,B} = \mu_B \left(B_x g_x \frac{1}{\sqrt{2}} \begin{bmatrix} 0 & 1 & 0 \\ 1 & 0 & 1 \\ 0 & 1 & 0 \end{bmatrix} + B_y g_y \frac{i}{\sqrt{2}} \begin{bmatrix} 0 & -1 & 0 \\ 1 & 0 & -1 \\ 0 & 1 & 0 \end{bmatrix} + B_z g_z \begin{bmatrix} 1 & 0 & 0 \\ 0 & 0 & 0 \\ 0 & 0 & -1 \end{bmatrix} \right)$$

$$\hat{H}_{zee}^{A,B} = \begin{bmatrix} \mu_B g_z B_z & \frac{1}{\sqrt{2}} \mu_B (g_x B_x - i g_y B_y) & 0 \\ \frac{1}{\sqrt{2}} \mu_B (g_x B_x + i g_y B_y) & 0 & \frac{1}{\sqrt{2}} \mu_B (g_x B_x - i g_y B_y) \\ 0 & \frac{1}{\sqrt{2}} \mu_B (g_x B_x + i g_y B_y) & -\mu_B g_z B_z \end{bmatrix}$$

Using the triplet Zeeman Hamiltonians, we can construct the triplet pair Zeeman Hamiltonian and rotate it into the coupled basis. As we defined the spin operators, the rows and columns are ordered from lowest to highest multiplicity (e.g S = 0, S = 1, S = 2) and highest M_s value to lowest (e.g. M_s = +2, M_s = +1, M_s = 0, M_s = -1, M_s = -2).

$$\hat{H}_{zee} = \hat{H}_{zee}^A \otimes I_3 + I_3 \otimes \hat{H}_{zee}^B$$

$$\hat{H}_{zee}$$

$$= \begin{bmatrix} 0 & 0 & 0 & 0 & 0 & 0 & 0 & 0 & 0 \\ 0 & \mu_B g_z B_z & \frac{1}{\sqrt{2}}\mu_B(g_x B_x - i g_y B_y) & 0 & 0 & 0 & 0 & 0 & 0 \\ 0 & \frac{1}{\sqrt{2}}\mu_B(g_x B_x + i g_y B_y) & 0 & \frac{1}{\sqrt{2}}\mu_B(g_x B_x - i g_y B_y) & 0 & 0 & 0 & 0 & 0 \\ 0 & 0 & \frac{1}{\sqrt{2}}\mu_B(g_x B_x + i g_y B_y) & -\mu_B g_z B_z & 0 & 0 & 0 & 0 & 0 \\ 0 & 0 & 0 & 0 & 2\mu_B g_z B_z & \mu_B(g_x B_x - i g_y B_y) & 0 & 0 & 0 \\ 0 & 0 & 0 & 0 & \mu_B(g_x B_x + i g_y B_y) & \mu_B g_z B_z & \mu_B(g_x B_x - i g_y B_y) & 0 & 0 \\ 0 & 0 & 0 & 0 & 0 & \mu_B(g_x B_x + i g_y B_y) & 0 & \frac{\sqrt{6}}{2}\mu_B(g_x B_x - i g_y B_y) & 0 \\ 0 & 0 & 0 & 0 & 0 & 0 & \frac{\sqrt{6}}{2}\mu_B(g_x B_x + i g_y B_y) & -\mu_B g_z B_z & \mu_B(g_x B_x - i g_y B_y) \\ 0 & 0 & 0 & 0 & 0 & 0 & 0 & \mu_B(g_x B_x + i g_y B_y) & -2\mu_B g_z B_z \end{bmatrix}$$

In the limit of an isotropic g-tensor ($g_x = g_y = g_z = g_e = g$), $\hat{H}_{zee}$ is independent of the orientation of the molecular frame with respect to the external field. As a result, we can take the magnetic field vector purely along the quantization axis B_z (i.e. $B_z = B$) and obtain a simplified, diagonal $\hat{H}_{zee}$:

$$\hat{H}_{zee} = \begin{bmatrix} 0 & 0 & 0 & 0 & 0 & 0 & 0 & 0 & 0 \\ 0 & \mu_B g B & 0 & 0 & 0 & 0 & 0 & 0 & 0 \\ 0 & 0 & 0 & 0 & 0 & 0 & 0 & 0 & 0 \\ 0 & 0 & 0 & -\mu_B g B & 0 & 0 & 0 & 0 & 0 \\ 0 & 0 & 0 & 0 & 2\mu_B g B & 0 & 0 & 0 & 0 \\ 0 & 0 & 0 & 0 & 0 & \mu_B g B & 0 & 0 & 0 \\ 0 & 0 & 0 & 0 & 0 & 0 & 0 & 0 & 0 \\ 0 & 0 & 0 & 0 & 0 & 0 & 0 & -\mu_B g B & 0 \\ 0 & 0 & 0 & 0 & 0 & 0 & 0 & 0 & -2\mu_B g B \end{bmatrix}$$

We next compute the zero-field splitting Hamiltonian $\hat{H}_{zfs}$ and rotate it into the coupled basis.

$$\widehat{H}_{zfs}^{A,B} = \begin{bmatrix} \hat{S}_x^{A,B} & \hat{S}_y^{A,B} & \hat{S}_z^{A,B} \end{bmatrix} \cdot \begin{bmatrix} -\frac{1}{3}D + E & 0 & 0 \\ 0 & -\frac{1}{3}D - E & 0 \\ 0 & 0 & \frac{2}{3}D \end{bmatrix} \cdot \begin{bmatrix} \hat{S}_x^{A,B} \\ \hat{S}_y^{A,B} \\ \hat{S}_z^{A,B} \end{bmatrix}$$

$$= \left(-\frac{1}{3}D + E\right)\hat{S}_x^{A,B^2} + \left(-\frac{1}{3}D - E\right)\hat{S}_y^{A,B^2} + \frac{2}{3}D\hat{S}_z^{A,B^2}$$

$$= D\left(\hat{S}_z^{A,B^2} - \frac{1}{3}\hat{S}^2\right) + E(\hat{S}_x^{A,B^2} - \hat{S}_y^{A,B^2})$$

$$\widehat{H}_{zfs}^{A,B} = \begin{bmatrix} \frac{1}{3}D & 0 & E \\ 0 & -\frac{2}{3}D & 0 \\ E & 0 & \frac{1}{3}D \end{bmatrix}$$

$$\widehat{H}_{zfs} = \begin{bmatrix} \frac{1}{3}D & 0 & E \\ 0 & -\frac{2}{3}D & 0 \\ E & 0 & \frac{1}{3}D \end{bmatrix} \otimes \begin{bmatrix} 1 & 0 & 0 \\ 0 & 1 & 0 \\ 0 & 0 & 1 \end{bmatrix} + \begin{bmatrix} 1 & 0 & 0 \\ 0 & 1 & 0 \\ 0 & 0 & 1 \end{bmatrix} \otimes \begin{bmatrix} \frac{1}{3}D & 0 & E \\ 0 & -\frac{2}{3}D & 0 \\ E & 0 & \frac{1}{3}D \end{bmatrix}$$

$$\hat{H}_{zfs} = \begin{bmatrix} 0 & 0 & 0 & 0 & \frac{2}{\sqrt{3}}E & 0 & \frac{2\sqrt{2}}{3}D & 0 & \frac{2}{\sqrt{3}}E \\ 0 & -\frac{1}{3}D & 0 & -E & 0 & 0 & 0 & 0 & 0 \\ 0 & 0 & \frac{2}{3}D & 0 & 0 & 0 & 0 & 0 & 0 \\ 0 & -E & 0 & -\frac{1}{3}D & 0 & 0 & 0 & 0 & 0 \\ \frac{2}{\sqrt{3}}E & 0 & 0 & 0 & \frac{2}{3}D & 0 & \frac{\sqrt{6}}{3}E & 0 & 0 \\ 0 & 0 & 0 & 0 & 0 & -\frac{1}{3}D & 0 & E & 0 \\ \frac{2\sqrt{2}}{3}D & 0 & 0 & 0 & \frac{\sqrt{6}}{3}E & 0 & -\frac{2}{3}D & 0 & \frac{\sqrt{6}}{3}E \\ 0 & 0 & 0 & 0 & 0 & E & 0 & -\frac{1}{3}D & 0 \\ \frac{2}{\sqrt{3}}E & 0 & 0 & 0 & 0 & 0 & \frac{\sqrt{6}}{3}E & 0 & \frac{2}{3}D \end{bmatrix}$$

As shown above, $\hat{H}_{zfs}$ is not diagonal in the coupled basis. Thus, the eigenstates of the total spin Hamiltonian $\hat{H}$ will not all strictly be of pure spin multiplicity S or M_S. In the limit of large exchange ($J \gg D$) or high magnetic fields, the zero-field splitting becomes a small contribution to the overall spin Hamiltonian, and thus the eigenstates of $\hat{H}$ approach the pure spin coupled basis we obtained by diagonalization of the $\hat{S}^2$ operator. Still, by examination of $\hat{H}_{zfs}$, there are off-diagonal elements connecting the $\left|\,{}^1(TT)_0\right\rangle$ state with $\left|\,{}^5(TT)_0\right\rangle$ depending on the parameter D and $\left|\,{}^5(TT)_{\pm 2}\right\rangle$ depending on the parameter E. If the initially generated triplet pair state of singlet fission is the pure singlet state $\left|\,{}^1(TT)_0\right\rangle$, these off-diagonal elements allow for the population of the quintet sublevels, which we can probe by EPR spectroscopy.

Last, we construct the exchange Hamiltonian $\hat{H}_{ex}$ using only the isotropic component of the J tensor and rotate it into the coupled basis.

$$\widehat{H}_{ex} = J\left(\frac{1}{\sqrt{2}}\begin{bmatrix}0 & 1 & 0\\ 1 & 0 & 1\\ 0 & 1 & 0\end{bmatrix}\otimes\frac{1}{\sqrt{2}}\begin{bmatrix}0 & 1 & 0\\ 1 & 0 & 1\\ 0 & 1 & 0\end{bmatrix}+\frac{i}{\sqrt{2}}\begin{bmatrix}0 & -1 & 0\\ 1 & 0 & -1\\ 0 & 1 & 0\end{bmatrix}\otimes\frac{i}{\sqrt{2}}\begin{bmatrix}0 & -1 & 0\\ 1 & 0 & -1\\ 0 & 1 & 0\end{bmatrix}\ldots\right.$$

$$\left.+\begin{bmatrix}1 & 0 & 0\\ 0 & 0 & 0\\ 0 & 0 & -1\end{bmatrix}\otimes\begin{bmatrix}1 & 0 & 0\\ 0 & 0 & 0\\ 0 & 0 & -1\end{bmatrix}\right)$$

$$\widehat{H}_{ex} = \begin{bmatrix}-2J & 0 & 0 & 0 & 0 & 0 & 0 & 0 & 0\\ 0 & -J & 0 & 0 & 0 & 0 & 0 & 0 & 0\\ 0 & 0 & -J & 0 & 0 & 0 & 0 & 0 & 0\\ 0 & 0 & 0 & -J & 0 & 0 & 0 & 0 & 0\\ 0 & 0 & 0 & 0 & J & 0 & 0 & 0 & 0\\ 0 & 0 & 0 & 0 & 0 & J & 0 & 0 & 0\\ 0 & 0 & 0 & 0 & 0 & 0 & J & 0 & 0\\ 0 & 0 & 0 & 0 & 0 & 0 & 0 & J & 0\\ 0 & 0 & 0 & 0 & 0 & 0 & 0 & 0 & J\end{bmatrix}$$

The isotropic exchange Hamiltonian is diagonal in the coupled basis. As can be observed, the S = 0 singlet state will be separated from the S = 1 triplets by J and by the S = 2 quintet manifold by $3J$. By the convention chosen, a positive J value places the singlet state lowest in energy.

We can then write the total spin Hamiltonian with the magnetic field aligned along the molecular z-axis.

$$\begin{bmatrix}-2J & 0 & 0 & 0 & \frac{2}{\sqrt{3}}E & 0 & \frac{\sqrt{6}}{3}D & 0 & \frac{2}{\sqrt{3}}E\\ 0 & \mu_B gB-\frac{1}{3}D-J & 0 & -E & 0 & 0 & 0 & 0 & 0\\ 0 & 0 & \frac{2}{3}D-J & 0 & 0 & 0 & 0 & 0 & 0\\ 0 & -E & 0 & -\mu_B gB-\frac{1}{3}D-J & 0 & 0 & 0 & 0 & 0\\ \frac{2}{\sqrt{3}}E & 0 & 0 & 0 & 2\mu_B gB+\frac{2}{3}D+J & 0 & \frac{\sqrt{6}}{3}E & 0 & 0\\ 0 & 0 & 0 & 0 & 0 & \mu_B gB-\frac{1}{3}D+J & 0 & E & 0\\ \frac{\sqrt{6}}{3}D & 0 & 0 & 0 & \frac{\sqrt{6}}{3}E & 0 & -\frac{2}{3}D+J & 0 & \frac{\sqrt{6}}{3}E\\ 0 & 0 & 0 & 0 & 0 & E & 0 & -\mu_B gB-\frac{1}{3}D+J & 0\\ \frac{2}{\sqrt{3}}E & 0 & 0 & 0 & 0 & 0 & \frac{\sqrt{6}}{3}E & 0 & -2\mu_B gB+\frac{2}{3}D+J\end{bmatrix}$$

Citations

(1) Weil, J. A.; Bolton, J. R. Basic Principles of Paramagnetic Resonance. In *Electron Paramagnetic Resonance*; John Wiley & Sons, Ltd, 2006; pp 1–35. https://doi.org/10.1002/9780470084984.ch1.

(2) McWeeny, R. *Spins in Chemistry*; Dover Publications, 2004.

(3) Merrifield, R. E. Magnetic Effects on Triplet Exciton Interactions. *Pure and Applied Chemistry* **1971**, *27* (3), 481–498. https://doi.org/10.1351/pac197127030481.

(4) Benk, H.; Sixl, H. Theory of Two Coupled Triplet States. *Molecular Physics* **1981**, *42* (4), 779–801. https://doi.org/10.1080/00268978100100631.

(5) Scholes, G. D. Correlated Pair States Formed by Singlet Fission and Exciton–Exciton Annihilation. *J. Phys. Chem. A* **2015**, *119* (51), 12699–12705. https://doi.org/10.1021/acs.jpca.5b09725.

(6) Collins, M. I.; McCamey, D. R.; Tayebjee, M. J. Y. Fluctuating Exchange Interactions Enable Quintet Multiexciton Formation in Singlet Fission. *J. Chem. Phys.* **2019**, *151* (16), 164104. https://doi.org/10.1063/1.5115816.

(7) Smyser, K. E.; Eaves, J. D. Singlet Fission for Quantum Information and Quantum Computing: The Parallel JDE Model. *Sci Rep* **2020**, *10* (1), 18480. https://doi.org/10.1038/s41598-020-75459-x.

(8) Lewis, S. G.; Smyser, K. E.; Eaves, J. D. Clock Transitions Guard against Spin Decoherence in Singlet Fission. *J. Chem. Phys.* **2021**, *155* (19), 194109. https://doi.org/10.1063/5.0069344.

(9) Bayliss, S. L.; Weiss, L. R.; Kraffert, F.; Granger, D. B.; Anthony, J. E.; Behrends, J.; Bittl, R. Probing the Wave Function and Dynamics of the Quintet Multiexciton State with Coherent Control in a Singlet Fission Material. *Phys. Rev. X* **2020**, *10* (2), 021070. https://doi.org/10.1103/PhysRevX.10.021070.

(10) Bencini, A.; Gatteschi, D. *EPR of Exchange Coupled Systems*; Courier Corporation, 2012.

Ryan D. Ribson

(585) 703-6623
ryan.ribson@gmail.com
514 N. Wilson Ave., Pasadena, CA 91106

Education History

California Institute of Technology — **PhD in Chemistry**
Pasadena, CA — 2014 – 2022

Adviser: Professor Ryan G. Hadt

University of Rochester — **BS in Chemistry**
Rochester, NY — 2010 – 2014

Adviser: Professor Daniel J. Weix

Employment History

September 2014 – June 2020 Teaching Assistant for the Chemistry Department at the California Institute of Technology

August 2011 – May 2014 Teaching Assistant for the Chemistry Department at the University of Rochester

May 2011 – November 2011 Technical Assistant for Professor Lynne Maquat, Department of Biochemistry and Biophysics, University of Rochester

Teaching Assistant Experience

California Institute of Technology

Ch 153c – Advanced Inorganic Chemistry, Spring 2020
Ch 112 – Inorganic Chemistry, Fall 2016
Ch 102 – Introduction to Inorganic Chemistry, Spring 2016
Ch 4a,b – Synthesis and Analysis of Organic and Inorganic Compounds, Winter and Spring 2015
Ch 8 – Experimental Procedures of Synthetic Chemistry for Premedical Students, Fall 2014

University of Rochester

CHM 204 – Organic Chemistry II, Spring 2013, 2014
CHM 203 – Organic Chemistry I, Fall 2012, Fall 2013
CHM 132 Lab – Chemical Concepts, Systems, Practice II Lab, Spring 2013
CHM 211 – Inorganic Chemistry I, Fall 2012
CHM 172Q – Freshman Organic Chemistry, Spring 2012
CHM 171Q – Freshman Organic Chemistry, Fall 2011

Publications

1. Ribson, R. D.; Choi, G.; Hadt, R. G.; Agapie, T. "Controlling Singlet Fission with Coordination Chemistry-Induced Assembly of Dipyridyl Pyrrole Bipentacenes", *ACS Cent. Sci.* **2020**, *6*, 2088 – 2096.

2. Follmer, A. H.†; Ribson, R. D.†; Oyala, P. H.; Chen, G. Y.; Hadt, R. G. "Understanding Covalent versus Spin-Orbit Coupling Contributions to Temperature Dependent Electron Spin Relaxation in Cupric and Vanadyl Phthalocyanines", *J. Phys. Chem. A.* **2020**, *124*, 9252 – 9260. †Co-first authors.

3. Stroscio, G. D.; Ribson, R. D.; Hadt, R. G. "Quantifying Entatic States in Photophysical Processes: Applications to Copper Photosensitizers", *Inorg. Chem.* **2019**, *58*, 16800-16817.

4. Wotal A. C., Ribson, R. D., and Weix. D. J. "Stoichiometric Reactions of Acynickel(II) Complexes with Electrophiles and the Catalytic Synthesis of Ketones", *Organometallics*. **2014**, *33*, 5874 – 5881.

Presentations

- "Influencing Singlet Fission via Coordination Chemistry in Dipyridyl Pyrrole Bipentacenes" - ACS National Meeting Spring 2021, Virtual (oral)
    - Physical Division Symposium: Singlet Fission Materials and Mechanisms for Solar Energy Conversion
- "Controlling Singlet Fission with Coordination Chemistry" – Division of Chemistry and Chemical Engineering, Caltech Seminar Day, Pasadena, CA 2020 (oral)

Honors & Awards

- National Science Foundation Graduate Research Fellowship Honorable Mention (2014, 2015, 2016)
- University of Rochester:
    - Graduated *cum laude* with highest distinction
    - Phi Beta Kappa honor society member
    - Carl A. Whiteman, Jr. Teaching Award (2014)
    - ACS Undergraduate Organic Chemistry Award (2014)
    - Merck Index Award (2011)